Synthesis and Characterization of Nanocrystalline CuCl Hybrid Films for Electroluminescent Device Fabrication

A Thesis Submitted in Partial Fulfilment of the Requirements for the Degree of Doctor of Philosophy (Electronic Engineering)

By

Md. Monjarul Alam

B. Sc. (Hon.), M.Sc., M. Phil

Research Supervisor

Prof. Patrick J. McNally, BE, MSc, PhD, CPhys, FInstP, FIEI, C Eng, MIEEE

November, 2011

Declaration

I hereby certify that this material, which I now submit for assessment on the programme of study leading to the award of Doctor of Philosophy is entirely my own work, that I have exercised reasonable care to ensure that the work is original, and does not to the best of my knowledge breach any law of copyright, and has not been taken from the work of others save and to the extent that such work has been cited and acknowledged within the text of my work.

Student Number: _ 57126739 _ _ Signed: _ _ _ _ _ _ _ _ _ _ _

Date: _ _ _ _ _ _ _ _ _ _ _ _ _ _ _ _ _ _

Dedication

THIS THESIS IS DEDICATED

TO MY LATE

FATHER (MD. JANARUDDIN BISWAS)

&

DAUGHTER (FATHIMA BINTHY MONJARUL)

Acknowledgements

First of all, I am grateful to almighty ALLAH, who is the most merciful and most compassionate to me for the strength to complete this work.

I would like to express my sincere thanks to my supervisor, Prof. Patrick J. McNally, School of Electronic Engineering in Dublin City University. Without his wisdom and foresight, I may have never started down the path that I have taken. His immensely erudite leadership and guidance have made the trip enjoyable and fruitful. I can only hope that one day I can be as good as a role model for future engineers and scientists as he has been for me.

I am also thankful to Dr. Stephen Daniels, Executive Director of the National Centre for Plasma Science and Technology (NCPST) for his, inspiration and constructive suggestions from time to time during my research work.

I would also like to thank our collaborators on this project, Dr. Louise Bradley and D. Danieluk of the Semiconductor Photonics Group, Trinity College, Dublin, Ireland, for granting me access to carry out temperature dependent photoluminescence measurements in their laboratory.

The assistance of all the staff in the School of Electronic Engineering is greatly appreciated. Particular thanks to Billy Roarty and Robert Clare for their technical support.

I am especially grateful to Dr. Francis Olabanji Lucus, Dr. M. Morshed and Dr. Sumsun Naher for their valuable discussion and inspiration throughout this work. I wish to thank all of my fellow postgraduate students within NPL, Dublin City University for their support and friendship; special thanks to Aidan Cowley, Ken Horan, David Allen, K.V.

Rajani, Ameera Ahmed, Barry Foy, Chiu-S Wons, Yang Zhang and Evgueni Gudimenko.

I would like to acknowledge the project funding provided by Enterprise Ireland, Science Foundation Ireland and the Irish Higher Education Authority.

I would like to acknowledge Islamic University, Kushtia, Bangladesh for approving my study leave to acquire the PhD degree. Also thanks to my entire departmental (Applied Physics, Electronic & Com. Eng.) teachers and colleagues for their support.

There are many people that I would like to thank, without their mental and physical support this Ph.D. thesis would not have been possible. Finally, I would love to express my sincere thanks to my family. To my Mother, Monjuara Begum: For mentoring, monitoring and persistently pointing out the importance of good education to me right from the beginning up to this stage. Your endless financial support and guidance has allowed me to acquire my goals and dreams. I can never repay you for what you have given me.

To my brothers and sister, Abdul Ohab, Toki, Sadia and Shakira: For their endless love, care, encouragement and understanding during this period.

To my wife Nupur: There are no words that can describe what she means to me. She has been beside me as a friend and a loyal supporter. I thank her so much for enduring the long experiments that made me disappear for years, for being there when I needed her most, and for being the love of my life.

[MD. MONJARUL ALAM]

Dublin, 2011

Abstract

Cuprous (I) chloride (CuCl) is an intensively studied inorganic material, particularly for its excitonic related linear/non-linear optical processes. This is due in large measure to its very large excitonic binding energies (~190 meV) which are much larger than those of III-V and II-VI semiconductors resulting in a high stability of the exciton even at room temperature. Thus CuCl should be an extremely efficient light emitter due to exciton-mediated electron-hole recombination.

In this study, CuCl nanocrystals were synthesized, embedded in organic Polysilsesquioxane (PSSQ) matrices, deposited on a variety of substrates via the spin coating method and its properties studied optimized for optical and electrical behaviour. Room temperature X-ray diffraction (XRD) confirmed the preferential growth of CuCl nanocrystals whose average radius size was ≈14-22 nm in the (111) orientation. Scanning Electron Microscopy (SEM) measurements revealed that the average surface area of the films covered by the CuCl nanocrystals was ≈40-60 % of its total surface area. Atomic Force Microscopy (AFM) revealed that the average roughness of the film increases with the annealing time.

Room temperature UV-Vis absorption revealed both $Z_{1,2}$ and Z_3 excitonic absorption features at ≈368 nm (≈3.37 eV) and ≈377 nm (≈3.29 eV), respectively. Room temperature photoluminescence (PL) and cathodoluminescence (CL) measurements exhibit strong emission in the UV region. Electronic transitions of the CuCl hybrid films were studied using temperature and power dependent PL spectroscopy measurements. Thermal quenching of the Z_3 free exciton PL emission in hybrid films has been observed. The bi-exciton emission peak intensity follows a quadratic dependency on power in the excitation power range <10 $kWcm^{-2}$. The results obtained for the CuCl hybrid films are comparable to those of vacuum evaporated and sputtered CuCl films reported in the literature.

Room temperature electrical characterization and electroluminescence (EL) emission were investigated using Au/CuCl hybrid film/ITO structures. Field dependent DC conduction studies exhibit ohmic conduction in the lower field region and electrode

limited Schottky emission type conduction for higher field regions. The device showed bright electroluminescent emission at ~384 nm when subjected to an AC voltage of about 100 volts peak to peak.

One challenge linked with the use of CuCl is that it is sensitive to moist air, i.e. CuCl is not stable in ambient conditions; it forms oxyhalides of Cu(II) within a few days of exposure to air. The ageing effects on CuCl hybrid films were extensively investigated and this research indicates that the blend of CuCl with an organic material in particular PSSQ may be a useful interim solution to the degradation of CuCl films.

Proof-of-concept p-CuCl/n-ZnO heterojunction diodes were fabricated and their structural, optical and electrical properties were investigated. XRD measurements confirm that no intermediate compound forms at the heterojunction. Room temperature I-V characteristics show diode-like behaviour with the values of barrier height and ideality factor equal to 0.72 eV and 4.6, respectively. This structure could be useful for photovoltaic cell fabrication, particularly for the blue/UV spectral regions.

Table of Contents

		Page No.
Declaration		II
Dedication		III
Acknowledgements		IV
Abstract		VI
Table of Contents		VII
Chapter 1	**INTRODUCTION AND OVERVIEW**	
1.1	General Introduction	02
1.2	Lighting Applications of Electroluminescent Devices (ELDs)	03
1.3	Electroluminescent Device Structures	05
1.4	Wide Band Gap Materials	08
1.5	Motivation of this Research	08
1.6	Thesis Organization	12
Chapter 2	**MATERIALS AND METHODS**	
2.1	Materials	20
	2.1.1 Copper (II) Chloride	20
	2.1.2 Copper (I) Chloride	22
	2.1.3 α-D-Glucose	26
	2.1.4 Polysilsesquioxane (PSSQ)	27
2.2	Spin Coating Method	29
	2.2.1 Introduction	29
	2.2.2 Substrate Preparation	29
	2.2.3: Coating Solution	29
	2.2.4 Coating Environment	30
	2.2.5 Spin Coating Process	30
	2.2.6 Advantages and Disadvantages	32

2.3	Hybrid Film Deposition	33
Chapter 3	**CHARACTERIZATION TECHNIQUES**	
3.1	X-Ray Diffraction (XRD)	39
	3.1.1 Introduction	39
	3.1.2 Bragg's law	40
	3.1.3 Experimental Techniques for X-ray Diffraction	42
3.2	Scanning Electron Microscopy (SEM)	43
	3.2.1 Introduction	43
	3.2.2 X-ray Microanalysis	44
	3.2.3 Scanning Process	45
3.3	Atomic Force Microscopy (AFM)	47
3.4	X-ray Photoelectron Spectroscopy (XPS)	49
3.5	Absorption Spectroscopy	50
	3.5.1 UV-Vis Spectroscopy	51
	3.5.2 Fourier Transform Infrared (FTIR) Spectroscopy	52
3.6	Luminescence Spectroscopy	55
	3.6.1 Photoluminescence (PL)	56
	3.6.1.1 Experimental Techniques for PL Measurement	57
	3.6.2 Cathodoluminescence (CL)	58
	3.6.3 Electroluminescence (EL)	59
3.7	Electrical Characterization	60
	3.7.1 Current-Voltage (I-V) Characteristics	60
Chapter 4	**STRUCTURAL & MORPHOLOGICAL PROPERTIES**	
4.1	Introduction	67
4.2	Synthesis of CuCl Nanocrystals & Film Deposition	68
4.3	X-ray Diffraction	69
4.4	Scanning Electron Microscopy	74
4.5	Atomic Force Microscopy	77

Chapter 5 **OPTICAL PROPERTIES**

5.1 Introduction 85

5.2 Fourier Transform Infrared Spectroscopy 86

5.3 Surface Chemical Analysis by XPS 87

5.4 UV-Vis Absorption 90

5.5 Photoluminescence 92

5.6 Temperature Dependent Photoluminescence of CuCl Hybrid Films 96

5.6.1 Excitonic Transitions in γ-CuCl Hybrid Film 96

5.6.2 Thermal Quenching of PL Intensity 99

5.6.3 Exciton Line Broadening 101

5.6.4 Exciton Energy Shifting 102

5.6.5 Exciton Line Shift with Temperature 105

5.7 Cathodoluminescence 107

Chapter 6 **ELECTRICAL PROPERTIES**

6.1 Introduction 118

6.2 Conductivity Measurements 120

6.3 Arrhenius Plot 122

6.4 Charge Transport Mechanism Through the Organic-Inorganic CuCl Hybrid Film 123

6.5 Evaluation of Electronic Parameters for the Au/hybrid film/ITO Structure 129

6.6 Voltage and Temperature Dependent Capacitance Measurements 133

6.7 Interface State Density Properties of the Au/CuCl hybrid film/ITO Schottky Diode 135

6.8 Electroluminescence (EL) 138

Chapter 7 **AGEING EFFECTS**

7.1 Introduction 147

7.2 X-ray Diffraction Spectra 148

7.3 Fourier Transform Infrared Spectra 149

7.4 UV-Vis Spectra 150

7.5 Photoluminescence Spectra 151

7.6 Electroluminescence 152

Chapter 08 **HETEROJUNCTION LIGHT EMITTING DIODES**

8.1 Introduction 157

8.2 Structural Properties 158

8.3 Optical Properties 159

8.4 Electrical properties 162

Chapter 09 **CONCLUSIONS AND FUTURE WORK**

9.1 Conclusions 170

9.2 Suggestions for Further Work 172

APPENDIX A 175

APPENDIX B 180

List of Tables 181

List of Figures 182

List of Publications 187

Table of Acronyms 189

CHAPTER 1

INTRODUCTION AND OVERVIEW

Excessive use of the earth's resources causes an increase in the demand on the resources and also causes environmental problems. Global warming is now almost universally accepted as a serious problem caused by human activity mainly via burning fossil fuels that demands strong remedial action as soon as possible. Nanotechnology will continue to provide breakthrough solutions for energy conversion, energy storage, and carbon encapsulation. This chapter presents the background, a brief literature review and the motivation for this research.

1.1 General Introduction

Globally, energy consumption is one of the major problems in the 21st century. Development of civilization and technology increases the demand for energy. The World Energy Council projects that primary energy demands will be tripled by 2050 [1]. Annually, more than ~10^{13} kWh of electricity is produced in the world, and approximately 20% of this electricity is used for lighting applications [2, 3]. Today, 80% of the world's electrical production comes from fossil and nuclear fuels, and virtually all transportation is fuelled by liquid petroleum. The use of oil, coal and other fossil energy sources are polluting the planet with greenhouse gases [4]. The supply of oil, which is the primary source of energy, is gradually running out [5]. There are two ways of improving the energy supply problem: (i) by using renewable energy or natural energy resources such as air, solar, ocean wave, etc. and (ii) reducing the use of energy i.e. saving energy [6]. Nanotechnology research may contribute to the latter possibility in particular. It should be possible to reduce significantly energy consumption in the world by converting all conventional white-light sources into energy efficient light emitting diode (LED) light sources [7].

In September 2009, the United States Department of Energy announced the Bright Tomorrow Lighting Prize competition [8]. This is the first government-sponsored technology competition to promote the development and manufacture of high-quality, high-efficiency solid-state lighting (SSL) products to replace conventional incandescent light bulbs [9]. Following that, U.S. Department of Energy announced a fund of $25 million for advanced research, development, and market adoption of SSL technology [10]. Similarly, the European Union (EU) funded €12.5 million

through the Seventh Framework Programme (FP7) for the development of organic-light-emitting-diode (OLED) technology for the commercial market [11]. This project included participants from six countries including lighting specialist Novaled, the University of Ghent, Philips and Siemens. Several companies currently offer LED lamps for general lighting purposes [12], for example, the American C. Crane Company has a product called the "Geobulb" [13], in the Netherlands, a company called Lemnis Lighting offers a dimmable LED lamp called Pharox [14], and Eternleds Inc. offers a bulb called HydraLux-4 which uses liquid cooling of the LED chips [15]. Toshiba, one of the largest lighting production companies in Japan ended the production of incandescent bulbs from March 2010 and they plan to focus on more energy efficient LED lights. In a related development the Philips Lighting Company has ceased research on compact fluorescents, and decided to invest > 5% of the company's global lighting revenue on research and development of solid-state lighting [16].

1.2 Lighting Applications of Electroluminescent Devices (ELDs)

Electroluminescence is the process whereby light is emitted in response to an electric current passed through a material. In 1907, British scientist H. J. Round discovered electroluminescence using a crystal of silicon carbide and a cat's-whisker detector [17]. In 1955, Rubin Braunstein reported on infrared emission generated by simple diode structures using gallium antimonide (GaSb), gallium arsenide (GaAs), indium phosphide (InP), and silicon-germanium (SiGe) alloys at room temperature and 77 K [18]. In 1962, N. Holonyak developed the first practical visible-spectrum (red) light emitting diode (LED) [19]. S. Nakamura of the Nichia Corporation first demonstrated a high-brightness blue LED in 1995 [20]. This blue LED quickly led to the development of the first white LED by using $Y_3Al_5O_{12}$:Ce, otherwise known as "YAG", phosphor coating to mix yellow light with blue to produce a light that appears white [20]. Since the incandescent light bulb was developed in the late 1800s, various methods have been investigated to produce more efficient light sources.

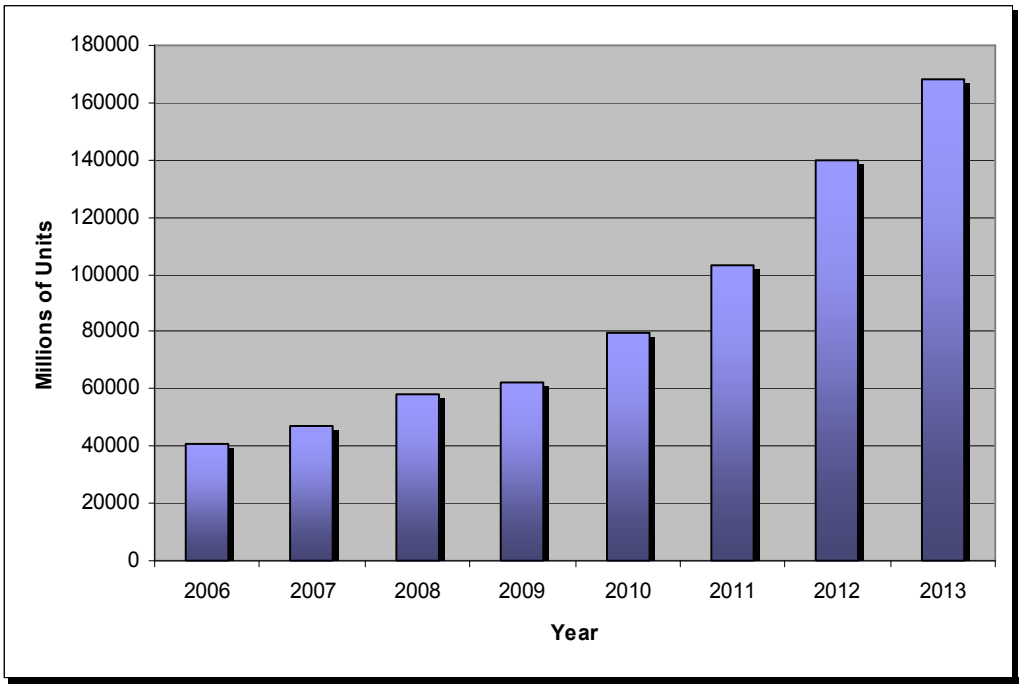

Figure 1.1: Global LED shipment forecast [21]

The efficiency of incandescent lamps and even "high efficiency" compact fluorescent lamps (CFL) are approximately 5% and 20-25%, respectively [22]. European Union and other countries banned the use of incandescent bulbs from 2010. Mercury, an essential material used in compact fluorescent lamps is well known to be a hazardous material. There are some significant issues such as energy consumption, environmental impact and the health of individuals that have inspired research into white light sources based on LEDs [23]. **Figure 1.1** shows that the worldwide demand of LEDs will increase rapidly. Advanced lighting based on solid-state technology will eventually replace conventional incandescent and fluorescent sources in general-lighting applications. Solid-state lighting could be used to reduce the amount of energy required to provide lighting when compared to incandescent light, which are associated with a light output of less than 20 lumens per watt. The efficiency of light emitting diodes is of the order of 160 lumens per watt [24]. Optoelectronic devices operating beyond the 3 electron volts (eV) range also have applications in environmental contaminant decomposition [25]. Increases in efficiency, lifetime, total luminous flux, and reliability are also necessary for solid-state lighting to be a successful general-lighting source. The first-generation devices

use a blue LED with a yellow phosphor for white lighting applications as alluded to earlier. Efficient UV emitters represent a means of pumping highly efficient phosphors to create white light for next-generation solid-state lighting sources. They are particularly attractive because of the wider range of phosphors that can be fluoresced with UV light, and because they can be manufactured more easily than red-green-blue (RGB) white-light devices. If all the conventional white-light sources in the world are converted into energy efficient LED light sources, the total energy consumption could be reduced by ~1,000 TW h yr^{-1}, the equivalent of about 230 typical ~500 MW coal plants, and consequent greenhouse gas emission can be reduced by around 200 million tonnes [26]. As mentioned previously the efficiency of incandescent lamps and "high efficiency" CFLs are approximately 5% and 20-25%, respectively. Solid-state lamps (SSL) have an efficiency of more than 80 % [27] and producing novel CuCl-based solid-state light emitters is the main goal of this research.

1.3 Electroluminescent Device Structures

There are two main types of electroluminescent device (ELD) structures: p-n junction and Metal-Insulator- Semiconductor (MIS) based ELDs. In the p-n junction ELD the p-region is dominated by positive electric charges (holes) and the n-region is dominated by negative electric charges (electrons). The junction serves as a barrier to the flow of the electrons between the p- and the n-regions. This is somewhat similar to the role of the bandgap because it determines how much voltage is needed to be applied to the semiconductor device before the current can flow and the electrons pass across the junction into the p-region. The band structure and schematic diagram of a p-n junction ELD is shown in **figure 1.2**. The energy levels are shifted when a forward voltage is applied across the ELD. Under this condition the concentration of electrons in the conduction band near the junction on the n-side and the concentration of holes in the valence band near the junction on the p-side are significantly increased. The electrons recombine with the holes resulting in the release of energy in the form of photons.

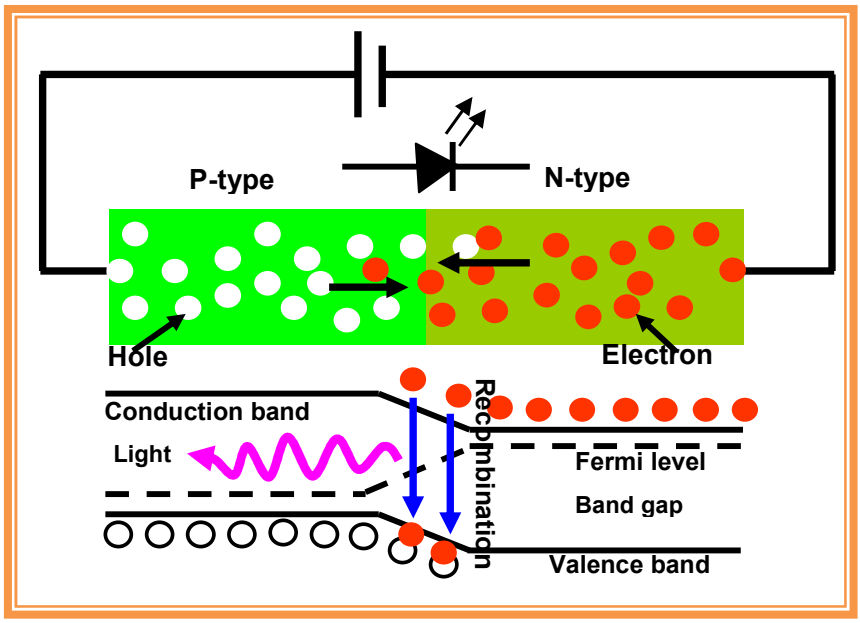

Figure 1.2: Band structure and basic operation of a p-n junction ELD

In the Metal Insulator Semiconductor structure, the light emission occurs due to the hot electron impact excitation of electron-hole pairs. For the MIS structure the EL process involves six primary physical phenomena which are illustrated in **Figure 1.3**.

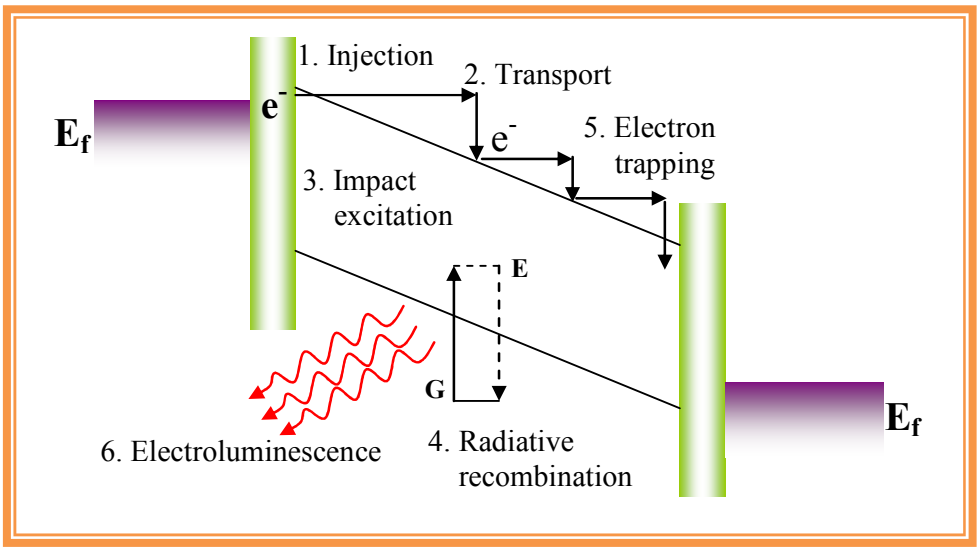

Figure 1.3: Energy band diagram illustrating the six primary physical processes of importance for operation of an MIS based ELD

Firstly, when a sufficiently large voltage is applied to the MIS device, the electrons trapped in interface states are tunnel-emitted into the semiconductor conduction band. Then, these injected electrons are transported across the semiconductor after gaining energy from the applied field. In step 3, during the transition of hot electrons to the semiconductor layer, a fraction of them excite luminescent centres from their ground state to their excited states; concurrently the hot electrons lose energy during this impact excitation. Subsequently the luminescence centre relaxes from its excited state to its ground state, with a probability of releasing energy in the form of photons. In step 5, the transported electrons eventually reach and are trapped in the semiconductor/insulator anode interface. Finally, in step 6, photons are generated by radiative recombination and are emitted as a light from the device [28]. Generally, the luminescence intensity, efficiency and device reliability is higher in p-n junction based ELDs than in MIS structure based ELDs. For a MIS structure based ELD a relatively small fraction of hot electrons release energy as photons and a large number of electrons remain trapped in the insulator whereas in p-n junction based ELDs most of the electrons and holes recombine to release the energy as photons. In this research, the proposed ELD device structure will be initially based on an MIS structure and then later on, we will report on trials of a p-n junction based device.

Material	**E_g(eV)**	**Exciton Binding Energy (meV)**	**Lattice Constant (Å)**	**Structure**
ZnO	3.44	63	3.249	Wurtzite
GaN	3.43	26	4.53	Wurtzite
γ-CuCl	3.39	190	5.420	Zincblende
γ-CuBr	3.072	108	5.677	Zincblende
γ-CuI	3.118	58	6.13	Zincblende
Si	1.12	-	5.431	Diamond

Table 1.1: A selection properties of different semiconductor materials [29]

1.4 Wide Band Gap Materials

The semiconductor band gap, commonly referred to as the energy gap, is defined as the energy difference between the top of the valence band and bottom of the conduction band. Semiconductor materials with an electronic band gap greater than 1 or 2 eV are referred to as wide band gap semiconductor materials. Recently, wide band gap semiconductor materials have become a very important field for research, due to their excellent thermal, optical and electrical characteristics [30]. For the development of blue/UV light emitting devices, II-VI materials such as ZnS, ZnSe and ZnO, III-V materials such as AlN, BN, AlGaN, GaAs and GaN, group IV SiC and group I-VII CuCl has been extensively investigated [31-40]. **Table 1.1** shows some properties of a selection of wide band gap materials.

1.5 Motivation of this Research

At present, III-N compound semiconductor materials has been the most successful materials for the fabrication of short wavelength optoelectronics and also white light emitting diodes (WLED) [41]. III–N compound semiconductor materials such as GaN, InGaN and AlGaN have a wurtzite lattice structure with typically direct band gap energies from 1.9 to 6.2 eV depending on the composition. The growth of GaN single crystal epilayers is still a difficult task because of the lack of high quality non-polar and low-cost substrates lattice matched to GaN. Therefore, they are grown epitaxially in thin single crystal layers on suitable substrates. In these processes, the main problem is the large lattice constant differences between the epilayers and substrate, which leads to the generation of misfit dislocations [42-44]. These misfit dislocations are deleterious to the performance of LEDs produced thereupon.

In 1971, Pankove *et al.* first demonstrated a GaN LED based on the MIS structure since p-type GaN was not available at that time [45]. In 1989, Akasaki *et al.* used Mg as a dopant material to demonstrate a p-type GaN film, and following that they fabricated the first GaN p-n junction LED [46]. The carrier concentration of p-type GaN film was very small. Short lifetimes of these devices due to high defect densities prevented their commercialization. LEDs based on GaN nanocrystals have been reported by many researchers [47-50]. Several processes are used to synthesize

GaN nanocrystals such as the vapor-liquid-solid process, the hydrothermal process, use of single-source precursors, the ammonothermal method, etc. [51-54]. Most of these methods are not usually straightforward and need high temperatures to obtain good quality GaN nanocrystals.

Zinc Oxide (ZnO) is another promising wide direct band gap II-VI semiconductor material with the wurtzite structure for efficient room temperature ultra-violet (UV) light emitting devices. The exciton binding energy of ZnO is 60 meV [55], which is comparatively larger than GaN and ZnO is usually deposited naturally as n-type semiconductor material. It is still difficult to produce highly conductive p-type ZnO semiconductor material [56]. Therefore, for the time being, homo-junction based optoelectronics applications of ZnO are limited. There has been some success on the demonstration of ZnO nanocrystal (nc-ZnO) UV/White ELDs in recent years [57-59]. [$ZnO(CH_3COO)_2 2H_2O$] is a common precursor material for the synthesis of nc-ZnO, while monoethanolamine, and 2-methoxyethanol are well known solvents for [$ZnO(CH_3COO)_2 2H_2O$]. These solvents are harmful to humans and require extra precautions when being used. A high processing temperature of the order of 500 ^{o} C is also required. LEDs based on nanocrystals of other materials like CdSe along with conjugated polymers have also been reported [60-67]. However these devices applications are seriously limited due to the toxicity of cadmium. **Table 1.2** outlines typical precursor materials, solvents and processing temperatures for the synthesis of GaN, ZnO and CuCl nanocrystals by the sol-gel technique. The precursor materials and solvents for GaN and ZnO are much more dangerous than CuCl precursor materials.

Material	Raw Materials and Solvents	Technique	Temperature (^{o}) C
GaN[68]	$Ga(NO_3)_3/HNO_3/NH_3$/Citric acid	Sol-gel	900
ZnO[69]	$Zn(CH_3COO)_2 2H_2O/CH_3OH$	Sol-gel	500
CuCl[70]	$CuCl_2 2H_2O/C_6H_{12}O_6/H_2O$	Sol-gel	120

Table 1.2: Precursor materials, solvents and processing temperature for synthesis of GaN, ZnO and CuCl nanocrystals

The synthesis of CuCl nanocrystals requires a relatively lower curing temperature than for both GaN and ZnO nanocrystals. CuCl is one of the most studied inorganic materials for excitonic related linear/non-linear optical processes due to its large excitonic binding energies. Excitonic-based luminescence in CuCl crystals has attracted much attention for the past few decades [71-77]. The free exciton binding energies of the order of 190 meV are much larger than those of III-V and II-VI semiconductors resulting in a high stability of the exciton even at room temperature [78]. Thus the CuCl should be an efficient light emitter via exciton-mediated electron-hole recombination. The effective total spontaneous luminescence emission of an emitting material may be given as [79]:

$$A_{eff} = \sum_i A_i \frac{\gamma_i}{\gamma_i + d_i} \tag{1.1}$$

where A_i is the spontaneous emission rate into the i^{th} optical mode, d_i is the absorption rate of photons in the i^{th} optical mode and γ_i is the output coupling rate of photons in the i^{th} optical mode. To first order $A_{eff} \approx A_i$. This rate is directly dependent on the Von Roosbroeck-Schockley rate of recombination per unit volume $R_{CV}(\hbar\omega)$[80]. But $R_{CV}(\hbar\omega) \propto \alpha(\hbar\omega)$, the frequency (ω) dependent absorption coefficient and $\alpha \propto \sqrt{E_b}$, where E_b is the exciton binding energy. A rough comparison with ZnO and GaN leads to the first order estimate for an improvement of quantum efficiency utilizing CuCl instead of the more common ZnO and GaN of

$$\sqrt{\frac{E_b^{CuCl}}{E_b^{ZnO}}} = \sqrt{\frac{190meV}{60meV}} = 1.779$$

$$\sqrt{\frac{E_b^{CuCl}}{E_b^{GaN}}} = \sqrt{\frac{190meV}{26meV}} = 2.703$$

Therefore the quantum efficiency improvement of CuCl based ELDs is ≈1.78 and ≈2.70 times greater than ZnO and GaN based ELDs, respectively. The biexciton binding energy of CuCl is 34 meV [81]. This is considerably larger than the bi-exciton binding energies of II-VI semiconductors such as ZnSe, CdS, and ZnO (BM_3 and BM_7 band) which are approximately 3.5, 6.3 and 15 meV, respectively [82]. In 1971, Shaklee *et al.* first demonstrated the optical gain mechanism due to the

biexciton in CuCl bulk crystal [83]. The biexciton emission can be used as a quantum bit pair for quantum processing [84].

Owing to the environmentally friendly synthesis of CuCl nanocrystals and the massive improvement of quantum efficiency of CuCl when compared to GaN and ZnO, we will report on the study of a new organic-inorganic nanocrystalline Copper (I) Chloride (CuCl) hybrid film on a flexible substrate deposited by the spin coating technique. A hybrid film is a mixture of more than one kind of material with its own unique characteristics. In hybrid materials, it is possible to combine organic and inorganic compounds [85]. In recent years, researchers in this laboratory have fabricated ELDs based on CuCl thin films deposited by vacuum evaporation and sputtering techniques on silicon substrates [86, 87]. The vacuum evaporation and sputtering methods are more complicated as both of these methods need pure CuCl material. In ambient conditions the CuCl films deposited by these methods degrade rapidly, thus an extra layer is needed to protect from oxidation. In nanocrystalline CuCl hybrid films, optical properties are comparable with vacuum evaporation and sputtered deposited thin films; no encapsulation layer is needed and the materials system benefits from the use of nanocrystals. The effects of chemical stoichiometry and nanostructure of the films are crucial from the device point of view. Using various chemistry and process parameters such as spin speed and duration, annealing temperature and time duration, the nanostructures are synthesized to yield stoichiometric and high optical quality hybrid films. In this research work, we use $CuCl_2.2H_2O$ instead of pure CuCl, which is much cheaper than CuCl. We use a simple spin-coating technique to deposit our hybrid film. This method is environmentally friendly and produces no harmful by-products. Only a small quantity of coating fluid is required even for large substrates, the process is very rapid and simple and good for multilayer applications. The process can be performed at room temperature and is cost effective. We can summarise the stimulus to conduct this research as follows:

- Higher quantum efficiency than GaN and ZnO
- Flexible substrate
- Repeatable stoichiometry

- Improved optical properties
- Higher film stability than vacuum evaporated and sputtered deposited films
- Inexpensive, environmentally friendly and low temperature process
- Finally, the development of ELDs to meet the requirements of lighting applications will provide an environmentally-friendly and energy-saving light source and research in this area helps promotes the adoption of ELDs for general lighting applications in the 21st century.

In this research, the CuCl nanocrystals were synthesised by the reaction of $CuCl_2.2H_2O$ alpha D-glucose and de-ionized (DI) water and embedded in glass matrices and deposited on variety substrates via a simple low temperature spin coating technique. Studies were carried out to optimise the films' structural, optical, and electrical properties in order to develop prototype devices for flexible UV/White–light emitters.

1.6 Thesis Organization

In Chapter 1 a literature review on electroluminescent devices followed by the motivation for this research has been briefly described. The fundamental aims of this research have been outlined.

Chapter 2 gives the description of materials, sample preparation techniques including the growth mechanisms for CuCl nanocrystals, their synthesis and the deposition of hybrid films via the spin coating method.

Chapter 3 provides a brief description of the structural, optical and electrical characterization techniques: X-ray diffraction (XRD), Scanning Electron Microscopy (SEM) and atomic force microscopy (AFM), ultraviolet-visible absorption measurements (UV-Vis), Fourier Transform Infrared spectroscopy (FTIR), X-ray photoelectron spectroscopy (XPS), photoluminescence (PL), cathodoluminescence (CL) and electroluminescence (EL) spectroscopy and their applications in semiconductor materials.

In Chapter 4 detailed experimental structural and morphological results of the organic–inorganic CuCl nanocrystalline hybrid films are presented.

In Chapter 5 detailed experimental optical results of the organic–inorganic CuCl nanocrystalline hybrid films are presented.
Chapter 6 outlines detailed experimental electrical and electroluminescence results for the organic–inorganic CuCl nanocrystalline hybrid films.

Chapter 7 outlines the impacts of atmospheric ageing effects on nanocrystalline CuCl hybrid films.

In Chapter 8 detailed experimental results for proof-of-concept p-CuCl/n-ZnO heterojunction diodes are presented.

In conclusion, chapter 9 summarizes the subject matter of the thesis and outlines future research directions.

References

[1] www.worldenergy.org/publications/1316.asp

[2] W.W. Stoffels; Europhysics News **36** (2007) 35

[3] The International Energy Association (www.iea.org) and the International Association for Energy Efficient Lighting (www.iaeel.org)

[4] www.ecology.com/2011/09/06/fossils-fuels-vs-renewable-energy-resources

[5] www.independent.co.uk/news/science

[6] www.nanotech-now.com/Ineke-Malsch/IMalsch-energy-paper.htm

[7] apps1.eere.energy.gov/buildings/publications/pdfs/ssl/caliper_round-9_summary.pdf

[8] www.lightingprize.org/news_phillips.stm

[9] D. Sperling; U. S. Department of Energy Solid-State Lighting Program; September 24 (2009)

[10] www1.eere.energy.gov/buildings/ssl/light/current_light.html

[11] ec.europa.eu/environment/etap/inaction/showcases/eu/421_en.html

[12] ec.europa.eu/environment/etap/inaction/showcases/eu (www.oled100.eu)

[13] www.hysoocled.com/content/13-led-light-bulb

[14] www.celcomgroup.co.za/green%20generation_energy%20saving.html

[15] www.engadget.com/2009/07/15/eternaleds-debuts-worlds-first-liquid-cooled-led-light-bulb/

[16] Eric A. Taub; the New York Times, Published: July 28 (2008)

[17] H. J. Round; “A Note on Carborundum" Electrical World **19** (1907) 309

[18] Braunstein, Rubin; "Radiative Transitions in Semiconductors" Physical Review **99** (1955) 1892

[19] N. Holonyak, Jr. Lemelson; “MIT Prize Winner" Lemenson-MIT Pro (2004)

[20] I. Akasaki, H. Amano, S. Sota, H. Sakai, T. Tanaka and M. Koike; Jpn. J. Appl. Phys **34** (1995) L1517

[21] News.cnet.com; LED shortage likely this year, 2, March (2010)

[22] en.wikipedia.org/wiki/Luminous_efficacy

[23] S. Pimputkar, J. S. Speck, S. P. DenBaars and S. Nakamura; Nature Photonics **3** (2009) 180

[24] en.wikipedia.org/wiki/Wide-bandgap-semiconductors (2010)

[25] Y. Taniyasu, M. Kasu and T. Makimoto; Nature **441** (2006) 325

[26] S. Pimputkar, J. S. Speck, S. P. DenBaars and S. Nakamura; Nature Photonics **3** (2009) 180

[27] www1.eere.energy.gov/buildings/ssl

[28] G. Natarajan; PhD Thesis; "Optimisation and Fabrication of Ultra-Violet Emitting CuCl Thin Films by RF Sputtering" Dublin City University, Dublin (2007) 4

[29] O. Madelung; Semiconductors: Data Handbook, Springer, 3rd ed. (2004)

[30] F. O. Lucas; PhD Thesis, "Evaluation of the Microstructural, Electronic and Optoelectronic Properties of γ–CuCl Thin Films and Their Fabrication on Si Substrates", Dublin City University, Dublin (2007)

[31] H. Ishikura, N. Fukuda, M. Itoi, K. Yasumoto, T. Abe, H. Kasada, K. Ando; Journal of Crystal Growth **214/215** (2000) 1130

[32] A. Rizzo, Y. Li, S. Kudera, F. D. Sala, M. Zanella, W. J. Parak, R. Cingolani, L. Manna, and G. Gigli; Applied Physics Letters **90** (2007) 051106

[33] P. Chen, X. Ma, and D. Yangb; Applied Physics Letters **89** (2006) 111112

[34] J. Shakya, K. Knabe, K. H. Kim, J. Li, J. Y. Lin, and H. X. Jiang; Applied Physics Letters **86** (2005) 091107

[35] H. Amano, N. Sawaki, I. Akasaki, Y. Toyoda; Appl. Phys. Lett **48** (1986) 353

[36] S. Nakamura, T. Mukai and M. Senoh; Appl. Phys. **71** (1992) 5543

[37] H. Amano, M. Kito, K. Hiramatsu and I. Akasaki; Japan. J. Appl. Phys. **28** (1989) L2112

[38] S. Nakamura, N. Iwasa, M. Senoh and T. Mukai; Japan J. Appl. Phys. **31** (1992) 1258

[39] S. D. Lester, F. A. Ponce, M. G. Craford and D. A. Steigerwald; Appl. Phys. Lett. **66** (1995)1249

[40] S. Chichibu, T. Azuhata, T. Sota, S. Nakamura; Appl. Phys. Lett **69** (1996) 4148

[41] I. Vurgaftman, J. R. Meyer and L. R. Ram-Mohan; J. Appl. Phys **89** (2001) 5815

[42] O. Ambacher, J. Phys. D: Appl. Phys. **31** (1998) 2653

[43] A. Usui, H. Sunakawa, A. Sakai and A. A. Yamaguchi; Japan J. Appl. Phys. **36** (1997) L899

[44] H. Marchand, X. U. Wu, J. P. Ibbetson, P. T. Fini, P. Kozodoy, S. Keller, J. S. Speck, S. P. DenBaars and U. .K. Mishra, Appl. Phys. Lett. **73** (1998) 747

[45] J. I. Pankove, E.A. Miller and J. E. Berkeyheiser; RCA, Rev **32** (1971) 383

[46] H. Amano, M. Kito, K. Hiramatsu and I. Akasaki; Japan J. Appl. Phys. **28** (1989) L2112

[47] B. Chitara, S. V. Bhat, S. R.C. Vivekchanda, A.Gomathi, C. N. R. Raoa; Solid State Communications **147** (2008) 409

[48] B. Damilano, N. Grandjean, F. Semond, J. Massies, and M. Leroux; Appl. Phys. Letters **75** (1999) 716

[49] S. Nizamoglu, T. Ozel, E. Sari and H. V. Demir; Nanotechnology **18** (2007) 065709

[50] R. Kudrawiec, M. Nyk, M. Syperek, A. Podhorodecki and J. Misiewicz; Appl. Phys. Letters **88** (2006) 181916

[51] J. Ahn, M. A. Mastro, J. Hite, C. R. Eddy, Jr. and J. Kim; Appl. Phys. Letters **96** (2010) 132105

[52] W. Y. Wang, Y. P. Xu, D. F. Zhang, X. L. Chen; Materials Research Bulletin **36** (2001) 2155

[53] I. S. Chun, K. Bassett, A. Challa and X.Li; Appl. Phys. Letters **96** (2010) 251106

[54] K. Sardar, M. Dan, B. Schwenzer, C. N. R. Rao; J. Mater Chem. **15** (2005) 2175

[55] Y. R. Ryu, T. S. Lee and H. W. White; Appl. Phys. Lett **83** (2003) 87

[56] D. C. Look, B. Claflin; Phys. Stat. Sol. **241** (2004) 624

[57] S. S. Kurbanov, K. T. Igamberdiev, and T. W. Kang; J Phys. D: Appl. Phys. **43** (2010) 115401

[58] C. Y. Lee, J. Y. Wang, Y. Chou, C. L. Cheng, C. H. Chao, S. C. Shiu, S. C. Hung, J. J. Chao, M. Y. Liu, W. F. Su, Y. F. Chen and C. F. Lin; Nanotechnology **20** (2009) 425202

[59] K. Suzuki, M. Inoguchi, K. Fujita, S. Murai, K. Tanaka, N. Tanaka, A. Ando, and H. Takag; J. Appl. Phys. **107** (2010) 124311

[60] Y. Lee, A. Rizzo, R. Cingolani, G. Gigli; Adv. Mater **18** (2006) 2545

[61] J. Xu, D. Cui, B. A. Lewis, A. Y. Wang, S. Xu, M. Gerhold; IEEE Photon. Technol. Lett. **17** (2005) 2008

[62] S. Coe, W. K. Woo, M. Bawendi, V. Bulovic, Nature **420** (2002) 800

[63] V. L. Colvin, M. C. Schlamo, A. P. Alivisatos, Nature **370** (1994) 354

[64] P. O. Anikeevo, J. E. Halpert, M. G. Bawendi, V. Bulovic; NanoLett. **7** (2007) 2196

[65] Z. Tan, F. Zhang, J. Xu, A. Y. Wang, J. D. Dixon, L. Li, Q. Zhang, S. E. Mohney, J. Ruzyllo; NanoLett.**7** (2007) 3803

[66] A. H. Mueller, M. A. Petruska, M. Achermann, D. J. Werder, E. A. Akhadov, D. D. Koleske, M. A. Hoffbauer, V. I. Klimov; NanoLett. **5** (2005) 1039

[67] N. Tessler, V. Medvedev, M. Kazis, S. Kan; Science **295** (2002) 1506

[68] H. Qiu, C. Cao, H. Zhu; Materials Science and Engineering B **136** (2007) 33

[69] S. S. Kurbanov, G. N. Panin, T. W. Kimd, T. W. Kang; J. Luminescence **129** (2009) 1099

[70] Y. C. Zhang, J. Y. Tang; J. Materials Letters **61** (2007) 3708

[71] M. Nakayama, A. Soumura, K. Hamasaki, H. Takeuchi and H. Nishimura; Phys. Rev. B **55** (1997) 10099

[72] H. Ichida, and H. Nishimura; J. Phys.: Condens. Matter **11** (1999) 7653

[73] M. Cardona; Phys. Rev. **129** (1963) 69

[74] A. Goldmann, J. Tejeda, N. J. Shevchik, M. Cardona; Phys Rev. B **10** (1974) 4388

[75] T. Goto, T. Takahashi and M. Ueta; J. Phys. Soc. Japan **24** (1968) 314

[76] Y. Kaifu and T. Komatsu; Phys. Stat. Sol. B **48** (1971) K125

[77] M. Nakayama, H. Ichida, H. Nishimura; J. Phys. Cond.Matter **11** (1999) 7653

[78] M. M. Alam, F. Olabanji Lucas, D. Danieluk, A. L. Bradley, K.V. Rajani, S.Daniels, P. J. McNally; J. Phys. D: Appl. Phys **42** (2009) 225307

[79] S. Fan, P. R. Villeneuve and J. D. Joannopoulos; IEEE J. Quantum Electron, **36** (2000)1123

[80] H. T. Grahn; Introduction to Semiconductor Physics, World Scientific (1999)

[81] Y. Masumoto, S. Okamoto and S. Katayangi; Phys. Rev. B **50 (**1994) 18658

[82] A. Yamamoto, K. Miyajima, T. Goto, H. J. Ko, T. Yao; Phys. Stat. Sol. (B), **229 (**2002) 871

[83] K. L. Shaklee, R. F. Leheny and R. E. Nahory; Phys. Rev. Lett **26** (1971) 888

[84] M. Koch, K. Kheng, I. C. Robin, R. André; phys. stat. sol. C **11** (2006) 3916

[85] T. Ogoshi, H. Itoh, K. M. Kim, Y. Chujo; Macromolecules **35** (2002) 334

[86] A. Mitra, F. O. Lucas, L. O'Reilly, P. J. McNally, S. Daniels, G. Natarajan; J Mater Sci: Mater Electron **18** (2007) S21

[87] L. O'Reilly, O. F. Lucas, P. J. McNally, A. Reader, G. Natarajan, S. Daniels, D. C. Cameron, A. Mitra, M. M. Rosas, A. L. Bradley; Journal Of Applied Physics **98** (2005) 113512

CHAPTER 2

MATERIALS AND METHODS

Materials and processing method selection is one of most important factors involved in device fabrication. For the synthesis of nanocrystalline CuCl hybrid films to fabricate prototype devices for flexible UV/White-light emission, a number of different materials are used. In this chapter we briefly describe the materials and the methods employed.

2.1 Materials

2.1.1 Copper(II) Chloride

Copper(II) chloride, alternatively known as cupric chloride, is a chemical compound with the formula $CuCl_2$. It is a yellow-brown solid which slowly absorbs moisture to form a blue-green dihydrate, orthorhombic crystalline structure, which results in $CuCl_2.2H_2O$. By heating the hydrated copper chlorides water can be driven off from the $CuCl_2.2H_2O$ crystals to form anhydrous copper(II) chloride. Due to the Jahn-Teller effect, the anhydrous $CuCl_2$ forms a distorted cadmium iodide structure compared to its idealized octahedral geometry [1]. The Crystal structure of copper(II) chloride hydrate as shown in **Figure 2.1**.

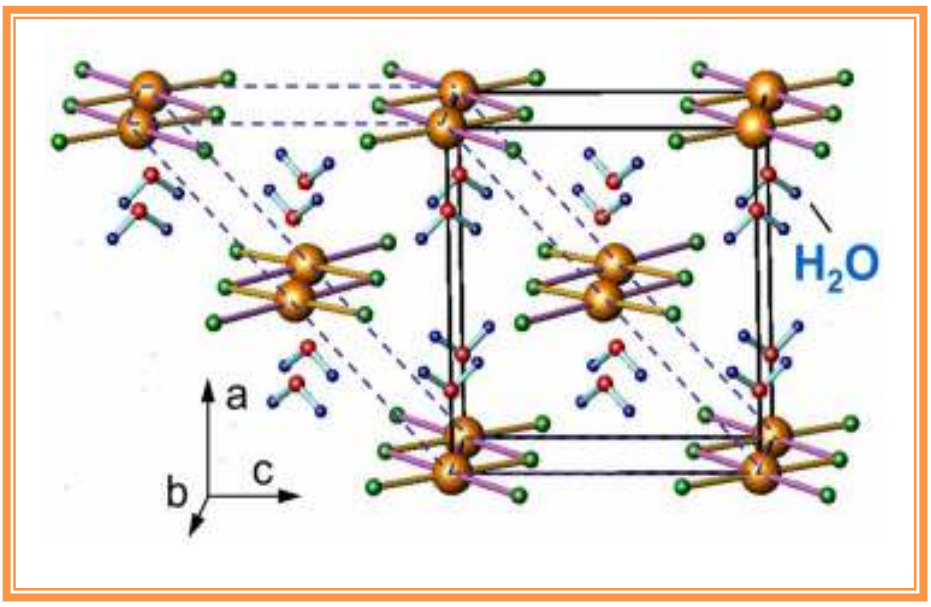

Figure 2.1: Crystal structure of copper(II) chloride hydrate [2]

Copper (II) chloride is highly soluble in water and produces a blue solution, but a high concentration in aqueous solution appears to be dark green. Solutions of Cu(I)Cl in HCl or NH_3 absorb carbon monoxide to form colourless complexes such as the chloride-bridged dimer $[CuCl(CO)]_2$.

Molecular formula	$CuCl_2$
Molar mass	134.45g/mol (anhydrous) 170.48 g/mol (dihydrate)
Appearance	yellow-brown solid (anhydrous) blue-green solid (dehydrate)
Density	3.386 g/cm^3 (anhydrous) 2.51 g/cm^3 (dehydrate)
Melting point	498 °C (anhydrous) 100 °C (dehydration of dihydrate)
Boiling point	993 °C (anhydrous, decomp)
Solubility in water	70.6 g/100 mL (0 °C) 75.7 g/100 mL (25 °C)
Crystal structure	distorted CdI_2 structure
Coordination geometry	Octahedral

Table 2.1: Some Properties of Copper (II) Chloride [6]

The same hydrochloric acid solutions also react with acetylene gas to form [CuCl (C_2H_2)]. Ammoniacal solutions of CuCl react with acetylenes to form the explosive copper(I) acetylide [3]. In aqueous solution Copper(II) chloride will segregate and give the blue colour compound $[Cu(H_2O)_6]^{2+}$ and yellow or red coloured halide complexes, of the formula $[CuCl_{2+x}]^{x-}$ [4]. Concentrated solutions of $CuCl_2$ appear green because of the combination of these various chromophores. The dilute solution colour depends on temperature; at ~100^{o}C it appears green and is blue at room temperature [4, 5]. **Table 2.1** shows some properties of copper (II) chloride. When copper(II) chloride is heated in a flame it emits a green-blue colour. Cupric chloride

can also be prepared by the reaction of hydrochloric acid with copper(II) oxide, copper(II) hydroxide or copper(II) carbonate, as indicated by:

$$CuO(s) + 2\ HCl(aq) \rightarrow CuCl_2 + H_2O \qquad (2.1)$$

By combining the element copper and chlorine, anhydrous $CuCl_2$ may be prepared directly. $CuCl_2$ can be purified via crystallization from hot dilute hydrochloric acid, as well as by cooling in a $CaCl_2$-ice bath [7]. Copper(II) chloride is mostly used in organic synthesis, as a co-catalyst, for hydrolysis of acetonides, in pyrotechnics and is also used as a root killer [7-10]. $CuCl_2.2H_2O$ was used as the source for copper and chlorine in this study.

2.1.2 Copper(I) Chloride

Copper(I) chloride, commonly known as cuprous chloride, is a chemical compound with the formula CuCl. At room temperature and atmospheric pressure, the prevalent phase of CuCl is called γ-CuCl. Intrinsic γ-CuCl (E_g= 3.395eV at 4 K) has a direct, wide band-gap, and is an ionic I-VII compound semiconductor material with a zincblende structure at room temperature [11].

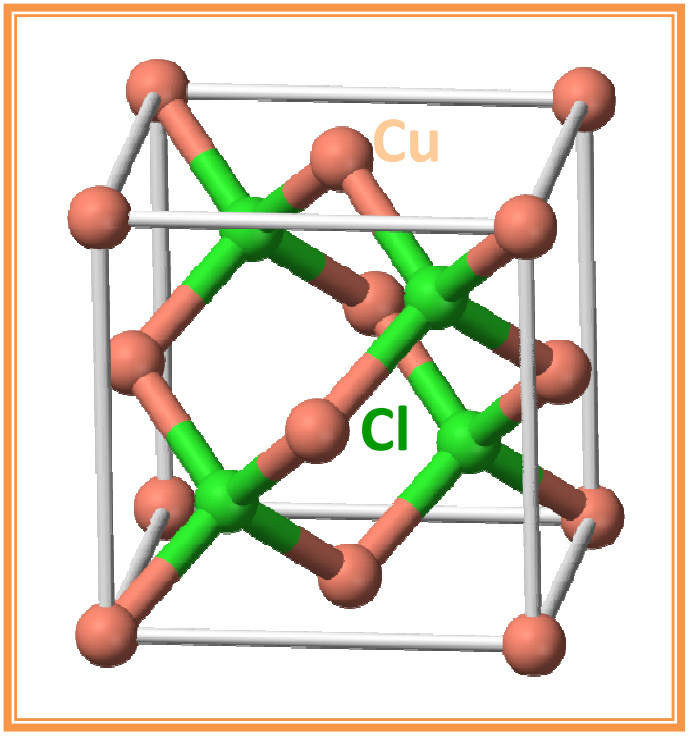

Figure 2.2: Crystal structure of copper (I) chloride [13]

The substance is a white solid sparingly soluble in water, but very soluble in concentrated hydrochloric acid. Impure samples appear green due to the presence of copper(II) chloride [12]. The zincblende lattice is composed of two interpenetrating FCC (face-centred-cubic) sub-lattices occupied by Cu^+ and Cl^- atoms respectively. These are shifted relative to each other diagonally by ¼ of the unit space. The crystal lattice structure of CuCl is shown in **Figure 2.2** and **Table 2.2** shows some properties of copper(I) chloride.

Molecular formula	CuCl
Molar mass	98.999 g/mol
Appearance	White powder, slightly green from oxidized impurities
Density	4.145 g/cm^3
Melting point	426 ° C (703 K)
Boiling point	1490° C (1760K) (decomp.)
Solubility in water	0.0062 g/100 mL (20 °C)
Solubility product, K_{sp}	1.72×10^{-7}
Solubility	Insoluble in ethanol acetone; soluble in concentrated HCl, NH_4OH
Refractive index (n_D)	1.930
Crystal structure	Zinc blende structure

Table 2.2: Some properties of copper(I) chloride [6, 14]

The schematic band diagram is shown in **Figure 2.3**. The valance band of copper(I) chloride is split into two exciton absorption bands separated by spin-orbit splitting, these having energies in the near ultraviolet region; one band is a doublet and the other is a singlet and are historically called $Z_{1,2}$ and Z_3,respectively [15]. The top valance band of CuCl is the split-off hole band (Γ_7), roughly 60 meV away from the degenerate heavy-hole and light-hole (Γ_8) bands. The exciton consisting of the Γ_7 (Γ_8) hole and Γ_6 electron has been called the Z_3 ($Z_{1,2}$) exciton [16]. The $Z_{1,2}$ and Z_3 edge excitons originate from the coupling of the lowest conduction-band state Γ_6 to both the uppermost valence band holes Γ_8 ($Z_{1,2}$) and Γ_7 (Z_3), respectively [17] . The

numbers in brackets indicate the degeneracy of the corresponding state. Cardona proved experimentally that this spin-orbit splitting in CuCl is reversed with respect to the typical Cu-halide and Ag-halide zincblende semiconductors resulting in the Z_3 exciton appearing at a lower energy than the $Z_{1,2}$ exciton [15].

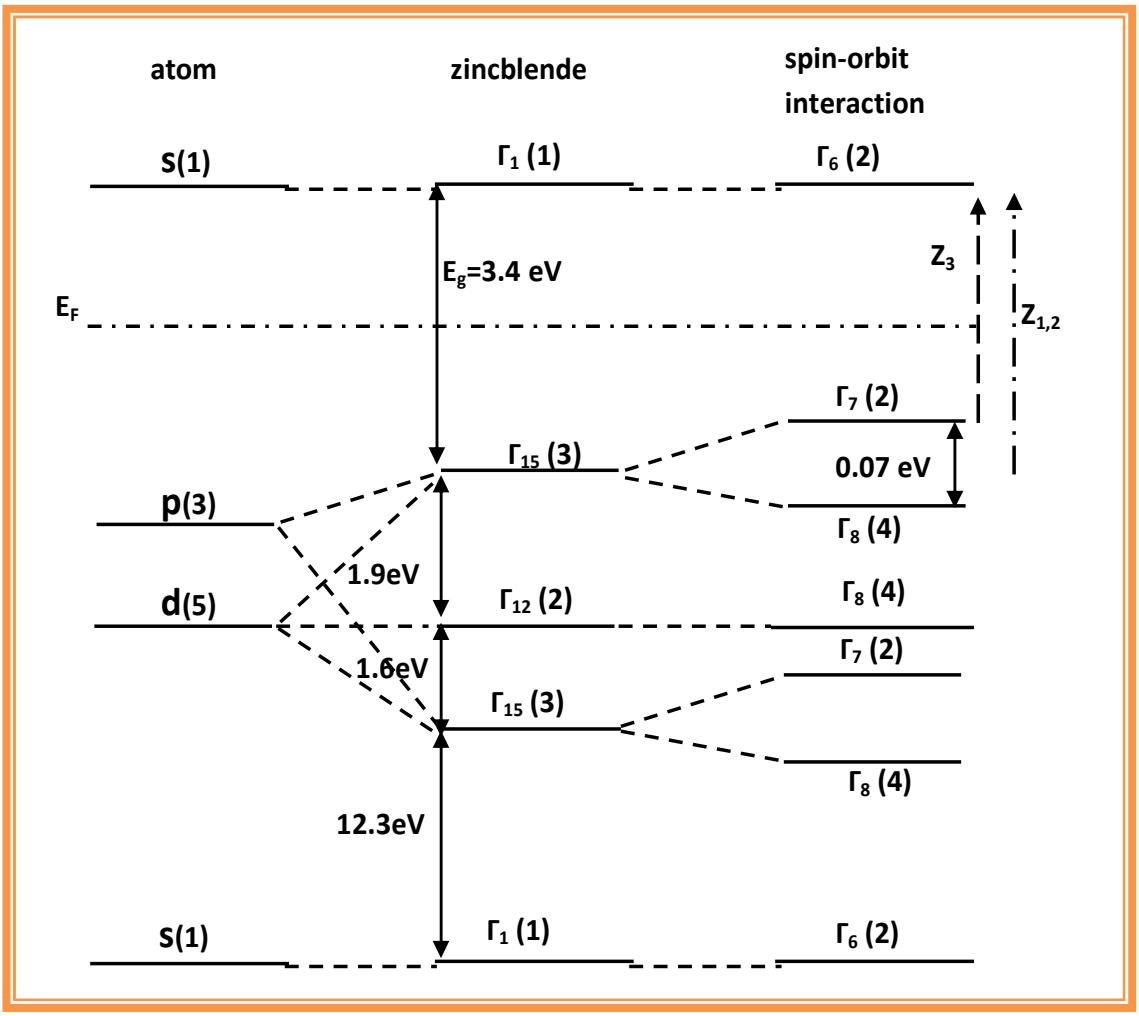

Figure 2.3: Schematic development of conduction and valence states due to s, p and d electrons at the Brillouin Zone Centre Γ in the cubic crystal field of the zincblende structure (not to scale). Energies given are experimental results for CuCl [12, 18].

In the middle of the seventeenth century, Robert Boyle first prepared Copper(I) chloride from mercury(II) chloride and copper metal using the reaction below [19]:

$$HgCl_2 + 2Cu \rightarrow 2CuCl + Hg \quad (2.2)$$

In 1799, J. L. Proust characterized the two different chlorides of copper. He prepared CuCl by heating $CuCl_2$ in the absence of air, causing it to lose half of its combined chlorine. This was followed by removing residual $CuCl_2$ by washing with water [20]. Commercial copper(I) chloride is made by passing a mixture of hydrochloric acid solution and argon over 99.999% copper metal at 950 ^oC (1223 K) [21]. The precipitated CuCl powder is washed in organic solvents, dried, and stored in a sealed bottle under argon gas. The process reaction is governed by the chemical equation:

$$2Cu + 2HCl \rightarrow 2CuCl\downarrow + H_2\uparrow \quad (2.3)$$

Besides these, there are several alternate methods reported in the literature, such as, the reaction of copper metal with tetrachlorocabornate [22], carbonation of palladium in a solution containing cupric sulphate-chloride [23], thermal decomposition of organic copper compounds [24], exposure of copper single crystals to chlorine gas in an ultra high vacuum chamber [25], reaction of copper oxide with ammonium chloride at 673 K and an ion implantation method combined with post heating at high temperatures [26]. Almost all of these techniques require complicated equipment, high reaction temperatures, utilize toxic reactants and organic solvent, or produce pollutive byproducts. Recently, Zhang *et. al* demonstrated the hydrothermal reaction of copper (II) chloride ($CuCl_2$) and alpha-D-glucose ($C_6H_{12}O_6$), a mild renewable, inexpensive and non toxic reducing agent, in the presence of distilled water and at a temperature of 120 ^oC (393 K) to synthesise purified CuCl nanocrystals [27]. It was suggested that the formation of nanocrystalline CuCl powder from this method is by complexation-reduction-precipitation mechanism, and the equation for the process was summarised as:

$$2CuCl_2 + C_6H_{12}O_6 + H_2O \rightarrow 2CuCl\downarrow + C_6H_{12}O_7 + 2HCl \quad (2.4)$$

They called the method *"A green hydrothermal route to nanocrystalline CuCl"* because the combined use of safe and renewable reactants and a benign solvent medium involved in the synthesis. In this study, we use this method to synthesise the CuCl nanocrystals for nanocrystalline CuCl hybrid films. The structural, optical and

electrical properties of γ-CuCl will be briefly presented independently within the pertinent chapters.

2.1.3 α-D-Glucose

The name “glucose” comes from the Greek word *glukus* meaning "sweet", and the suffix "-ose," which denotes a sugar. This is a very important carbohydrate in biology. There are two mirror-image isomers that exist for glucose molecules, the right hand isomer forming D-glucose. This is also known as dextrose monohydrate, or more commonly dextrose [28]. **Table 2.2** shows some physical properties and **Figure 2.4** shows the chemical structure of α-D-Glucose. There are six carbon atoms contained in glucose ($C_6H_{12}O_6$). One of these is a part of an aldehyede group and therefore it is referred to as an aldohexose. The glucose molecule in solution can be in an open-chain form or a ring form in equilibrium.

Name	α-D-Glucose
Molecular formula	$C_6H_{12}O_6$
Molar mass	180.16 g/mol
Density	1.54 g/cm^3
Melting point	146° C

Table 2.3: Some physical properties of Dextrose [6]

The covalent bond between the aldehyde C atom and the C-5 hydroxyl group forms a six-membered cyclic hemiacetal which results in the cyclic form. The cyclic form is predominant at pH≈ 7. The glucose assumes the cyclic form in the solid phase. Due to the fact that the ring contains five carbon atoms and one oxygen atom, the cyclic form of glucose is also referred to as glucopyranose.

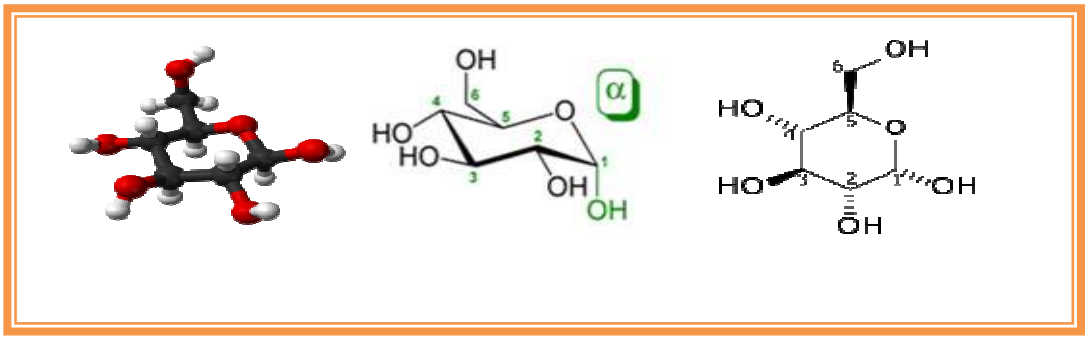

Figure 2.4: Chemical structure of alpha-D-glucose [29].

In the ring, each carbon is linked to a hydroxyl side group with the exception of the fifth atom, which links to a sixth carbon atom outside the ring, forming a $-CH_2OH$ group. Glucose is usually available in the form of a white substance or as a solid crystal. Glucose is highly soluble in water. In this research, $CuCl_2.2H_2O$ was used as the copper and chlorine source and alpha-D-glucose ($C_6H_{12}O_6$) is a polyol containing an aldehyde group (polyol is an organic molecule with three or more alcohol groups attached) was selected as the reducing agent, where it releases Cu^{2+} ions from the dissolution of $CuCl_2.2H_2O$ in water from relatively stable complex ions, namely $Cu(C_6H_{12}O_6)_x^{2+}$. One of the indicators of this reaction is, when the alpha-D-glucose is added to the $CuCl_2$ aqueous solution, the colour of the $CuCl_2$ aqueous solution changes rapidly from light to dark blue [30].

2.1.4 Polysilsesquioxane (PSSQ)

Polysilsesquioxane (PSSQ) was developed more than 6 decades ago and it has since found applications in many industries. For example, the first commercialized silicon devices used PSSQ as a high temperature dielectric material [31]. In recent years, poly(hydridosilsesquioxane) (PHSQ with R) (H) and poly(methylsilsesquioxane) (PMSQ with R) (CH_3) have emerged as low dielectric constant interlayer materials for interconnects in microelectronic devices because of their excellent thermal and electrical properties. PSSQ is an essential part of hybrid organic-inorganic composites designed with the good physical properties of ceramics and a superb selection of functional group chemical reactivity. One and a half (sesqui) oxygen atoms and one hydrocarbon group (ane) are bonded with every silicon atom. The

general empirical formula of poly(silsesquioxane)s is $(RSiO_{1.5})_n$, where R can be hydrogen, methyl, phenyl, or higher molecular weight organic groups [31].

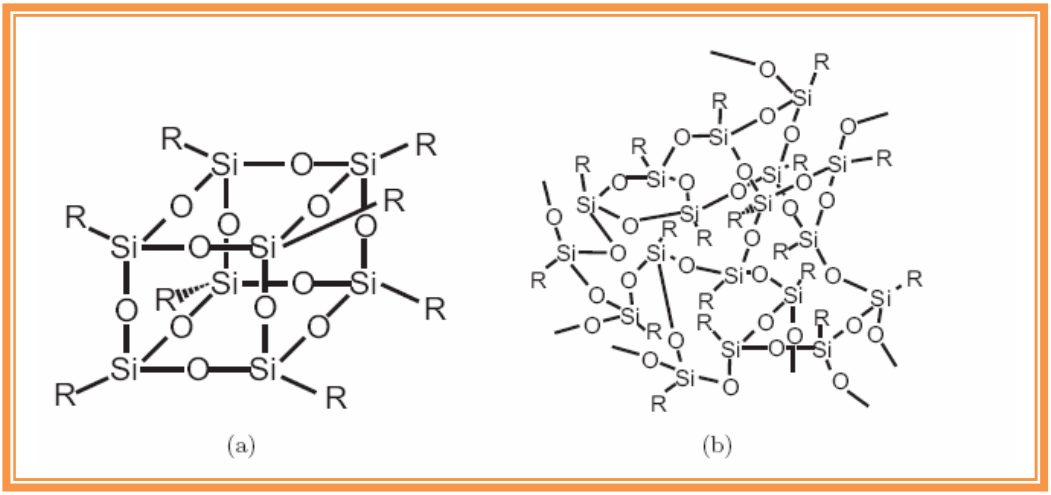

Figure 2.5: Chemical structure of polysilsesquioxane in (a) cage form and (b) network form [32]

The dielectric constant of PSSQ is low and its dielectric properties are very good with high breakdown strength comparable to that of SiO_2 [33]. The acid–catalysed hydrolytic condensation reactions of trifunctional organosilicon monomers such as alkyltrialkoxysilane, alkyltrihalosilane or trimethoxysilane are usually used to prepare Silsesquioxanes [32, 33]. **Figure 2.5** shows the chemical structure of PSSQ; it consists of mixed cage and network structures before thermal conversion, with part of the cage structure transforming into a network structure after thermal conversion [33, 34]. The PSSQ film structural and dielectric properties are highly sensitive to heat treatment [35]. Commercially supplied PSSQ generally comes in flaked form, which is soluble in different types of organic solvents such as methanol, ethanol, iso-propanol, butanol, hexanol, butanone and acetone, and the quality of the PSSQ film mainly depends on the solvent and the underlying substrates used [36]. In this study, the PSSQ (which contains methanol 3-5 % and ethyl alcohol 70-80 % in the solution form) is used as a host matrix and its source was commercially supplied PSSQ solution from Emulsitone Inc., USA.

2.2 Spin Coating Method

2.2.1 Introduction

Spin coating is a process in which solution is spread uniformly over the substrate surface using centrifugal force. In 1958 Emslie *et al*. first developed the spin coating model, which most subsequent models have followed [37]. This model predicts that initially the uniform fluid coating will stay uniform and that non-uniform coatings will tend to become more uniform as the coating layer thins down during spinning. Other investigators have used the Emslie model as the basis for improved spin coating models. Acrivos, Shah, and Peterson investigated the behavior of non-Newtonian fluids, while Meyerhofer investigated the effects of evaporation [38, 39]. Many other models improve on early developments by modelling other phenomena, such as fluid and gas-phase resistance to solvent diffusion, the effects of topography, and the effects of relative humidity in the air flowing over the wafer [40-42].

2.2.2 Substrate Preparation

Samples were prepared on rectangular silicon or glass substrates cut from standard commercial silicon wafers (approximately 1.5 cm x 1.5 cm in size) and standard glass object slides (approximately 2 cm x 2 cm in size). The silicon substrates are single-side polished, p-type with a resistivity in the range of ~20 Ωcm. The samples were cleaned first by scrubbing with Decon™ solution, then dipping in trichloroethylene, acetone and methanol, each for 5-10 minutes to degrease the substrate. The solvents were removed by dipping in de-ionized water for 5 minutes. Finally, the substrates were dried with a flow of nitrogen.

2.2.3 Coating Solution

Normally high-purity solvents and reagents are used in the preparation of coating solutions though the possibility of contamination after preparation is always present. This contamination happens either via the environment or from deterioration of the solution. The solution to be used for spin coating should be filtered prior to spin coating, especially if the solutions contain water-sensitive components which give solid by-products, e.g. metal alkoxides. For our hybrid film deposition we use

Cellulose Acetate Filter Syringes of pore size 0.2 μm. We have found that the film's surface smoothness depends on the pore size of the filter.

2.2.4 Coating Environment

The ideal coating environment is a clean room, preferably at least Class 100 to avoid contamination. If a clean room is not possible then at the very least clean hoods should be used for the spin coating process. The flow of air should be clean because the pollutant air can contaminate the film. The variation of air flow over the sample can lead to thickness inhomogeneities, therefore the air flow should be uniform and unidirectional. The spin coating environment temperature should be controlled as the environment temperature can affect the film thickness [43]. In this study, a Class 100 clean room was used to deposit the nanocrystalline CuCl hybrid films.

2.2.5 Spin Coating Process

Figure 2.6 shows a schematic diagram of a Laurell WS-400A-6PP/LITE spin coater, which was used in our hybrid film synthesis. For the spin-coating process a certain amount of solution (for small samples of 15 to 25 mm dimensions, 0.1 mL for concentrations of 1-15 mg/mL up to 0.2 mL, for a concentration of 20 mg/mL) was carefully pipetted centrally onto the cleaned substrate. The solution was spread over the surface, and immediately after the solution had wetted the whole substrate, the sample was spun. Spin coating uses centrifugal force to the spread solution over the surface of the substrate to produce a thin film. The process has three phases: (i) solution is first dispensed onto a wafer or substrate, (ii) then it is spread across the substrate, and finally (iii) the substrate is spun at a high angular speed to decrease the thickness of the solution layer to the final film thickness and uniformity. During this third phase, the film thins to its final thickness by flowing outward off the wafer in concentric "waves". The ultimate film thickness also depends on the solvent evaporation due to high convection over the substrate surface. The solvent fraction in the solution gradually decreases with acceleration, the viscosity of the residue increases, causing the outward flow of residue to diminish until it almost ceases. Subsequent thinning of the films comes almost entirely from solvent evaporation [44,

45]. In ideal conditions the film thickness can be calculated using the following equation [46]:

$$t \propto 1/\sqrt{v} \tag{2.5}$$

where t is thickness of the film and v is the speed .

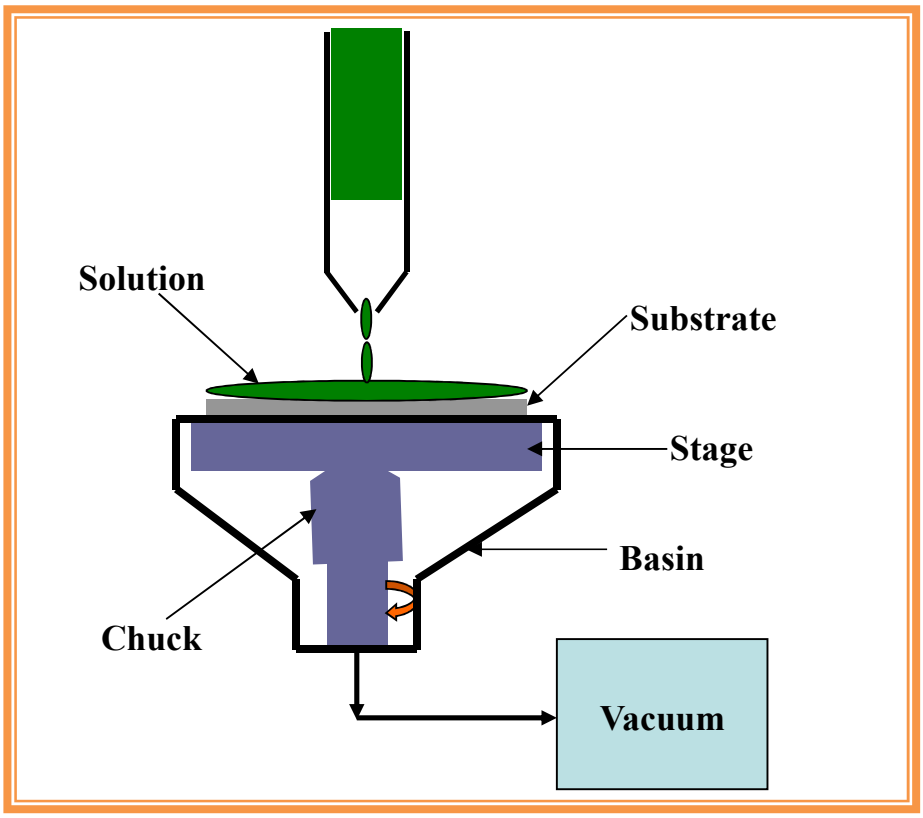

Figure 2.6: Schematic diagram of the spin coating system used in this study

Since the coating thickness is inversely proportional to the square root of the rotation speed, thinner films are obtained at higher speeds. Coating thickness can also be varied by changing the concentration of the coating solution. Besides this, other factors can have an impact on film thickness such as viscosity, surface tension, temperature, etc.

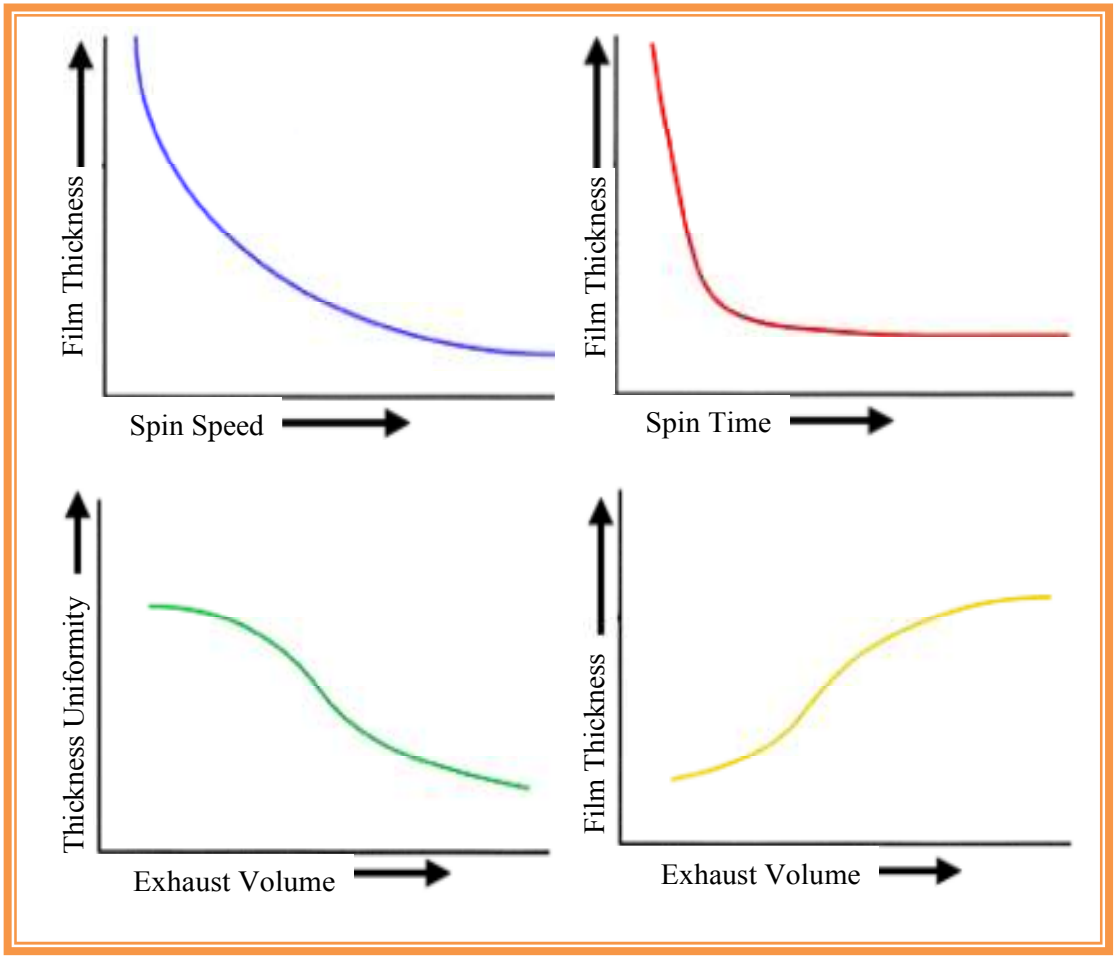

Figure 2.7: The film thickness depends on different process parameters [47]

Figure 2.7 shows a series of generic charts representing general trends for the various process parameters. For most resin materials the final film thickness will be inversely proportional to the spin speed and spin time. Final thickness will be also be somewhat proportional to the exhaust volume although uniformity will suffer if the exhaust flow is too high since turbulence will cause non-uniform drying of the film during the spin process.

2.2.6 Advantages and Disadvantages

A selection of advantages of the spin coating method:

1. Environmentally friendly and no harmful by-products are produced.
2. Only a small quantity of coating fluid is required even for large substrates.

3. Process is very rapid and simple.
4. Process is good for multilayer applications.
5. There are many types of commercial equipment available.
6. Process can be performed at room temperature.
7. Cost effective process typically.

A selection of disadvantages of this method:

1. Only really good for circular substrates. Odd shapes require fairings to smooth air and liquid flow over the edges and corners.
2. Requires stringent solvent properties.
3. Difficult to keep clean.
4. Only good for Newtonian fluids.
5. Large substrates (e.g. > 20 cm diameters) are difficult to coat uniformly.

2.3 Hybrid Film Deposition

CuCl hybrid films were deposited on several clean (cleaning process described in section 2.2.2) substrates including silicon, glass and Indium Tin Oxide (ITO) coated glass, by the aforementioned spin coating method using a Laurell WS-400A-6PP/LITE spin coater in a class 100 clean room environment to avoid contamination. The flow diagram representing the optimum process parameters for synthesis of CuCl nanocrystals and deposition of hybrid films is shown in **Figure 2.8**. A typical solution was prepared using 0.50, 0.60 and 0.75 gm of $CuCl_2.2H_2O$ powder (laboratory reagent grade, Fisher Scientific Company) and 0.50, 0.40 and 0.25 gm of alpha-D-Glucose powder (99.5% Sigma-Aldrich Inc., Germany) with 1, 2 and 3 ml of de-ionized water. The powders were dissolved completely in the de-ionized water after vigorous stirring of the solution. 2.1 gm of a PSSQ based solution known as Emulsitone glass forming solution (Emulsitone Company, New Jersey, USA.) was added to the $CuCl_2$ glucose aqueous solution.

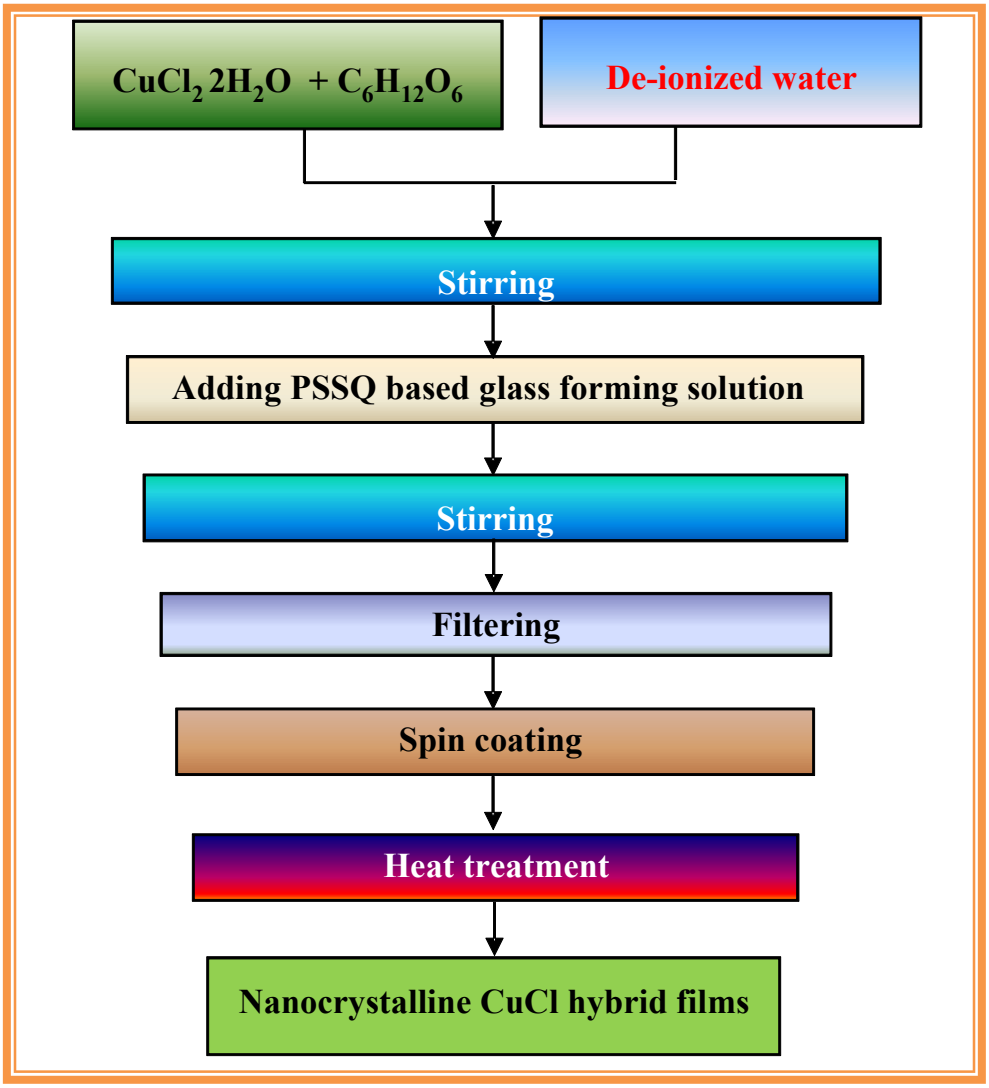

Figure 2.8: Flow diagram representing the optimum process parameters for synthesis of CuCl nanocrystalline hybrid films

The solution was stirred for 5 minutes and finally filtered by using a 0.2 µm filter (Cellulose Acetate Filter Syringe). Approximately 0.75 ml of the solution was dropped at the centre of the substrate (2x2 cm^2) and spun. The film was spin coated by gradually increasing the speed from 0 to 2000, 3000, 4000 and 5000 rpm (typical thicknesses of ≈ 200-500 nm) over a period of one minute. The coating was performed at room temperature. The films were subsequently heated at 80 ^oC, 100 ^oC 120 ^oC and 140 ^oC for durations between 1 and 24 hours *in vacuo*.

References

[1] A.F. Wells; Structural Inorganic Chemistry, Oxford: Clarendon Press (1984) ISBN 0-19-855370-6

[2] M. Schmitt, O. Janson, M. Schmidt, S. Hoffmann, W. Schnelle, S. L. Drechsler, and H. Rosner; Physical Review B **79** (2009) 245119

[3] Nicholls, D. Complexes and First-Row Transition Elements, Macmillan Press, London (1973)

[4] A. S. Taylor and R. E. Griffith; On Poisons, in Relation to Medical Jurisprudence and Medicine (1848) 378

[5] L. M. Mirica, X. Ottenwaelder, T. D. P. Stack, Chem. Rev. **104** (2004) 1013

[6] D. R. Lide; CRC Handbook of Chemistry and Physics (2003)

[7] S. H. Bertz, E. H. Fairchild; In Handbook of Reagents for Organic Synthesis, Wiley, New York **1** (1999) 220

[8] J. Brussee, J. L. G. Groenendijk, J. M. Koppele; A. C. A. Jansen Tetrahedron **41** (1985) 3313

[9] M. Chandrasekhar, K. L. Chandra, and V. K. Singh; J. Organic Chemistry **68** (2003) 4039

[10] Krishna, P. Radha, G. Dayaker; Tetrahedron Letters **48** (2007) 7279

[11] L. O. Reilly, A. Mitra, G. Natarajan, S. Daniels, P. J. McNally; J. Cryst Growth **287** (2006) 139

[12] United States Patent US4582579 "method of preparing cupric ion free cuprous chloride"

[13] http://en.wikipedia.org/wiki/File:Nantokite-unit-cell-3D-balls.png

[14] P. Patnaik; Handbook of Inorganic Chemicals, McGraw-Hill (2002) ISBN 0-07-049439-8

[15] M. Cardona, Phys. Rev. **129** (1963) 69

[16] A. Goldmann, Phys. Status Solidi B **20** (1977) 9

[17] H. Ichida, and H. Nishimura, J. Phys.: Condens. Matter **11** 7653 (1999) 45A

[18] A. Goldmann, J. Tejeda, N.J. Shevchik and M. Cardona, Phys. Rev.B **10** 4388 (1974)

[19] R. Boyle; "Considerations and experiments about the origin of forms and qualities" Oxford As reported in Mellor (1666)

[20] J. L. Proust; Ann Chim Phys. **32**(1799) 26

[21] L. Brewer, N.L. Lofgren; J. American Chem. Society **72** (1950) 3038

[22] J. P. Remeika, B. Batlogg; Materials Research Bulletin **15** (1980) 1179

[23] I. V. Fedoseev, A. A. Ponomarev, E. N. Gilbert, L. N. Shabanova G. A. Kolosova; U.S.S.R. SU 1,696,543 (Cl. C22 B15/00) (1991)

[24] I. L. Botto and O.R. Nascimento; An. Asoc. Quim. Argent **80** (1992) 321

[25] W. Sesselmann, T. J. Chuang; Surface Science **176** (1986) 32

[26] K. Fukumi, A. Chayahara, H. Kageyama; J. non-Crystal Solids **259** (1999) 93

[27] Y. Zhang and J. Y. Tang; Materials Letters **61** (2007) 3708

[28] Dextrose, Merriam-Webster Online Dictionary

[29] http://images.google.ie/images, D-Glucose, May (2009)

[30] Y. C. Zhang, J.Y. Tang; J. Materials Letters **61** (2007) 3708

[31] E. S. Park, H. W. Ro, C. V. Nguyen, R. L. Jaffe, and D. Y. Yoon; Chem. Mater. **20** (2008) 1548

[32] S. Murarka, P. Eizenberg, M and A. Sinha, Interlayer dielectrics for semiconductor technologies, Academic Press (2003)

[33] F. Olabanji Lucas; PhD Thesis, "Evaluation of the Microstructural, Electronic and Optoelectronic Properties of γ–CuCl Thin Films and Their Fabrication on Si Substrates" Dublin City University, Ireland, December (2007)

[34] W.C. Liu, C.C Yang, W.C. Chen, B.T. Dai and M.S. Tsai; Journal of Non-Crystalline Solids **311** (2002) 223

[35] C. C. Yang, W.C. Chen, L. M. Chen, C. J. Wang; Proc. Nat. Sci. Counc. ROC (A) **25** (2001) 339

[36] Y. Abe, K. Kagayama, N. Takamura, T. Gunji, T. Yoshihara and N. Takahashi; Journal of Non-Crystalline Solids **261** (2000) 39

[37] A.G. Emslie, F.T. Bonncr, and L.G. Peck; J. Applied Physics **29** (1958) 858

[38] A. Acrivos, M.J. Shah, and E.E. Peterson; J. Appl. Phys **31** (1960) 963

[39] D. Meyerhofer; J. Appl. Phys **49** (1978) 3993

[40] E. Bokelberg and W. Venet; SPIE: Advances in Resist Technology and Processing XII (1996) 2438

[41] D. E. Bornside and R. A. Brown, J. Appl. Phys. **73** (1993) 585

[42] L. E. Stillwagon and R.G. Larson; Physics of F1uids A **2** (1990) 1937

[43] M. Zhao, Z. Yang, D. Zhu and X. Jin and D. Huang; J. Opt. Soc. Am. B **22** (2005) 1330

[44] D. B. Bornside, C.W. Macosko, L.E. Scriven; J. Appl. Phys. **66** (1989) 5185

[45] P. C. Sukanek; J. Imaging Technology **11** (1985) 184

[46] C. Lisa, Sol-gel optics, Klein **153** (2006) A799

[47] www.clean.cise.columbia.edu

CHAPTER 3

CHARACTERIZATION TECHNIQUES

To fabricate a device, materials optimization is very important, and to optimize materials, characterization is a key factor. This chapter presents a brief description of structural, optical and electrical characterization techniques used in this report.

3.1 X-Ray Diffraction (XRD)

3.1.1 Introduction

X-rays occupy the region of the electromagnetic spectrum between ultra-violet and gamma radiation and are produced by bombarding a target, usually made of tungsten, (Cu, Mo targets are also used) with high-speed electrons [1]. X-rays were discovered accidentally in 1895 by the German physicist Wilhelm Conrad Roentgen while he was studying cathode rays in a high-voltage, gaseous-discharge tube. Despite the fact that the tube was encased in a black cardboard box, Roentgen noticed that a barium-platinocyanide screen, inadvertently lying nearby, emitted fluorescent light whenever the tube was in operation. After conducting further experiments, he determined that the fluorescence was caused by invisible radiation of a more penetrating nature than ultra-violet rays [2]. He named the invisible radiation "X-rays" because of its unknown nature. Subsequently, X-rays were also known as Roentgen rays in his honour. This extremely short wavelength electromagnetic radiation is produced by deceleration of charged particles or the transitions of electrons in atoms. The wavelengths of X-rays lie in the range of 10 to 0.01 nanometres, corresponding to frequencies in the range 30 petahertz to 30 exahertz (3×10^{16} Hz to 3×10^{19} Hz) and energies in the range 120 eV to 120 keV [1, 3]. The electromagnetic spectrum is shown in **Figure 3.1**. Like other forms of electromagnetic radiation (gamma rays, ultra-violet, visible light, infra-red, and radio waves), X-rays have the same speed in vacuo ($c = 3\times10^8$ metres per second) and show phenomena associated with its wavelike nature, such as interference, diffraction, and polarization. It was not until 1912 that the exact nature of X-rays was established, the first application of which was in the study of the internal structure of opaque objects (radiography) [4]. In 1912 Max von Laue discovered X-ray diffraction the same year that W.H. Bragg and his son, W.L. Bragg, analysed Laue's experiment and gave the necessary conditions for diffraction in a simpler mathematical form than that of Laue.

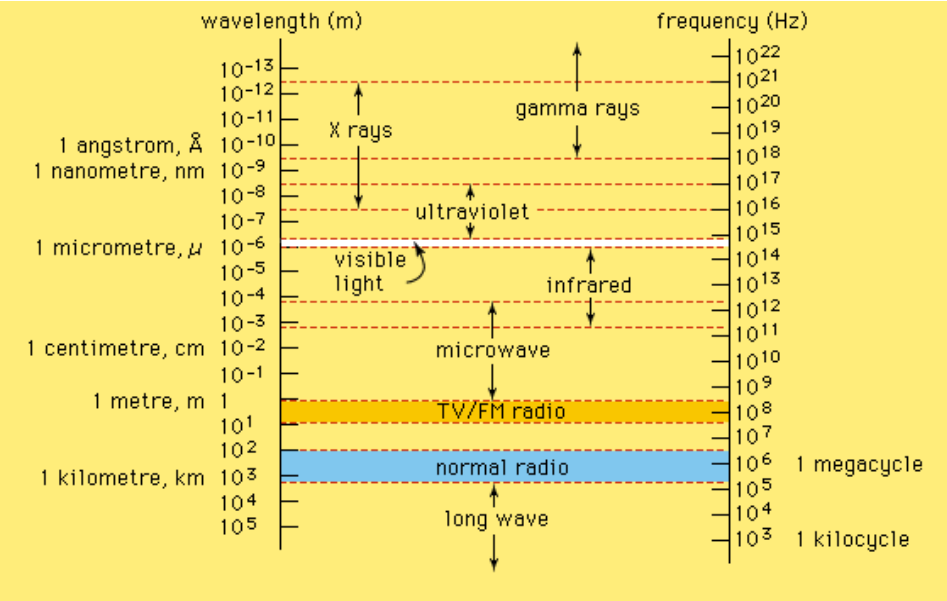

Figure 3.1: The electromagnetic spectrum [2].

They proceeded by applying x-ray diffraction to crystal structures and in the following year and deduced the structures of sodium chloride (NaCl), potassium chloride (KCl), potassium bromide (KBr), and potassium iodide (KI) for the first time ever, which were all face-center-cubic (FCC) in structure [5].

3.1.2 Bragg's Law

In physics, Bragg's law gives the angles for coherent and incoherent scattering from a crystal lattice. Bragg's Law is the result of experiments into the diffraction of X-rays or neutrons off crystal surfaces at certain angles. The law was first formulated by the English physicist Lawrence Bragg. Bragg's diffraction scheme is shown in **Figure 3.2**. From this we can derive Bragg's Law by observing that the rays of the incident beam are always in phase and parallel up to the point at which the top beam strikes the top layer at atom A. The second beam continues to the next layer where it is scattered by atom B. The second beam must travel the extra distance BC + BD if the two beams are to continue travelling adjacent and parallel.

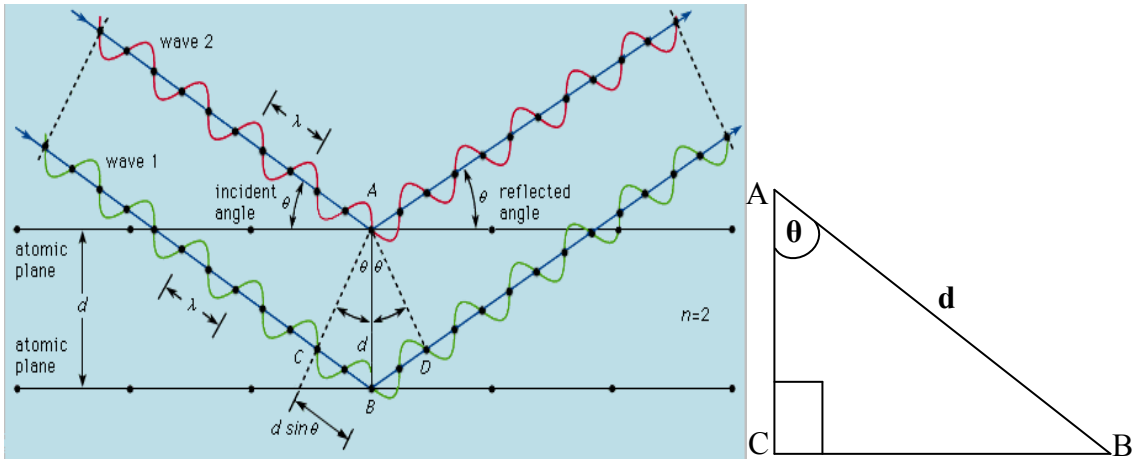

Figure 3.2: Bragg's Diffraction Scheme [2].

This extra distance must be an integral (n) multiple of the wavelength (λ) for the phases of the two beams to be the same, i.e.

$$n\lambda = BC + BD \tag{3.1}$$

The lower beam must travel the extra distance (BC + BD) to continue travelling parallel and adjacent to the top beam. Recognizing d as the hypotenuse of the right triangle ABC, we can use trigonometry to relate d and θ to the distance (BC + BD). Thus

$$BC = d \sin \theta \tag{3.2}$$

Because BC = BD eq. (3.1) becomes,

$$n\lambda = 2BC \tag{3.3}$$

Substituting eq. (3.2) in eq. (3.3) we have,

$$n\lambda = 2d \sin \theta \tag{3.4}$$

Equation 3.4 is known as Bragg's Law [6]. As may be seen from the diagram, when n = 2 there is only one wavelength along path CB; also, the reflected angle will be smaller than that for, say, n = 3. Waves reflected through an angle corresponding to n = 1 are said to be in the first order of reflection; the angle corresponding to n = 2 is the second order, and so on. For any other angle (corresponding to fractional n) the reflected waves will be out of phase and will result in destructive interference. Bragg's law is useful for measuring wavelengths and for determining the lattice spacing of crystals. To measure a particular wavelength, the radiation beam and the detector are both set at some arbitrary angle θ. The angle is then modified until a

strong signal is received at what is defined as the Bragg angle and the wavelength is deduced directly from the Bragg equation. This is the principal way of producing precise energy measurements of X-rays and low-energy gamma rays. The energies of neutrons, which by quantum theory also have wave attributes, are frequently determined by Bragg reflection.

3.1.3 Experimental Techniques for X-ray Diffraction

X-ray diffraction is a versatile non-destructive analytical technique for identification and quantitative determination of various crystalline phases of powdered or solid samples of any compound. The most basic setup of the x-ray diffractometer is the Bragg-Brentano geometry as shown in figure 3.3.

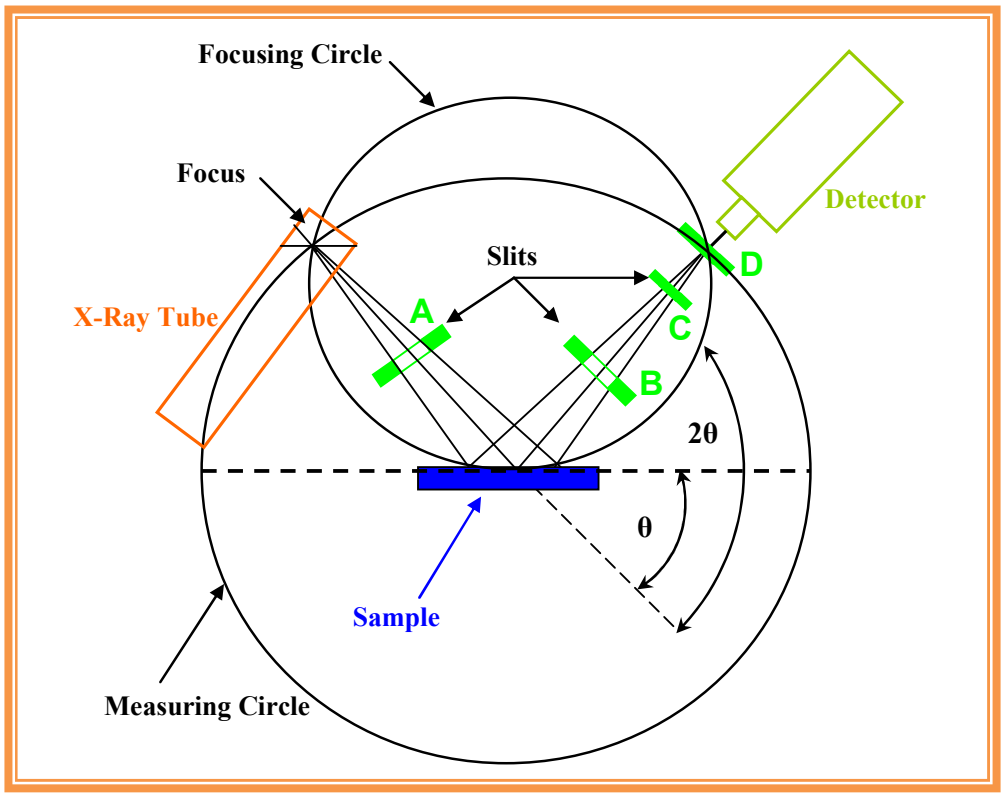

Figure 3.3: Basic setup of D8 Advance X-Ray Diffractometer, Bragg-Brentano Geometry [7]. A: aperture slit, B: scattered radiation slit, C: Kα filter, D: detector slit.

The sample rotates at a constant angular velocity such that the angle of incidence of the primary beam changes whilst the detector rotates at double the angular velocity

around the sample. The diffraction angle 2θ is thus always equal to twice the glancing angle, θ. The focus, sample and detector slit are on the focusing circle; the focus and detector slit are also located on the measuring circle. The radiation emanating from the line focus of the x-ray tube is diffracted at the sample and recorded by the detector. Each time the Bragg condition is satisfied the primary beam is reflected from the sample to the detector. The detector and the connected measuring electronics measure the intensity of the reflected radiation; the angular position of the reflections is displayed at the controller. Pulse counts of diffraction patterns are obtained in this way. In this study, XRD measurements were carried out by using a Bruker AXS D8 Advance X-ray diffractometer, using monochromatic CuK_α radiation ($\lambda = 1.54056$ Å) at room temperature. The standard setting for the X-rays generator was 40 kV at 40 mA. The scans were measured in the aforementioned Bragg–Brentano geometry (θ–2θ) in a range of 5º to 60º, a step size of 0.005^o and a step time of 0.2 seconds.

3.2 Scanning Electron Microscopy (SEM)

3.2.1 Introduction

The scanning electron microscope creates various high magnification images by focusing a high energy beam of electrons onto the surface of a sample in a raster scan pattern and detecting signals from the interaction of the incident electrons with the sample's surface. The electrons interact with the atoms and produce the signals that contain information about the sample's surface topography, composition and other properties such as electrical conductivity. In 1935, Max Knoll obtained the first SEM image of silicon steel showing electron channeling contrast [8]. Following this, in 1937 Manfred von Ardenne worked on the physical principles of the SEM and beam specimen interactions [9, 10]. In 1965, Professor Sir Charles Oatley and his student Gary Stewart further developed the SEM and it was subsequently marketed by the Cambridge Instrument Company as the "Stereoscan". The first instrument was delivered to DuPont [10].

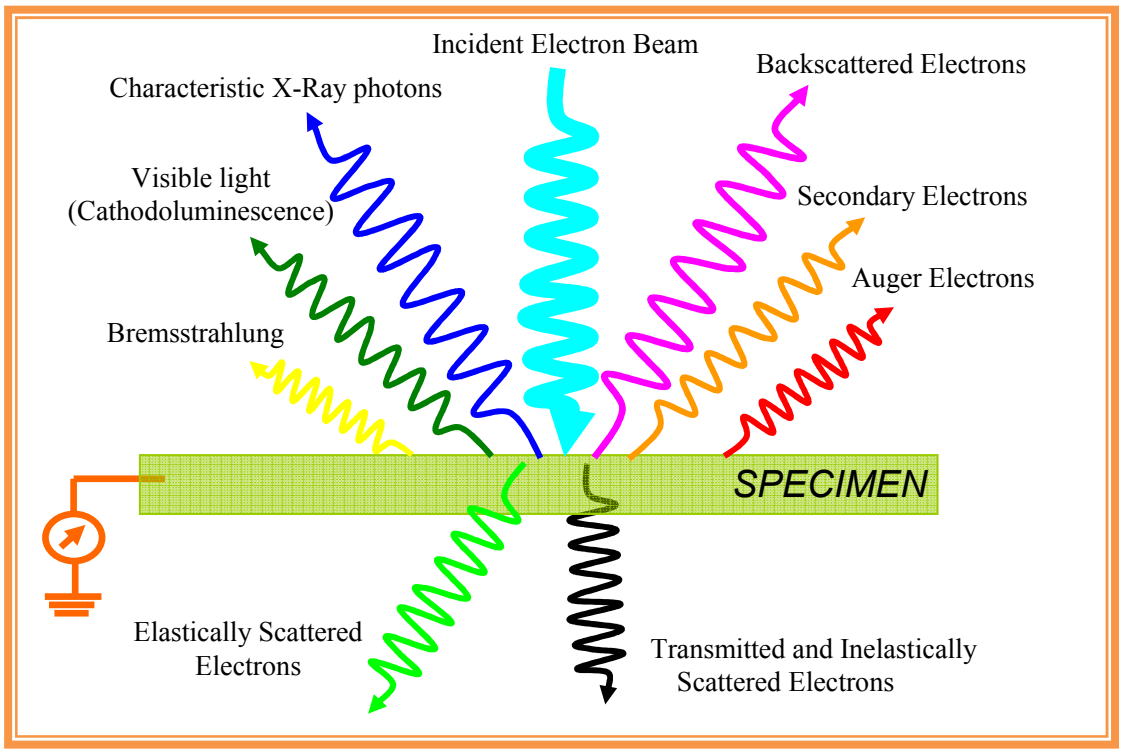

Figure 3.4: Signals produced when an electron beam is incident on a sample [11].

3.2.2 X-ray Microanalysis

When the sample is bombarded by an electron beam the following signals/products may occur as shown in **Figure 3.4** backscattered electrons, secondary electrons, x-rays, cathodoluminescence and Auger electrons. Backscattered and secondary electrons are used to obtain a detailed topographical image of the surface of the sample. Besides these, scanning electron microscopes are often equipped with Energy Dispersed Spectroscopy (EDS) or Energy Dispersed Analysis of X-rays (EDAX) detectors that analyse the emitted X-ray energies. With such instruments, it is possible to determine which elements are present in the surface layer of the sample (at a depth in the micrometre range) and where these elements are present. This particular microscope also allows one to capture directly reflected electrons, the so-called backscattered electrons, from which one can obtain a global appreciation whether one or several elements are present in the surface layer of the sample. Also the Auger electrons, which are emitted just under the surface, provide information about the nature of the atoms in the sample.

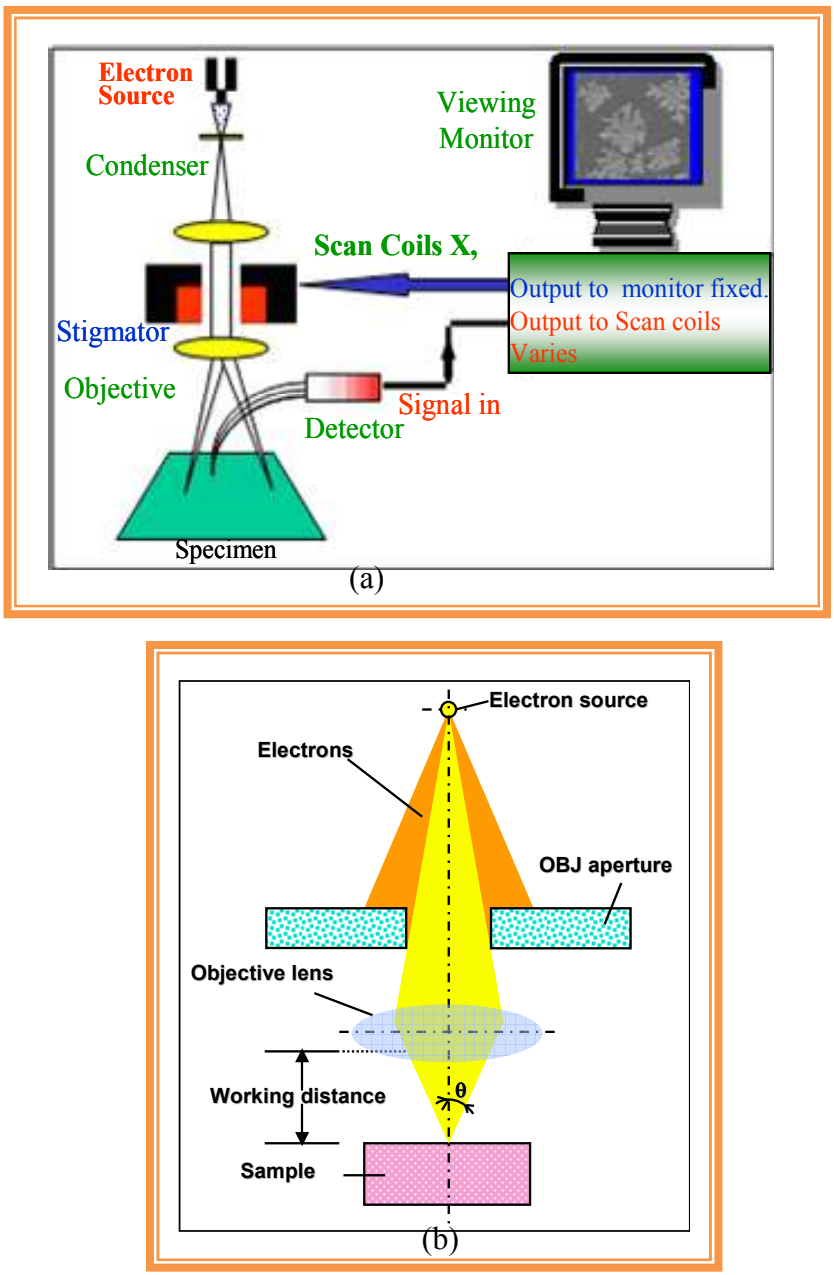

Figure 3.5: Schematic of (a) typical SEM and (b) path of the electron beam in this system [12]

3.2.3 Scanning Process

In a typical SEM, electrons are thermionically emitted from a tungsten or lanthanum hexaboride (LaB_6) cathode and are accelerated towards an anode; alternatively, electrons can be emitted via field emission (FE). Tungsten is used because it has the highest melting point and lowest vapour pressure of all metals, thereby allowing it to

be heated for electron emission. The electron beam, which typically has an energy ranging from a few hundred eV to 100 keV, is focused by one or two condenser lenses into a beam with a very fine focal spot sized 0.4 nm to 5 nm, typically. The beam passes through pairs of scanning coils or pairs of deflector plates in the electron optical column, typically in the objective lens, which deflect the beam horizontally and vertically so that it scans in a raster fashion over a rectangular area of the sample surface. **Figure 3.5** shows the schematic of a typical SEM system. When the primary electron beam interacts with the sample, the electrons lose energy by repeated random scattering and absorption within a teardrop-shaped volume of the specimen known as the interaction volume, which extends from less than 100 nm to around 5 μm into the surface. The size of the interaction volume depends on the electron's arrival energy, the atomic number of the specimen and the specimen's density. The energy exchange between the electron beam and the sample results in the reflection of high-energy electrons by elastic scattering, emission of secondary electrons by inelastic scattering and the emission of electromagnetic radiation, each of which can be detected by specialized detectors. The beam current absorbed by the specimen can also be detected and used to create images of the distribution of specimen current. Electronic amplifiers of various types are used to amplify the signals which are displayed as variations in brightness on a screen. The raster scanning of the display is synchronized with that of the beam on the specimen in the microscope, and the resulting image is therefore a distribution map of the intensity of the signal being emitted from the scanned area of the specimen. The image may be captured by photography from a high resolution cathode ray tube, but in modern machines it is digitally captured and displayed on a computer monitor and saved to a computer's hard disc. In this study, the surface morphology and composition of as-deposited and heat treated CuCl hybrid films were investigated using an ‘EVO LS 15’ scanning electron microscope developed by Carl Zeiss. An accelerating voltage of 15-19 keV and probe current of ~800 pA was used for a qualitative comparison of the CuCl composition as a function of time and heat treatment.

3.3 Atomic Force Microscopy (AFM)

Atomic force microscopy (AFM) is a high-resolution scanning tool for imaging, measuring and manipulating matter at the nanoscale. It can create three dimensional highly magnified images of a surface. The advantage of AFM over scanning tunnelling microscopy (STM) is the ability to image both conductive and non-conductive materials [13]. In the early 1980s, Gerd Binnig and Heinrich Rohrer developed the scanning tunnelling microscope which was the precursor of the AFM; this development won them the Nobel Prize for Physics in 1986. Binnig *et al.* invented the first AFM in 1986. Since the invention of AFM it has found applications in surface science based technology including the semiconductor, telecommunications, biological, chemical automotive, aerospace and energy industries [14].

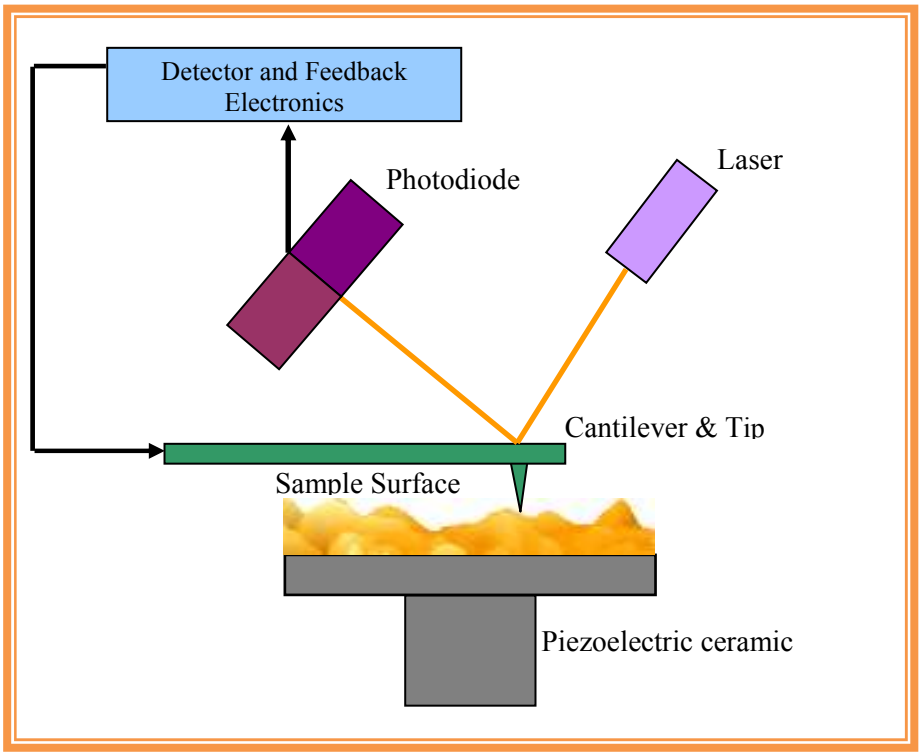

Figure 3.6: Schematic representation of a typical modern AFM [15]

The AFM consists of a cantilever with a sharp tip (probe) at its end that is used to scan the specimen surface [13, 14]. The cantilever is typically silicon or silicon nitride with a tip radius of curvature on the order of nanometres. When the tip is

brought into proximity with a sample surface, the force F between the tip and the sample leads to a deflection of the cantilever according to Hooke's law:

$$F = kx \tag{3.6}$$

where x is the deflection of the cantilever out of equilibrium position and k is directly proportional to the Coulomb forces between the tip and the surface sample. The schematic diagram of the AFM is shown in **Figure 3.6**. When the sample surface is scanned then a motion or force is generated on the atomically sharp probe. The forces exist over a short range, and measuring them via the cantilever deflection on the surface gives a pictorial representation of the atom on the surface and thus the surface topography. Typically, the deflection is measured using a laser spot reflected from the top surface of the cantilever into an array of photodiodes. The photodiode array determines the position of the reflected spot and this is compared with the equilibrium value. The change of the surface height corresponds to the deflection of the laser spot via the deflection of the cantilever. An electronic feedback control system is used to adjust the tip–to–sample distance in order to keep the force between the tip and the sample constant. The AFM can be operated in several different imaging modes, depending on the application. In contact mode operation of the static tip deflection is used as a feedback signal. The force between the tip and the surface is kept constant during scanning by maintaining a constant deflection [16]. In tapping mode the cantilever is driven to oscillate up and down near its resonance frequency by a small piezoelectric element mounted in the AFM tip holder [17]. A tapping AFM image is therefore produced by imaging the force of the oscillating contacts of the tip with the sample surface. The commonest modes of operation are contact and tapping modes [18]. In non-contact mode, the tip of the cantilever does not contact the sample surface. The cantilever is instead oscillated at a frequency slightly above its resonance frequency where the amplitude of oscillation is typically a few nanometers (<10 nm). In comparison, imaging in contact mode and tapping mode shows that soft surfaces are less modified in the tapping mode [19], thus they are very useful in imaging biological and soft samples. In this study, the contact mode was used to obtain surface topography and roughness analysis for all the samples using a Pacific Nanotechnology Nano-R AFM system.

3.4 X-ray Photoelectron Spectroscopy (XPS)

X-ray photoelectron spectroscopy, also known as Electron Spectroscopy for Chemical Analysis (ESCA), is a quantitative spectroscopic technique that measures the elemental composition, empirical formula, chemical state and electronic state of the elements that exist within a material. XPS based on the photoelectric effect [20, 21] was developed in the mid 1960s by K. Siegbahn and his research group [22].

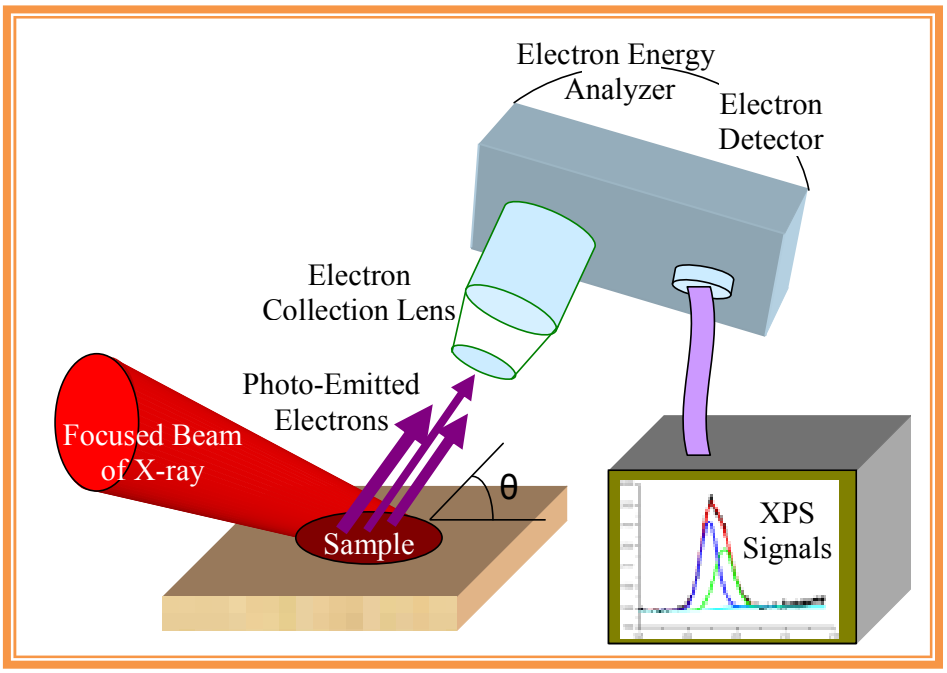

Figure 3.7: The schematic diagram of a monochromatic XPS system

Each atom in the surface has core electrons with characteristic binding energies. When an X-ray beam is directed to the sample surface, the energy of the X-ray photon is absorbed completely by the core electron of an atom. If the photon energy, $h\nu$, is large enough, the core electron will then escape from the atom and be emitted from the surface. The emitted electron with kinetic energy of E_k is referred to as the photoelectron. The binding energy of the core electron is given by the Einstein relationship:

$$E_b = h\nu - E_k - \phi \tag{3.7}$$

where $h\nu$ is the X-ray photon energy, E_k is the kinetic energy of the photoelectron, which can be measured by an energy analyzer; and ϕ is the work function induced

by the analyzer. Since the work function ϕ, can be compensated artificially, it is eliminated, giving the binding energy as follows:

$$E_b = h\nu - E_k \tag{3.8}$$

The basic mechanism of an XPS instrument is shown in **Figure 3.7**, where photons of a specific energy are used to excite the electronic states of atoms below the surface of the sample. Electrons ejected from the surface are energy filtered via an analyzer before the intensity for a defined energy is recorded by a detector. Since core level electrons in solid-state atoms are quantized, the resulting energy spectra exhibit resonance peaks characteristic of the electronic structure for atoms at the sample surface [23]. In this research, the nanocrystalline CuCl hybrid film composition was studied using a Vacuum Generators XPS system operating at base pressures in the preparation and analysis chambers of 2×10^{-6} and 1×10^{-9} mbar, respectively, equipped with a Al K_α ($h\upsilon$ = 1486.6 eV) X-ray source. The pass energy of the analyser was typically set at 20 eV yielding a resolution of approximately .1 eV. The XPS peaks were fitted with mixed ratios of Gaussian and Lorentzian line shapes and a Shirley background function. The calibration of the binding energy scale was performed with the $C1_S$ line (285 eV) from the carbon contamination layer.

3.5 Absorption Spectroscopy

Absorption spectroscopy is one of the most direct and perhaps simplest methods for probing the band structure of semiconductor materials. During the absorption process, a photon of known energy excites an electron from a lower to a higher energy state. The Bouguer-Lambert-Beer law forms the mathematical-physical basis of light absorption measurements in the UV-Vis and IR regions [24]:

$$A_{\nu'} = \log\left(I_0/I\right)_{\nu'} = \log\left(100/T(\%)\right)_{\nu'} = \varepsilon_{\nu'}cd \tag{3.9}$$

where $A_{\nu'} = \log\left(I_0/I\right)_{\nu'}$ is the absorbance and $T_{\nu'}$ in % is the transmittance, $\varepsilon_{\nu'}$ is the molar decadic extinction coefficient. I_0 is the intensity of the monochromatic light entering the sample and I is the intensity of this light emerging from the sample; c is the concentration of the light–absorbing substance and d is the path length of the sample. Therefore by placing a semiconductor sample at the output of a

monochromator and studying the changes in the transmitted radiation, one can discover the possible transitions being made by the electron.

3.5.1 UV-Vis Spectroscopy

Optical spectroscopy is based on the Bohr-Einstein frequency relationship [25]:

$$\Delta E = E_1 - E_2 = h\nu \tag{3.10}$$

$$\Delta E = E_1 - E_2 = hc\,\nu', \qquad [\nu = \nu' c] \tag{3.11}$$

where ν' is the wavenumber. This relationship links the discrete or molecular energy states E_i with the frequency ν of the electromagnetic radiation. Absorbed or emitted radiation of frequency ν can thus be assigned to specific energy differences:

$$\nu' = \Delta E/h = E_1/hc - E_2/hc \tag{3.12}$$

The energy differences correspond to those of the electronic states of atoms and molecules; hence the concept of "electronic spectroscopy".

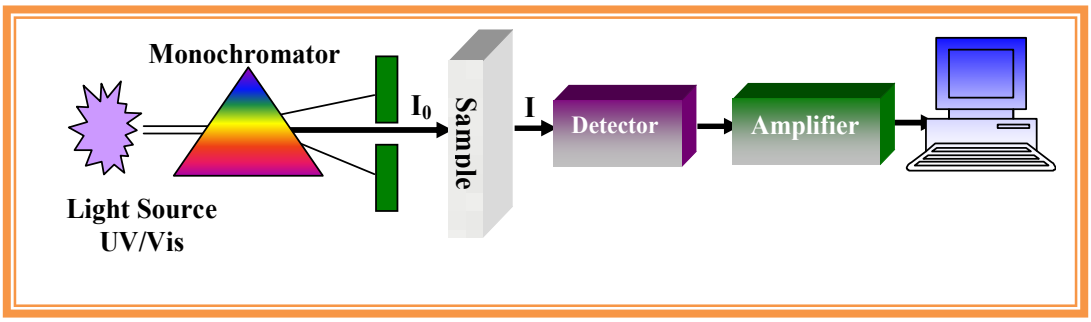

Figure 3.8: Schematic diagram of a UV/Vis spectrophotometer

The schematic of a UV/Visible light (UV/Vis) spectrophotometer is shown in **Figure 3.8**. A deuterium and tungsten lamp are typically used as a source of UV and Visible light, respectively. The functioning of this instrument is relatively straightforward. A beam of light from the UV/Visible light source is separated into its component wavelengths by a prism or diffraction grating. The monochromatic beam is then split into two paths using a half-mirrored device. The intensities of these light beams are then measured by electronic detectors and compared. The intensity of the reference beam, which should have suffered little or no light absorption, is defined as I_0. The

intensity of the sample beam is defined as I. Over a short period of time, the spectrometer automatically scans all the component wavelengths in the manner described. The ultraviolet (UV) region scan is typically from 200 to 400 nm, and the visible portion is from 400 to 800 nm. The UV-Vis absorption measurements of the CuCl films were carried out at room temperature using a Perkin Elmer Lambda 40 UV-Vis spectrometer in the range 300 to 750 nm with a resolution of 4 nm.

3.5.2 Fourier Transform Infrared (FTIR) Spectroscopy

Infrared Spectroscopy is an extremely powerful analytical technique for both qualitative and quantitative analysis. Fourier Transform Infrared Spectroscopy is a measurement technique whereby spectra are collected based on measurements of the coherence of a radiative source, using time-domain or space-domain measurements of the electromagnetic radiation or other radiation. It can be applied to a variety of spectroscopies including optical spectroscopy, infrared spectroscopy, Fourier transform (FT) nuclear magnetic resonance [26] mass spectrometry and electron spin resonance spectroscopy. In 1880, an optical device was invented by Albert Abraham Michelson, which was called the Michelson interferometer [27]. The Michelson interferometer was not originally designed to perform infrared spectroscopy but could be utilized to obtain spectra by manually measuring interferograms. Unfortunately, the time consuming calculations required to convert an interferogram into a spectrum made using an interferometer to obtain spectra impractical. The invention of computers made calculating Fourier transforms faster but that was not enough. J.W. Cooley and J.W. Tukey at Bell Labs invented what is known as the "Fast Fourier Transform" (FFT), or "Cooley-Tukey Algorithm" which quickly performs Fourier transforms on a computer [28]. In 1960, the first commercially available FTIRs were manufactured by the Digilab subsidiary of Block Engineering in Cambridge, Massachusetts, USA and since then other companies manufacture and sell FTIRs [29, 30]. Infrared Spectroscopy is the study of the interaction of infrared light with matter. Light is composed of electric and magnetic waves. The electric part of the light called the electric vector interacts with the molecules. The basic components of an FTIR are shown schematically in **Figure 3.9**. The most important and unique part of an FTIR spectrometer is the interferometer.

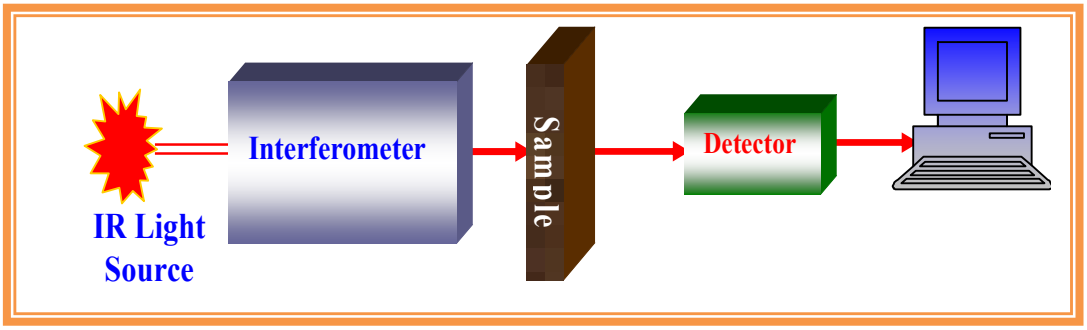

Figure 3.9: Block diagram of FTIR spectrometer

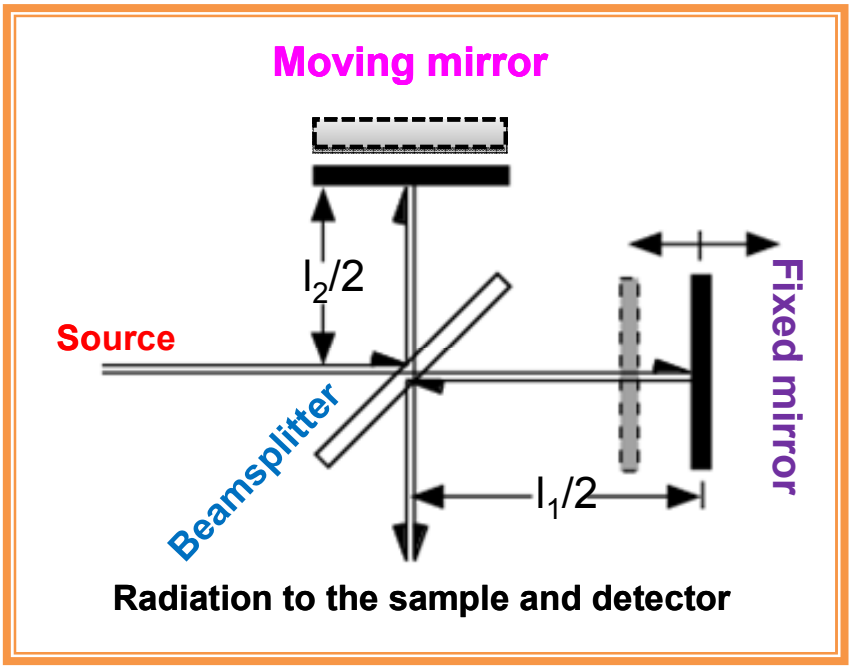

Figure 3.10: Michelson interferometer

The interferometer is the component that analyses the infrared or near infrared and hence enables us to generate a spectrum. A Michelson type plane mirror interferometer is shown in **Figure 3.10**. Light from the source enters the interferometer along one arm and strikes a half-mirrored glass called a beamsplitter. The beamsplitter ideally transmits one half of the radiation, and reflects the other half. Both transmitted and reflected beams strike mirrors, which reflect the two beams back to the beamsplitter. Thus, one half of the infrared radiation that finally goes to the sample has first been reflected from the beam splitter to the moving mirror, and then back to the beam splitter. The other half of the infrared

radiation going to the sample has first gone through the beam splitter and then reflected from the fixed mirror back to the beam splitter. When these two optical paths are reunited, interference occurs at the beamsplitter because of the optical path difference caused by the scanning of the moving mirror. The optical path length difference between the two optical paths of a Michelson interferometer is two times the displacement of the moving mirror. The interference signal measured by the detector as a function of the optical path length difference is called the interferogram. A typical interferogram produced by the interferometer is shown in figure 3.11. The graph shows the intensity of the infrared radiation as a function of the displacement of the moving mirror.

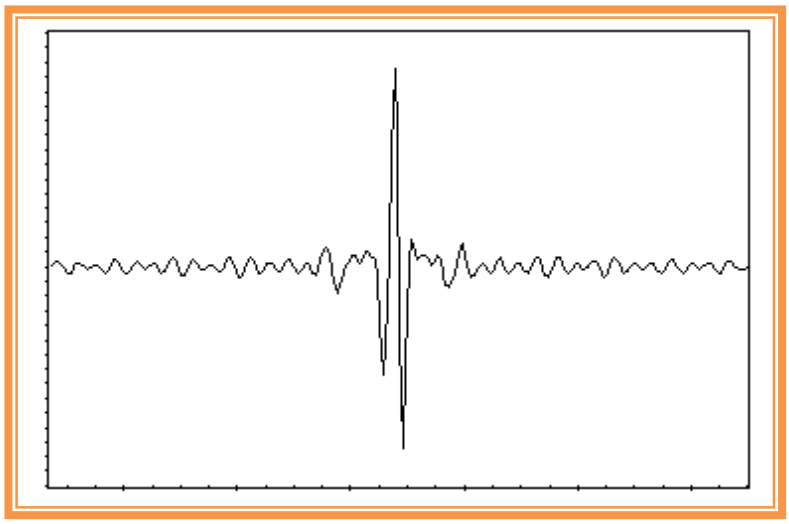

Figure 3.11: A typical interferogram

At the peak position, the optical path length is exactly the same for the radiation that comes from the moving mirror as it is for the radiation that comes from the fixed mirror. The spectrum can be computed from the interferogram by performing a Fourier transform. The Fourier transform is performed by the same computer that ultimately performs the quantitative analysis of the spectrum. The infrared source emits a broad band of different wavelengths of infrared radiation. The IR radiation goes through an interferometer that modulates the infrared radiation. The interferometer performs an optical inverse Fourier transform on the entering IR radiation. The modulated IR beam passes through the sample where it is absorbed to various extents at different wavelengths by the various molecules, phonons, etc.

present. Finally the intensity of the IR beam is detected by a detector. The detected signal is digitized and Fourier transformed by the computer to get the IR spectrum of the sample. The infrared spectrum can also provide quantitative information such as the concentration of a molecule in a sample. The basis of all quantitative analyses in FTIR is Beer's law, which relates concentration to absorbance as follows [31]:

$$A = \varepsilon lc \tag{3.13}$$

where A = absorbance, ε = absorptivity, l = path length and c = concentration. The absorbance is measured as a peak height, peak height ratio, peak area, or peak area ratio from the FTIR spectrum. The Fourier Transform Infrared absorption spectra were recorded on a Perkin-Elmer GX FTIR system with a resolution of 16 cm^{-1} in a spectral range of 400 to 4000 cm^{-1} and scanned 30 times (absorbance mode), in order to exploit the instrumental built-up noise reduction algorithm.

3.6 Luminescence Spectroscopy

Luminescence is the general term to describe the emission of radiation from a material after being subjected to applied energy. Luminescence may be split up into several categories (**Table 3.1**).

Luminescence type	**Typical application**	**Luminous efficiency**
Blackbody radiation	Tungsten filament lamp	~5%
Photoluminescence	Fluorescent lamp	~20%
Cathodoluminescence	Television screen	~10%
Electroluminescence	Light-emitting diode, flat panel display	0.1-50%

Table 3.1: Luminescence types, applications and typical efficiencies [32]

Light interaction with semiconductors is an important and powerful means of characterization. It is non-contacting and non-destructive. Semiconductors emit light as a result of electronic transitions between quantum mechanical states separated by energy levels of typically less than 1 eV to about 4 eV. Energy and momentum must be conserved during the electronic transitions.

3.6.1 Photoluminescence (PL)

Photoluminescence is a process in which a substance absorbs photons (electromagnetic radiation) and then re-radiates photons. Quantum mechanically, this can be described as an excitation to a higher energy state and then a return to a lower energy state accompanied by the emission of a photon. During the photoluminescence process, photo-excitation causes electrons in the semiconductor material to move into permissible excited states. After a short while, the electrons return to their equilibrium states thereby recombining with holes, or by relaxation to a lower energy state, and liberating energy which may include light (radiative emission) or heat (non-radiative emission). The energy of the emitted light is related to the difference in the energy levels between the excited state and the equilibrium state while the intensity of the emitted light is related to the relative contribution of the radiative process. In photoluminescence, the photo-excitation is usually implemented using a laser with a fixed wavelength and the emitted light is measured over a wavelength region. Some common radiative recombination processes that occur in semiconductor materials are shown in **Figure 3.12**.

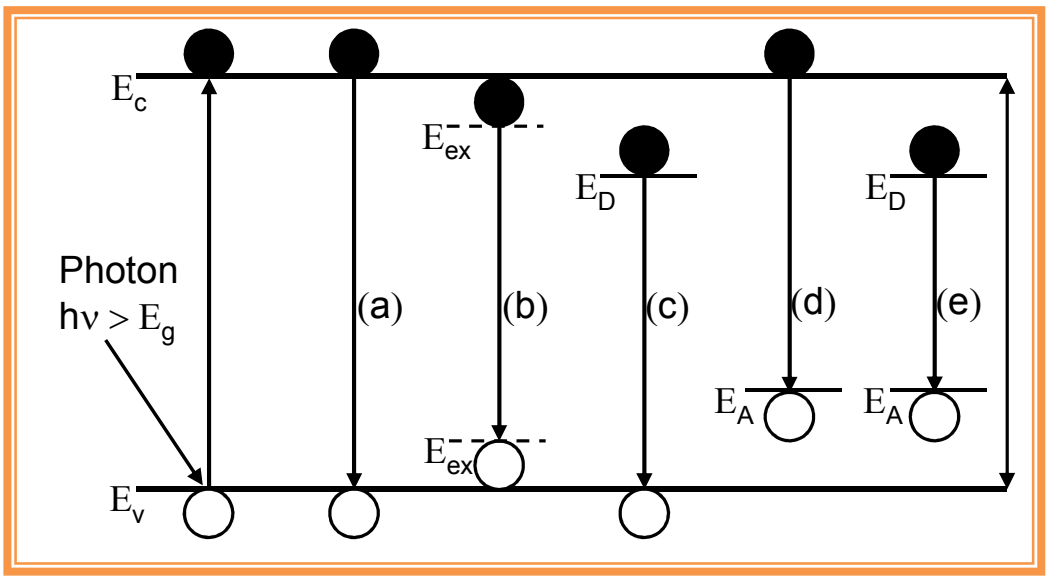

Figure 3.12: Schematic diagram of radiative transitions in a semiconductor material; (a) Conduction to valence band (b) excitonic recombination (c) donor and valence band (d) conduction band and (e) donor to acceptor.

When a sample is excited with an optical source such as a laser, with energy hν >E_g, electron-hole pairs are generated which recombine by one of several mechanisms. Process (a) is an interband transition resulting from the recombination of electrons in the conduction band with holes in the valence band. Band-to-band recombination dominates at room temperature in typical semiconductors. If the material is sufficiently pure, free excitons form and recombine by emitting photons as shown in process (b) of **Figure 3.12**. The photon energy of an exciton in a direct band-gap semiconductor is

$$h\nu = E_g - E_x \tag{3.14}$$

where E_x is the excitonic binding energy. Transitions which start or finish on localised states of impurities, e.g. donors just below the conduction band, or acceptors just above the valence band are illustrated in **Figure 3.12 (c)** and **(d)**. A free hole can combine with a neutral donor to form a positively charged excitonic ion known as a bound exciton. The electron bound to the donor travels in a wide orbit about the donor. Similarly, an electron can combine with a neutral acceptor also forming a bound exciton. In the presence of impurities, free and bound excitons can occur simultaneously in the same material. The emission of the bound exciton is characterised by a narrow spectral width at lower photon energy than that of the free exciton, therefore it is possible to distinguish between them. In **Figure 3.12 (e)** a donor acceptor (D-A) recombination process is shown, where an electron on a neutral donor recombines with a hole on a neutral acceptor.

3.6.1.1 Experimental Techniques for PL Measurement

PL is simple, versatile, and non-destructive. The instrumentation that is required for ordinary PL work is relatively modest: an optical source and an optical power meter or spectrophotometer. A typical PL setup is shown in **Figure 3.13**. Because the measurement does not rely on electrical excitation or detection, sample preparation is minimal. This feature makes PL particularly attractive for material systems having poor conductivity or undeveloped contact/junction technology. Measuring the continuous wave PL intensity and spectrum is quick and straightforward [33-37]. On the other hand, investigating transient PL is more challenging, especially if recombination processes are fast. Instrumentation for time-resolved detection, such

as single photon counting, can be expensive and complex. Even so, PL is one of the only techniques available for studying fast transient behavior in materials.

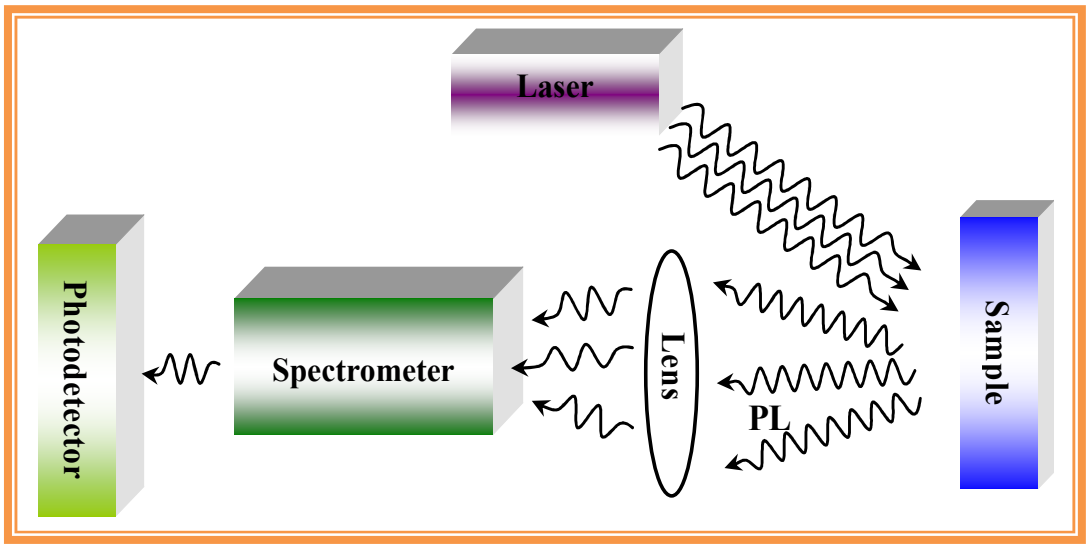

Figure: 3.13: Typical setup for the measurement of PL

The measurement of photoluminescence from semiconductor materials has become an important characterization method and is widely used to provide information on, e.g. carrier doping levels, alloy compositions, film structures, band gap and edge effects, etc. in applications ranging from scientific research, process monitoring, to device characterization. In this study, photoluminescence measurements were carried out from room temperature to 15 K by employing a UV Ar^{+} Innova laser with a second harmonic generation BBO crystal producing a 355 nm photo excitation. The PL spectra were collected on a Jobin Yvon-Horiba Triax 190 spectrometer with a spectral resolution of 0.3 nm, coupled with a liquid nitrogen-cooled CCD detector.

3.6.2 Cathodoluminescence

Cathodoluminescence is an optical and electrical phenomenon. When a high energy electron beam impinges on the specimen, electrons are promoted from the valence band into the conduction band and their subsequent dexcitation results in the release of energy in form of photons [38]. The energy of the emitting photon depends on the material, its purity, and its defect state. Light emission from a sample excited by an

electron beam gives a good indication of whether it will be possible for light to be emitted by injection of an electron current and is therefore a good early indicator of the possibility of producing a light emitting device. As it does not require an ohmic contact or Schottky barrier to operate, semiconductor samples can be examined without elaborate and time consuming preparation. In materials science and semiconductor engineering, cathodoluminescence is mostly performed in either a scanning electron microscope or a scanning transmission microscope. In these cases, the highly focused beam of electrons impinges on a sample and induces it to emit light from a localized area. This light is collected by an optical system, such as an elliptical mirror. From there, a fiber optic will transfer the light out of the microscope where it is dispersed by a monochromator and then detected with a photomultiplier tube. By scanning the microscope's beam in an X-Y pattern and measuring the light emitted with the beam at each point, a map of the optical activity of the specimen can be obtained. The primary advantages to the electron microscope based technique is the ability to resolve features down to 10-20 nanometers, the ability to measure an entire spectrum at each point if the photomultiplier tube is replaced with a CCD camera, and the ability to perform nanosecond to picosecond-level time-resolved measurements if the electron beam can be "chopped" into nano- or pico-second pulses. However, as the abilities are improved, the cost of the electron-microscope based techniques becomes very high. These advanced techniques are useful for examining low-dimensional semiconductor structures, such a quantum wells or quantum dots. CL scans were performed at room temperature using a Carl Zeiss EVO 50 Series SEM with an attached CL mirror and micrometer. Spectra were captured using the Gatan MonoCL monochromator with a 1200 lines/mm grating and a constant probe current of 300 pA.

3.6.3 Electroluminescence (EL)

When a material emits electromagnetic radiation as result of the application of an electric field this process is known as electroluminescence. The EL phenomenon was discovered by Round in 1907. He observed the generation of yellowish light from a carborundom crystal (SiC) when a potential of 10 V was applied between two points on the crystal [39]. The schematic diagram of an electroluminescence measurement

system is shown in **Figure 3.14**. By way of example for the electroluminescent device (ELD) the CuCl hybrid film was deposited on ITO coated glass substrate by the spin coating method (spin coating method described in chapter 2). A non-transparent gold (≈ 200 nm thick) contact top electrode was deposited on the CuCl hybrid film layer using an Edwards Auto 306A vacuum deposition system at a base pressure of $1x10^{-6}$ mbar.

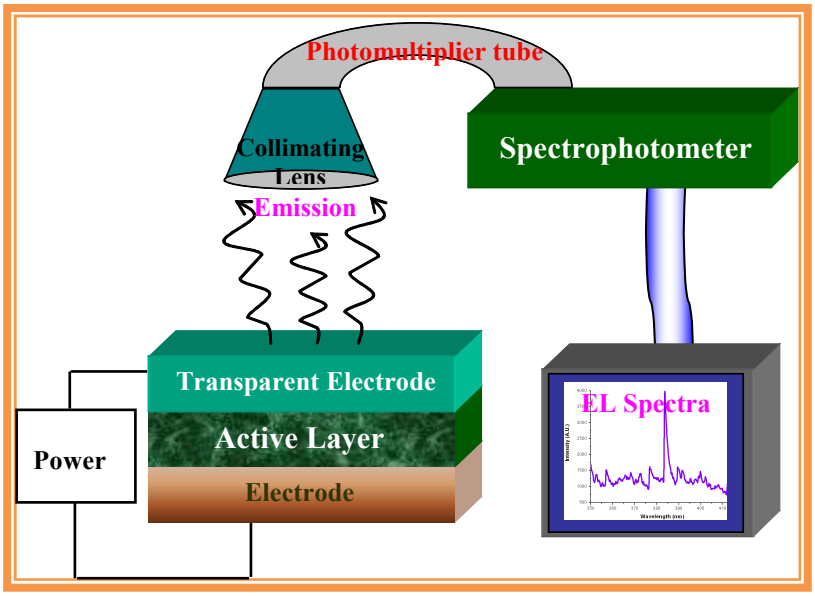

Figure 3.14: Schematic illustration of electroluminescence system

The Au top electrode was non-transparent and electroluminescence (EL) emission was observed principally through the transparent ITO coated glass. The ELD device was driven by an AC sinusoidal waveform with a typical frequency of 50 Hz and a peak-to-peak voltage of 70-130 V. The electroluminescence measurements of the test devices were evaluated using a SOFIE spectrophotometer with a photomultiplier tube (spectral range of 200–900 nm).

3.7 Electrical Characterization

3.7.1 Current-Voltage (I-V) Characteristics

Electrical characterization is an essential part of semiconductor material and device analysis. Electrical resistivity (ρ) is a measure of how strongly a material opposes the flow of electric current. The resistivity is one of the most important characteristics of a semiconductor or fabricated semiconductor device because it contributes series

resistance and capacitance, and impacts threshold voltages and other electrical properties in the device. In semiconductor materials the resistivity depends on the free electron and hole densities, n and p, and the electron and hole mobilities, μ_n and μ_p, respectively. The resistivity ρ can be calculated from the measured carrier densities and mobilities using the relationship [40]:

$$\rho = \frac{1}{q\left(\mu_n n + \mu_p p\right)} \tag{3.15}$$

and

$$\rho \propto \frac{V}{I} t \tag{3.16}$$

where q is the electronic charge and t is the thickness of the films, V is voltage, I is current. In this study all electrical measurements were carried out using a Keithley 4200 SCS semiconductor parameter analyzer.

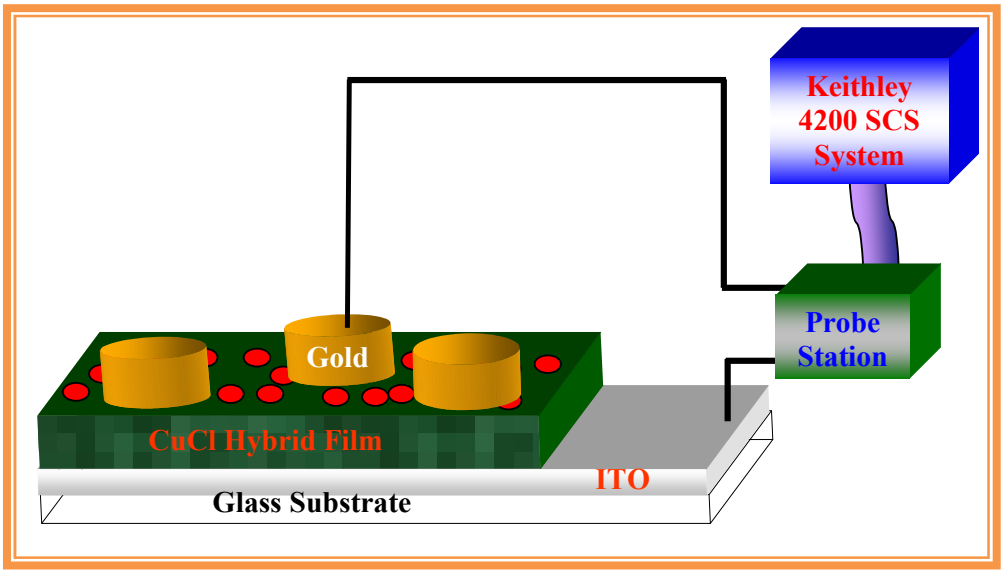

Figure 3.15: Schematic of the CuCl hybrid film electrical characterization system

A schematic diagram of the current-voltage characteristic investigation structure is shown in **Figure 3.15**. In order to typically measure the current-voltage characteristics of the CuCl hybrid films the films were deposited on Indium Tin Oxide (ITO) coated glass substrate by spin coating. Again, a gold contact top electrode was deposited using an Edwards Auto 306A vacuum deposition system at a base pressure of ~$1x10^{-6}$ mbar. A spring loaded probe station was designed and used

for the measurements to avoid damaging the hybrid film surface layer. The Keithley 4200 system has a built-in voltage source, which was used to measure the current voltage characteristics of the samples. The voltage across the sample was increased in steps of 0.05 V with a 5 second hold for time on each increment. Automated current voltage measurements were performed using LabVIEW® software interfaced with the Keithley system.

Reference

[1] H. A. Enge, M. R. Wehr and J. A. Richards; Introduction to Atomic physics Addison-Wesley Publishing Company: Reading (1972)

[2] M. M. Alam; M. Phil Thesis, "Synthesis and Optical Properties of Semiconductor Nanostructures" Islamic University, Kushtia, Bangladesh, (2008)

[3] R. Novelline; Squires Fundamentals of Radiology, Harvard University Press, 5th ed. (1997)

[4] B. D. Cullity and S. R. Stock; Elements of X-ray Diffraction, 3rd ed. Prentice Hall (2001) 1

[5] P. P. Ewald, Fifty years of X-Ray Diffraction, International Union of Crystallography (1962)

[6] B. D. Cullity and S. R. Stock Elements of X-ray Diffraction, 3rd ed. Prentice Hall (2001) 95

[7] Bruker Advanced X-Ray Solutions, D8 X-Ray Diffractometer User's Manual Volume I, pp. 1-2

[8] K. Max; Zeitschrift für Technische Physik **16** (1935) 467

[9] V. Ardenne, Manfred; Zeitschrift für Physik **108** (1938) 553

[10] V. Ardenne, Manfred; Zeitschrift für Technische Physik **19** (1986) 407

[11] EVO Series SEM Operator User Guide, PDF 28

[12] SEM user manual Leo 400 operational notes page 2-3

[13] S. N. Magonov and M. Whangbo; Surface Analysis with STM and AFM: Experimental and Theoretical Aspects of Image Analysis, Wiley-VCH (1996)

[14] G. Binnig, C. Quate, Ch. Gerber; Physical Review Letters **56** (1986) 930

[15] P J Brown and J B Forsyth, The Crystal Structure of Solids Edwards Arnold (1979)

[16] D. Sarid; Scanning Force Microscopy, Oxford University Press: New York (1991)

[17] Q. Zhong, D. Innis, K. Kjoller and V. B. Elings; Surface Science Letters **290** (1993) L688

[18] T. Ando, N. Kodera, E. Takai, D. Maruyama, K. Saito and A. Toda; Proceedings of the National Academy of Science of the United States of America **23** (2001) 12468

[19] A. Wawkushewski, K. Crämer, H-J Cantow and S. N. Magonow; Ultra microscopy **58** (1995) 185

[20] H. Hertz; Ann. Physik **31** (1887) 983

[21] A. Einstein; Ann. Physik **17** (1905) 132

[22] K. Siegbahn, C.N. Nordling, A. Fahlman, R. Nordberg, K. Hamrin, J. Hedman, G. Johansson, T. Bemark, S.E. Karlsson, I. Lindgren and B. Lindberg; ESCA: Nova Acta Regiae, Soc, Sci. Ser. **20** (1967)

[23] E. I. Solomon, L. Basumallick, P. Chen and P. Kennepohl; Coordination Chemistry Reviews **249** (2005) 229

[24] G. Kortum, Kolorimetrie; Photometric and Spectrometric, Springer Kap **15** (1962) 4

[25] H. H. Perkampus; UV-Vis Spectrosopy and its Application, Springer laboratory (1992) 1

[26] A. Abragam; Principles of Nuclear Magnetic Resonanc, Cambridge University Press: Cambridge, UK (1968) 895

[27] D. M. Livingston; the Master of Light: The University Press of Chicago, Chicago (1973)

[28] J. W. Cooley and J. W. Tukey; Math Comut **19** (1965) 297

[29] L. Mertz; J. Astron **70** (1965) 548

[30] P. R. Griffiths, R. Curbelo, C.T. Foskett, and S. T. Dunn; Analytical Instrumentation (Inst. Society of America) **8** (1970) 4

[31] B. C. Smith; Fundamental of Fourier Transform Infrared Spectroscopy, CRC (1996) 4

[32] A. H. Kitai; Luminescent Materials and Applications, J. Willy & Sons, (2008) 2

[33] D. L. Rie, E. R; Fluorescence of paint and varnish layers (part 1) Studies in Conservation, **27** (1982) 1

[34] D. L Rie, E. R; Fluorescence of paint and varnish layers (part 2) Studies in Conservation, **27** (1982) 65

[35] D. L Rie, E. R; Fluorescence of paint and varnish layers (part 3) Studies in Conservation **27** (1982) 102

[36] B. Guineau; Non-destructive analysis of organic pigments and dyes using Raman microprobe, micro-fluorometer or absorption micro-spectrophotometer **34** (1989) 38

[37] T. Miyoshi; Japanese J. Appl. Phys. **21** (1982) 1032

[38] L. F. Zagonel, S. Mazzucco, M. Tence, K. March, R. Bernard, B. Laslier, G. Jacopin, M. Tchernycheva, L. Rigutti, F. H. Julien, R. Songmuang, M. Kociak; Nano Lett.**11** (2011) 568

[39] H. J. Round, "A note On Carborundum," Electron. World **19** (1907) 309

[40] D. K. Schroder; Semiconductor material and device characterization, 2nd Ed. New York: John Wiley and Sons (1998) 22

CHAPTER 4

STRUCTURAL & MORPHOLOGICAL PROPERTIES

This chapter presents the synthesis of CuCl nanocrystals and detailed experimental results of structural and morphological properties for CuCl hybrid films investigated using X-ray diffraction (XRD), scanning electronic microscopy (SEM) and atomic force microscopy (AFM). These properties are important because they reveal much information about the nature of the embedded semiconductor material.

4.1 Introduction

γ-CuCl (E_g= 3.395 eV) is an ionic I-VII compound semiconductor material with the zincblende structure at room temperature [1]. A solid-state phase transition occurs with increasing temperature from the zincblende structure (γ-phase) to the wurtzite (β-phase) structure. γ-phase CuCl transforms to β-phase CuCl at 407 ^{o}C before melting at ~430 ^{o}C [2]. CuCl has been extensively used in the manufacture of electrooptic modulators and optical fibers [3], adsorbent and air purifying agents [4], catalysts [5], solid-state batteries [6], and as a candidate material for blue-UV light-emitting devices [7]. Potential applications include high-density optical storage, laser printing, projection displays, spectro-fluorometry, photo-catalytic reactions, counterfeit detection, chemical detection, traffic signals, and medicine (e.g., the use of UV radiation in treating cancer and cerebral apoplexy) [8]. There are many physical and chemical procedures that have been demonstrated in preparing CuCl powders, nanocrystals and thin films, such as the reduction of copper(II) chloride ($CuCl_2$) with elemental copper in concentrated hydrochloric acid solution [9], ion implantation combined with post-heating at high temperatures [10], exposure of a Cu single crystal to Cl_2 gas in an ultra–high vacuum chamber [11], reaction of copper chloride and glycerol [12], solvothermal methods [13], γ-irradiation [14], etc. All of these methods require complex equipment and/or high reaction temperatures to synthesize CuCl powders.

In this work, CuCl nanocrystals were embedded in PSSQ and deposited on a variety of substrates via a simple low temperature spin coating technique to develop prototype devices for flexible UV/White–light emitters. In order to investigate the structural and morphological properties of these organic-inorganic CuCl hybrid films, they were deposited on several substrates including glass, indium tin oxide

(ITO) coated glass and silicon by the spin coating method. The films were subsequently heated at 120 ^{o}C for durations between 1 and 24 hours *in vacuo*. This chapter presents detailed experimental results of structural and morphological properties for the CuCl hybrid films.

4.2 Synthesis of CuCl Nanocrystals (NC) and Film Deposition

To synthesise hybrid films, alpha-D-glucose ($C_6H_{12}O_6$), a polyol containing an aldehyde group, was selected as the reducing agent, and $CuCl_2.2H_2O$ was used as the copper and chlorine source, respectively [9]. Being also a strong chelating reagent, alpha-D-glucose can coordinate with the Cu^{2+} ions released from the dissolution of $CuCl_2 \cdot 2H_2O$ in water to form relatively stable complex ions, $Cu(C_6H_{12}O_6)_x^{2+}$. One piece of evidence of this reaction was, when alpha-D-glucose was added into the $CuCl_2$ aqueous solution the solution colour changed rapidly from light to dark blue. The short distance between oxygen and Cu atoms in the intermediate complex ions is favourable for electron transfer from O^{2-} to Cu^{2+}, resulting in the reduction of $Cu(C_6H_{12}O_6)_x^{2+}$ to Cu^{+}. On the other hand, the excessive alpha-D-glucose was partly oxidized to gluconic acid ($C_6H_{12}O_7$). The main chemical process for the synthesis is given as follows [15]:

$$CuCl_2.2H_2O = Cu^{2+} + 2Cl^{-} + 2H_2O \quad (4.1)$$

$$Cu^{2+} + xC_6H_{12}O_6 = [Cu\,(C_6H_{12}O_6)_x]^{2+} \quad (4.2)$$

$$2[Cu\,(C_6H_{12}O_6)_x]^{2+} + H_2O = 2Cu^{+} + C_6H_{12}O_7 + (2x-1)\,C_6H_{12}O_6 + 2H^{+} \quad (4.3)$$

$$Cu^{+} + Cl^{-} = CuCl \quad (4.4)$$

$$C_6H_{12}O_6 + 2CuCl_2 + H_2O + [RSiO_2] = 2CuCl + C_6H_{12}O_7 + 2HCl + [RSiO_2] \quad (4.5)$$

where R is methanol or ethyl alcohol. A typical solution was prepared using 0.60 gm of $CuCl_2.2H_2O$ powder (Laboratory reagent grade, Fisher Scientific Company) as the copper and chlorine sources and 0.40 gm of alpha-D-Glucose powder (99.5% Sigma-Aldrich Inc., Germany), a polyol containing an aldehyde group as the reducing agent with 3 ml of de-ionized water. The powders were dissolved completely in the de-ionized water after vigorous stirring of the solution. 2.1 gm of the PSSQ based solution known as Emulsitone glass forming solution was added to

the $CuCl_2$ glucose aqueous solution. The solution was stirred for 5 minutes and finally filtered by using 0.2μm filter. Approximately 0.75 ml of the solution was dropped at the centre of the substrate (2x2 cm) and spun. The film was spin coated by gradually increasing the speed from 0 to 5000 rpm over a period of one minute (resulting in typical thicknesses of ≈200-500 nm). The coating was performed at room temperature. The films were subsequently heated at 120^{o}C for durations between 1 and 24 hours *in vacuo*. The newly generated Cu^{+} ions will combine with Cl^{-} ions in the aqueous solution to form CuCl precipitate. The formation of CuCl nanocrystals in the organic material is believed to be via a typical complexation-reduction-precipitation mechanism in the presence of heat that can be described by equations (4.1) to (4.4) and summarized in (4.5).

4.3 X-ray Diffraction

The structural properties of the CuCl hybrid films deposited on glass, ITO coated glass and silicon substrates were measured by using a Bruker D8 Advance X-ray Diffractometer with CuK_{α} radiation of wavelength λ = 1.54056 Å. The X-ray diffraction (XRD) measurements were carried out in the locked coupled (Bragg-Brentano) mode in the 2θ range of 5^{o} to 60^{o}. These XRD scans were then compared to powder diffraction software files provided by the manufacturer. The positions of the main CuCl peaks and their relative intensities as measured by powder diffraction are listed in **Table 4.1**.

2θ (º)	Plane (hkl)	Relative Intensity (%)	d–Spacing (Å)
28.522	(111)	100	3.1270
33.027	(200)	8	2.7100
47.437	(220)	55	1.9150
56.290	(311)	30	1.6330
69.348	(400)	6	1.3540
76.590	(331)	10	1.2430
88.350	(422)	8	1.1054

Table 4.1: Expected ratios of different CuCl peaks from powder diffraction files [16]

Figure 4.1 shows the room temperature θ-2θ X-ray diffraction spectra taken for a selection of films deposited on glass substrates. In these spectra, the non-heated film shows very sharp peaks at 2θ ≈ 16.16° and 22.1° which correspond to copper methanol Chloride ($CH_3OH.CuCl_2$) [17] and there was no diffraction peak that indicated the formation of CuCl nanocrystals. The films heated for 1 and 12 hours show two peaks at 2θ ≈ 16.16° and 2θ ≈ 28.5°, which are Copper Chloride Hydrate and (111) oriented Copper Chloride (CuCl), respectively. The Copper Chloride Hydrate diffraction peaks disappear entirely for anneal times >12 hours. The film annealed for 18 hours shows three different peaks at 2θ ≈28.51°, 47.44° and 56.27°, which correspond to (111), (220) and (311) crystal plane orientations of cubic phase γ-CuCl. This is in excellent agreement with data from the previous evaporated and sputtered CuCl films [18-20].

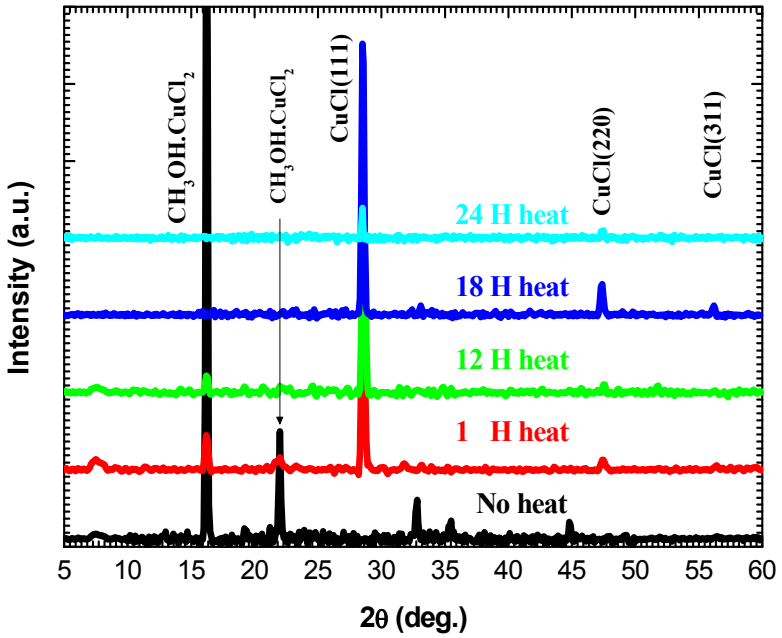

Figure 4.1: X-ray θ-2θ diffraction spectra of CuCl hybrid films grown on glass substrates (film thickness ≈300 nm).

The film annealed for 24 hours shows only the (111) and (220) γ-CuCl peaks albeit with reduced intensity when compared to the 18 hour annealed film. It is well known that the size of the full width at half maximum (FWHM) is an indication of the

crystal quality [21]. The FWHM of the nanocrystalline CuCl hybrid films were measured using the following relation:

$$B^2 = B^2_{measured} - B^2_{instrument} \tag{4.6}$$

where $B_{measured}$ is the measured FWHM of the CuCl hybrid films and $B_{instrument}$ is the instrumental broadening FWHM. A standard strain free single crystal Si (100) was used for the calibration.

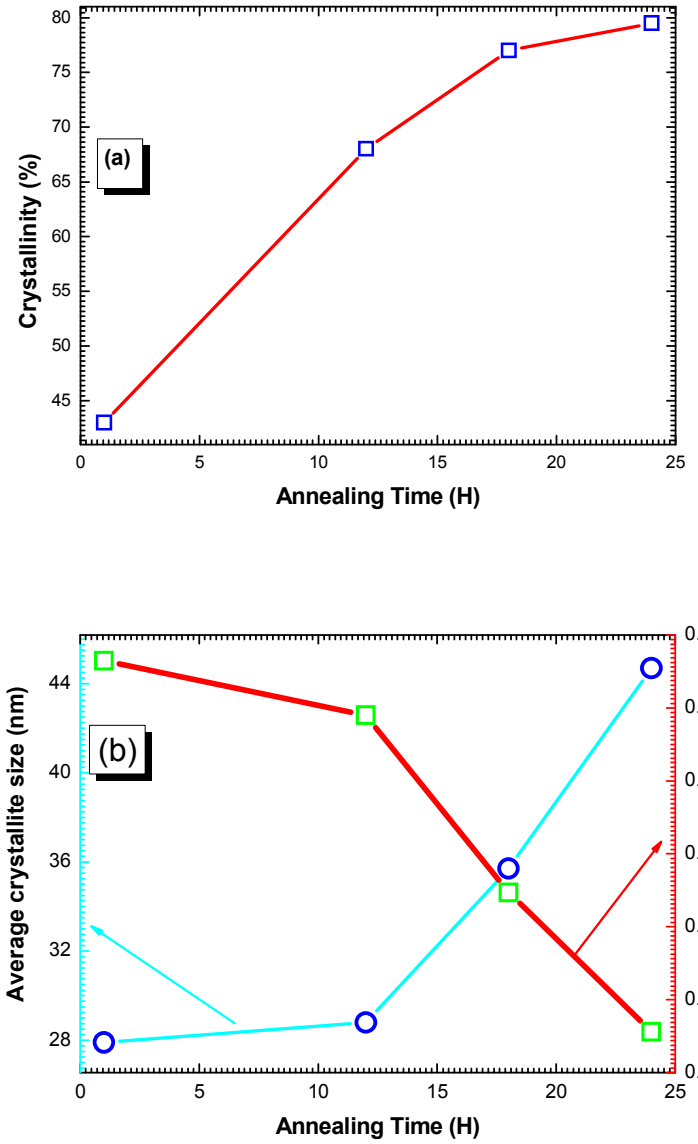

Figure 4.2: % Crystallinity of CuCl (a), FWHM and average crystallite size (b) vs. annealing time

The average crystallite size of the CuCl hybrid film (111) peak was estimated using the Scherrer formula [22].

$$L = \frac{0.9\lambda}{BCos\theta_B} \tag{4.7}$$

where B is the FWHM of the (111) CuCl peak broadening, and L is the average crystal size.

The Scherrer model uses the FWHM to evaluate the average crystal size, which is derived from the overall microcrystalline quality of the probed region. While the statistical distribution of crystallite sizes cannot be determined, the average crystallite size, as inferred by the Scherrer model, is never the less, a useful metric for material quality evaluation. The average crystal size of the CuCl hybrid films deposited on glass substrates was estimated to be 27.9, 29.8, 35.7 and 44.7 nm for the 1, 12, 18 and 24 hour annealed films, respectively.

X-ray diffraction patterns were also used to determine the percentage or fractional crystallinity of the CuCl-hybrid film employing the Rutland method [23, 24]. The crystallinity was calculated using the crystalline peaks in the region $2\theta=25^{o}$ to 60^{o} and the integrated area of the amorphous diffuse background in this region. The areas of interest were determined using the area calculation tool in the Bruker Diffract Plus EVA software. The crystallinity was then calculated using following equation [24]:

$$Crystallinity(\%) = \frac{\sum A_c}{\sum A_c + A_a} \times 100 \tag{4.8}$$

where $\sum A_c$, is the sum of the areas of all CuCl crystalline peaks and $\sum A_a$ is the sum of the area under the amorphous peak. The % crystallinity, FWHM and average crystallite size of CuCl increases with the increased annealing times as shown in **Figure 4.2**. From the XRD measurements, it is clear that the film annealed for 18 hours gave the optimum CuCl characteristics, and upon further annealing although the % crystallinity and the crystal size increases, it appears to lead to a reduction of the CuCl (111) peak intensity. The reduction in this peak is linked to an excessive thermal budget, which may result in the reaction of the CuCl crystals with the organic matrix. Confirmation of this reduction in quality is observed in the UV-Vis and PL data, which show that, anneal times > 18 hours produce sub-optimal films.

Figure 4.3 shows the room temperature θ-2θ X-ray diffraction spectra taken for 18 hours annealed CuCl hybrid films deposited on glass, ITO coated glass and silicon substrates, which henceforth we take as our optimal film. In these spectra, one observes peaks at 2θ ≈28.51°, 47.44° and 56.27°, corresponding to (111), (220) and (311) crystal plane orientations of cubic phase γ-CuCl, as previously stated, this also being in excellent agreement with previously reported CuCl thin film data [25]. The film deposited on ITO substrates displays an additional two peaks at 2θ ≈30.25°, 35.16° corresponding to (222) and (400) planes of indium tin oxide substrate [26].

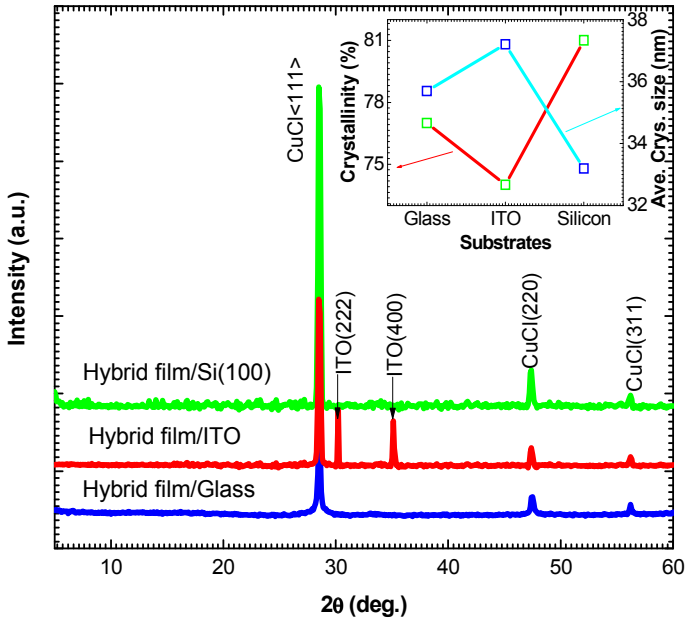

Figure 4.3: X-ray θ-2θ diffraction spectra for 18 hours annealed CuCl hybrid films deposited on different substrates, inset: % crystallinity and average crystallite size vs. substrates (film thickness ≈300 nm)

The average crystal size of the CuCl hybrid films deposited on glass, ITO coated glass and silicon substrates were 35.7, 37.2 and 33.2 nm, respectively. The % crystallinity of CuCl is higher for the silicon substrate (see inset of **Figure 4.3**). XRD measurements suggest that the hybrid films are somewhat influenced by the substrate and this may be due to the surface smoothness, hydrophobicity/hydrophilicity and the nature of adherence between the organic-inorganic solution and the substrates.

4.4 Scanning Electron Microscopy (SEM)

While the other films were also examined, we focus here on the 18 hours annealed films as they produced optimal optical and electronic performance. The surface morphology of 18 hours annealed CuCl hybrid films deposited on glass, ITO coated glass and silicon substrates was investigated using an EVO(R) Series ZEISS scanning electron microscope in secondary electron emission (SEE) mode. The SEM images were obtained at an accelerating voltage of 17.8 keV and a beam current of 88.88 pA. Typical SEM images of the nanocrystalline CuCl hybrid films deposited on a variety of substrates are shown in **Figure 4.4 (a-c)**. These show a distribution of crystal clusters relatively uniformly distributed on the surface of the PSSQ matrix. Analysis of the hybrid films was carried out by (i) measuring the average diameter of the crystal cluster and hence inferring an estimate for the area of crystal clusters (ii) determining the number of crystal clusters per unit surface area and (iii) calculating the total area covered by the crystal clusters.

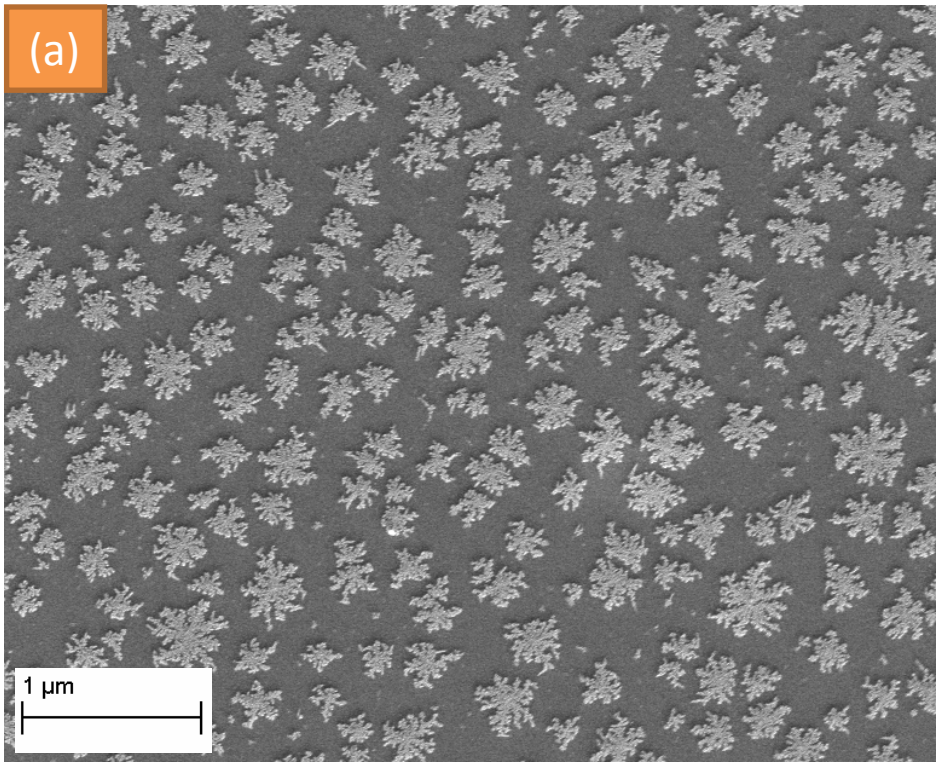

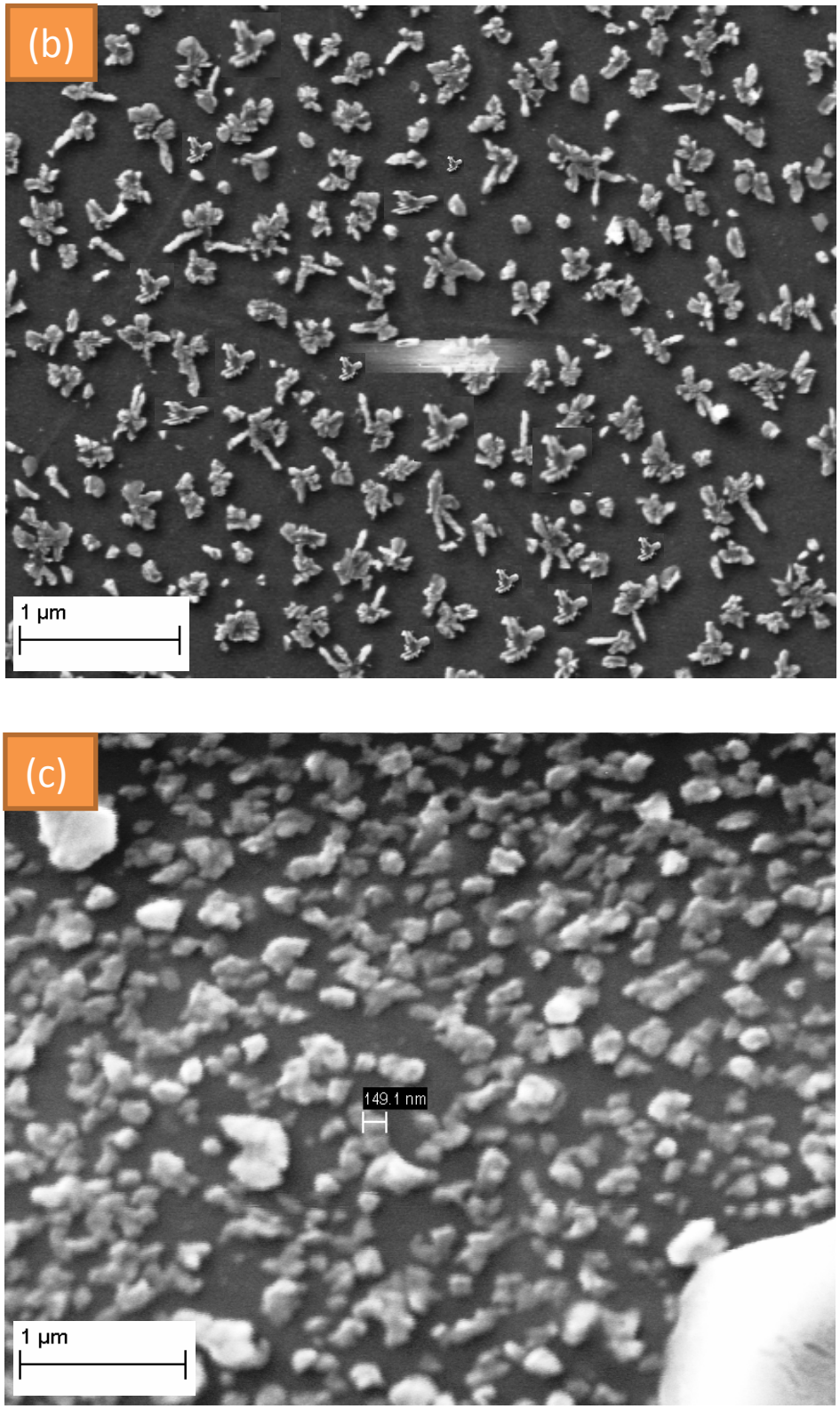

Figure 4.4: SEM images of typical CuCl hybrid films grown on (film thickness ≈300 nm) (a) glass (b) ITO and (c) silicon substrate.

The average fractional area covered by the CuCl nanocrystals is estimated to be ≈45, 42 and ≈59 % for glass, ITO coated glass and silicon substrates, respectively. The crystal shapes on glass and ITO coated glass substrates are quite similar, whereas for the silicon substrate it is completely different. The remainder of the area comprises of the host matrix, Polysilsesquioxane (PSSQ). The average grain size is estimated to be ≈175, 155 and 150 nm for glass, ITO coated glass and silicon substrates, respectively. The grain sizes obtained from SEM analysis are much larger than particle sizes deduced from the XRD analysis. Similar results were reported for sputtered CuCl and CuCl:Zn thin films using AFM, SEM and XRD [19, 27].

Compositional analysis carried out on the same film using energy dispersive X-ray analysis (EDX) confirms the above conclusion.

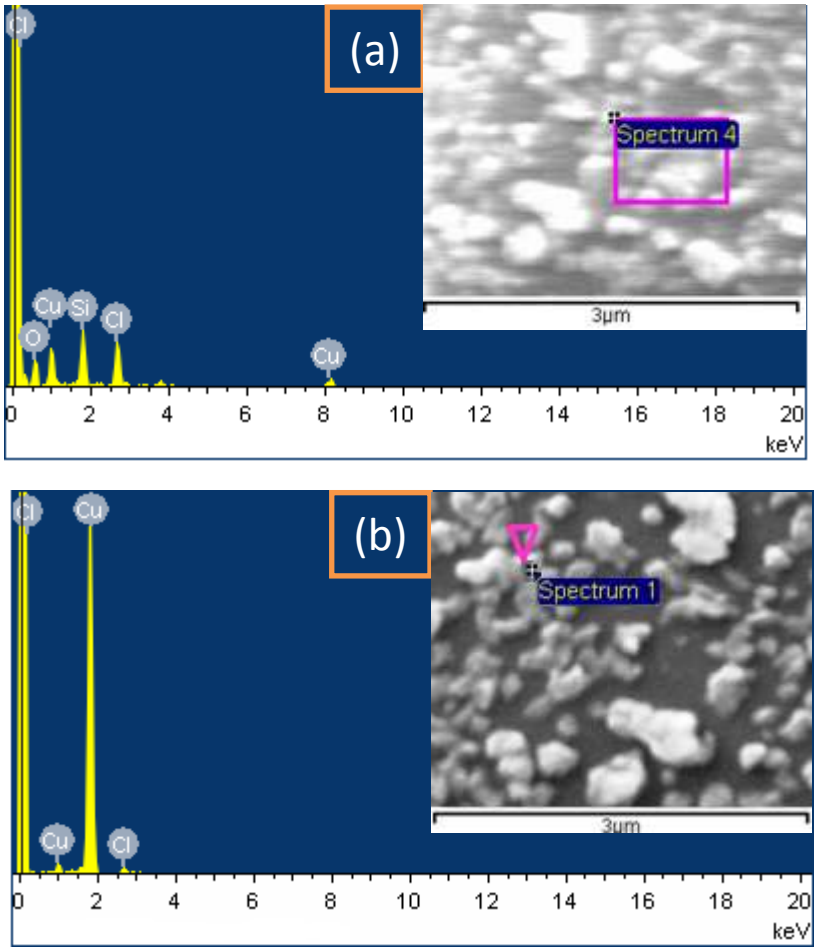

Figure 4.5: EDX spectrum for 18 hours annealed CuCl hybrid films (film thickness ≈300 nm) (a) area and (b) point scan

A Princeton Gamma Tech energy dispersive X-ray (EDX) analyzer was used with a Si (Li) detector and accelerating voltage and probe current of 18 keV and 800 pA, respectively. **Figure 4.5 (a-b)** shows the area (data capture from a selected area of the sample) and point (data capture from a particular point of the sample) scan for compositional analysis of the 18 hours annealed CuCl hybrid film deposited on a silicon substrate. **Figure 4.5 (a)** confirms the presence of Cu, Cl, Si and oxygen, whereas in **Figure 4.5 (b)** one only observes the presence of Cu and Cl. The presence of Si and oxygen is due to the PSSQ solution. The energy dispersive x-ray microanalysis measurement confirms that the incorporated crystals are indeed CuCl crystals.

4.5 Atomic Force Microscopy (AFM)

The surface morphology of CuCl hybrid films was examined using a Pacific Nanotechnology Nano-R Atomic Force Microscopy (AFM) in contact mode. **Figure 4.6** shows some typical three-dimensional (3D) AFM images of the CuCl hybrid films grown on (100) Si substrates for different anneal times: (a) 1 H (b) 12 H (c) 18 H and (d) 24 H . The annealing duration appears to influence the grown CuCl crystal sizes and the average surface roughness. The root mean square surface (RMS roughness) and average roughness (RA) were analyzed using the Pacific Nanotechnology NanoRule +1.10 software and in each case four separate image data sets were used to calculate the average surface roughness of the hybrid films. The film surfaces are not completely homogeneous and are not completely pore or void free.

The surface roughness of the nanocrystalline CuCl hybrid film was calculated in terms of a root mean square (RMS) which was calculated using the following expression [28, 29]:

$$R_{rms} = \sqrt{\frac{1}{n}\sum_{i=1}^{n}\left[Z_i\right]^2} \tag{4.9}$$

where Z_i is the value of Z at the i^{th} point, n is the total number of sampling positions and R_{rms} is the root mean-square deviation from the profile mean over the sampling area.

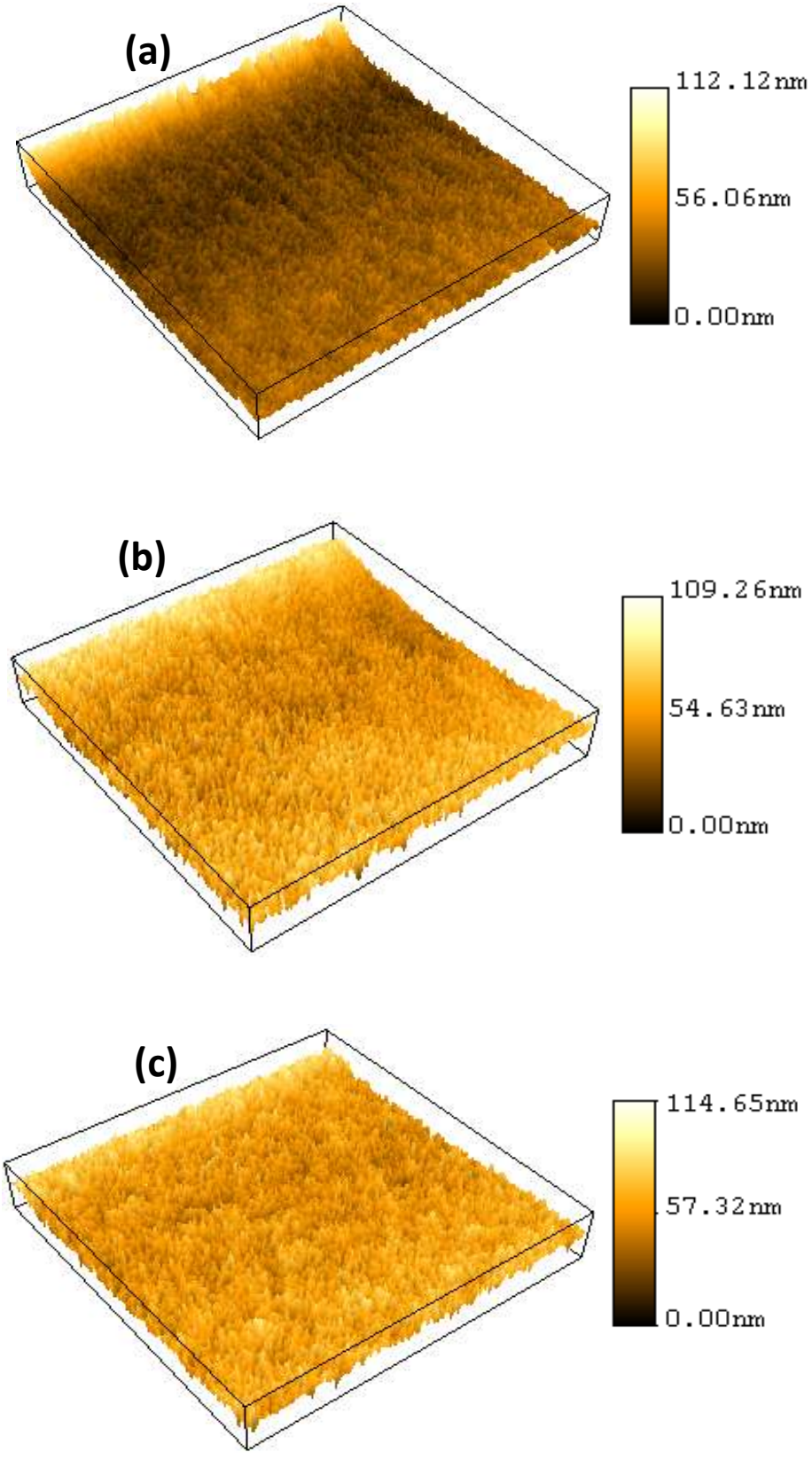
(a)
112.12nm
56.06nm
0.00nm
(b)
109.26nm
54.63nm
0.00nm
(c)
114.65nm
57.32nm
0.00nm

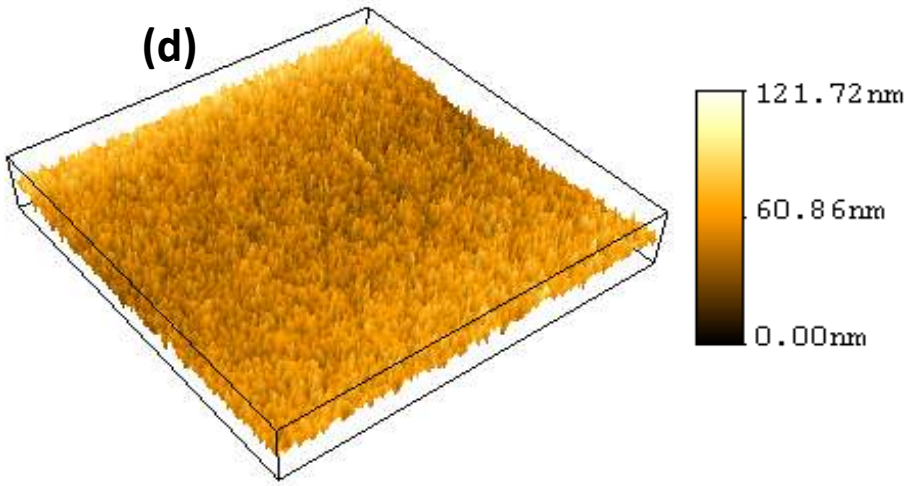

Figure 4.6: 3D AFM micrographs of CuCl hybrid films deposited on silicon substrates for different anneal times (film thickness ≈300 nm). All images are 10.5 μm x 10.5μm. (a) 1 H (b) 12 H (c) 18 H and (d) 24 H

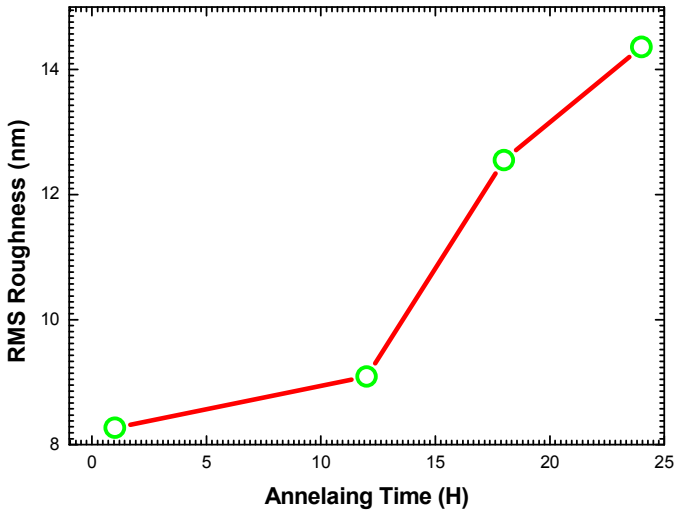

Figure 4.7: Average film surface roughness as a function of annealing time. CuCl hybrid films on silicon substrates.

The average surface roughness of the CuCl hybrid films is shown in **Figure 4.7**. The average roughness of the CuCl hybrid films gradually increase with increased annealing duration. The increasing of the average roughness with annealing time may be due to the improvements in crystallinity of CuCl crystals with annealing and changes to the preferred (111) crystalline orientation.

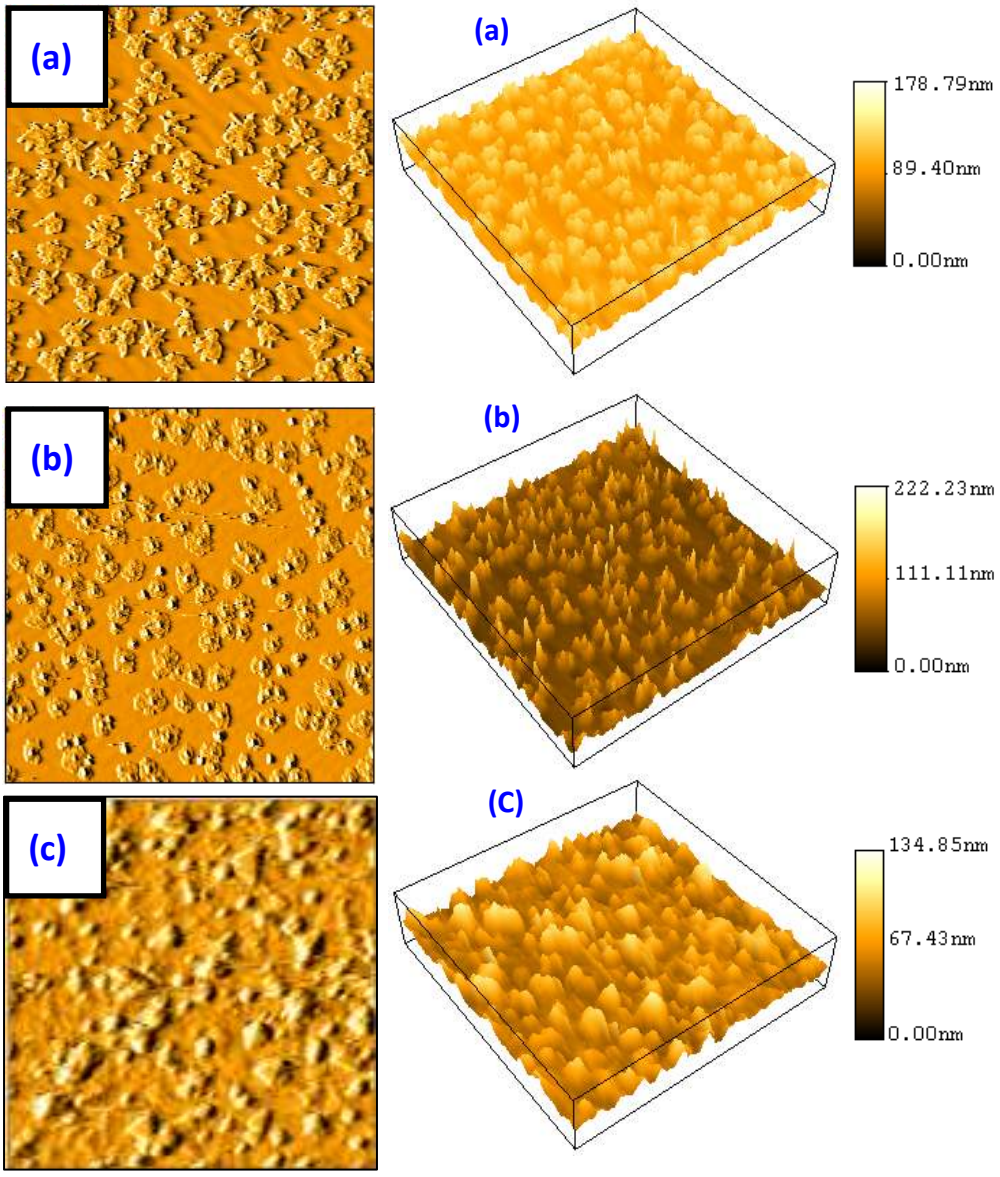

Figure 4.8: 2D and 3D AFM micrographs of CuCl hybrid films deposited on (a) glass (b) ITO and (c) silicon substrates. All images are 2.5 μm x 2.5μm.

Thus, enlarged crystal size so can lead to an effective roughening of the surface [30, 31]. The surface morphology of deposited nanocrystalline CuCl hybrid films on different substrates was also studied by AFM. The two-dimensional (2D) and three-dimensional (3D) AFM images are shown in **Figure 4.8**, which also reveal similar results to the SEM measurements. The RMS surface roughness of the CuCl hybrid films deposited on glass, ITO coated glass and silicon substrates were estimated to be 10.25, 12.2 and 14.5 nm, respectively.

Summary

Nanocrystalline CuCl hybrid films have been successfully deposited on a variety of substrates by the spin coating method based on the hydrothermal reaction of $CuCl_2.2H_2O$, alpha-D-glucose and de-ionized water using a glass forming liquid as the host matrix. The deposited films were heated at 120 ^oC for different times which resulted in the formation of CuCl nanocrystals via a complexation-reduction-precipitation mechanism. The structural properties for nanocrystalline CuCl hybrid film deposited on several substrates were examined by X-ray Diffraction (XRD), Scanning Electron Microscopy (SEM) and Atomic Force Microscopy (AFM) at room temperature. XRD confirmed the preferential growth of CuCl nanocrystals whose average (radius) size was ≈14-22 nm in the (111) orientation. From the XRD measurements, it was clear that the film annealed for 18 hours gave the optimum CuCl characteristics, and on further annealing appears to lead to a reduction of the CuCl (111) peak intensity. SEM measurements revealed that the average surface area of the films covered by the CuCl nanocrystals is ≈40-60 % of its total surface area and the growing crystals were confirmed by EDX measurement. The AFM measurements revealed that the average RMS roughness of the film increases as the annealing time duration increases and the average RMS roughness of nanocrystalline CuCl hybrid film was ≈10-14 nm.

References

[1] L. O. Reilly, A. Mitra, G. Natarajan; J. Crystal Growth **287** (2006) 139

[2] M. Soga, R. Imaizumi, Y. Kondo, T. Okabe; J. Electrochemical Soc.: Solid State Sci. **114** (1967) 388

[3] O. Ambacher, J. Phys. D: Appl. Phys. **31** (1998) 2653

[4] V. Recupero, L. Pino, M. Cordaro, Fuel Process. Technol. **85** (2004) 1445

[5] Z. Li, K. Xie, R.C.T. Slade, Appl. Catal, A Gen **209** (2001) 107

[6] A. Brune, S. Jiang, Mater. Res. Bull. **30** (1995) 573

[7] F.O. Lucas, L.O. Reilly, G. Natarajan, J. Cryst. Growth **287** (2006) 112

[8] Young Cai Zhang, Jing Yuan Tang, J. Materials Letters **61** (2007) 3708.

[9] R. Gong, Y. Chen, W. Liu; J. Yunnan Univ. **27** (2005) 184

[10] W. Sesselmann, T. J. Chuang; Surface Sci. **176** (1986) 32

[11] J. P. Remeika, B. Batlogg; Materials Research Bull **15** (1980) 1179

[12] B. K. Vaidya; Nature **123** (1929) 414

[13] Y. Zhu, Y. Qian, Y. Cao; Materials Sci. Eng. B **57** (1999) 247

[14] K. Fukumi, A. Chayahara, H. Kageyama; J. Non-Crystalline Solids **259** (1999) 93

[15] Y. C. Zhang, J. Y. Tang; J. Materials Letters **61** (2007) 3708

[16] Bruker Advanced X-ray Solutions, powder diffraction files

[17] Diffract plus-PDFMint-[JCP2.2CA:19-1796]

[18] F. O. Lucas, A. Mitra, P. J. McNally, S. Daniels, A. L. Bradley, D M Taylor, Y. Y. Proskuryakov, K. Durose, D. C. Cameron; J. Phys D: Appl. Phys. **40** (2007) 3461

[19] G. Natarajan, S. Daniels, D. C. Cameron, L. O'Reilly, A. Mitra, P. J. McNally, O. F. Lucas, R. T. Rajendra Kumar, Ian Reid and A. L. Bradley, J. Appl. Phys. **100** (2006) 033520

[20] L. O'Reilly, G. Natarajan, P. J. McNally, D. Cameron, O. F. Lucas, M. M. Rosas, L. Bradley, A. Reader; J. Mater. Sci: Mater. Electron **16** (2005) 415

[21] B. D. Cullity and S. R. Stock; Elements of X-ray Diffraction, 3rd ed. Prentice Hall (2001) 169

[22] B. D. Cullity and S. R. Stock; Elements of X-ray Diffraction, 3rd ed. Prentice Hall (2001) 170

[23] M. F. Morks and A. Kobayashi; Applied Surface Science **253** (2007) 7136

[24] T. J. Levingstone; PhD, Thesis "Optimisation of Plasma Sprayed Hydroxyapatite Coatings", Dublin City University, Ireland, (2008) 60

[25] F. O. Lucas, A. Mitra, P J McNally, S. Daniels, AL Bradley, D. M. Taylor, Y. Y. P. Yakov, K. Durose, D. C. Cameron; J. Phys D: Appl. Phys. **40** (2007) 3461

[26] Diffract plus-PDFMint-[JCP2.2CA:39-1058]

[27] K. V. Rajani, F. O. Lucas, S. Daniels, D. Danieluk, A. L. Bradley, A. Cowley, M. M. Alam and P. J. McNally; Thin Solid Films **519** (2011) 6064

[28] X. Wen, X. Wang, N. Zhang; Biomedical Mater Eng. **6** (1996) 173

[29] A. Itälä, E. G. Nordström, H. Ylänen, H. T. Aro, M. Hupa; J. Biomedical Materials Research **56** (2001) 282

[30] K. S. Shim, H. K. Yang, B. K. M, B. C. Choi, J. H. Jeong, J. S. Bae, K.H. K; J. Thin Solid Films **517** (2009) 5137

[31] Z. B. Fang, Z. J. Yan, Y. S. Tan, X. Q. Liu, Y.Y. Wang; J. Applied Surface Science **241** (2005) 303

[25] G. Natarajana, S. Daniels, L. O'Reilly, A. Mitra, P. J. McNally, O. F. Lucas, R. T. R. Kumar, I. Reid, A. L. Bradley; J. Applied Physics **100** (2006) 033520

CHAPTER 5

OPTICAL PROPERTIES

The electronic structure, luminescence and photochemical properties of semiconductor materials can be evaluated by monitoring a selection of the optical characteristics of these materials. In this chapter we present the experimental results for FTIR, XPS, UV-Vis, and detailed temperature dependent PL spectroscopy of CuCl hybrid films to determine the thermal quenching behaviour and its electronic transitions.

5.1 Introduction

Semiconductor quantum dots (QDs) have attracted great attention due to their unique optical and electronic properties, such as size, composition-tunable fluorescence emission from visible to infrared wavelengths, large absorption coefficients across a wide spectral range and high levels of brightness and photo-stability [1-4]. The average distance between the electron and hole within an exciton is called Bohr radius of the exciton. Quantum confinement effects occur if the dimensional scale of a semiconductor material is reduced to the same order as the exciton radius, and in this situation modified and novel optical properties are expected. Therefore, these nanostructures are good candidates for the development of high-performance opto-electronic devices including semiconductor light-emitting diodes and laser diodes. The exciton Bohr radius of CuCl is very small, of the order of 0.7 nm [5]. In nanocrystals, the electrons, holes and excitons are spatially confined, and the energy levels are quantized. Depending on the ratio (σ) of the radius of the nanocrystal to the exciton Bohr radius, a_B, the quantum size effect is classified into two types: (1) for $\sigma > 1$, the exciton translational motion is confined and this is called weak confinement and (2) for $\sigma < 1$, the translational motion of an electron and hole are individually confined, this being called strong confinement. CuCl nanocrystals exhibit weak confinement due to typical nanocrystal sizes being much larger than its Bohr radius. Its absorption coefficient is of the order of 10^5 cm^{-1} at the peak of the exciton absorption band and the excitons are considered to arise from the allowed optical transition at the centre of the Brillouin zone at k=0 [6]. Two exciton absorption bands separated by spin-orbit splitting appear in the near ultraviolet region; one band is a doublet and the other is a singlet and these are called, respectively, $Z_{1,2}$ and Z_3 [7]. CuCl tends to produce light emission in the blue-UV range at room temperature. In

order to investigate the optical properties of organic-inorganic CuCl hybrid films, these films were deposited on several substrates including silicon, glass and indium tin oxide (ITO) coated glass, by the spin coating method. The films were subsequently heated at 120 ^{o}C for durations between 1 and 24 hours *in vacuo*. This chapter presents detailed experimental results of the optical properties of these CuCl hybrid films.

5.2 Fourier Transform Infrared (FTIR) Spectroscopy

FTIR spectroscopy of the CuCl hybrid films (HF) deposited on silicon substrates was carried out at room temperature. The FTIR absorption spectra were recorded on the Perkin-Elmer GX FTIR system which was used to obtain 16 cm^{-1} resolution spectra in the range 400 to 4000 cm^{-1}, this region having been scanned 30 times (absorbance mode), in order to exploit the instrumental noise reduction algorithms. **Figure 5.1** shows FTIR spectra of as-deposited (ASD) CuCl hybrid films and for those annealed at 120 ^{o}C for different times (1-24 hours). The most intense absorption peaks for films are at approximately 1050, 1630, 1737 and 3375 cm^{-1}. The strong absorption peak at 1050 cm^{-1} occurring in the 1000-1100 cm^{-1} band may be attributed to asymmetric Si-O-Si stretching vibrations of the Si-O functional group present in the PSSQ emulsion. The absorption at ~1050 cm^{-1} is most likely due to linear small-chain siloxanes and at ~1085 cm^{-1} due to long-chain polymers [8, 9].

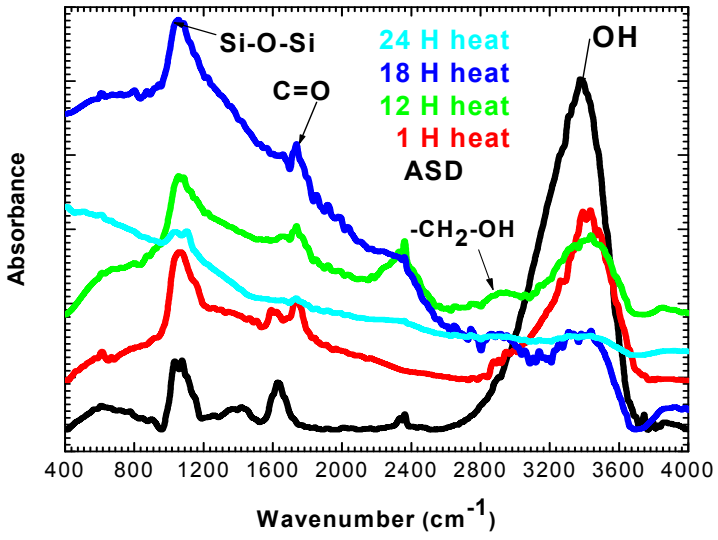

Figure 5.1: FTIR absorption spectra of CuCl HFs grown on silicon substrates.

The weak absorption peak located at ~1630 cm^{-1} may be assigned to the bending vibration of the H-O-H group of adsorbed water, which may be due to the use of water as a solvent [10, 11]. A medium intense absorption at 1737 cm^{-1} in the band 1735-1785 cm^{-1} is assigned to the C=O stretch of aryl and unsaturated diacyl peroxides, which may be due to $C_6H_{12}O_6$ [12]. The weak absorption at 2910 cm^{-1} in the band 2840-2935 cm^{-1} may be attributed to symmetric CH_2 stretch vibrating in the primary alcohol $–CH_2–OH$ group this being present in both PSSQ and $C_6H_{12}O_6$ [13]. The broad and strong absorption centered at 3375 cm^{-1} can be assigned to the hydrogen bonds of the O–H stretch vibration, which may be due to H_2O or indeed the PSSQ emulsion [14]. It is apparent from figure 5.1 that not all organic compounds were not removed and a large fraction of Si-O bonds were not cross linked even for 24 hr anneals whereas the most intense O–H absorption peak intensity and broadness almost disappeared after annealing for 24 hrs. However, the peaks due to the organic compounds decrease with increases in the annealing time duration.

5.3 Surface Chemical Analysis by XPS

The chemical state of the surfaces of the CuCl hybrid films were studied using the Vacuum Generator X-ray photoelectron spectrometer (XPS) at base pressures in the preparation and analysis chambers of 2×10^{-6} and 1×10^{-9} mbar, respectively, using an Al K_α ($h\gamma$=1486.6 eV) X-ray source. The pass energy of the analyser was set at 20 eV yielding a resolution of approximately 0.1 eV. To compensate for the surface charge effect, binding energies (E_b) were calibrated using C1s line (285 eV) from the carbon contamination layer [15]. **Figure 5.2 (a-b)** shows the broad scan survey XPS spectra for CuCl hybrid films as-deposited and after 18 hours annealing at 120 ^oC. **Figure 5.2** shows the photoelectron peaks of the main elements, copper, chlorine, silicon, oxygen and carbon, Auger copper LMM and oxygen LMM peaks for both samples. Silicon (Si) and oxygen (O) signals may come from the PSSQ host matrix. The Carbon signal is most likely due to the use of alpha-D-glucose ($C_6H_{12}O_6$). The elemental and bond energy data for the CuCl hybrid films analysed by XPS are presented in **Table 5.1**. The data confirms that the most of the peak positions of the annealed films are shifted to the higher binding energies compared to the ASD films.

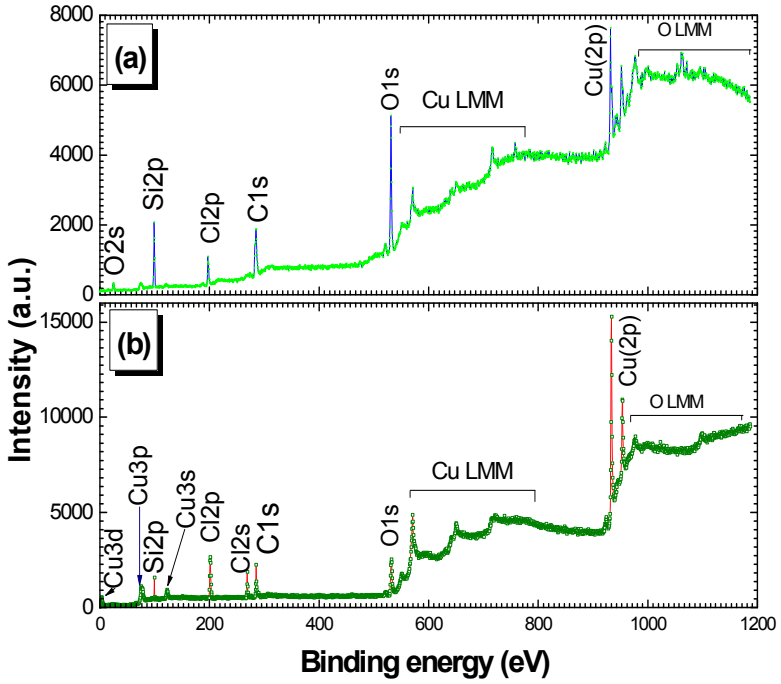

Figure 5.2: The survey scan XPS spectra of organic-inorganic CuCl HFs (a) as deposited (b) annealed at 120^{o} C for 18 hours.

Element	XPS Peak Position (eV)	
	ASD film	annealed film
Silicon (Si 2p)	99.5	100.3
Oxygen (O 1s)	531.3	532
Oxygen (O 2s)	25.27	X
Chlorine (Cl $2p_{3/2}$)	197.3	198.8
Chlorine (Cl $2p_{1/2}$)	198.7	200.5
Chlorine (Cl 2s)	X	269.3
Copper ($2p_{3/2}$)	932.3	932.8
Copper ($2p_{1/2}$)	951.7	952.4
Copper (3p)	X	75.5
Copper (3s)	X	122.5
Copper (3d)	X	3.3
Copper (LMM)	570.3, 649.5 &715.2	571, 650, & 721

X=not determined

Table 5.1: XPS experimental results for CuCl HFs

The Si 2p peak obtained for as deposited film is at 99.5 eV which corresponds with Si-Si bonding. After annealing this peak is shifted towards higher binding energies i.e. to 100.3 eV which may be due to Si-O bonding [16]. The O1s peaks are shifted from lower binding energies at 531.3 eV towards higher binding energies at 532 eV, which is a close match to the standard location of oxygen is peak energy within the Si-O bond [17]. For a closer investigation of the Cu and Cl binding data prior to and post annealing, the detailed spectra for the Cu(2p) and Cl(2p) peak regions are shown in **Figure 5.3 (a-b)**, respectively. Four peaks with binding energy at ~934.3 (with a shoulder at ~936.2), ~943.7, ~953.7 and ~964.6 eV appear in the as-deposited film (see **Figure 5.3 (a)**). The features at ~934.3 and ~953.7 eV are due to the excitation from the Cu($2p_{3/2}$) and Cu($2p_{1/2}$) orbitals [18]. The additional peaks at ~943.7 and ~964.6 eV are due to a shake-up process (the ejected core electron simultaneously transfers some of its energy to another electron). The additional shoulder peak at ~936.2 eV and the shake-up peaks are the signature for the presence of bivalent $Cu^{2+}2p_{3/2}$ because the shake-up is due to the open $3d^9$ shell of Cu^{2+}[19]. This Cu^{2}+ species appears in addition to the peaks (shake up peak, ~943.7 and ~964.6 eV) for species ligated with alcohol groups. This observation is in good agreement with the XRD results for as-deposited film (see sec. 4.2), which indicated the presence of some CuO or $CuCl_2$ in the film [20-22]. **Figure 5.3 (b)** displays only a Cl(2p) broad peak at ~198.3 eV for the as-deposited film, i.e. the Cl($2p_{3/2}$) and Cl($2p_{1/2}$) peaks do not appear separately, which is usually the situation for CuCl.

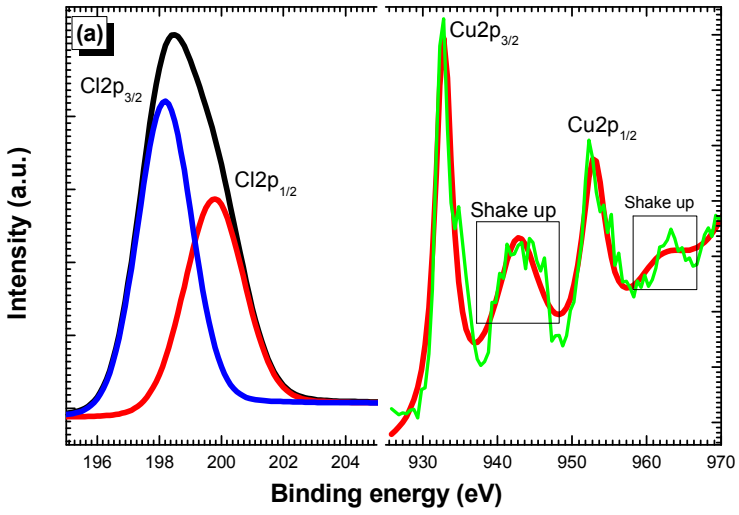

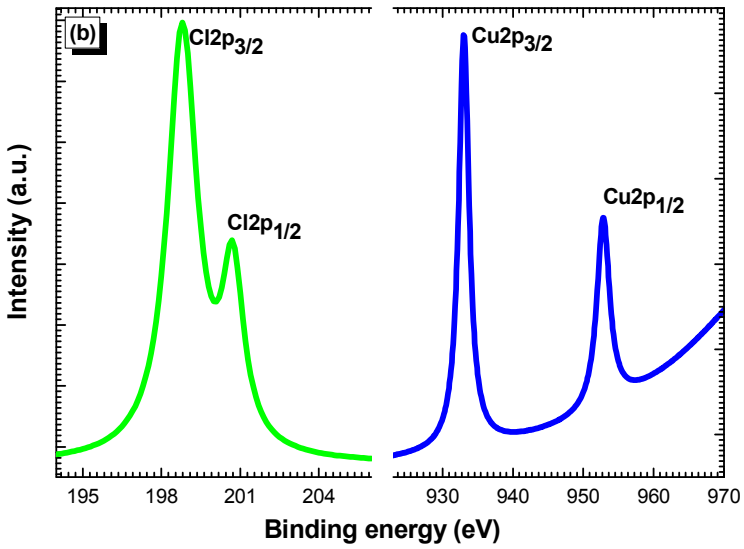

Figure 5.3: XPS spectra taken from the Cu 2p and Cl 2p regions of the CuCl HF (a) ASD film (b) annealed film

On the other hand for the annealed film, two separate peaks were indeed observed at ~932.7 and ~952.8 eV in the Cu(2p) region corresponding to Cu($2p_{3/2}$) and Cu($2p_{1/2}$) transitions. Based on the previously reported XPS analysis, these peaks can be ascribed to Cu^{+} species [18, 19, 23, 24]. No shake-up peak appears in this region, which is a clear indication for the presence of the CuCl structure. The peaks in the Cl(2p) XPS spectral region at ≈198.3 and ≈199.7 eV can be assigned to the binding energies of Cl($2p_{3/2}$) and Cl($2p_{1/2}$), respectively, and correspond to Cl^{-} [18, 25]. The binding energy values obtained for Cu(2p) and Cl(2p) of the CuCl hybrid film are consistent with the data in the literature for CuCl, i.e. after annealing the hybrid film Cu^{+} and Cl^{-} form CuCl by ionic bonding [18, 26].

5.4 UV-Vis Absorption

The optical absorption properties of the CuCl hybrid films were studied at room temperature using the Perkin Elmer Lambda 40 UV-VIS spectrometer in the range 300 to 420 nm with a resolution of 4 nm. **Figure 5.4** shows the room temperature UV-Vis absorption spectra for the ASD and annealed CuCl hybrid films deposited on glass substrates. In these spectra the as-deposited films showed no significant absorption peaks; however after annealing all films reveal both high and low energy

excitonic bands historically related to the presence of the $Z_{1,2}$ and Z_3 free excitons, respectively. It is well known that the band structure of CuCl is in reverse order to what is typically observed in semiconductors [27]. The top of the valence band is the split-off hole (Γ7) band, roughly 60 meV away from the degenerate heavy-hole and light-hole (Γ8) bands. The $Z_{1,2}$ and Z_3 excitons originate from the coupling of the lowest conduction-band state Γ6 to both the uppermost valence band holes at Γ8 ($Z_{1,2}$) and Γ7 (Z_3), respectively [28].

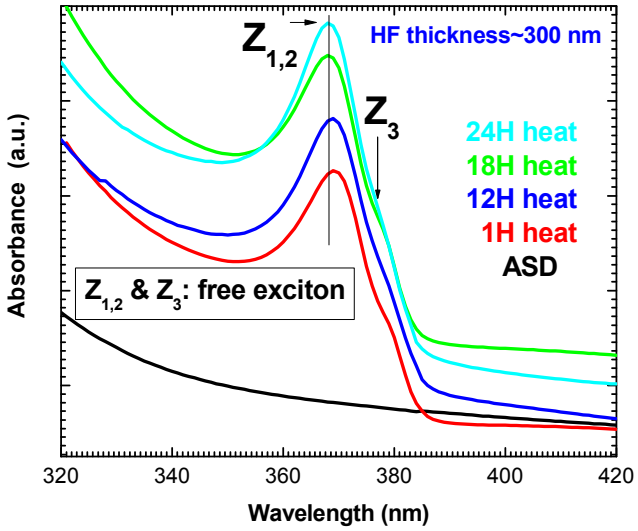

Figure 5.4: UV-Vis absorption spectra of CuCl HF grown on glass substrates.

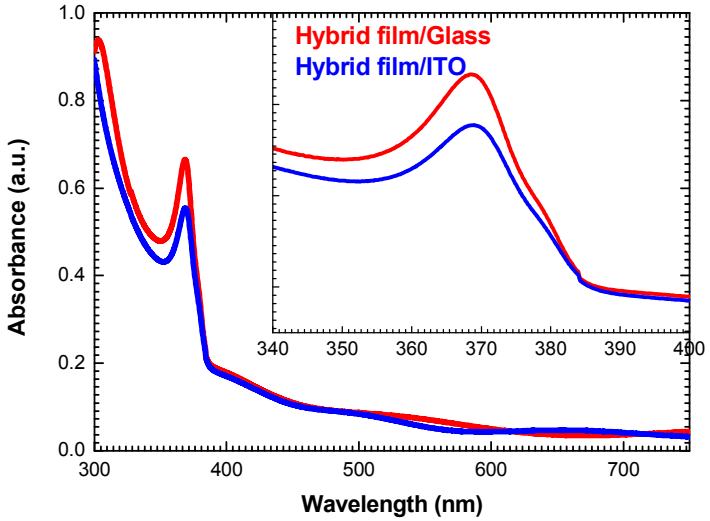

Figure 5.5: UV-Vis absorption spectra for CuCl HF annealed for 18 hours

At room temperature all heated films show the free exciton $Z_{1,2}$ absorption peak at ≈367.8 nm (≈3.371 eV) and the free exciton Z_3 peak at ≈377.1 nm (≈3.288 eV), which is in excellent agreement with the values reported by other authors for vacuum evaporated and sputtered films [27-30]. The absorption intensity increases and the peak positions are shifted to higher energies with increased annealing times. This may be due to increased crystallinity; the density of macroscopic defects such as hollow core dislocations, inclusions, small-angle boundaries and long-range lattice warp has been reduced. **Figure 5.5** shows the UV-Vis spectra for the 18 hours annealed CuCl hybrid film deposited on glass and indium tin oxide (ITO) coated glass substrates. The UV-Vis absorption spectra reveal the $Z_{1,2}$ and Z_3 free excitonic absorption features, occurring at 3.371 and 3.288 eV, respectively, for both glass and ITO coated glass substrate films. The CuCl hybrid films deposited on ITO coated glass substrates display only the CuCl absorption peak in the UV-Vis region, which confirms that no new intermediate compounds are produced. Therefore, to fabricate an excitonic based electroluminescent device from CuCl nanocrystals ITO can be used as a transparent electrode.

5.5 Photoluminescence (PL)

The photoluminescence (PL) properties were studied using temperature dependent photoluminescence spectroscopy in the range between 15 K to room temperature, by employing a UV Ar^+ Innova laser with a second harmonic generation BBO crystal producing a 355 nm photo-excitation. As previously outlined The PL spectra were collected on a Jobin Yvon-Horiba Triax 190 spectrometer with a spectral resolution of 0.3 nm, coupled with a liquid nitrogen-cooled CCD detector. The samples were kept under vacuum conditions at all times, to prevent the oxidation of the CuCl nanocrystal hybrid films. Low temperature (at 15 K) photoluminescence emission spectra of a selection of CuCl hybrid films are shown in **Figure 5.6**. All films show the Z_3 free exciton emission peak and the peak intensity increases with the annealing time. This increase may due to increased crystallinity as describe previously. The Z_3 excitons originate from the coupling of the lowest Γ_6 conduction-band state to the uppermost Γ_7 valance band holes [31, 32]. The film annealed for 1 hour exhibits only

one emission peak at ~383.2 nm (E ≈ 3.235 eV) which is attributed to the Z_3 free exciton peak.

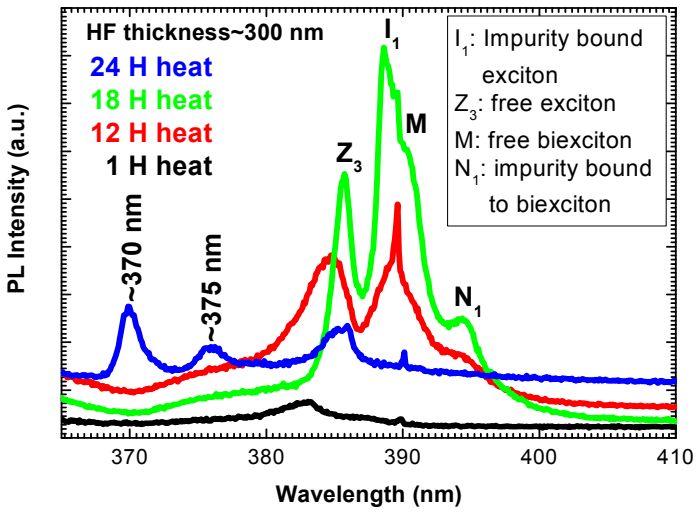

Figure 5.6: Low (15 K) temperature PL spectra of CuCl HFs

The film annealed for 12 hours displays three peaks at ~384.8, 388.9 and 394.3 nm (E ≈ 3.222, 3.188 and 3.144 eV), which are attributed to Z_3 free exciton, I_1 impurity bound exciton and N_1 biexciton bound to an impurity, respectively. The film annealed for 18 hours reveals four peaks. The peak centered at ~386 nm (E ≈ 3.213 eV) is the Z_3 free exciton peak. On the higher wavelength side of the PL emission, the peak that occurs at ~388 nm (E ≈ 3.191 eV) is attributed to emission from an exciton bound to an impurity, which has been called the I_1 impurity bound exciton. This impurity has previously been identified as a neutral acceptor, possibly a Cu vacancy [33]. The peak at ~391 nm (E ≈ 3.170 eV) is identified as a free biexciton, M [33]. The low intensity peak at ~394 nm (E ≈ 3.141 eV) conventionally labeled N_1 is evident, and likely originates from a biexciton bound to an impurity. Similar to the I_1 bound exciton, the most probable candidate for this impurity is a neutral acceptor [33]. The film annealed for 24 hours shows three peaks at ~386.2, ~375.3 and 370.1 nm (E ≈ 3.210, 3.304 and 3.350 eV); one of these peaks could be the Z_3 free exciton emission. It is interesting to note that the excitonic peak for the 24-hour annealed samples appear at approx. 370 and 375 nm this may be due to the formation of new compounds upon degradation of the sample under heat treatment. However there is

no XRD data to confirm the formation of new compounds. It is noteworthy that similar peaks were observed in the Liquid Phase Epitaxy growth of CuCl using a Kbr flux a similar set of unidentified PL peaks were observed [33A]. The 24 hours annealed CuCl hybrid film PL emission spectrum is very different to the other annealed hybrid films.

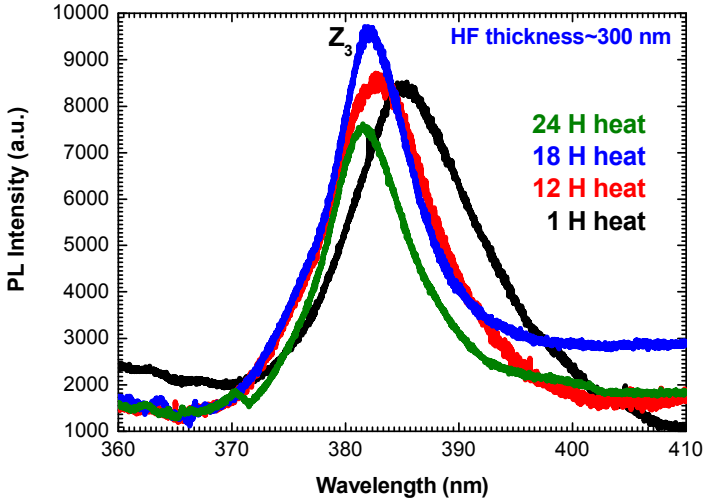

Figure 5.7: Room temperature PL spectra of a selection CuCl HFs

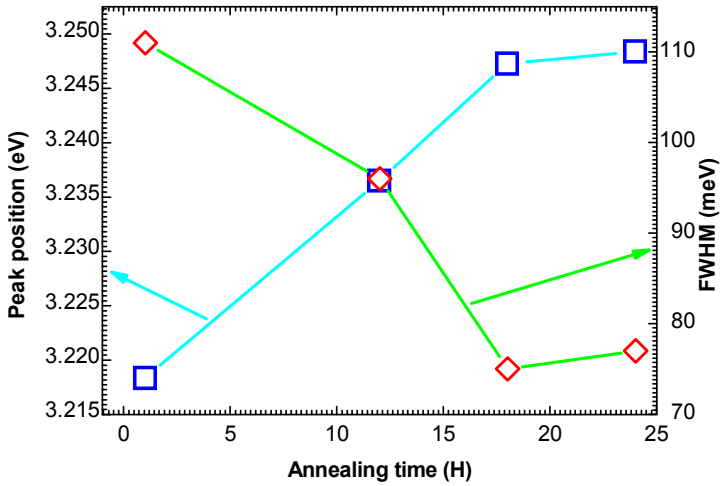

Figure 5.8: Room temperature Z_3 free excitonic emission peak position and FWHM for typical CuCl HFs as a function of annealing time

Figure 5.7 shows the room temperature PL emission spectra centred on the Z_3 free exciton spectral emission region. The Z_3 free exciton emission peak position for

different annealing times are at ~385.3, ~383.2, ~381.8 and ~381.7 nm (E ~3.218, 3.235, 3.246 and 3.248 eV) for the film annealed for 1, 12, 18 and 24 hours, respectively. The full width at half maximum (FWHM) of the Z_3 free exciton peaks was also estimated for each of the CuCl hybrid films. The FWHM of the Z_3 free exciton emission decreases and the peak position shifts to the higher energies with increased anneal times which is shown in **Figure 5.8**. The films which are annealed for 24 hours could be anomalous, as seen from **Figure 5.6**, and trends extrapolated out to this annealing time should be treated with caution. Generally at low temperature PL measurements of CuCl thin films/single crystals exhibit: the free exciton (Z_3), impurity bound exciton (I_1), free biexciton (M) and impurity bound to biexciton (N_1) emission peaks, which normally indicate good quality films. From our photoluminescence studies it is clear that the film annealed for 18 hours gave the optimum PL properties (at 15 K and room temperature) for CuCl, which is excellent agreement with vacuum deposited and sputtered CuCl thin films [34-36].

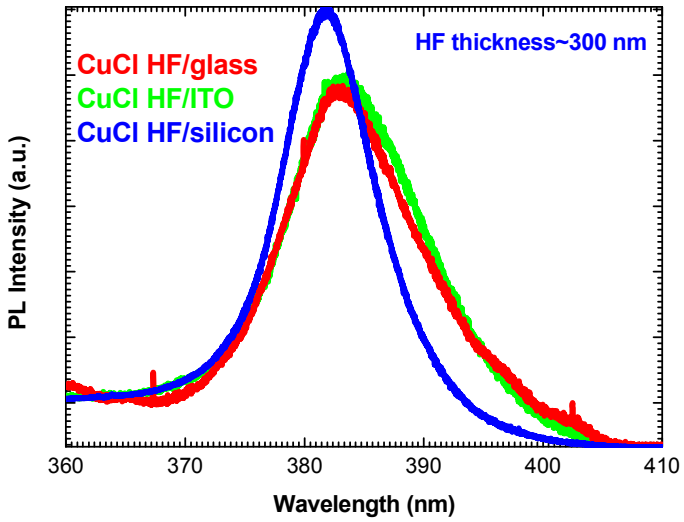

Figure 5.9: Room temperature PL spectra CuCl HFs annealed for 18 hours

The room temperature PL emission spectra for CuCl hybrid films annealed for 18 hours which were deposited on glass, ITO and silicon substrates are shown in **Figure 5.9**. All samples produced an intense free exciton Z_3 peak due to the large excitonic binding energy of the order 190 meV. The Z_3 free exciton emission peak position for ITO and glass substrate samples are almost same at ~383.1 nm (E ~3.36 eV) with a

FWHM ~102 meV, whereas the peak position for the hybrid film on the silicon substrate is at ~381.8 nm (E ~3.247 eV) with a FWHM ~77 meV. The free exciton energy is higher and FWHM is smaller for silicon substrate perhaps because of improvements of the crystal quality and quantity (confirmed by XRD and SEM analysis), lattice mismatch and substrate transparency.

5.6 Temperature Dependent Photoluminescence of CuCl HF

5.6.1 Excitonic Transitions in γ-CuCl Hybrid Film

The photoluminescence spectra for a typical CuCl hybrid film deposited on silicon and annealed for 18 hours, acquired at different temperatures in the range between 15 and 300 K are shown in **Figure 5.10**. **Figure 5.11** and **5.12** show the contributions of different recombination centres associated with the emission peaks at 15 K and 300 K, respectively. The CuCl photoluminescence peaks were fitted with Lorentzian line shapes to ascertain the FWHM. There are four peaks evident in the spectra measured from 15 to 60 K. At 15 K, the peak centered at 3.213 eV (≈385.9 nm) is the Z_3 free exciton peak (Figure 5.10 and 5.11) whereas the room temperature Z_3 free exciton PL emission is at 3.254 eV (≈381 nm) which is shown in **Figure 5.12**.

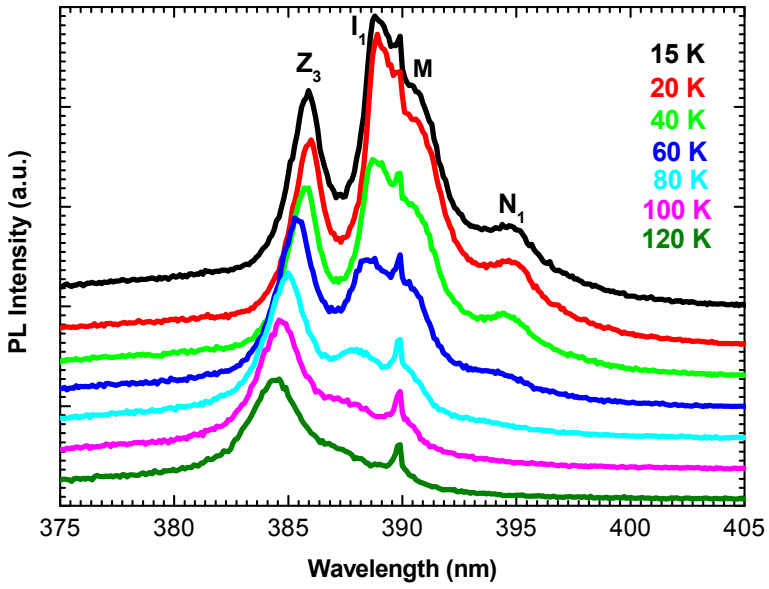

Figure 5.10: Photoluminescence spectra of typical CuCl hybrid film deposited on silicon substrate at different temperature

The exciton emission energy increases from 3.213 eV at 15 K to 3.254 eV at room temperature. Moving to longer wavelengths of the emission spectra of **Figure 5.10** and **5.11**, one can observe a peak occurring at 3.191 eV (≈388.6 nm). This peak is attributed to emission from an exciton bound to an impurity (see sect. 5.4).

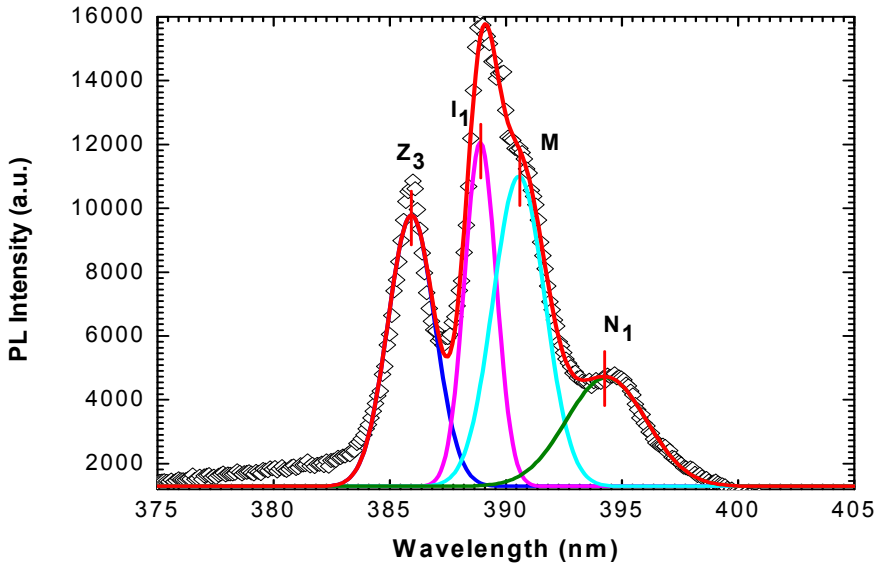

Figure 5.11: Fitted photoluminescence spectra of CuCl HF with fit (solid curve) based on Lorentzian line shapes at 15 K

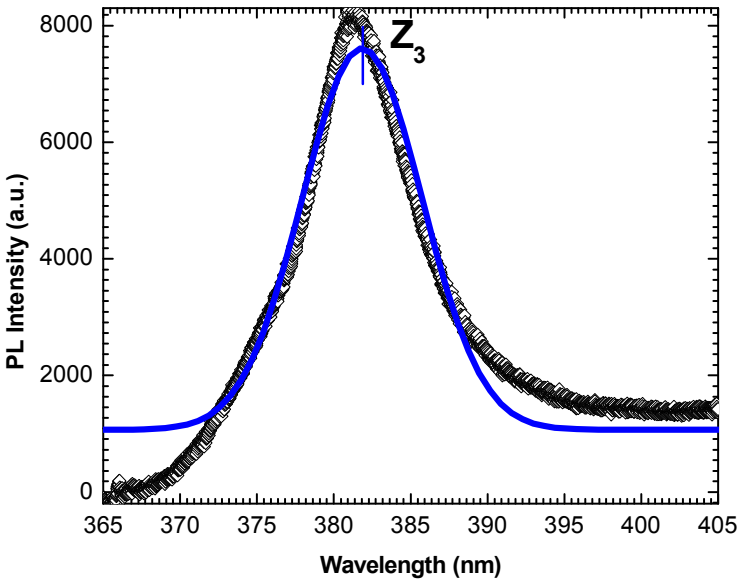

Figure 5.12: Photoluminescence spectra of CuCl HF with fit (solid curve) based on Lorentzian line shapes at 300 K

The intensities of the impurity bound exciton (I_1) and the impurity bound biexciton (N_1) peaks decrease more rapidly in comparison with the free exciton (Z_3) peak as the temperature increases. In the temperature range from 60 K to room temperature, the spectra were dominated by the Z_3 free exciton peak. The dominance and the stability of the Z_3 exciton peak is due to the large binding energy of the order 190 meV. The bound exciton and biexciton both disappear simultaneously at approx. 100 K.

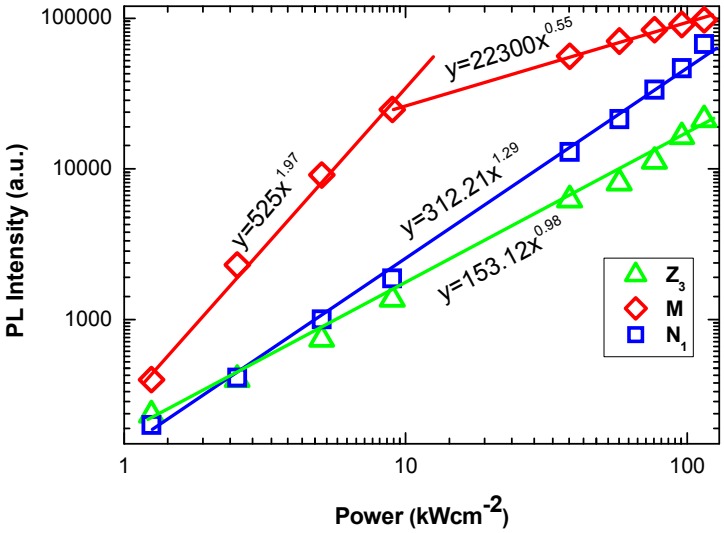

Figure 5.13: Excitonic, biexcitonic and bound biexciton emission line intensity vs. excitation power analysis on double logarithmic scale.

Figure 5.13 shows the variation the of excitonic (Z_3) and biexcitonic (M) and bound biexcitonic (i.e. N_1) emission intensities with excitation power analysed on a double logarithmic scale for the CuCl hybrid film at 15 K. Excitation power dependent PL measurements can be used to confirm the excitonic or biexcitonic nature of the emission. For low power excitation conditions, the excitonic and bound biexcitonic PL emission display a linear dependence on excitation power, whereas free biexcitonic PL emission typically displays a quadratic dependence on excitation power [37, 38]. The biexciton emission intensities for the CuCl hybrid film clearly show a quadratic dependency on excitation power for lower excitation power densities of <10 kWcm^{-2}. The free exciton and bound biexciton emission line intensities show a linear dependence on power, similar to results reported by other

researchers for CuCl nanocrystals embedded in NaCl matrices and InGaAs/GaAs quantum dash structures [38-40]. For the higher excitation regimes the biexciton emission intensities appear to have a linear dependence on power. Phillips *et al.* suggested that this reversion to linear dependence was due to shorter recombination times of biexcitons in such direct-band gap materials [41]. The binding energy of the bound exciton (E_{bX}^{b}), the free biexciton (E_{XX}^{b}) and the bound biexciton (E_{bXX}^{b}) of the nanocrystalline CuCl hybrid film can be calculated by using the energy calculation scheme based on equations (5.1-5.3) [42, 43]:

$$E_{bX}^{b} = E_{X} - E_{bX} \tag{5.1}$$

$$E_{XX}^{b} = E_{X} - E_{XX} \tag{5.2}$$

$$E_{bXX}^{b} = 2E_{X} - E_{bXX} - E_{bX} - E_{XX}^{b} \tag{5.3}$$

where E_X (3.213 eV), E_{XX} (3.170 eV), E_{bX} (3.191 eV) and E_{bXX} (3.141 eV) are the free exciton, biexciton, bound exciton and bound biexciton energies, respectively, taken from the PL spectrum at 15 K as shown in **Figures 5.10** and **5.11**. The calculated binding energy of the bound exciton is about 22±2 meV and is in excellent agreement with previously reported values for vacuum deposited CuCl thin film on silicon substrates [44] and bulk CuCl [45]. The free biexciton binding energy is 43±2 meV, which is approximately 11 meV higher than reported for bulk CuCl and almost the same as for CuCl quantum dots embedded in NaCl matrices [45]. Although, the mechanism for the increase in the biexciton binding energy is not entirely clear at present [46], it is known that the biexciton binding energy significantly increases with decreasing crystal size as reported by Masumoto *et al.* [45]. The calculated bound biexciton binding energy is 51±2 meV; this value is ~7 meV less than for CuCl films deposited on silicon substrates [44]. This is considerably larger than the biexciton binding energies of II-VI semiconductors such as ZnSe, CdS, and ZnO (BM_3 and BM_7 band) which are approximately 3.5, 6.3 and 15 meV, respectively [47]. The high quality biexciton (two confined electron–hole pairs) can be used as a quantum bit pair for quantum processing, as was shown conceptually in Edamatsu *et al.* [48].

5.6.2 Thermal Quenching of PL Intensity

An Arrhenius plot of the natural logarithm of the integrated Z_3 excitonic PL intensity as a function of inverse temperature is shown in **Figure 5.14**.

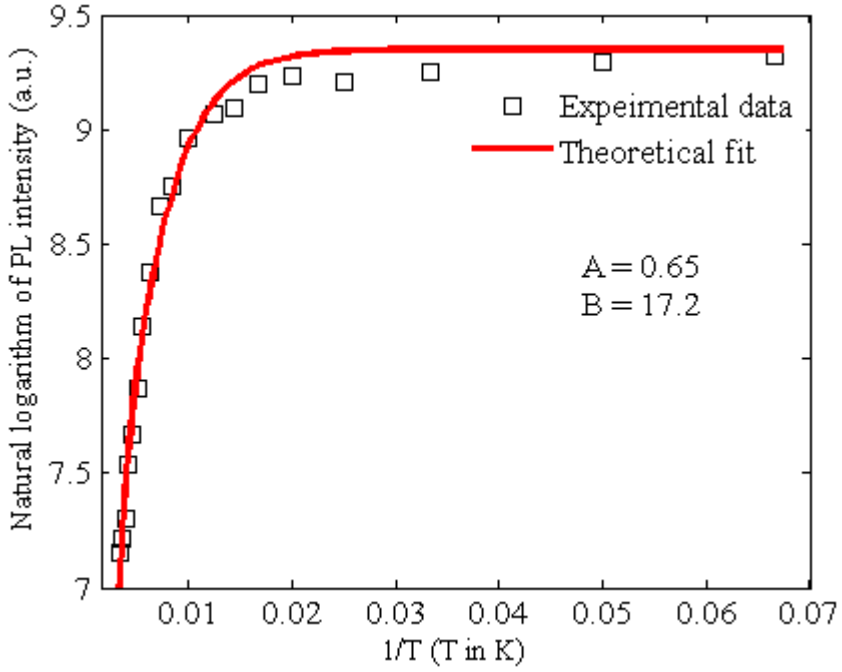

Figure 5.14: Arrhenius plot of the integrated Z_3 excitonic PL intensity vs. inverse temperature. Fitting with a two-step thermal quenching process is shown with a solid line for CuCl HF

One can observe clearly that the PL emission intensity is almost independent of temperature below 80 K, and above 100 K the PL emission intensity decreases rapidly. Therefore, the thermal quenching of the Z_3 PL emission can be described by means of a two-step process, and the experimental data are fitted by equation (5.4) below [49, 50]:

$$I = I_0\left(1 + A\exp\left(\frac{-E_1}{kT}\right) + B\exp\left(\frac{-E_2}{kT}\right)\right)^{-1} \qquad (5.4)$$

where E_1 and E_2 are the thermal activation energies and A, B are constants related to the lifetime of the excited state and the effective scattering time from the excited state to the non-radiative centre. These thermal activation energies were calculated to be $E_1 \approx 23$ meV and $E_2 \approx 140$ meV, respectively. The higher thermal activation energy (≈140 meV) connected with the thermal dissociation of the free excitons

should be same as the binding energy of the excitons. This calculated value is lower than the exciton binding energy of 190 meV [34]; but it is in agreement with the reported thermal activation energy for CuCl films on silicon substrates [43], higher than for sputtered CuCl films [32] and lower than the value (150 meV) reported for single crystal CuCl [6, 51]. This value indicates that the hybrid films' excitonic properties lie between those of the sputtered and single crystal CuCl films. Since the other activation energy $E_1 \approx 23$ meV lies close to the biexciton binding energy values it is reasonable to associate this thermal activation energy with the biexciton bound impurity [52].

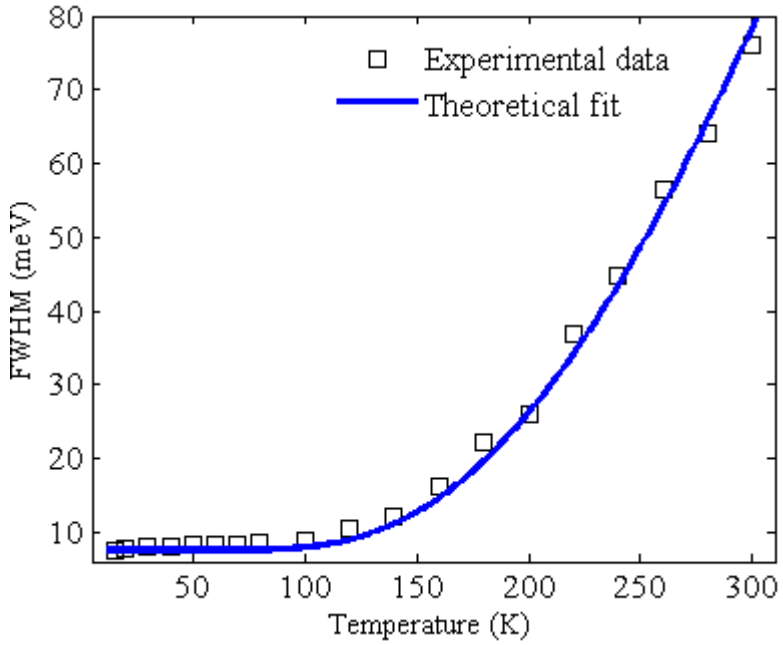

Figure 5.15: Temperature dependence of full width at half maximum (FWHM) of the CuCl hybrid film Z_3 free exciton peak; the solid line is the theoretical fit.

5.6.3 Exciton Line Broadening

The full width at half maximum (FWHM) of the Z_3 free exciton PL emission peak increases with temperature due to increased exciton-phonon interactions [7]. The PL emission peak was fitted to a Lorentzian distribution to estimate the full width at half maximum. **Figure 5.15** shows the variation of the FWHM of the Z_3 free exciton emission peak for a typical CuCl hybrid film. The FWHM experimental data are fitted with the following expression [44]:

$$\Gamma = \Gamma_0 + \gamma_{LA} T + \frac{\gamma_{LO}}{\left(\exp\left(\frac{nh\nu_{LO}}{kT} \right) - 1 \right)} \quad (5.5)$$

where Γ is the line-width broadening of the free exciton line, n is the number of phonons involved, Γ_0 is the FWHM of the Z_3 free exciton emission peak at 0 K, γ_{LA} and γ_{LO} describe the interaction of excitons with longitudinal acoustic and optical phonons of the lattice, respectively. $h\nu_{LO}$ (26 meV) is the energy of the LO phonon of CuCl [53] and T is the temperature. By fitting the experimental data with equation (5.5) the following parameters were extracted: Γ_0 = 7.25±0.025 meV, γ_{LA}≈ 30±0.2 μeVK^{-1}, γ_{LO} ≈ 945±2 meVK^{-1} and $nh\nu_{LO}$= 70.15±3.5 meV. The value of $nh\nu_{LO}$ is ~70 meV, which suggests that 3 phonons are involved in the exciton-phonon interaction (i.e. 3 x $h\nu_{LO}$ ≈ 78 meV) [54]. The values of γ_{LA} and γ_{LO} are larger than the values reported for ZnO [55] and GaN [56], and, interestingly, are also higher than for sputtered CuCl films [32]. This suggests that the CuCl hybrid film appears to have a stronger exciton-phonon interaction than these other semiconductors, which is most likely due to the polar nature of CuCl bonding [57] From figure 5.15 it clear that the increase of the FWHM at temperatures below 120 K is quite linear and very small, while above 120 K to room temperature the FWHM increases exponentially. This indicates that up to 120 K acoustic phonons contribute and above 120 K the LO optical phonons are mostly responsible for the increase of the FWHM [56]. The FWHM of the room temperature Z_3 PL emission peak is ~76 meV for the CuCl nanocrystalline hybrid films and is in excellent agreement with earlier reports for sputtered CuCl film (74 meV) [32], and comparatively better than GaN (100 meV) [58] and ZnO (106 meV) [59] nanostructures for UV light emitting materials.

5.6.4 Exciton Energy Shifting

The Z_3 transition occurs at an energy of 3.213 eV (≈385.9 nm) at 15 K. This represents a blue shift of approximately 3 meV compared to the Z_3 transition energy in bulk CuCl of 3.210 eV (≈386.3 nm) [60]. In CuCl nanocrystals, the size dependent blue-shift of the exciton energy can be expressed by an exciton quantum confinement model described by the following expression [61]:

$$\Delta E = \frac{\hbar^2 \pi^2}{2M\left(a^*\right)^2} \tag{5.6}$$

where ΔE is the blue shift of the exciton energy, M is the Z_3 excitation translation mass ($M = 2.3m_0$, where m_0 is the electron rest mass) and $a^* = a\text{-}0.5a_B$, where a is the radius of the CuCl nanocrystals and a_B is the Bohr radius of the exciton (0.7 nm for CuCl) [5]. Using the measured blue shift of $\Delta E \approx 3$ meV, an average CuCl nanocrystal radius of approx. 7.73 nm is obtained. To observe the strong or weak quantum confinement effect the radius of the particle should be close to the Bohr radius ($R/a_B < 1$ for strong and $R/a_B > 1$ for weak confinement). However in our measurements the nominal radial dimension of the CuCl nanocrystals is more than 11 times greater than the CuCl Bohr radius. Thus it is unlikely that the blue shift is due to the phenomenon of exciton quantum confinement.

Another cause could be pressure and polarization effects induced by the PSSQ matrix. Hydrostatic pressure induced exciton energy shifts in bulk CuCl (7.65 meV/GPa) [62], for CuCl microcrystals embedded in alkali-chloride matrices (8.22 meV/GPa) [63] and for nanocrystals in a LiCl matrix (4.1 meV/GPa) [64] were reported previously. The hydrostatic pressure in nanocrystalline CuCl hybrid films is, however, very small, so the energy shift associated with this effect is not considerable. Brus reported that there is a polarization effect on the exciton energy for microcrystals surrounded by a dielectric matrix. The change of exciton energy ΔE is assumed to be mainly associated with the exciton internal motion and is expressed by [65]:

$$\Delta E = \frac{6\left(\varepsilon_2 - \varepsilon_1\right)}{\varepsilon_2 + 2\varepsilon_1}\left(\frac{a_B}{R}\right)^3 Ryd^* \tag{5.7}$$

where ε_1 and ε_2 are the dielectric constants of the PSSQ matrix and CuCl, respectively, Ryd^*=213 meV for CuCl [66], and R is calculated to be about ~3.39 nm, which is smaller than the nanocrystal radii obtained via XRD analysis, but is at least of the same order.

Another cause of this blue shift may be the presence of micro-strain in the CuCl nanocrystals embedded in the PSSQ matrices. Generally, the crystal symmetry can be altered by strain in the film. A variation in the crystal symmetry is reflected in the electronic band structure and shifts the energy levels. Uniaxial stress on

semiconductors produces a change in the lattice constant and symmetry of the crystal, and as a consequence, these cause important changes in the electronic properties. A Z_3 free exciton energy increase due to the uniaxial stress was reported by Koda *et al*. [67]. The film strain along the lattice constant axis, a, can be measured using the following expression [68]:

$$\varepsilon = \left(\frac{a_s - a_o}{a_o} \right) \times 100 \ \% \tag{5.8}$$

where a_o = 5.4160 Å is the lattice constant of unstrained CuCl [69] and a_s = 5.4337 Å is the lattice parameter of the CuCl hybrid films calculated from the XRD data. Computing the strain using the above relationship we found that the hybrid films are under tensile strain of approx. + 0.32%. According to the work of Kim *et al*. [70] and Blacha *el al.* [71] the tensile strain induced shift in the observed exciton energy should be ≈ -1.31 meV, i.e. a red shift when in fact the observed exciton energy reported herein is blue shifted. Thus it is unlikely that strain is the major source of the observed blue shift of 3 meV. For nanocrystals with $R>a_B$, the electron and hole motion around their centre of mass prevents the centre of mass from reaching the nanocrystal surface, thus forming a layer which is called a "dead layer" near the nanocrystal surface. In other words the near surface regions cannot be reached by the centre of mass of the exciton due to the finite size of the quasiparticle. Taking the exciton dead layer into account, the exciton energy shift can be expressed as [72]:

$$\Delta E = \frac{\hbar^2 \pi^2}{2M\left(R - \eta a_B\right)^2} \tag{5.9}$$

where η is a constant whose numerical value is a function of m_h^*/m_e^*; for m_h=4.2m_0, m_e=0.43m_0 [73] then η=9.77 and M is the Z_3 excitation translation mass (M = 2.3m_0, where m_0 is the electron rest mass). The nanocrystal radius was calculated using the above values and was found to ~14.23 nm, whose value is close to the value of the average nanocrystal radius (~17.5 nm) obtained from XRD analysis. From the above investigation, the average radius of the CuCl nanocrystals is much larger than its Bohr radius for the quantum confinement effect to play a major role; the hydrostatic pressure is also too small to account for the exciton energy shifts. The CuCl crystal radius obtained by considering the polarization effect on the exciton energy is also

~5 times smaller than the value obtained by XRD analysis and thus this effect does not contribute significantly. Strain effects are also not considered likely. The radius of the CuCl crystals calculated by considering the operation of a dead layer effect (~14.23 nm) is very close to the value obtained by XRD analysis (~17.5 nm) and therefore it is likely that the observed blue shift in the nanocrystalline CuCl hybrid films can be attributed to a dead layer effect near the CuCl nanocrystal surface.

5.6.5 Exciton Line Shift with Temperature

The variation of the CuCl hybrid film Z_3 free exciton emission peak position as a function of temperature is shown in **Figure 5.16**. This reveals that the effective exciton energy increases from 3.213 eV at 15 K to 3.254 eV at room temperature. This blue shift as a function of temperature is in contrast to other semiconductors, i.e. the variation of the band gap energy of CuCl in hybrid films does not follow the Varshni or Einstein models [44, 74, 75]. The Z_3 exciton energy shift as a function of temperature for the CuCl hybrid film is similar to those previously reported for vacuum evaporated and sputtered CuCl thin film [32, 44]. The exciton energy increase with increasing temperature can be explained on the basis of the model of Garro *et al.* who postulated that the Cu ions, vibrating principally at low frequencies lead to an increase in the exciton energy, whereas the Cl ions, vibrating at high frequencies, lead to a reduced exciton energy [76]. When these two competing processes are taken together, the exciton energy tends to increase at low temperature (<70 K) and will continue to increase, but above 70 K the exciton energy gap increase rate is significantly reduced. To explain the energy shift as a function of temperature the experimental data was fitted by using the two oscillator model proposed by Göbel *et al*. [77]. They describe the mass (Cu and Cl) and temperature dependence of the exciton energy in the following expression [77]:

$$E(T,M) = E_0 + \frac{A_{Cu}}{\nu_{Cu} M_{Cu}}\left(\frac{1}{\exp(h\nu_{Cu}/k_B T)-1}+\frac{1}{2}\right)+\frac{A_{Cl}}{\nu_{Cl} M_{Cl}}\left(\frac{1}{\exp(h\nu_{Cl}/k_B T)-1}+\frac{1}{2}\right) \quad (5.10)$$

where ν_{Cl} and ν_{Cu} are the phonon frequencies of Cl and Cu (6 THz and 1 THz, respectively), E_0 is the unrenormalized exciton energy, and A_{Cu} and A_{Cl} are the electron-phonon interaction parameters for copper and chlorine, respectively, which can be determined from the fitting of the experimentally determined temperature

dependence of the exciton energy gap. By fitting the equation to the experimental data we obtain the unrenormalized exciton energy E_0 = 3.214 eV and this result is in excellent agreement with the work of Göbel *et al.* (E_0 = 3.221 eV) [77].

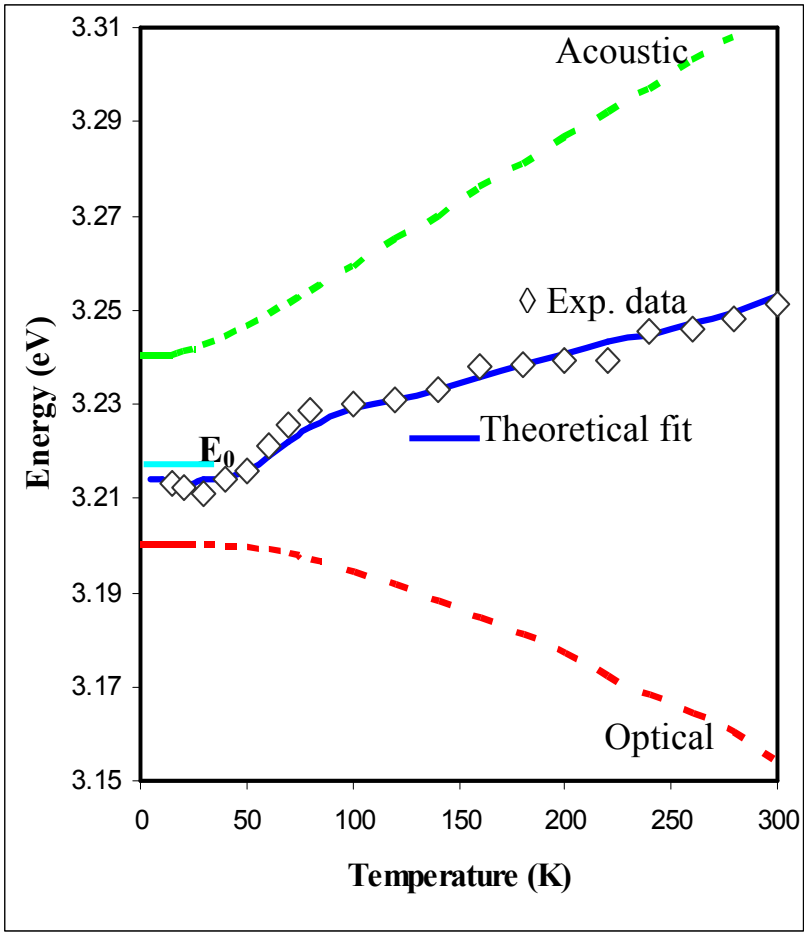

Figure 5.16: Z_3 free exciton emission peak position shift as a function of temperature; the solid line is the theoretical fit.

Further to this we obtain the value of $A_{Cu} \approx 0.00301$ eV^2 amu and $A_{Cl} \approx -0.04917$ eV^2 amu. These are also very close to the values previously reported for sputtered [32] and evaporated CuCl films [44]. In addition the Z_3 exciton energy blue shift for the CuCl nanocrystalline hybrid films of about 41 meV for a temperature increase from 15 K to room temperature is also in good agreement with [77]. This blue shift for the CuCl nanocrystalline hybrid films can be understood in terms of a local empirical pseudo-potential approach for the copper ion vibrations [76], which includes a shifting of remote d-like (copper) plane waves to a lower energy, so that they are

close to the chlorine atomic p levels, and allows for p-d mixing. According to [77], the resulting level splitting in the valence band is to a large extent determined by a Cu atomic pseudopotential. The introduction of a Debye-Waller factor to ‘‘weaken’’ this pseudopotential with increasing temperature results in a decreasing hybridization energy. This lowers the top of the valence band and therefore the band gap increases with increasing temperature.

5.7 Cathodoluminescence (CL)

The cathodoluminescence scan for a typical CuCl thickness ≈500 nm hybrid film deposited on a silicon substrate and annealed at 120^{o} C for 18 hours, was performed at room temperature using the Carl Zeiss EVO 50 Series SEM with an attached CL mirror and micrometer for different electron beam energy and probe current. Spectra were captured using a Gatan MonoCL monochromator with a 1200 lines/mm grating and various accelerating voltage and probe current. **Figure 5.17** shows the room temperature CL spectrum for this typical CuCl hybrid film deposited on silicon excited with an electron beam of 8 keV and probe current of 14 nA.

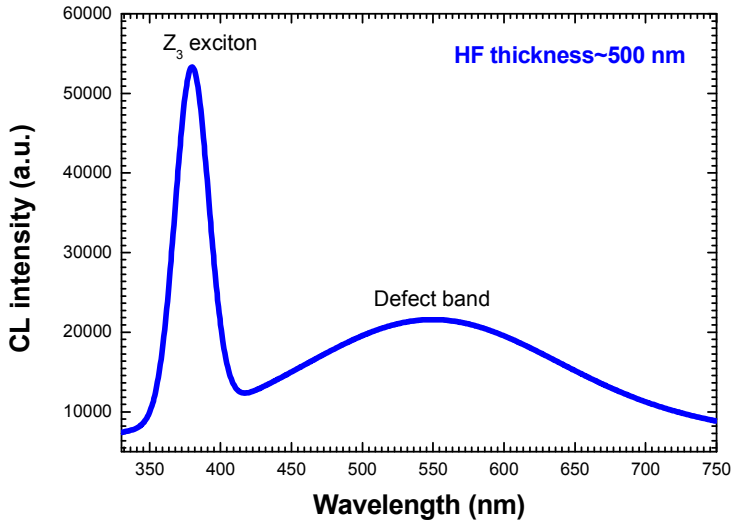

Figure 5.17: Room temperature CL spectrum of a typical CuCl HF annealed for 18 hours on a silicon substrate

A strong UV emission appears at λ≈381 nm (~3.254 eV), which is due to the recombination governed by the Z_3 free exciton and a relatively low intensity broad

green emission centered at λ≈545 nm (~2.275 eV) is also observed. Sub-band gap emission such as this is generally considered to originate from impurities, defects, and nonstoichiometry. Similar deep level emission is reported by several authors [6, 29, 53, 78].

During the CL measurements it is possible to vary both the accelerating voltage and the probe current of the beam. Both parameters were investigated to find the optimum values for investigating the CL properties of the CuCl hybrid films. The interaction between keV electrons and a semiconductor has been extensively investigated past few decades [79-81]. The incident electron undergoes a successive series of elastic and inelastic scattering events in the semiconductor. As the result of these scattering events within the material, the original trajectories of the electrons are randomized, with the range of the electron penetration being a function of the electron-beam energy E_b [79, 82]:

$$R_e = \left(k / \rho \right) E_b^{\alpha} \tag{5.11}$$

where ρ is the density of the material, k depends on the atomic number of the material and is also a function of energy, α depends on the atomic number and the electron-beam energy E_b. A more general expression derived by Kanaya and Okayama was found to agree well with experimental results in a wider range of atomic numbers [83]. The range according to Kanaya and Okayama is given by [79, 83, 84]:

$$R_e = \left(0.0276 \; A / \rho Z^{0.889} \right) E_b^{1.67} \; \mu m \tag{5.12}$$

where E_b is in keV, A is the atomic weight in g/mol, ρ is in g/cm^3 and Z is the atomic number. The excitation electrons, volume in the sample can be controlled by changing the energy of the electron beam and the consequent depth profiling of the sample may allow one to investigate changes in the optical quality of the sample as a function of distance from surface to the substrate. According to equation 5.12 for a 500 nm thick CuCl hybrid film the most intense CL emission should be obtained for the electron beam energy of ~8 keV. A selection of accelerating voltages has been plotted in **Figure 5.18**. The CL emission peak intensity for CuCl hybrid film increases with increase accelerating voltage up to 8 keV, then the peak intensity

decreases. The electron beam energy at 8 keV excites the CuCl hybrid film through to its total thickness of ≈500 nm, resulting in the most intense CL emission.

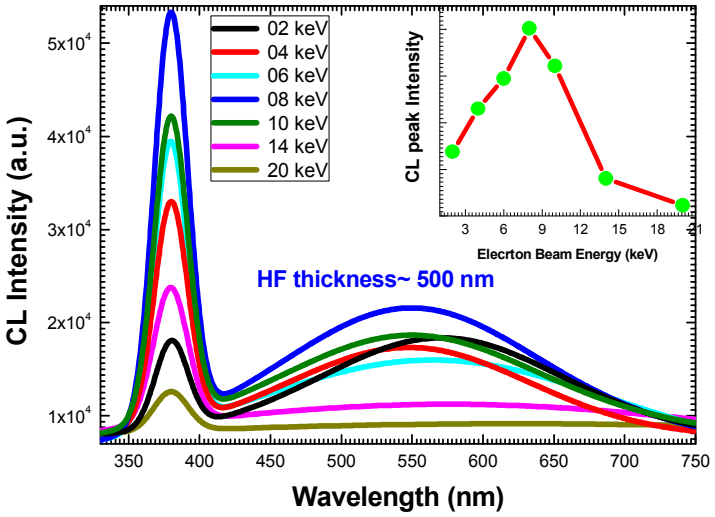

Figure 5.18: CL spectra of a typical CuCl hybrid film for different accelerating voltages, inset CL peak intensity as a function of accelerating voltage

Further increasing the accelerating voltage resulted in a decrease in the CL emission peak intensity, most likely because an increasing fraction of the electrons were penetrating into the silicon substrate.

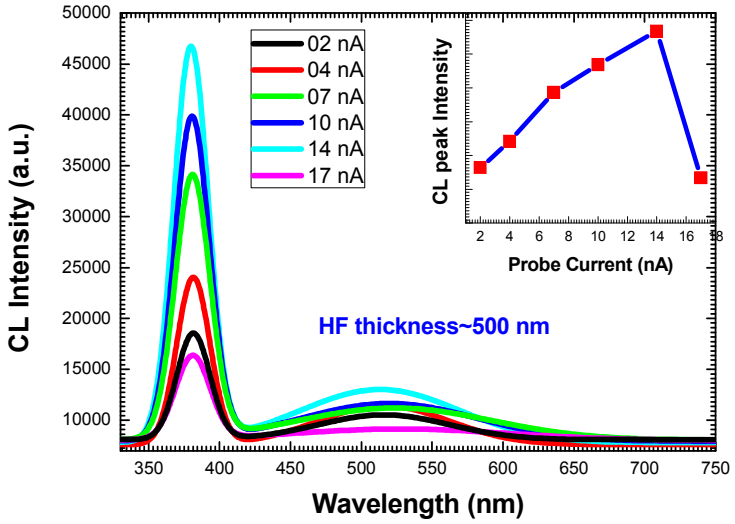

Figure 5.19: CL spectra of a typical CuCl hybrid film for different probe currents, inset CL peak intensity as a function of probe current

Figure 5.19 shows the CL spectra of thickness ≈500 nm CuCl hybrid film for different probe currents (2-17 nA). The figure exhibits that as the probe current is increased the CL emission peak intensity also increases for both the Z_3 free exciton emission and the broad band emission up to 14 nA. The relationship between the probe current (range from 2 to 14 nA) and CL emission peak intensity for Z_3 free exciton is approximately linear. For further increases of probe current the CL UV emission peak intensity rapidly decreases and the green emission almost disappears, which may be due to the high probe current induced surface charging damage the CuCl hybrid film.

Summary

The optical properties have been investigated for nanocrystalline CuCl hybrid films deposited on several substrates including silicon, glass and ITO coated glass, by the spin coating method and annealed at 120^{o} C for durations between 1 and 24 hours *in vacuo*. FTIR absorption peak intensities decreased as the annealing time duration increased. XPS analysis reveals that after 18 hours annealing Cu^{+} and Cl^{-} formed CuCl by ionic bonding. Room temperature UV-Vis measurements showed that the as-deposited film has no absorption but the absorption intensity increases with annealing duration up to 18 hours then slightly decreases. The photoluminescence studies revealed that the film annealed for 18 hours gave the optimum PL properties for CuCl, including low temperature PL confirmation of the presence of free excitons (Z_3), impurity bound excitons (I_1), free biexcitons (M) and impurity bound biexciton (N_1) emission peaks. The power dependent PL measurement confirmed the existence of both free biexciton (M) and bound biexciton (N_1) emission. At low temperatures we confirm that acoustic phonons are responsible for PL linewidth broadening and above 120 K the LO optical phonons are responsible the Z_3 excitonic FWHM broadening. The Z_3 exciton energy gap exhibits a blue shift of 3 meV at 15 K, which is most likely due to a dead layer effect near the CuCl nanocrystal surface. By increasing the temperature from 15 K to room temperature, the phonon induced interactions with exciton transitions have the following effects on the material properties: (a) PL intensity decrease (b) disappearance of transitions related to the impurity bound, free biexciton and impurity bound biexciton states due to the low binding energy of the impurity bound excitons (c) PL emission line broadening due to an increase of the exciton-phonon interaction and (d) a blue shift of the energy gap due to the interaction of lattice vibrations with excitons. Room temperature CL measurements exhibit strong emission in the UV region. The optical properties of the nanocrystalline γ-CuCl hybrid films are comparable with vacuum deposited and sputtered CuCl films.

References

[1] D. Gerion, F. Pinaud, S. Williams, W. Parak, D. Zanchet, S.Weiss, A. Alivisatos; J. Phys. Chem. B **105** (2001) 8861

[2] L.Manna, E.C. Scher, A.P. Alivisatos, J. AmChem. Soc. **122** (2000) 12700

[3] A. L. Efros, M. Rosen, Annu. Rev. Mater. Sci. 30 (2000) 475

[4] M. Nirmal, L. Brus, Acc. Chem. Res. **32** (1999) 407

[5] A. S. Castillo, F. P. Rodrıguez; J. Appl. Phys. **90** (2001) 3662

[6] T. Goto, T. Takahashi, M. Ueta; J. Phys. Soc. Japan **24** (1968) 314

[7] M. Cardona; Phys. Rev. **129** (1963) 69

[8] G. Socrates; Infrared and Raman Characteristic Group Frequencies table and charts, Wiley, 3rd Ed. (2001) 245

[9] W. Noll; Angew Chem. Int. Ed. Engl. **2** (1963) 73

[10] Judeinstein P, Morineau R, Livage; J. Solid State Ionics **51** (1992) 239

[11] Kirm I, Medina F, Rodriguez X, Cesteros Y, Salagre P, Sueiras; J. Appl. Catal. A: Gen **272** (2004) 175

[12] G. Socrates; Infrared and Raman Characteristic Group Frequencies table and charts, Wiley, 3rd Ed. (2001) 105

[13] G. Socrates; Infrared and Raman Characteristic Group Frequencies table and charts, Wiley, 3rd Ed. (2001) 96

[14] J. Coates; Interpretation of infrared spectra, a practical approach, in: R. A. Meyers (Ed.), Encyclopedia of Analytical Chemistry (2000)1815

[15] X. Wang, T. Yang, G. Du, H. Liang, Y. Chang, W. Liu, Y. Xu; J. Cryst. Growth **285** (2005) 521

[16] S. Nam, S. W. Nam, J. H. Yoo and D. H. Ko; Mat. Res. Soc. Symp. Proc. **716** (2002) B4.25.1

[17] J. M. Howard, V. Craciun, C. Essary, and R. K. Singh; Applied Physics Letters **81** (2002) 3431

[18] C. D. Wagner; Handbook of X-ray Photoelectron Spectroscopy, Perkin-Elmer Corporation, Minnesota (1979) 527

[19] N. Kulbe, O. Höfft, A. Ulbrich, S. Z. El Abedin, S. Krischok, J. Janek, M. Pölleth, F. Endres; Plasma Process. Polymer **8 (**2011) 32

[20] P. E. Larson, J. Electron. Spectrosc **4** (1974) 213

[21] G. Schön, Surf. Sci. **35** (1973) 96

[22] N. Kulbe, O. Höfft, A. Ulbrich, S. Z. E. Abedin, S. Krischok, J. Janek, M. Pölleth, F. Endres; Plasma Process. Polym. **8** (2011) 32

[23] C. D. Wagner, L. H. Gale and R. H. Raymond; Anal. Chem. **51** (1979) 46

[24] A. J. Pertsin and Y. M. Pashumin, Appl. Sruf. Sci. **47** (1991) 115

[25] S. R. Carlo, C. Perry, J. Torres and D. H. Fairbrother; J. Vac. Sci. Technol. A **20** (2002) 350

[26] R. P. Vasquez; Surface Science Spectra **2** (1994) 138

[27] L. O'Reilly, G. Natarajan, P. J. McNally, D. Cameron, O. F. Lucas, M. M. Rosas, L. Bradley, A. Reader; J. Mater. Sci: Mater. Electron **16** (2005) 415

[28] M. Nakayama, H. Ichida, and H. Nishimura; J. Phys.: Condens. Matter **11** (1999) 45A

[29] A. Mitra, F. O. Lucas, L. O'Reilly, P. J. McNally, S. Daniels and G. Natarajan; J Mater Sci: Mater Electron **18** (2007) S21

[30] L. O'Reilly, O. F. Lucas, P. J. McNally, A. Reader, G. Natarajan, S. Daniels, D. C. Cameron, A. Mitra, M. M. Rosas, A. L. Bradley; J App. Phys. **98** (2005) 113512

[31] M. Nakayama, H. Ichida, H. Nishimura; J. Phys.: Condens. Matter, **11** 45A (1999) 7653

[32] G. Natarajan, A. Mitra, S. Daniels, D.C. Cameron, P. J. McNally; J. Thin Solid Films **516** (2008) 1439

[33] N. Nagasawa, N. Nakata, Y. Doi, M. Ueta; J. Phys. Soc. Japan **39** (1975) 987

[33A] A. Cowley, B. Foy, D. Danilieuuk, P.J.McNally, A.L.Bradly, E. McGlynn and A.N. Danilewsky ; Phys. Stat. Sol(a) **206 (5)** (2009) 923

[34] M. E. Jouad, M. A. Lamrani, Z. Sofiani, M. Addou, T. E. Habbani, N. Fellahi, K. Bahedi, L. Dghoughi, A. Monteil, B. Sahraoui, S. Dabos, N. Gaumer; J. Optical Materials **31** (2009) 1357

[35] G. Socrates, Infrared and Raman Characteristic Group Frequencies table and charts, Wiley, 3rd Ed. (2001) 96

[36] F.O. Lucas, A. Mitra, P J McNally, S Daniels, AL Bradley, D M Taylor, Y. Y. P. Yakov, K Durose, D. C. Cameron; J. Phys D: Appl. Phys. **40** (2007) 3461

[37] J. I. Pankove, Optical Processes in Semiconductors, Prentice-Hall, Englewood Cliffs NJ (1971) 123

[38] S. Yano, T. Goto, T. Itoh, A. Kasuya; Physical Review B **55** (1997) 1667

[39] Y. Masumoto, T. Kawamura and K. Era; Appl. Phys. Lett. **62** (1993) 225

[40] A. Musiał, G. Sęk, P. Podemski, M. Syperek, J. Misiewicz, A. Löffler, S. Höfling and A. Forchel; J. Phys.: Conference Series **245** (2010) 012054

[41] R. T. Phillips, D. J. Lovering, G. J. Denton and G. W. Smith; Physical Review B **45** (1992) 4308

[42] D. Danieluk A .Bradley, A. Mitra, L. O'Reilly, O. F. Lucas, A. Cowley, P. J. McNally, B. Foy and E. McGlynn; J. Mater Sci: Mater Electron **20** (2009) S76

[43] M. Nakayama, H. Ichida and H. Nishimura, J. Phys.: Cond. Matter **11** (1999) 7653

[44] A. Mitra, L. O'Reilly, O. F. Lucas, G. Natarajan, D. Danieluk, A. L. Bradley, P. J. McNally, S. Daniels, D. C. Cameron, A. Reader, M. M. Rosas, J. phys. stat. sol. **245** (2008) 2808

[45] Y. Masumoto, S. Okamoto, S. Katayangi; Phys. Rev.B **50** (1994) 18658

[46] K. Kouyama, M. Inoue, Y. Inose, N. Suzuki, H. Sekiguchi, H. Kunugita, K. Ema, A. Kikuchi, K. Kishino; J. Luminescence **128** (2008) 969

[47] A. Yamamoto, K. Miyajima, T. Goto, H. J. Ko, T. Yao; Phys. Stat. Sol. B **229** (2002) 871

[48] K. Edamatsu, G. Oohata, R. Shimizu, and T. Itoh; Nature (London) **431** (2004) 167

[49] H. J. Lozykowski, V. K. Shastri; J. Appl. Phys. **69** (1991) 3235

[50] W. Bala, Z. Ukasiak, M. R. Barz, P. Dalasiski, A. Bratkowski, D. Bauman, and R. Hertmanowski; Opto-Electronics Review **12** (2004) 445

[51] K. Saito, M. Hasuo, T. Hatano, N. Nagasawa; Solid State Comm. **94** (1995) 33

[52] X. Liu; "Photoluminescence and Extended X-ray Absorption Fine Structure Studies on CdTe Material" PhD thesis, University of Toledo, USA (2006) 80

[53] M. Nakayama, H. Ichida, H. Nishimura; J. Phys.: Cond. Matter **11** (1999) 7653

[54] D. Kovalev, B. Averboukh, D. Volm, B. K. Meyer, H. Amano, I. Akasaki; Phys. Rev. B **54** (1996) 2518

[55] X. T. Zhang, Y.C. Liu, Z. Z. Zhi, J. Y. Zhang, Y. M. Lu, D. Z. Shen, W. Xu, X. W. Fan, X.G. Kong; J. Lumin. **99** (2002) 149

[56] A. K. Viswanath, I. Lee, S. Yu, D. Kim, Y. Choi, C. Hong; J. Appl. Phys. **84** (1998) 3848

[57] D. K. Shuh, R. S. Williams; Phys. Rev. B **44** (1991) 5827

[58] B. Damilano, N. Grandjean, S. Dalmasso, J. Massies; Appl. Phys. Letters **75** **(**1999) 2413

[59] X. Liu, X. Wu, H. Cao, R. P. H. Chang; J. Appl. Phys. **95** (2004) 615

[60] Y. Kaifu, T. Komatsu; Phys. Status Solidi B **48** (1971) K125

[61] T. Wamura, Y. Masumoto, T. Kawamura; J. Appl. Phys. Lett. **59** (1991) 1758

[62] K. Reimann, ST. Rubenacke; Phys. Rev. B **49** (1994) 11021

[63] A. Blacha, S. Ves, M. Cardona; Phys. Rev. B **27** (1983) 6346

[64] K. Reimann, M. Haselhoff, ST. Rubenacke, M. Steube; phys. stat. sol. B **198** (1996) 71

[65] L. E. Brus; J. Chem. Phys. **80** (1984) 4403

[66] S. Nikitine; Progr Semiconductor **6** (1962) 235

[67] T. Koda, T. Murahashi, T. Mitani, S. Sakoda, Y. Onodera; Phys. Rev. B **5** (1972) 705

[68] H. C. Ong, A. X. E. Zhu, G. T. Du; Appl. Phys. Lett **80** (2002) 941

[69] International Centre for Diffraction, [JCPDS Card No. 06-344] (1997)

[70] D. Kim, M. Nakayama, O. Kojima, H.Ichida, T. Nakanishi, H. Nishimura; Physical Review B **60** (1999) 13879

[71] A. Blacha, S. Ves, M. Cardona; Phys. Review B **27** (1983) 6346

[72] Y. Kayanuma; Phys. Rev. B **38** (1988) 9797

[73] C. I. Yu, T. Goto, M. Ueta; J. Phys. Soc. Jpn. **34** (1973) 693

[74] Y. P. Varshini; Physica E **34** (1967) 149

[75] X. T. Zhang, Y. C. Liu, Z. Z. Zhi, J. Y. Zhang, Y. M. Lu, D. Z. Shen, W. Xu, X. W. Fan, X. G. Kong; J. Lumin. **99** (2002) 149

[76] N. Garro, A. Cantarero, M. Cardona, T. Ruf, A. Göbel, C. Lin, K. Reimann, S. Rtibenacke, M. Steube, Solid State Comm. **98** (1996) 27

[77] A. Göbel, T. Ruf, M. Cardona, C. T. Lin, J. Wrzesinski, M. Steube, K. Reimann, J. C. Merle, M. Joucla; Phys. Rev. B **57** (1998) 15183

[78] G. Natarajan, S. Daniels, D. C. Cameron, L. O'Reilly, A. Mitra, P. J. McNally, O. F. Lucas, R. T. Rajendra Kumar, Ian Reid and A. L. Bradley; J. Applied Physics **100** (2006) 033520

[79] B. G. Yacobi, D. B. Holt; J. Appl. Phys. **59** (1986) R1

[80] H. I. Leamy; J. Appl. Phys. **53** (1982) R51

[81] H. E. Bishop; "Electron-Solid Interactions and Energy Dissipation", Academic, New York (1974) 41

[82] T. E. Everhart, and P. H. Hoff; J. Appl. Phys. **42** (1971) 5837

[83] K. Kanaya, S. Okayama; J. Phys. D **5** (1972) 43

[84] J. I. Goldstein, D. E. Newbury, P. Echlin, D. C. Joy, C. Fiori, and E. Lifshin. Scanning Electron Microscopy and X-Ray Microanalysis (Plenum, New York, (1981))

CHAPTER 6

ELECTRICAL PROPERTIES

It is important to know the conductivity and conduction mechanisms of CuCl hybrid films to help improve the fabrication of efficient electroluminescent devices and this knowledge will help inform their optimisation in future. Field dependent charge carrier transport mechanisms and electroluminescence for the Au/CuCl hybrid film/ITO structure are reported in detail in this chapter.

6.1 Introduction

Polymer and polymer-nanocomposite based electronics devices provide a number of alternative approaches, including the use for adaptive circuits or neural network-based processor architectures. It is possible to achieve the desired conductivity mechanism by changing the combination of organic/polymer compound such as poly(acetylene) and poly(thiophenes), which show some potential for fabrication of low molecular weight organic and polymer-based optoelectronic, electronic and photonic devices, such as light emitting diodes (LEDs), photodiodes, solar cells, gas sensors, field effect transistors [1-3]. Some of the extraordinary advantages of polymer based devices have recently attracted much research in this field. These include: (a) low materials and production cost (b) easy and cost effective manufacture of large area devices such as LEDs or photovoltaic cells as well as development of nanoscale size for the device structural elements without significant difficulties and (c) by changing the composition and hence properties of the organic/polymer materials, it is possible to build completely new material morphologies and device geometries. For most of the polymer-hybrid based devices, stability is higher than that of the fully organic-based devices and this is particularly true for hybrids composed of inorganic nanoparticles in non-conductive polymer matrix [1]. This is because the polymer matrix prevents, to some extent, interdiffusion of the inorganic substituents. It is possible to obtain p-n nanojunctions in organic-inorganic hybrid materials, whereas, to date, this is impossible in polymer-polymer systems. In addition, it is possible to obtain new effective bandgap materials, or to fabricate a single crystal that works as a non-scattering media of light, simply by changing particle size and reducing the particle size to less than half of the visible light wavelength. The interface area between the nanoparticles and the polymer matrix is extremely high in polymer-hybrids, and this interface determines

many of its properties [1]. Most polymers are insulators (σ <10^{-8} Scm^{-1}) and the current conduction mechanisms through the insulating polymer can be distinctly different from those in doped semiconductors or metals [4]. When electrically conducting particles are randomly distributed within an insulating matrix such as polymer matrix composites, the composite is non-conducting, until the volume fraction of the conducting phase reaches the so-called percolation threshold, at which point the conductivity of the composite becomes antistatic or in the low-semiconductive range [5-8]. At certain threshold values of conductive particle concentration the conductivity of the composite changes abruptly; the absolute value of this change can reach 10^{7}-10^{8} Ohm-cm, which makes this effect similar to the metal-insulator transition in doped compensated semiconductors. Most amorphous insulators at imposed electric fields in excess of 10^{4} Vcm^{-1} show a range of nonlinear current-voltage dependencies, which can be interpreted based on certain conduction mechanisms such as Fowler-Nordheim (FN) tunnelling, Poole-Frenkel (PF) emission, as well as direct tunnelling transport, Schottky emission and ohmic behaviour [9].

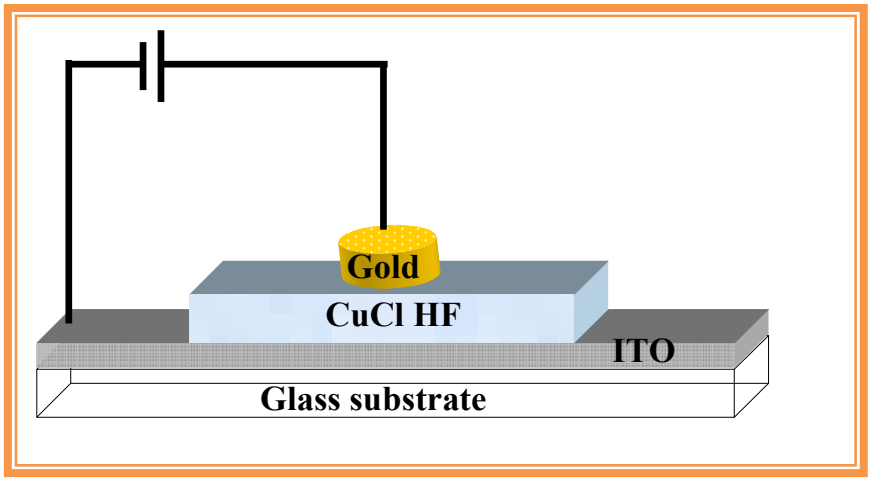

Figure 6.1: Au/CuCl hybrid film/ITO diode structure

γ-CuCl is a mixed ionic-electronic I-VII compound semiconductor material with p-type conductivity [10, 11]. The CuCl nanocrystals were synthesized by as previously described a complexation–reduction–precipitation mechanism reaction of $CuCl_2.2H_2O$, alpha D-glucose and de-ionized (DI) water with a PSSQ solution as the

host matrix material. In order to investigate the electrical properties of organic-inorganic CuCl hybrid film, organic-inorganic γ-CuCl nanocrystalline hybrid films with typical layer thicknesses of ~200 nm were deposited on indium tin oxide (ITO) coated glass substrates by the spin coating method. The films were subsequently heated at 120^{o}C for durations of 18 hours *in vacuo*.

A gold contact top electrode was deposited using an Edwards Auto 306A vacuum deposition system at a base pressure of ~1x10^{-6} mbar. The standard geometry of the Au/CuCl hybrid film/ITO diode is the sandwich structure, as shown in **Figure 6.1** with a contact area of ~7.85x10^{-7} m^2. A Keithley SCS 4200 system with a built-in voltage source was used to measure the current-voltage characteristic of the Au/CuCl hybrid film/ITO structure. Field dependent electrical studies were carried out at room temperature in the range 2.5×10^5 to 3.5×10^6 Vm^{-1}. The voltage across the sample was increased in steps of 0.05 V with a 5 second hold on time on each increment. The automated current-voltage measurements were performed using LabVIEW® software interfaced with the Keithley electrometer system.

6.2 Conductivity measurement

Gold and ITO are used as positive and negative electrodes, respectively, for the electrical measurement of the CuCl hybrid films. A typical room temperature current–voltage (I–V) characteristic for the Au/CuCl hybrid film/ITO structure is shown in **Figure 6.2**. The I-V characteristic confirms that the current increases exponentially in both forward and reverse bias conditions, i.e. the curve exhibited non-ohmic behaviour. It is well known that CuCl is a mixed ionic–electronic semiconductor with p-type conductivity [12, 13]. According to the work of Wagner *et. al*. [13] the exponential current–voltage relation for p-type mixed conduction material can be expressed by the following relationship (for ionic current suppressed by the blocking electrode gold):

$$\ln I = \ln\left(\frac{\sigma^{+} ART}{dF}\right) + \left(\frac{VF}{RT} - 1\right) \tag{6.1}$$

where V is the applied voltage, I is the current, A is the cross-sectional area, d is the film thickness, F is the Faraday constant, R is the gas constant (J Kmol^{-1}), T is the absolute temperature in Kelvin, and σ^{+} is hole conductivity.

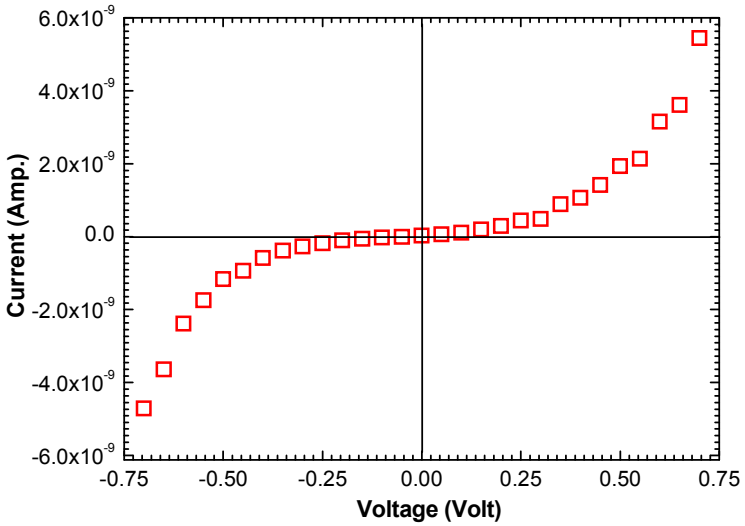

Figure 6.2: A typical current-voltage plot of organic-inorganic CuCl hybrid film

The hole conductivity was calculated for the hybrid film to be ~5.54×10^{-9} Scm^{-1}. Naturally, given the presence of the PSSQ matrix the conductivity obtained for the CuCl hybrid film is much smaller than for previously reported CuCl thin films [14]. The CuCl hybrid films used in this study typically comprise of a combination of 83% organic PSSQ and 17% inorganic CuCl by total volume. This ratio was deduced by analyzing the scanning electron microscopy data. The conductivity for the CuCl hybrid film can be approximated by equation (6.2) and (6.3) which originally derived by Maxwell, and Bruggeman, respectively [15-17]:

$$\frac{\sigma_{HF}}{\sigma_O} = 1 + 3\left(\frac{\sigma_I - \sigma_O}{\sigma_I + 2\sigma_O}\right) f \tag{6.2}$$

$$\left(\frac{\sigma_I - \sigma_{HF}}{\sigma_I - \sigma_O}\right)\left(\frac{\sigma_O}{\sigma_{HF}}\right)^{1/3} = 1 - f \tag{6.3}$$

where σ_{HF} is the hole conductivity of the hybrid films, $\sigma_I \approx 2.3\times10^{-7}$ Scm^{-1}[14] and $\sigma_O \approx 1.1\times10^{-9}$ Scm^{-1} [18] are the hole conductivity of the vacuum evaporated CuCl thin film and spin coated PSSQ, respectively and f is the volume fraction of CuCl.

The hole conductivity of CuCl hybrid film obtained using equation (6.2) and (6.3) to be ≈ 1.52×10^{-9} and 1.75×10^{-9} Scm^{-1}, respectively.

6.3 Arrhenius Plot

The dependence of conductivity with temperature for the CuCl hybrid films was investigated in the temperature range 80 to 350 K. The temperature dependent conductivity in Arrhenius plot format, for a typical CuCl hybrid film is shown in **Figure 6.3**. From this figure it is clear that the conductance of the CuCl hybrid films increases with temperature and it should be mentioned that contact resistance could be assumed to be negligible owing to the high resistivity of the materials under consideration.

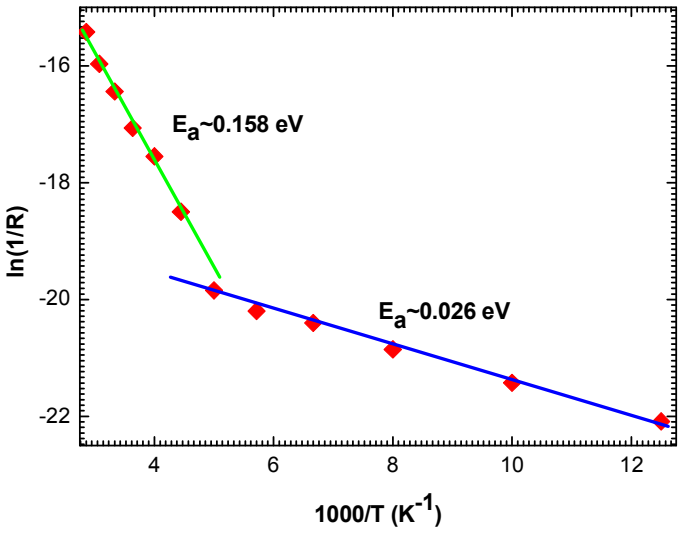

Figure 6.3: Arrhenius plot for conductance of a typical CuCl hybrid film

The activation energy has been measured from the Arrhenius plot using the equation [19]:

$$\sigma = \sigma_o \exp(-E_a / kT) \tag{6.4}$$

where E_a is the activation energy and σ_o is often regarded as a temperature independent constant. In fact, two activation energies are observed and the activation energy measured from the Arrhenius plot in the 80 to 200 K range and the 225 to 350 K range have been found to be 0.026 eV and 0.158 eV, respectively. The

activation energy in the low temperature region is less than the energy in the high temperature region, which is most likely due to a shift from one conduction mechanism to another upon heating. In the lower temperature region the activation energy is smaller, presumably because a small thermal energy is quite sufficient for the activation of charge carriers to take part in the conduction process. In other words the vacancies/defects weakly attached in the lattice can easily migrate. In the high temperature regime the electrical conductivity is mainly determined by the intrinsic defects and is often called intrinsic conduction. The high values of activation energy obtained for this region may be attributed to the fact that the energy needed to form defects is much larger than the energy required for carrier drift. Thus the intrinsic defects caused by the thermal variations determine the electrical conductance of the samples only at these elevated temperatures [20, 21].

6.4 Charge transport mechanism through the organic-inorganic CuCl hybrid film

For the hybrid film structure gold and indium tin oxide (ITO) are used as positive and negative electrodes, respectively. The work function difference of these two electrodes is ~0.4 eV [22, 23] and hence one would expect differences to be observed in the current values for opposite directions of the same applied voltage.

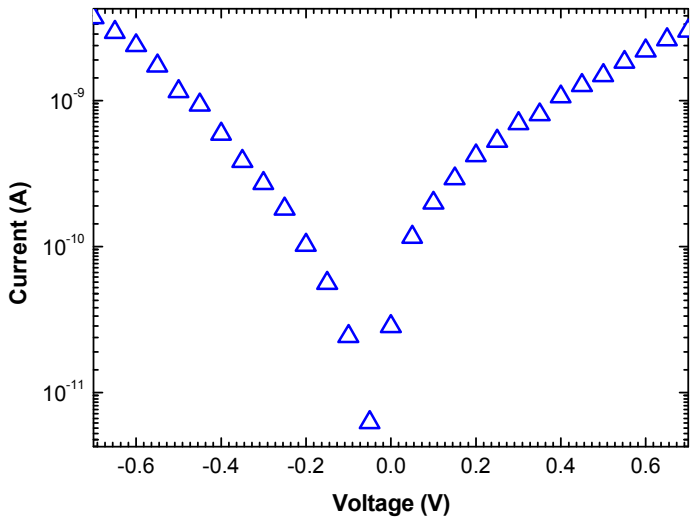

Figure 6.4: The semi-logarithmic current-voltage characteristics of the Au/CuCl hybrid film/ITO Schottky diode.

However, the observed differences are quite small as shown in the room temperature semi-logarithmic current-voltage *(I-V)* characteristics of **Figure 6.4**. The current increases exponentially for both forward and reverse biasing conditions, i.e. both bias directions exhibited diode-like behaviour. The electrical properties and electronic parameters of the Au/CuCl hybrid film/ITO structure have been investigated for forward bias current-voltage characteristics. Figure 6.5 shows the room temperature current-voltage plot of organic-inorganic CuCl hybrid films of thickness ~200 nm on a double logarithmic scale. The applied electric field was varied from 2.5×10^{5} to 3.5×10^{6} Vm^{-1}.

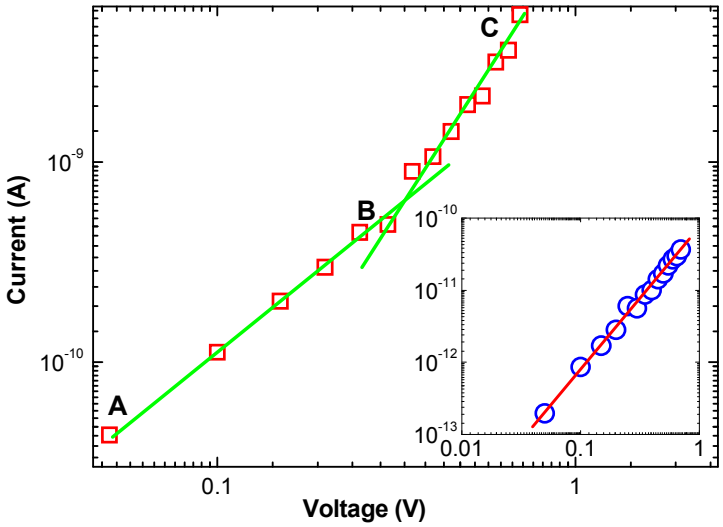

Figure 6.5: I-V characteristics of the Au/CuCl hybrid film/ITO diode on double logarithmic scale. The inset shows the plot for the Au/PSSQ/ITO structure for comparison.

In **Figure 6.5** two regions may be distinguished: labeled as AB and BC. For each of these regions the current-voltage characteristic can be approximated using the following relation:

$$I = c \times V^{m} \tag{6.5}$$

where I is the current, V is the voltage, c and m are constants. The values of m for regions AB and BC were found to be 1.10 and 2.73, respectively. The conduction of the hybrid film in the lower field region is found to be ohmic while in the higher field

region it is found to be non-ohmic. Note that the charge transport mechanism in the PSSQ film without embedded CuCl nanoparticles is found to be space charge limited (see inset of **Figure 6.5**). By changing the composition ratio of PSSQ and CuCl solution, the structural and electrical properties are also changed. The hybrid film conductivity decreases with an increase in the ratio of the PSSQ solution. For an electroluminescent device, the film conductivity should be high. Thus, one should endeavour to keep the PSSQ solution fraction as small as possible. But for low amounts of PSSQ solution the hybrid films develop pin holes, which cause the fabricated devices to short circuit. Several composition ratios were tested and we finally obtained an optimum ratio of 2:1 wt. % for the CuCl:PSSQ solution. For the composition ratio of 1:1, the current conduction mechanism goes to space charge limited conduction (SCLC).

In order to define the conduction mechanism at high fields, the current-voltage dependence was analyzed for different transport mechanisms including space charge limited conduction (SCLC), Fowler-Nordheim (FN) tunnelling, Pool-Frenkel (bulk limited) conduction and Schottky (electrode limited) conduction. For the space charge limited current conduction mechanism the slope of the log (*I*) vs. log (*V*) plot should yield a value of ~2 [24]. This is clearly not observed for the CuCl hybrid film and so the SCLC conduction mechanism can be omitted. The current density for the Fowler-Nordheim tunnelling mechanism is given by [25]:

$$J = \frac{m}{m^*}\frac{q^3}{8\pi h \phi_B} E^2 \exp\left(\frac{-8\pi}{3E}\left(\frac{2m^*}{h^2}\right)^{1/2}\frac{\phi_B^{3/2}}{q}\right) \qquad (6.6)$$

where J is the current density, E is the electric field, m is the electron rest mass, m^* is the effective electron mass, q is the electronic charge, h is Planck's constant and ϕ_B is the barrier height. Theoretically, a plot of ln (J/E^2) vs. $1/E$, the so called FN plot, should yield a straight line. But the FN plot for the organic-inorganic CuCl hybrid film does not generate such a straight line as can be seen in **Figure 6.6**. Hence the Fowler-Nordheim tunnelling mechanism can also be ruled out. The possibility of a Pool-Frenkel (PF) or Schottky emission (SE) conduction mechanism is now examined. The Pool-Frenkel conduction mechanism is associated with a bulk effect, where the charge carriers come from the bulk of the insulator.

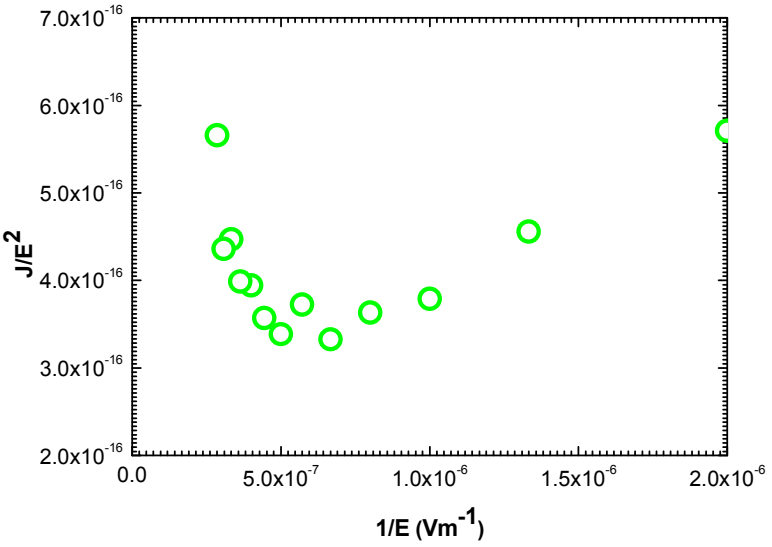

Figure 6.6: Fowler-Nordheim plot of CuCl hybrid film.

For Schottky emission the conduction mechanism is an electrode effect in which the charge carriers are supplied from the metal electrode. Generally, the SE conduction mechanism is an electrode-limited conductivity that depends strongly on the barrier between the metal and insulator and has the tendency to occur for insulators with fewer defects. For high electric field regimes, the coulombic potential barrier is lower for the Pool-Frenkel conduction mechanism. This implies that the bulk semiconductor supplies the charge carriers. The current-voltage relation for the PF conduction mechanism can be expressed as [26]:

$$J_{PF} = BV \exp\left(-\frac{q}{kT}\left[\phi_t - \left(\frac{qV}{\pi\varepsilon_0\varepsilon_r d}\right)^{1/2}\right]\right) \tag{6.7}$$

and the electron injection from the metal electrode into the semiconductor for the SE conduction mechanism can be expressed as [26]:

$$J_{SE} = A^* T^2 \exp\left(-\frac{q}{kT}\left[\phi_B - \left(\frac{qV}{4\pi\varepsilon_0\varepsilon_r d}\right)^{1/2}\right]\right) \tag{6.8}$$

where B is a constant and ϕ_t is the energy depth of a trap potential well, A^* is the Richardson constant given by $A^* = 120 \times \frac{m}{m_e} A.cm^{-2}.K^{-2}$ and $m = 0.43\ m_e$ for the

CuCl [27], ϕ_B is the barrier height of the Au electrode-hybrid film interface and the interface between the CuCl nanocrystal and the PSSQ taken as a hybrid film, ε_0 is the permittivity of free space, q is the electron charge, k is Boltzmann's constant, and T is the absolute temperature. ε_r and d are the dielectric constant and thickness of the CuCl hybrid film, respectively.

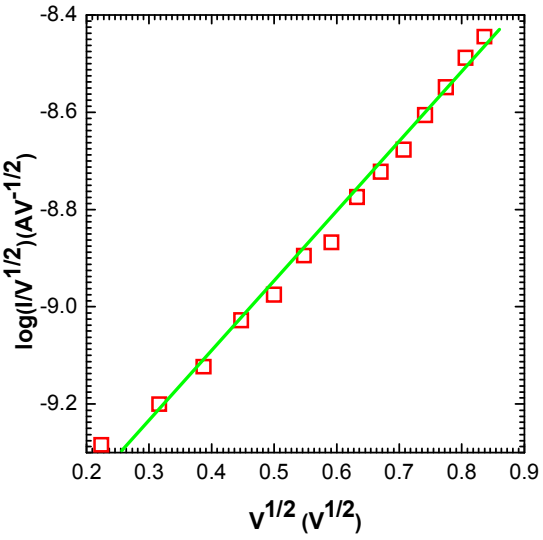

Figure 6.7: Voltage dependence of current plot of log ($I/V^{1/2}$) vs. $V^{1/2}$

To explore further the nature of the conduction mechanism for the hybrid films the experimental data was plotted according to log $(I/V^{1/2})$ vs. $V^{1/2}$ as shown in **Figure 6.7**. This gives a straight line plot. These line slopes (β) for PF and SE conduction can be expressed by Eqs. (6.9) and (6.10), respectively [28]:

$$\beta_{PF} = \frac{q}{kT}\left(\frac{q}{\pi\varepsilon_0\varepsilon_r d}\right)^{1/2} \tag{6.9}$$

$$\beta_{SE} = \frac{q}{kT}\left(\frac{q}{4\pi\varepsilon_0\varepsilon_r d}\right)^{1/2} \tag{6.10}$$

The slope of the CuCl hybrid film experimental plot for log $(I/V^{1/2})$ vs. $V^{1/2}$ was found to be ~1.47. Using the aforementioned equations 6.9 and 6.10 the dielectric constant of the CuCl hybrid film was calculated for both PF and SE conduction mechanisms. The calculated values for the dielectric constant based on PF and SE conduction were found to be ε_{PF} ~20.57 and ε_{SE} ~5.14, respectively. The refractive

index of the CuCl hybrid film was directly measured using ellipsometry. The dielectric constant of the CuCl hybrid films deposited on silicon substrates was also deduced from the refractive index value ($\varepsilon_r=n^2$), where *n* is the refractive index. This was found to be $\varepsilon_{measured}$ ~5.92. The CuCl hybrid films used in this study typically comprise of a combination of 83% organic PSSQ and 17% inorganic CuCl by total volume. This fraction of organic PSSQ and inorganic CuCl was deduced by analyzing the scanning electron microscopy data. For illustration and comparison with the obtained experimental dielectric constant value, we refer to the well-known Maxwell-Garnett approximation [29-31]:

$$\varepsilon_{HF} = \varepsilon_1 \left(1 + \frac{3 f_{CuCl} \beta}{1 - f_{CuCl} \beta} \right) \tag{6.11}$$

and the Bruggeman self-consistent effective medium approximation [29, 30, 32]:

$$\left(1 - f_{CuCl} \beta\right) \frac{\varepsilon_1 - \varepsilon_{HF}}{\varepsilon_1 + 2\varepsilon_{HF}} + f_{CuCl} \beta \frac{\varepsilon_2 - \varepsilon_{HF}}{\varepsilon_2 + 2\varepsilon_{HF}} = 0 \tag{6.12}$$

where ε_{HF} is the dielectric constant of the hybrid films, ε_1 and ε_2 are the dielectric constants of the CuCl and PSSQ, respectively. The dielectric constant of bulk CuCl was previously reported to be in the range of 7.4 to 10 [33-35], while the dielectric constant of PSSQ is reported to be in the range of 1.9 to 6.9 [35, 36]. The dielectric constant of hybrid film estimated using equations (6.11) and (6.12) is found to be in the range 2.42 to 6.91 and 2.46 to 6.30, respectively. The dielectric constant experimental value of the hybrid film obtained by equation (6.10) is clearly well within these ranges. A comparison of dielectric constant values of the directly measured and calculated values for ε indicates that the organic-inorganic CuCl hybrid film agrees well with the Schottky emission type conduction mechanism. The conduction mechanisms for ITO/hybrid film contacts were also investigated and we find a Schottky emission type mechanism with a different barrier height of 0.75±0.05 eV.

6.5 Evaluation of electronic parameters for the Au/hybrid film/ITO structure

From the above investigation it is clear that the organic-inorganic CuCl hybrid film charge transport mechanism is predominantly a Schottky emission type conduction mechanism with the formation of an emission barrier layer between the CuCl hybrid film and the gold electrode. To evaluate the barrier height of the Au/CuCl hybrid film/ITO structure the current-voltage experimental data was fitted by equation (6.13), and the comparison between experiment and theory is shown in **Figure 6.8**.

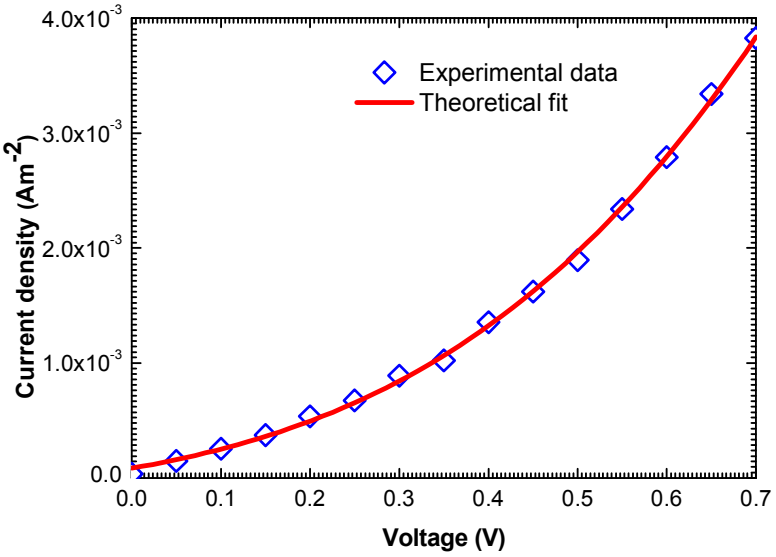

Figure 6.8: The plot of the Au/CuCl hybrid film/ITO structure forward bias current vs. applied voltage; the solid line is the theoretical fit.

Based on the fit of equation (6.13) and this experimental data the value of the barrier height was found to be 0.84±0.02 eV. In addition the full current-voltage characteristic of the structure can be analyzed by the diode equation [37]:

$$I = I_S \exp\left(\frac{qV}{nkT}\right)\left[1-\exp\left(-\frac{qV}{kT}\right)\right] \tag{6.13}$$

where V is the applied voltage, n is the ideality factor and I_S is the saturation current, which is given by [38]:

$$I_S = AA^*T^2 \exp\left(-\frac{q\phi_B}{kT}\right) \tag{6.14}$$

where A is the contact area and A^* is the Richardson constant. The saturation current is obtained from the extrapolated linear intercept with the ln (I) axis at $V=0$. The plot of ln (I) as function of applied voltage (V) for the Au/CuCl hybrid film/ITO structure is shown in **Figure 6.9**.

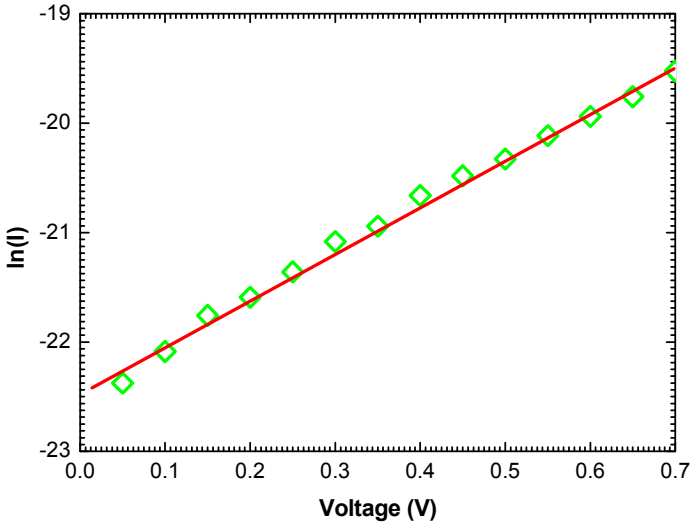

Figure 6.9: The plot of *ln (I)* vs. *V* for the Au/CuCl hybrid film/ITO structure

The barrier height of the Au/CuCl hybrid film/ITO structure was calculated using the I_S value and was found to be 0.86 eV. This value is very close to the previously calculated value of 0.84±0.02 eV.

The ideality factor of the diode structure was calculated using the following equation [39]:

$$n = \frac{q}{kT}\frac{dV}{d(\ln I)} \tag{6.16}$$

The value of the n was found to be 1.12. The deviation from the ideal *I-V* characteristics may be due to high probability of electron and hole recombination in the depletion region between the Au electrode and the hybrid film, tunneling current or the presence of an interfacial layer [40]. The most likely cause of this deviation is the presence of the interfacial oxide layer due to PSSQ, which is an oxide based material, and which suggests that the diode is not an intimate metal semiconductor (MS) contact but instead has a metal-insulator-semiconductor (MIS) configuration, and thus possesses a series resistance. The series resistance is significant in the non-

linear region of the I-V characteristics. The series resistance can be evaluated using a method developed by Cheung *et al.* to calculate the barrier height, ideality factor, and series resistance [41]. Using this work, three expressions are used:

$$\frac{dV}{d(\ln I)} = n\frac{kT}{q} + IR_S \tag{6.17}$$

$$H(I) = V - n\frac{kT}{q}\ln\left(\frac{I_S}{AA^*T^2}\right) \tag{6.18}$$

$$H(I) = IR_S + n\phi_B \tag{6.19}$$

where R_S is the series resistance.

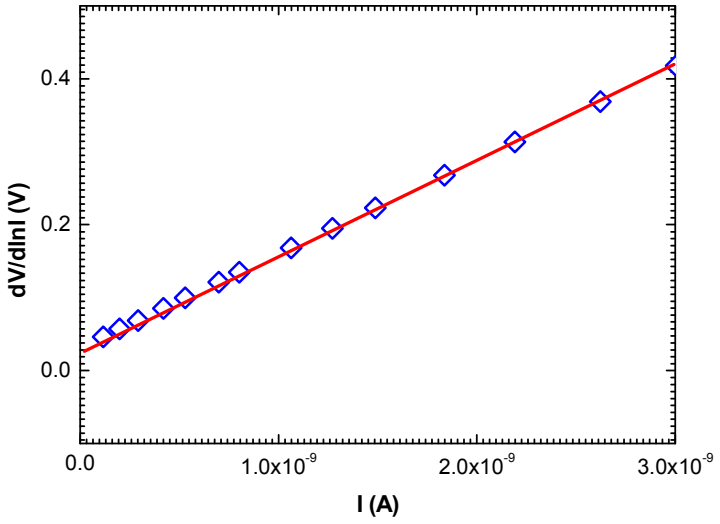

Figure 6.10: The plot of *dV/dln(I)* vs. *I* for the Au/CuCl hybrid film/ITO structure.

In **Figures 6.10** and **6.11**, experimental *dV/dln(I)* vs. *I* and *H(I)* vs. *I* plots are presented for the Au/CuCl hybrid film/ITO MIS structure, respectively. The values of R_S and *n* were determined from the slope and intercept of the *dV/dln* (*I*) vs. *I* plot and were found to be ~50 MΩ and 1.20, respectively. Using the *n* (1.12) value determined from Eq. (6.16), and the data of the forward bias *I-V* characteristics in Eq. (6.17) a plot of *H*(*I*) vs. *I* will also produce a predominantly linear characteristic (as shown in figure 6.11) whose y-axis intercept is equal to $n\phi_B$.

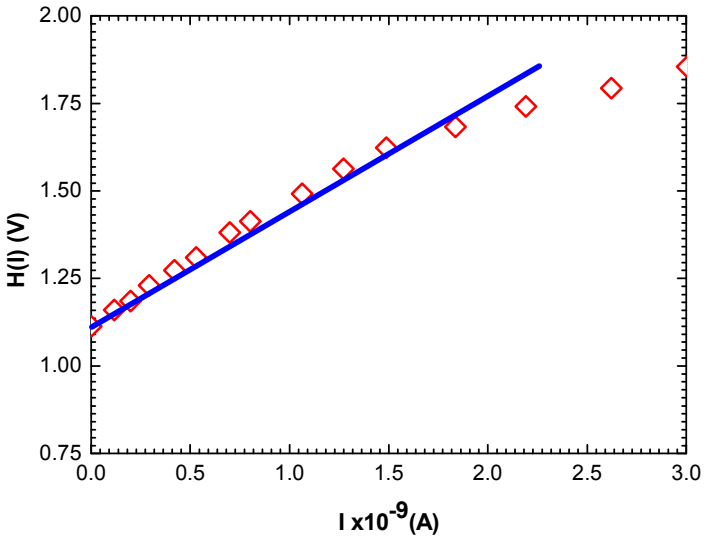

Figure 6.11: The plot of *H(I)* vs. *I* for the Au/CuCl hybrid film/ITO structure.

From this plot and using the obtained *n* (1.12) value, the values of ϕ_B and R_S we were found to be 0.89± 0.02 eV and ~48±1.5 MΩ, respectively, which is a useful check of the self-consistency of this approach.

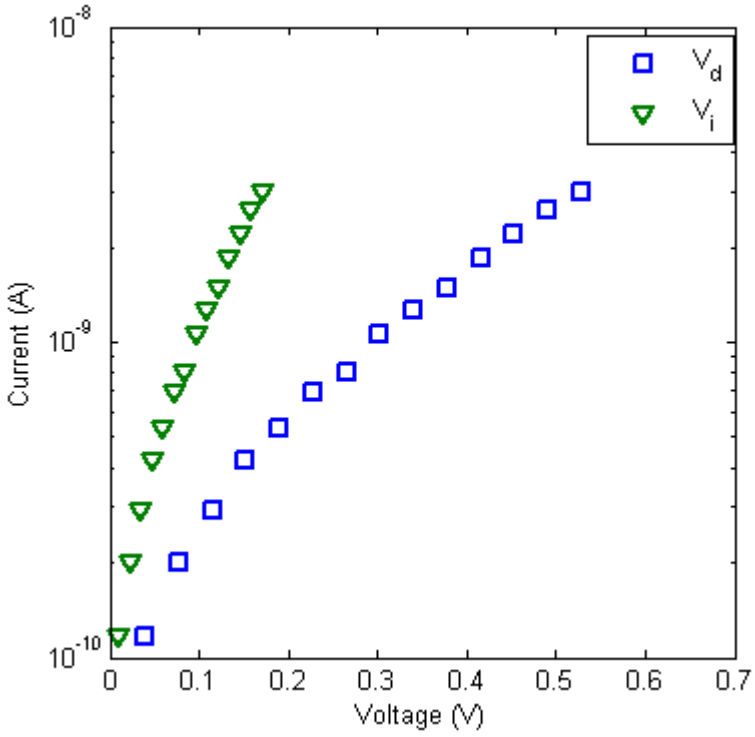

Figure 6.12: The plots of *I* vs. *V* for obtained V_d and V_i values of Au/CuCl hybrid film/ITO structure.

The presence of an interfacial layer leads to a voltage drop across this layer. The bias dependence of the voltage drop V_i across the interfacial layer between the Au electrode and the hybrid film can be expressed by [42, 43]:

$$V_i = \left(1 - \frac{1}{n}\right)V \tag{6.20}$$

Considering the effect of series resistance, equation (6.20) can be rearranged as follows:

$$V_i = \left(1 - \frac{1}{n}\right)(V - IR_S) \tag{6.21}$$

By using Eq. 6.20 the values of V_i were calculated. The voltage drop across the depletion layer between the Au and hybrid film V_d, can be determined by subtracting the voltage V_i from the total applied forward voltage V:

$$V_d = V - V_i \tag{6.22}$$

The plots of I vs. V_i, V_d, and V indicate the effect of any interfacial layer on the diode parameters and these are shown in **Figure 6.12**. From the $ln(I)$ vs. V_i plot the value of the n and ϕ_B were calculated and found to be 1.04±0.08 and 0.79±0.02 eV, respectively. These values are slightly lower than equivalent values obtained previously without considering the effect of the presence of the interfacial layer.

6.6 Voltage and Temperature Dependent Capacitance Measurements

Capacitance-voltage (C–V) and capacitance-temperature (C-T) measurements were performed for the Au/hybrid film/ITO diodes and a typical plot of C and $1/C^2$ as a function of bias voltage is shown in **Figure 6.13**. C-T measurements were carried out by applying a bias voltage of -1.0 V as shown in the inset of **Figure 6.13**. The capacitance of the sample was then monitored in the temperature range of 100 to 450 K, using a step of 3 K in free run mode. As can be seen there is an exponential relationship between the sample's capacitance and the applied temperature. From figure 11 the $1/C^2$ –V plot is linear for the bias region -2.5 V to 0.9 V. The C-V relation for a typical Schottky diode is given by [44, 45]:

$$\frac{1}{C^2} = \left(\frac{2}{q\varepsilon_s N_d A^2}\right)\left(V_{bi} - \frac{kT}{q} - V\right) \tag{6.23}$$

where $\mathcal{E}_s$ is the permittivity of the semiconductor, V is the applied voltage, A is the contact area, T is the absolute temperature, N_d is the donor concentration of the sample, and V_{bi} is the flat band voltage,.

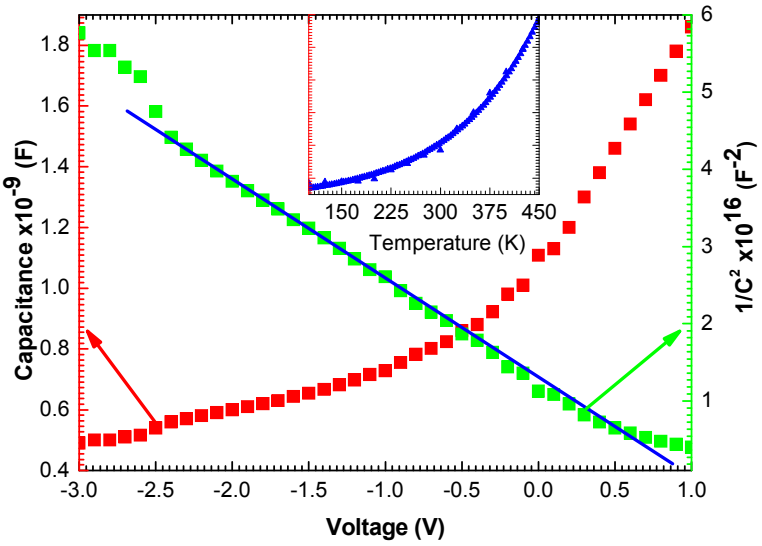

Figure 6.13: typical plots of C and $1/C^2$ versus V for the Au/hybrid film/ITO Schottky diode, inset: capacitance as a function of temperature

The x-intercept of the plot of $(1/C^2)$ versus V gives V_0 and it is related to the built in potential V_{bi} by the equation $V_{bi}=V_0+kT/q$. The donor concentration (N_d) of the sample can be calculated using [46]:

$$N_d = \frac{2dV}{q\varepsilon_s\varepsilon_o d(1/C^2)} \tag{6.24}$$

The donor concentration (N_d) for this sample is calculated to be $3.91\text{x}10^{17}$ cm^{-1}.

The barrier height $(_B)$ for the Schottky diode can be obtained from the linear extrapolation of $1/C^2$ to the voltage axis, using the following equation [46]:

$$\phi_B = V_{bi} + \frac{kT}{q}\ln\left(N_C/N_d\right) \tag{6.25}$$

where N_C is the density of states in the conduction band edge and it can be expressed by following relation [47]:

$$N_C = 2\left(2\pi m^* kT / h^2\right)^{3/2} \tag{6.26}$$

where $m^* = 2.3m_o$ is the effective electron mass for CuCl, and k is Boltzmann's constant, h is Planck's constant, and its value works out to be $N_C=8.73x10^{19}$ for hybrid film. From the *C-V* plot and using equation (6.25) the barrier height of Au/hybrid film/ITO Schottky diode estimated to be 1.05±0.05 eV. The barrier height obtained from the *C-V* measurement is somewhat larger than the value obtained from *I-V* ($\phi_B \approx 0.79$ eV). The barrier heights obtained from the *I-V* measurement are more meaningful for assessing the diode performance as the interface traps neither respond to applied ac signals nor contribute to capacitance at higher frequencies [46, 48]. For the case of the larger barrier height obtained from *C-V* measurements we can attributed this to interface states of an intervening insulator layer, contamination in the interfaces, fixed surface polarization charges, deep impurity levels and edge leakage currents these having been reported by other researchers [46, 49].

6.7 Interface state density properties of the Au/CuCl hybrid film/ITO Schottky diode

The value of an ideality factor $n>1$ is typically due to a voltage drop across an interfacial layer of the diode. When this layer is sufficiently thick and the transmission probability between the metal and the interface states is very small, the barrier height is shifted and this can be expressed as [50]:

$$\Delta\phi_e = \phi_e - \phi_B = \left(1 - \frac{1}{n}\right)\left(V - IR_S\right) \tag{6.27}$$

for forward bias, n is given by

$$n = \left(1 + \frac{q^2 N_{SS}\delta}{\varepsilon_i}\right) \tag{6.28}$$

where ϕ_e is the bias dependent effective barrier height due to the presence of the interfacial layer, δ is the thickness of the interfacial layer, ε_i is the dielectric constant of the interfacial layer and N_{SS} is the density of the interface state and interface states located at the interfacial layer-semiconductor interface. The ideality factor and the effective barrier height dependence on applied voltage are expressed as [39]:

$$n(V) = \frac{qV}{kT \ln\left(\frac{I}{I_S}\right)} \tag{6.29}$$

$$\frac{d\phi_e}{dV} = 1 - \frac{1}{n(V)} \tag{6.30}$$

For p-type semiconductors, the energy of the interface states E_{SS} with respect to the top of the valance band at the surface of the semiconductor can be expressed as [51, 52]:

$$E_{SS} - E_V = q(\phi_e - V) \tag{6.31}$$

Thus, we can use Eqs. (6.29) and (6.30) together with Eq. (6.27) to calculate the interface state density distribution. In order to calculate the N_{SS} values of the diode, n values were calculated for different voltages from Eq. (6.28).

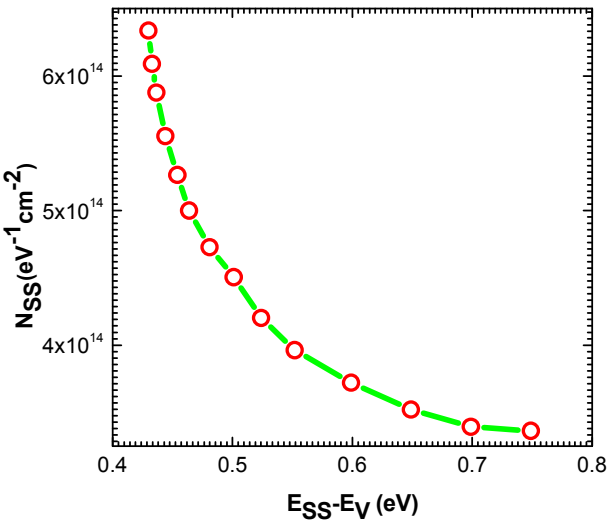

Figure 6.14: Calculated interface state energy distribution of the Au/CuCl hybrid film/ITO Schottky diode

Thus using these n values and the other parameters of the diode $\delta \approx 3.5$ nm and (the organic part of our hybrid film is closely related to SiO_2, thus the interfacial layer dielectric constant should be close to the SiO_2, and as an approximation we consider the dielectric constant value =3.9) $\varepsilon_i = 3.9$ in Eqs. (6.27, 6.28) [53]. Thus using these n values and other parameters of the diode ($\delta = 2$ nm and $\varepsilon_i = 4\ \varepsilon_o$) [54] in Eq. (6.28), we estimate the values of N_{SS}. The variation of N_{SS} with E_{SS} -E_V is shown in **Figure**

6.14. The values of N_{SS} decrease with increasing E_{SS} -E_V values and the density distribution of the interface states changes from ~ 6.3 x10^{14} to ~3.4x10^{14} $eV^{-1}cm^{-1}$, whose values are of the same order of magnitude as reported for e.g. a Al/MEH-PPV/p-Si Schottky diode [55]. The hybrid film behaves as a single semiconducting material having an effective single electronic band structure. We propose a simple energy level diagram for the fabricated diode devices, with the assumption a PSSQ band gap energy being similar to the SiO_2 energy gap as shown in **Figure 6.15** [56-58].

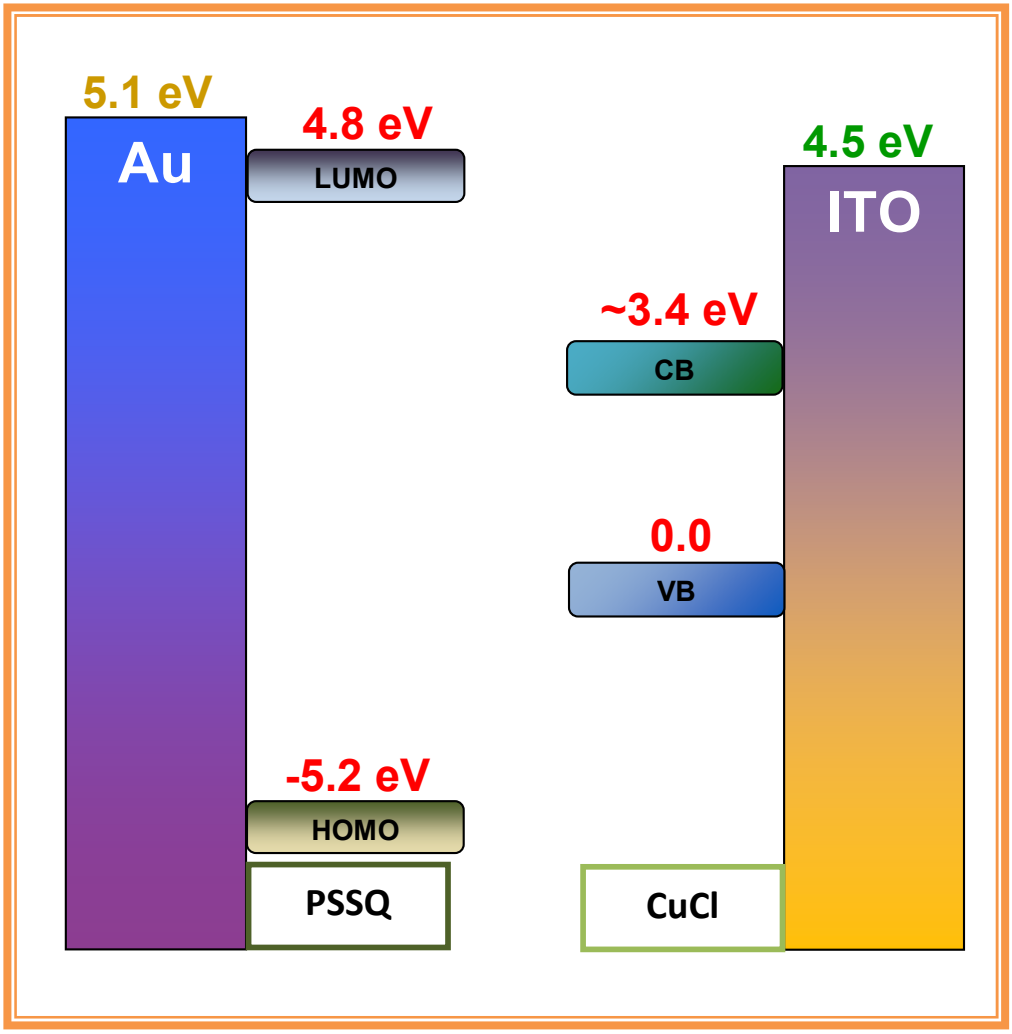

Figure 6.15: Schematic energy level diagram for the Au/CuCl hybrid film/ITO Schottky diode

6.8 Electroluminescence (EL)

For the metal-semiconductor-metal structure, light emission most likely occurs through hot-electron impact excitation of electron-hole pairs. A test electroluminescence device (ELD) based on the organic-inorganic CuCl hybrid film was designed in our laboratory. In order to fabricate the EL device, organic-inorganic CuCl hybrid films with typical layer thicknesses of ~300 nm were deposited on indium tin oxide (ITO) coated glass substrates by the spin coating method. As usual, the films were subsequently heated at 120^{o}C for durations of 18 hours *in vacuo*. Non-transparent gold (≈150 nm thick) contact pads were deposited on the CuCl hybrid layer using the vacuum evaporation technique at a base pressure of ~1x10^{-6} mbar. A cross-sectional view of the ELD test structure is shown in **Figure 6.16**.

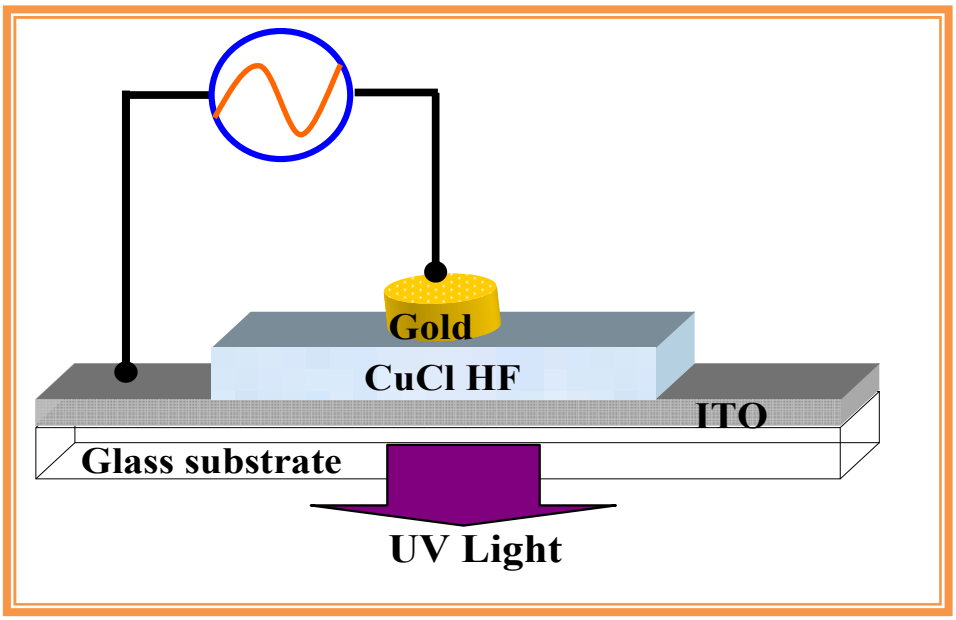

Figure 6.16: Schematic diagram of the CuCl hybrid electroluminescent device

To maximize the electric field in the active layer, the insulator should have a high dielectric constant and sufficient electric field strength to avoid breakdown [59]. In this device, the CuCl nanocrystals were embedded into the insulating PSSQ organic matrix. The electric field in the active layer can be estimated by the following equation [59]:

$$E_L = \frac{\varepsilon_i}{\varepsilon_i d_L + \varepsilon_L d_i} V_{tot} \approx \frac{\varepsilon_{PSSQ}}{\varepsilon_{HF} d_{HF}} V_{tot} \tag{6.32}$$

where ε_i and ε_L represent the insulator and the luminescent layer dielectric constant, respectively. ε_{PSSQ} and ε_{HF} is the dielectric constant of the PSSQ and CuCl hybrid film, respectively, and d is the hybrid film thickness.

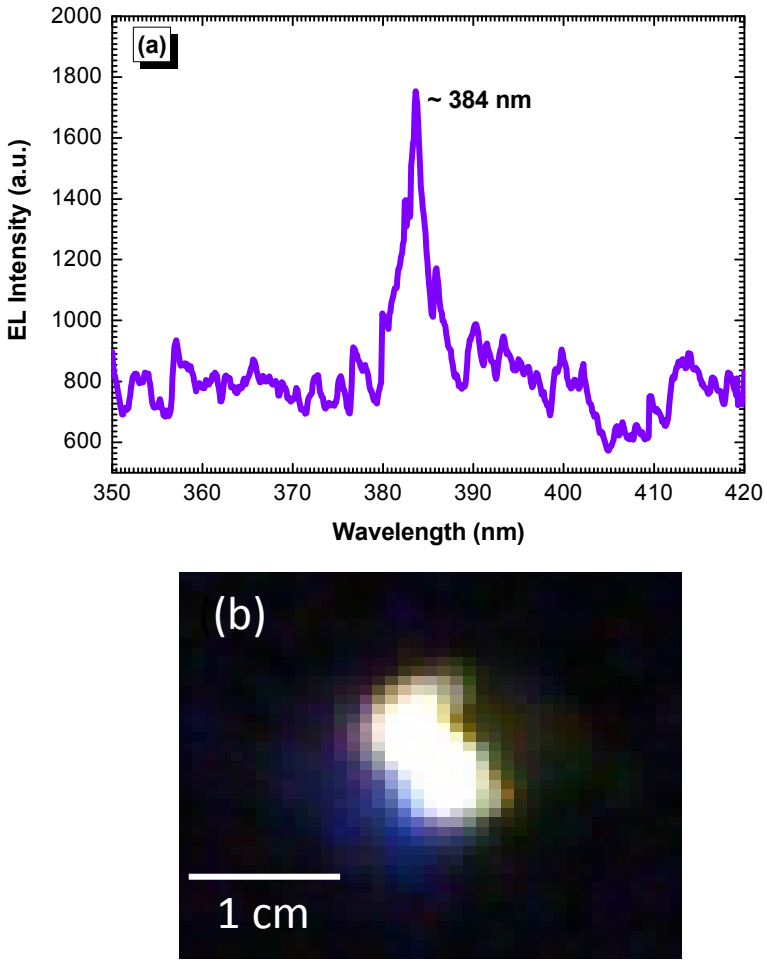

Figure 6.17: Average room temperature EL spectrum of 5 CuCl hybrid EL devices were biased with a 100 V AC (a) and a micrograph of the EL emission (b)

Using the dielectric constant value for CuCl hybrid film ($\varepsilon_{HF} \approx 5.14$) [60] and for PSSQ ($\varepsilon_{PSSQ} \approx 2.7$) [61] the electric field for the device is estimated to be 1.22- 2.27 $MVcm^{-1}$ for applied voltages in the range of 70-130 V. Due to these high electric fields, the injected electrons quickly accelerate to high energies resulting in light

emission through hot-electron impact excitation of electron-hole pairs. The electroluminescence measurements of the test devices were evaluated using a SOFIE spectrophotometer with a photomultiplier tube (spectral range of 200–900 nm). The ELD device was driven by an AC sinusoidal waveform with a frequency of 60 Hz and a peak-to-peak voltage of 70-130 V. The Au top electrode was non-transparent and electroluminescence (EL) emission was observed principally through the transparent ITO coated glass. **Figure 6.17** shows the average EL spectrum obtained from five CuCl hybrid electroluminescent devices. In the spectrum an optimal peak attributed to the Z_3 free exciton emission at 384 nm ($E \approx 3.22$ eV) is observed when the device was biased with a 100 V AC, 60 Hz supply. EL was observed for AC peak to peak voltages in the range 70-130 V. The EL of the hybrid films is in excellent agreement with the values reported for vacuum evaporated CuCl films on silicon [62]. The EL emission from the CuCl hybrid film based electroluminescent device is not continuous, i.e. the light emission stays on for ≈5-20 sec and then switches off for ≈10-15 sec. This repeatable behaviour was observed to last for ≈30 minutes. The EL emission from the CuCl hybrid film based electroluminescent device (ELD) blinks on and off. Light emission occurs for ≈5-20 sec and then switches off for ≈10-15 sec. This repeatable behaviour was observed to last for ≈30 minutes, and the blinking process may be due to the presence of extra electrical charges in a nanocrystals[63].

Summary

The electrical properties of organic PSSQ-inorganic CuCl hybrid films were characterized using room temperature current-voltage and capacitance-voltage and temperature dependent conductance and capacitance measurements. The hole conductivity was deduced for the CuCl hybrid film to be ~5.54×10^{-9} Scm^{-1}. Activation energes for conductivity of the CuCl hybrid films extracted from Arrhenius plots in the temperature ranges 80-200 K and 225-350 K range have been found to be 0.026 eV and 0.158 eV, respectively. At low fields the current-voltage characteristics exhibit ohmic conduction. By comparing the film properties (dielectric constant) obtained from theoretical and experimental data, high field conduction for E >$1.5x10^{6}$ Vm^{-1} was shown to be an electrode limited Schottky emission type conduction. The electronic parameters were evaluated and the values of barrier height, ideality factor and the series resistance for Au/hybrid film/ITO diodes were found to be 0.84±0.05 eV and 1.12±0.8 and 50±2 MΩ, respectively, whereas the barrier height obtained from C-V measurement was 1.05±0.05 eV. This value was higher than the value obtained from I-V measurement. This difference is most likely caused by the presence of a thin intervening insulating layer between the hybrid film surface and the Schottky metal. The values of N_{SS} decrease with increasing E_{SS} -E_V values and the density distribution of the interface states changes from ~$6.2\ x10^{14}$ to ~$3.3x10^{14}$ $eV^{-1}cm^{-1}$. We confirm that the hybrid film behaves as a single semiconducting material having the single electronic band structure.

Room temperature electroluminescence measurements of test ELD devices based on the Au/CuCl HF/ITO structure produce measurable emission which is attributed to Z_3 free exciton emission at 384 nm (E ≈ 3.229 eV) when the device was biased with a ~100 V AC, 60 Hz supply. This emission peak corresponds well with the Z_3 free excitonic emission which was also seen in the room temperature PL and UV-Vis absorption measurements. The EL emission from the CuCl hybrid film based electroluminescent device (ELD) shows a blinking behaviour on a timescale of many seconds.

References

[1] D.Y. Godovsky; Advances in polymer science **153** (2000) 166

[2] W. P. Su, J. R. Schreiffer, A. J. Heeger; phys Rev B **224** (1980) 2099

[3] L. S. Roman, W. Mammo, L. A. Pettersson, M. R. Andersson, O. Inganäs; Adv Mater **10** (1998) 774

[4] L. J. Huijbregts; PhD thesis "Charge transport and morphology in nanofillers and polymer nanocomposites" Eindhoven University of Technology, Netherlands (2008) 02

[5] E. K. Sichel, Carbon black-polymer composites, Marcel Dekker, inc., New York (1982)

[6] R. Schueler, J. Petermann, K. Schulte, and H. P. Wentzel, J. Appl. Polym. Sci. **63** (1997) 1741

[7] G. Wu, T. Miura, S. Asai, and M. Sumita, Polymer **42** (2001) 3271

[8] R. Taipalus, T. Harmia, M. Q. Zhang, and K. Friedrich, Composites Sci. Tech. **61** (2001) 801

[9] R. Nat; PhD thesis, "Detailed investigation of the charge storage in size-controlled Si nanocrystals" Martin-Luther-University Halle-Wittenberg, (2006) 27

[10] A. V. Joshi and J. B. Jr. Wagner; J. Electro-chem. Soc. **122** (1975) 1071

[11] J. B. Wagner and C. Wagner; J. Chem. Phys. **26** (1957) 1597

[12] A. V. Joshi and J. B. Jr Wagner; J. Electrochem Soc. **122** (1975) 1071

[13] J. B. Wagner and C. Wagner; J. Chem. Phys. **26** (1957) 1597

[14] F. O. Lucas, A. Mitra, P. J. McNally, S. Daniels, A. L. Bradley, D M Taylor, Y. Y. Proskuryakov, K. Durose, D. C. Cameron; J. Phys D: Appl. Phys. **40** (2007) 3461

[15] R. Pal; J. Composite Materials **41** (2007) 2499

[16] J. C. Maxwell; A Treatise on Electricity and Magnetism, Clarendon Press, Oxford 2nd Edn **1** (1881) 435

[17] D. A. G. Bruggeman; Ann. Phys. (Leipzig) **24** (1935) 636

[18] J. V. Masi; IEEE 0-941783-23-5/03 (2003) 199

[19] J. V. Manca, W. Wondrak, K. Croes, W. D. Ceuninck, V. D. Hacger, L. D. Schcpper, L. Tielemans; IEEE (1999) 0-7803-5795-71490

[20] R. Y. Borse, A. S. Garde; Electrical and Gas Sensing Properties of SnO2 Thick Film Resistors Prepared by Screen-printing Method, Sensors & Transducers **97** (2008) 64

[21] N. K. Pandey; Sensors & Transducers

[22] P. A. Anderson; Physical Review **115** (1959) 553

[23] Y. Park, V. Choong, Y. Gao, B. R. Hsieh, C. W. Tang; Appl. Phys. Lett. **68** (1996) 2699

[24] P. R. Emtage and W. Tantraporn; Physial Review Letters **8** (1962) 267

[25] S. Gaddipati, M. Mansouri, S. Jeedingunta, A. Kumar, Y. L. Chiou; ECS Transactions **25** (2006) 117

[26] L. Maissel, R. Glang; Handbook of Thin Film Technology, McGraw-Hill, New York (1970)

[27] S. M. Sze; Physics of Semiconductor Devices, 2nd ed., Wiley: New York (1981)

[28] G. Natarajan, R. T. Rajendra Kumar, S. Daniels, D. C. Cameron and P. J. McNally; J. Mater Sci: Mater Electron **19** (2008) 103

[29] C. W. Nan; Prog Mater Sci. **37** (1993) 1

[30] C. W. Nan; Phys. Rev. B **63** (2001) 17620

[31] Z. M. Dang, Y. Shen, C. W. Nan; Applied Physics Letters **81** (2002) 4814

[32] D. A. G. Bruggeman; Ann. Phys. (Leipzig) **24** (1935) 636

[33] S. Roberts; Phys. Rev. **76** (1949) 1215

[34] J. E. Potts, R. C. Hanson, C. T. Walker, C. Schwab; Phys. Rev. B **9** (1974) 2711

[35] J. H. Lee, J. Rhee, J. Kim, J. H. Yim, S. Chang; Mat. Res. Soc. Symp. Proc. **766** (2003) E8.3.1

[36] F. O. Lucas, L. O'Reilly, G. Natarajan, P. J. McNally, S. Daniels, D. M. Taylor, S. William, D. C. Cameron, A. L. Bradley, A. Miltra; J. Crystal Growth **287** (2006) 112

[37] E. H. Rhoderick, R. H. Williams; Metal Semiconductor Contacts, 2nd ed. Oxford University Press: Oxford (1988) 39

[38] M. Ferhata, A. Zaouia, M. Certierb, J. P. Dufourc, B. Khelifa; Materials Science and Engineering B **39** (1996) 95

[39] F. Yakuphanogle; J. Phys. Chem. C **111** (2007) 1505

[40] M. Campos, L. O. S. Bulhoes, C. A. Lindino; Sens. Actuators **87** (2000) 67

[41] S. K. Cheung, N. W. Cheung; Appl. Phys. Lett. **49** (1986) 85

[42] P. Chattopadhyay; Solid-State Electron **37** (1994) 1759

[43] C. Y. Wu; J. Appl. Phys. **51** (1980) 786

[44] E. H. Rhoderick and R. H. Williams, "Metal-Semiconductor Contacts," 2nd Edition, Clarendon Press, Oxford, (1988)

[45] S. M. Sze, "Physics of Semiconductor Devices", 2nd Edition, John Wiley and Sons, New York, (1981)

[46] S. M.Faraz, H. Ashraf, M. I. Arshad, P. R. Hageman, M. Asghar and Q. Wahab; Semicond Sci. Technol. **25** (2010) 095008

[47] D. S. Reddy, M. B. Reddy, N. N. K. Reddy, V. R. Reddy; Journal of Modern Physics **2** (2011) 113

[48] D. K. Schroder; Semiconductor Material and Device Characterization 3rd Ed. New York: Wiley-Interscience (2007)

[49] J. Pedrös, R. Cuerdo, R. Lossy, N. Chaturvedi, J. Würfl and F. Calle; Phys. Status Solidi (C) **3** (2006) 1709

[50] A. Türüt, B. Batı, A. Kökçe, M. Sağlam, N. Yalçin; Phys. Scripta **53** (1996) 118

[51] S. Pandey, S. Kal; Solid State Electron **42** (1998) 943

[52] M. E. Aydin, K. Akkiliç, T. Kiliçoğlu; Applied Surface Science **253** (2006) 1304

[53] P. R. Gray, P. J. Hurst, S. H. Lewis, R. G. Meyer; Analysis and Design of Analog Integrated Circuits (Fifth ed.), New York: Wiley (2009) 40

[54] E. H. Rhoderick, R. H. Williams; Metal Semiconductor Contacts, 2nd ed. Oxford University Press: Oxford, (1988) 28

[55] M. E. Aydin, F. Yakuphanoglu, J. H. Eom, D. H. Hwang; Physica B **387** (2007) 239

[56] A. Appleton, T. Chiranjivi, and M. J. Ghazvini; The Physics of SiO_2 and its Interfaces, New York (1978) 94

[57] T. Suzuki, M. Hirano, H. Hosono; J. Applied Physics **91** (2002) 4149

[58] F. J. Himpsel, F. R. McFeely, A. T. Ibrahimi, J. A. Yarmoff, G. Hollinger; Phys Rev B **38** (1988) 6084

[59] P. D. Rack, P.H. Holloway; Materials Science and Engineering, **R21** (1998) 171

[60] M. M. Alam, S. Daniels and P. J. McNally; Semiconductor Science and Technology SST/383581/PAP/236002

[61] J. H. Lee, J. Rhee, J. Kim, J. H. Yim, S. Chang; Mat. Res. Soc. Symp. Proc. **766** (2003) E8.3.1

[62] L. O'Reilly, O. F. Lucas, P. J. McNally, and A. Reader, G. Natarajan, S. Daniels, and D. C. Cameron, A. Mitra, M. Martinez-Rosas, and A. L. Bradley; J App Phys **98** (2005) 113512

[63 O. Graydon; Nature Photonics **3** (2009) 380

CHAPTER 7

AGEING EFFECTS

CuCl thin films deposited without a capping layer are not stable in ambient conditions. Since nanocrystalline CuCl hybrid films are a combination of organic and inorganic compounds it is necessary to know the impact of ambient atmospheric ageing effects on these newly developed hybrid films. In this chapter we present data on the impact of ambient atmospheric ageing effects on nanocrystalline CuCl hybrid films which have been investigated by X-ray diffraction, FTIR, UV-Vis, PL and EL spectroscopy.

7.1 Introduction

One challenge linked with the use of CuCl is that it is sensitive to moist air, i.e. CuCl is not stable in ambient conditions; it forms oxyhalides of Cu(II) within a few hours or days of exposure to air. Therefore the use of CuCl in large scale applications may be limited. In hybrid materials, it is possible to combine organics and inorganics in a nano-composite [1-9]. Most of the organic materials are stable in ambient atmosphere, so the incorporated inorganic materials may show improve abrasion resistance, chemical resistance, adhesion and other enhanced properties [5-9]. The most common and simple process employed to obtain organic-inorganic hybrid materials is sol-gel deposition, which allows the incorporation of inorganic domains into a polymer matrix [10]. There are two approaches in preparing these: (i) inorganic molecules can be just embedded into an organic material and (ii) the organic and inorganic groupings can be linked by stable chemical bonds [11]. In this study we have investigated the use of spin-coated organic-inorganic CuCl hybrid films as possible materials for optoelectronic applications. As usual the optimal CuCl hybrid films typical thickness ≈300 nm were deposited on variety of substrate including glass, indium tin oxide (ITO) coated glass and silicon substrates, and subsequently heated at 120^{o}C for 18 hours *in vacuo*. The CuCl hybrid films were kept in open ambient atmospheric conditions to observe any ageing effects. The impact of atmospheric ageing effects on nanocrystalline CuCl hybrid films is important for electroluminescence device fabrication as optimal properties must not deteriorate for typical device working lifetimes i.e. months to years.

7.2 X-ray Diffraction Spectra

Figure 7.1 shows the room temperature θ-2θ X-ray diffraction spectra of as deposited (ASD) nanocrystalline CuCl hybrid films and for films exposed to atmosphere for periods of 1 to 6 months, these having been deposited on glass substrates.

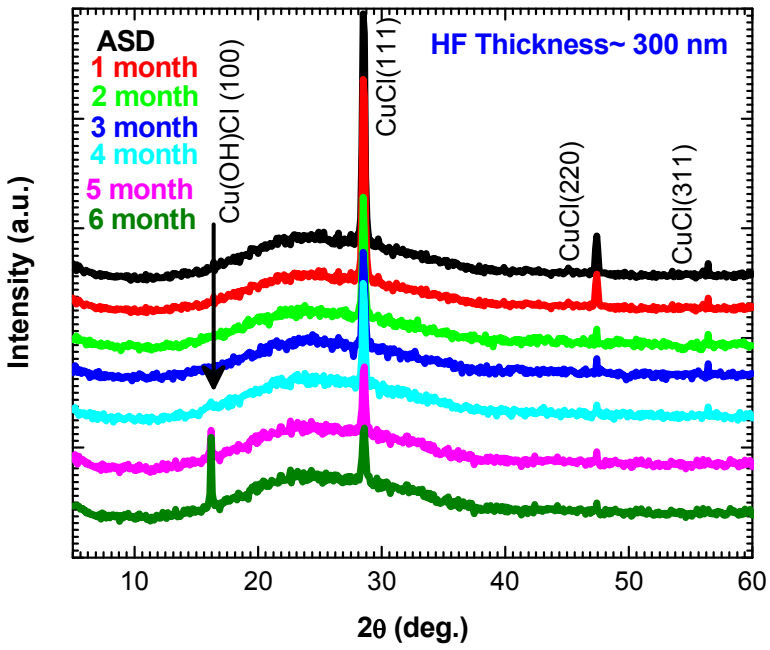

Figure 7.1: θ-2θ XRD spectra of CuCl hybrid films deposited on glass substrates.

In these spectra, the ASD films show three different peaks at 2θ ≈28.51°, 47.44° and 56.27°, which correspond to (111), (220) and (311) crystal plane orientations of cubic phase γ-CuCl [12, 13]. The observations are: (i) for samples aged up to four months there is no significant change in peak intensity and FWHM of all peaks. (ii) for the five month aged sample, the (111) peak position shifts slightly from 2θ ≈28.5° to 28.6°, which may be due to absorbed moisture (iii) for the five and six months aged samples, the (311) CuCl peak disappears and a new peak appears at 2θ≈15.95°, which corresponds to Cu(OH)Cl (100) and this peak intensity is now relatively higher than CuCl (111) peak [14]. This is most likely due to moisture absorption and FTIR spectroscopy measurements provide corroborative evidence, which will be discussed shortly.

7.3 Fourier Transform Infrared (FTIR) Spectra

Figure 7.2 shows FTIR spectra of the same ASD and CuCl hybrid films on Si aged for 1–6 months. The strong absorption peak at 1050 cm^{-1} for as-deposited and annealed films occurring in the 1000–1100 cm^{-1} band may be attributed to the asymmetric Si–O–Si stretching vibrations of the Si–O functional group present in the PSSQ emulsion. The absorption at ~1050 cm^{-1} is most likely due to linear small-chain siloxanes and at ~1085 cm^{-1} due to long-chain polymers [15, 16].

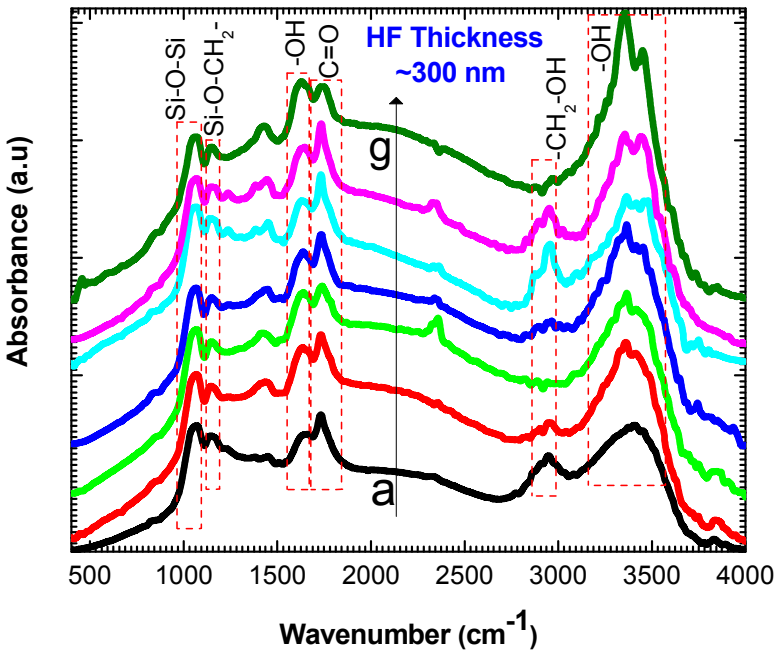

Figure 7.2: FTIR absorption spectra of CuCl hybrid films deposited on silicon substrates.

The weak absorption peak at ~1630 cm^{-1} may be assigned to the bending vibration of the O–H group of absorbed water, which may be due to the use of water as a solvent [17, 18]. The small absorption around 1620–1680 cm^{-1} can be assigned to alkenyl C=C stretching of the C=C functional group [19]. A medium intense absorption at 1737 cm^{-1} in the band 1735–1785 cm^{-1} is assigned to the C=O stretch of aryl and unsaturated diacyl peroxides, which may be due to $C_6H_{12}O_6$ [20]. The weak absorption at 2910 cm^{-1} in the band 2840–2935 cm^{-1} may be attributed to symmetric CH_2 stretch vibrating in the primary alcohol $–CH_2–OH$ group this being present in

both PSSQ and $C_6H_{12}O_6$ [21]. The broad and strong absorption centered at 3375 cm^{-1} can be assigned to the hydrogen bonds of the O–H stretch vibration, which may be due to H_2O or the PSSQ solution [19]. In this FTIR spectroscopy analysis we observed that for up to four months there was no significant change in the IR absorption. For six month aged samples the O–H absorption peak intensity is significantly enhanced which is most likely due to moisture absorption. These data are consistent with the XRD data in the previous section and confirm the integrity of the hybrid film system for periods of at least up to 4 months.

7.4 UV-Vis Spectra

The absorption spectrum of as deposited and 1-6 month aged hybrid films are shown in **Figure 7.3**. For all aged films, the absorption peaks attributed to $Z_{1,2}$ and Z_3 excitons are observed. The absorption spectra of the samples aged for up to four months showed no degradation, whereas uncapped pure CuCl thin films degrade within a few days [22].

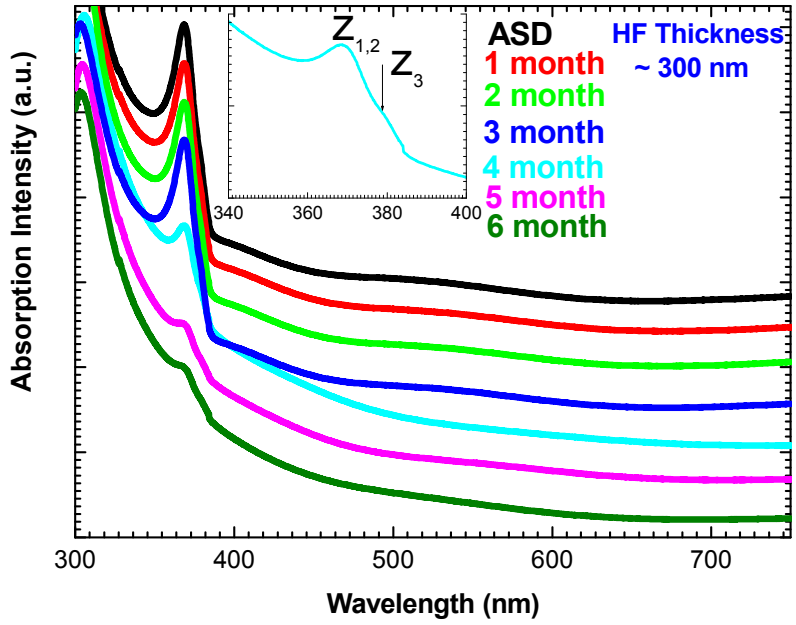

Figure 7.3: UV-Vis absorption spectra of the ASD and 1-6 month aged CuCl hybrid films deposited on glass substrates.

7.5 Photoluminescence Spectra

The impacts of atmospheric ageing (1-6 month) effects on the photoluminescence of nanocrystalline CuCl hybrid films were investigated and the obtained data was compared with the as-deposited films.

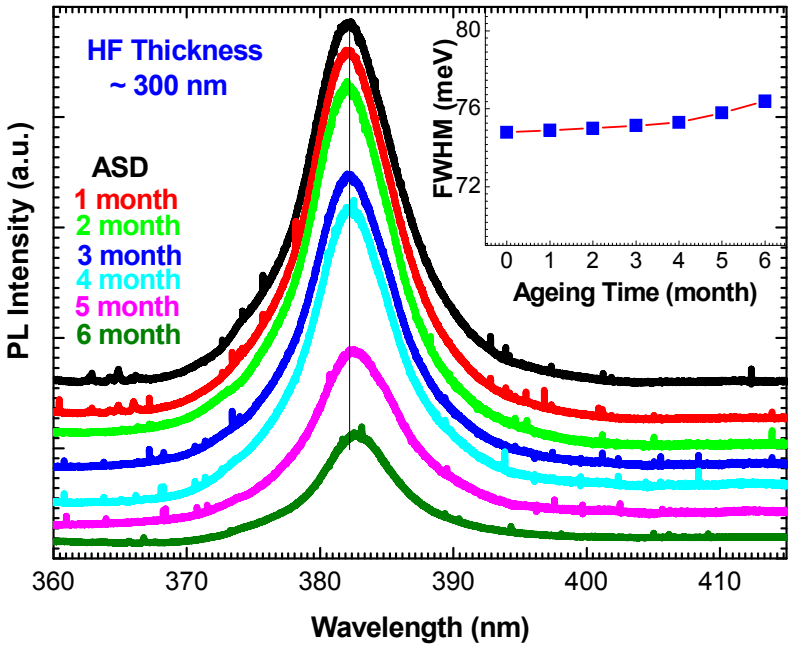

Figure 7.4: Room temperature PL emission spectra of CuCl hybrid films deposited on silicon substrates, inset variation of FWHM with ageing time.

Figure 7.4 shows the room temperature photoluminescence spectra of ASD and 1-6 month aged nanocrystalline CuCl hybrid films. Across the timescale of the ageing tests, all samples continued to show the Z_3 free exciton emission peak centered at ≈382 nm (E_g≈ 3.26 eV). For up to four months aging the free exciton emission peak position, FWHM and intensity is remain almost constant compared to the ASD film. However, after that the peak position is slightly redshifted and the FWHM slightly increases, whereas the peak intensity change is significant. The PL spectroscopy measurements confirm that nanocrystalline CuCl hybrid films are more stable than other CuCl film materials systems [22]. Hybrid film integrity can be maintained for periods of at least 4 months.

7.6 Electroluminescence

The impact of atmospheric ageing effect on electroluminescence for the CuCl hybrid film based electroluminescence device (ELD) was also investigated. The fabrication of CuCl hybrid film based EL device is described in detail in section 6.8. The ELD device was kept in the open atmospheric condition for three months.

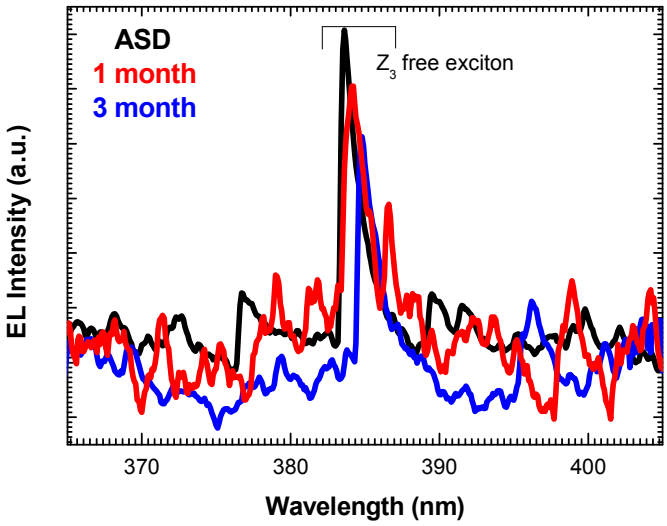

Figure 7.5: Room temperature EL spectrum of the ASD and 1-3 month aged CuCl hybrid film ELD.

The ELD device was driven by the usual AC sinusoidal waveform with a frequency of 60 Hz and a peak-to-peak voltage of 70-130 V. The Au top electrode was non-transparent and electroluminescence (EL) emission was observed principally through the transparent ITO coated glass. **Figure 7.5** shows the EL spectra obtained from CuCl hybrid electroluminescent devices of ASD and aged in ambient conditions for 1-3 months. The EL emission is easily observed when the device was biased with a 100 V AC, 60 Hz supply which was used as a reference. The EL peak attributed to the Z_3 free exciton emission at ≈383 nm (E ≈3.237 eV), ≈383.5 nm (E ≈3.233 eV) and ≈384 nm (E ≈3.23 eV) for ASD, 1 and 3 month aged devices, respectively. This device EL emission is nearly identical in intensity and wavelength to the fresh device EL emission, which confirms that the EL device based on a CuCl hybrid film, is more stable than other previously reported CuCl based EL devices [12].

Summary

The impacts of atmospheric ageing effects on spin coated organic-inorganic nanocrystalline CuCl hybrid films and ELDs was investigated and by XRD, UV-Vis, FTIR, PL and EL spectroscopy. For samples aged up to four months, little or no change is observed in all measurements. After that, some degradation was observed which is attributed to moisture absorption. CuCl is very hydroscopic but in the hybrid films this process is retarded and electronic and optical properties remain unperturbed for up to 4 months without any extra capping layer. It is clear that the hybrid film is more stable than vacuum or sputter deposited CuCl thin films for optoelectronic applications. This study indicates that the blend of CuCl with a matrix material such as PSSQ may be a step towards long term elimination of the degradation of CuCl films.

References

[1] R. M. Laine, C. Sanchez, C. J. Brinker, E. Giannelis; MRS Bull **628** (2000)

[2] C. Sanchez, B. Lebeau; MRS Bull **26** (2001) 377

[3] T. Ogoshi, H. Itoh, K. M. Kim, Y. Chujo; Macromolecules **35** (2002) 334

[4] C. Sanchez, F. Ribot; New J. Chem. **18** (1994) 1007

[5] S. Choi, B. Youngchu, D. Sunhwang, S.Goolee, W. Hopark, J. Kyoopark; Thin Solid Films **477** (2005) 233

[6] K.Yamamoto, H. Otsuka, S. Wada, D. Sohn, A. Takahara; Polymer **46** (2005) 12386

[7] Q. Yua, M. Shia, M. Deng, M. Wang, H. Chen; Materials Science and Engineering B **150** (2008) 70

[8] P. Viswanathamurthi, N. Bhattarai, C. K. Kim, H. Y. Kim, D. R. Lee; Inorganic Chemistry Communications **7** (2004) 679

[9] A. Tarek, T. Hajime, T.Tsutomu; Polymer **45** (2004) 7903

[10] A. D. Pomogailo; Russ Chem. Rev. **69** (2000) 53

[11] U. Schubert, N. Husing, and A. Lorenz; Chem. Mater. **7** (1995) 2010

[12] L. O'Reilly, O. F. Lucas, P. J. McNally, and A. Reader, Gomathi Natarajan, S. Daniels, and D. C. Cameron, A. Mitra, M. Martinez-Rosas, and A. L. Bradley, J App Phys **98** (2005) 113512

[13] F.O. Lucas, A. Mitra, P J McNally, S Daniels, AL Bradley, D M Taylor, Y Y Proskur Yakov, K Durose, D C Cameron, J. Phys D: Appl. Phys. **40** (2007) 3461

[14] Diffract plus-PDFMint-[JCP2.2CA:23-1063]

[15] G. Socrates; Infrared and Raman Characteristic Group Frequencies table and charts, Wiley, 3rd Ed. (2001) 245

[16] W. Noll; Angew Chem. Int. Ed. Engl. **2** (1963) 73

[17] Judeinstein P, Morineau R, Livage; J. Solid State Ionics **51** (1992) 239

[18] Kirm I, Medina F, Rodriguez X, Cesteros Y, Salagre P, Sueiras; J. Appl. Catal. A: Gen **272** (2004) 175

[19] J. Coates; Interpretation of infrared spectra, a practical approach, in: R. A. Meyers (Ed.), Encyclopedia of Analytical Chemistry (2000) 1815

[20] G. Socrates; Infrared and Raman Characteristic Group Frequencies table and charts, Wiley, 3rd Ed. (2001) 105

[21] G. Socrates; Infrared and Raman Characteristic Group Frequencies table and charts, Wiley, 3rd Ed. (2001) 96

[22] F. O. Lucas, L.O. Reilly, G. Natarajan, P. J. McNally, S. Daniels, D. M. Taylor, S. Williamc, D. C. Cameron, A. L. Bradley, A. Miltra; J. Cryst. Growth **287** (2006) 112

CHAPTER 8

HETEROJUNCTION DIODE STRUCTURE

This chapter presents preliminary data on results of structural, optical and electrical studies into the fabrication of a n-ZnO/p-CuCl heterojunction structure using XRD, UV-Vis, PL and I-V characterization to fabricate a p-n junction based light emitting or detecting diode.

8.1 Introduction

Due to the blinking phenomenon of EL emission from the electroluminescent device based on nanocrystalline CuCl hybrid film, we focused on the fabrication of a p-n junction based light emitting diode. CuCl is a p-type semiconductor material and n-type CuCl is not readily available. On the other hand ZnO is a naturally n-type semiconductor material with a similar bandgap to CuCl, therefore we consider ZnO as the n-type material for the test heterojunction diode fabrication. Zinc Oxide (ZnO) is a wide band gap semiconductor material that is showing much promise for applications in photodetectors, light emitting diodes, solar cells, lasers, etc. [1-8]. To date ZnO homojunction based LED fabrication failed due to the lack of high quality p-doped ZnO. Consequently, most research concentrates on heterojunction LEDs, e.g. polycrystalline n-ZnO thin films grown on single crystal p-GaN substrates since the possess similar bandgap, lattice mismatch and have near identical wurtzite crystal structures [9-13]. Since p-doped ZnO is not readily available we considered the fabrication of an alternative heterostructure.

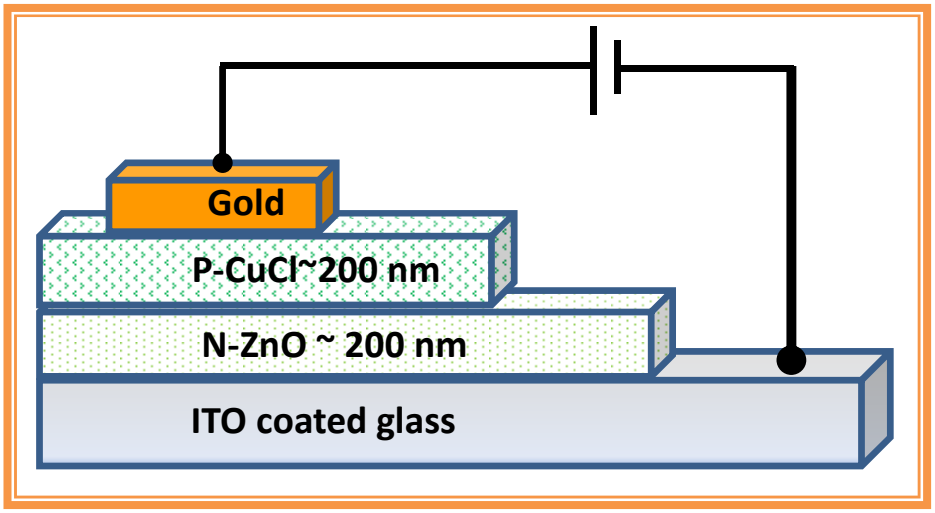

Figure 8.1: Au/CuCl/ZnO/ITO diode structure

In this chapter we report on the use of pulse laser deposited (PLD) n-ZnO and vacuum deposited (PVD) p-CuCl as polycrystalline thin films in order to fabricate proof-of-concept heterojunction based LEDs, noting also that CuCl has several advantages over GaN as descried previously (sec. 1.5). At the outset polycrystalline n-ZnO thin film [14] is deposited by PLD on cleaned indium tin oxide (ITO) coated glass substrate. Typical carrier densities in the ZnO films are $n \approx 1.1 \times 10^{20}$ cm^{-3} [15] and for p-CuCl, $p \approx 2.3 \times 10^{14}$ cm^{-3} have been reported [16] and were deposited on the n-ZnO thin film using an Edwards Auto 306A vacuum deposition system under a base pressure of 10^{-6} Torr. A gold contact top electrode was deposited using an Edwards Auto 306A vacuum deposition system at a base pressure of $\sim 10^{-6}$ Torr. The geometry of the Au/ZnO/CuCl/ITO diode is shown in **Figure 8.1** with a contact area of $\sim 7.85 \times 10^{-7}$ m^2.

8.2 Structural Properties

X-ray diffraction spectra for the n-ZnO/p-CuCl heterojunction, and the individual n-ZnO and p-CuCl films deposited on ITO coated glass substrates are shown in **Figure 8.2**. For the p-CuCl/ITO three main peaks are visible centred at 2θ≈28.5º, ≈47.5º and ≈56.4º, which correspond to the (111), (220) and (311) CuCl reflections, respectively.

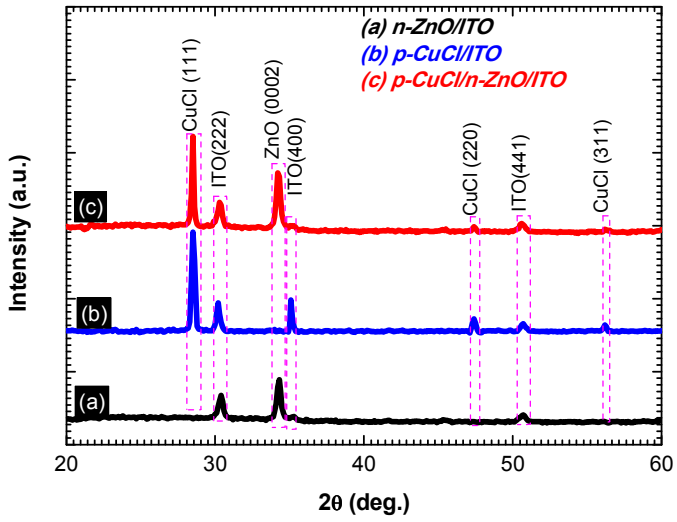

Figure 8.2: X-ray diffraction patterns of (a) n-ZnO/ITO, (b) p-CuCl/ITO and (c) n-ZnO/p-CuCl heterojunction layers deposited on ITO coated glass substrate.

These are characteristic of γ-CuCl in the zincblende configuration. The additional three 2θ peaks occurring at ≈30.55º, ≈35.22º and ≈50.47º on the CuCl/ITO structure corresponds to the ITO (222), ITO (400) and ITO (440), respectively [17]. The n-ZnO thin film deposited on ITO substrate shows only one ZnO peak centred at ≈34.30^{o} corresponding to the (0002) reflection and all other peaks come from the substrate ITO. The XRD spectrum for the n-ZnO/p-CuCl/ITO heterojunction structure reveals peaks at 2θ ≈ 28.5^{o}, 30.55º, 34.30^{o}, 47.5^{o}, and 50.47^{o}, which correspond to CuCl(111), ITO(222) ZnO(0002), CuCl(220), and ITO(441), respectively. Based on the XRD data, it can be concluded that there is no evidence of any intermediate compound formation and the obtained n-ZnO/p-CuCl heterojunction structure is structurally of high quality.

8.3 Optical Properties

Figure 8.3 shows the room temperature UV-Vis absorption spectra for p-CuCl/n-ZnO heterojunction, and the individual n-ZnO and p-CuCl films deposited on ITO coated glass substrates. This data shows that the absorption spectrum for the p-CuCl/n-ZnO heterojunction is dominated by the p-CuCl thin film (i.e. the absorption spectra for the p-CuCl/n-ZnO heterojunction and p-CuCl thin film is similar).

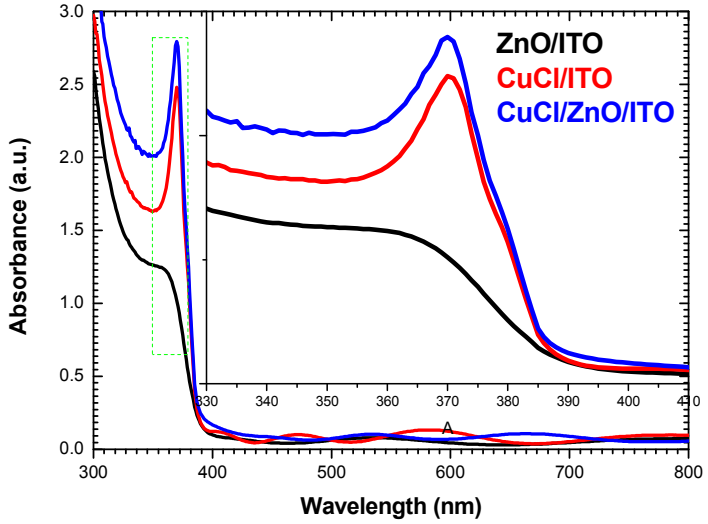

Figure 8.3: Room temperature UV-Vis absorption spectra of p-CuCl/n-ZnO heterojunction, and individual n-ZnO and p-CuCl films deposited on ITO coated glass substrate.

The p-CuCl/n-ZnO heterojunction and p-CuCl thin films both show high and low energy excitonic bands at ≈370 nm (≈3.351 eV) and at ≈377.1 nm (≈3.288 eV) historically related to the presence of the CuCl $Z_{1,2}$ and Z_3 free excitons, respectively (details in sec. 5.4). This is in excellent agreement with the values reported by other authors for vacuum evaporated and sputtered films [18-21].

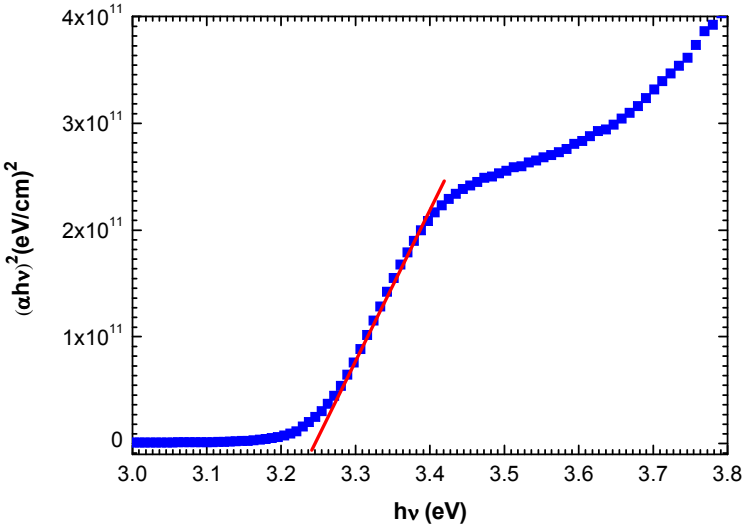

Figure 8.4: Plot of $(\alpha h\nu)^2$ vs. $h\nu$ (photon energy) for ZnO thin film deposited on ITO coated glass substrates for estimation of band gap energy.

The absorption feature for n-ZnO film is different with compared to the heterojunction or CuCl film, may be due to the high absorbance of p-CuCl film in the same region. The optical band gap of n-ZnO thin film was estimated from the absorbance spectra of n-ZnO thin film on ITO coated glass. The optical band gap of ZnO thin film was calculated by following relation [22]:

$$(\alpha h\nu) = A(h\nu - E_g)^{\beta} \tag{8.1}$$

where α is the absorption coefficient, $h\nu$ is the energy of absorbed photons, β=1/2 for a direct allowed transition, and A is the proportionality constant. The energy gap (E_g) of the n-ZnO was evaluated from the intercept of the linear portion of the $(\alpha h\nu)^2$ vs. $h\nu$ (photon energy) plot with the X-axis as shown in **Figure 8.4**. The band gap of n-ZnO thin film was estimated to be 3.24 eV (≈ 383 nm) by using the above method.

This value is higher by≈ 0.14 eV than previously reported thermally evaporated ZnO thin films deposited on ITO coated glass substrates [23].

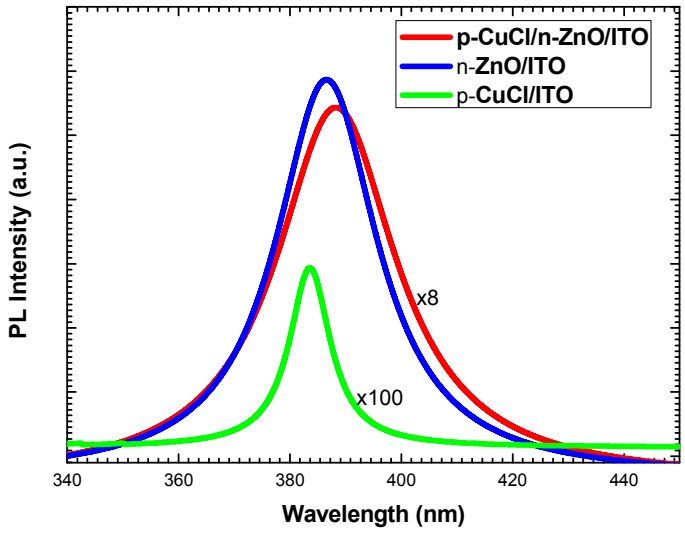

Figure 8.5 Room temperature PL spectra of p-CuCl/n-ZnO heterojunction, and individual n-ZnO and p-CuCl films deposited on ITO coated glass substrate.

The room-temperature PL spectrum of the p-CuCl/n-ZnO heterojunction and individual n-ZnO and p-CuCl films deposited on ITO coated glass substrate is shown in **Figure 8.5**. The PL spectrum of vacuum deposited CuCl without the ZnO film shows the familiar Z_3 free exciton-mediated PL emission peak at ≈383 nm (≈3.23 eV) [21]. The PL spectrum of the ZnO film exhibits a sharp peak in the vicinity of the band edge at ≈387 nm (≈3.20 eV), which might be attributed to the radiative annihilation of free and bound excitons [24]. A similar result has been reported for electrophoretic deposited ZnO thin films on ITO coated glass substrates [25]. Surprisingly the peak PL emission intensity for the ZnO film is higher than for the CuCl film. Equally interesting is the fact that the PL spectrum of the p-CuCl/n-ZnO heterojunction also displays a sharp peak at ≈389 nm (≈3.19 eV), which might be attributed to the exciton related recombination. The peak position is shifted towards the lower energy. The reason for this is currently under investigation. The PL behaviour of the p-CuCl/n-ZnO heterojunction is very similar to the ZnO film and the excitonic contribution of CuCl disappears. It is likely that photons emitted by the

CuCl (≈383 nm, E_g≈3.24 eV) are absorbed by the ZnO, whose optical band gap is also ≈3.24 eV as previously described. From the optical properties of the p-CuCl/n-ZnO heterojunction one can conclude that this structure could be of limited use for UV light emitters, due to self-absorption, but could be very promising for UV/Blue sensitive photovoltaic cells. We are continuing with research into this area.

8.4 Electrical properties

A typical *I-V* characteristic of the fabricated n-ZnO/p-CuCl heterostructure is shown in **Figure 8.6**. The figure shows definite diode-like characteristics. A turn on voltage of ~ 3.5 V and reverse bias breakdown voltage of -4.5 V was recorded.

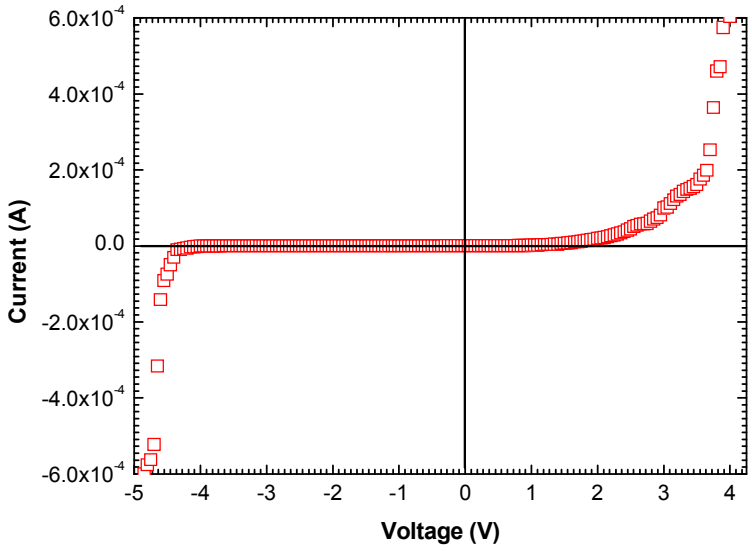

Figure 8.6: A typical current-voltage plot of the p-CuCl/n-ZnO heterojunction diode

In order to analyze the p-CuCl/n-ZnO heterojunction diode characteristics, we applied the thermionic emission model [26-28]. According to the thermionic emission model the diode forward biased current at temperature T can be expressed as:

$$I = I_0\left[\exp\left(\frac{qV}{nk_BT}\right)-1\right]. \qquad (8.2)$$

For V>> $3k_BT/q$, the expression (8.2) can be written as:

$$I = I_0 \exp\left(\frac{qV}{nk_BT}\right) \tag{8.3}$$

where I is the forward current, q is the electronic charge, V is the applied voltage, n is the ideality factor, k_B is Boltzmann's constant, T is the absolute temperature and I_0 is the saturation current, which can expressed as:

$$I_0 = AA^*T^2 \exp\left(-\frac{q\phi_B}{k_BT}\right) \tag{8.4}$$

where A is the effective diode area, ϕ_B is the Schottky barrier height A^* is the Richardson constant given by

$$A^* = \frac{4\pi q m^* k_B^2}{h^3} \tag{8.5}$$

where m^* is the effective electron mass, $m^* = 0.43\ m_0$ for the CuCl [26], and $m^* = 0.3\ m_0$ for the ZnO [26], and h is Planck's constant.

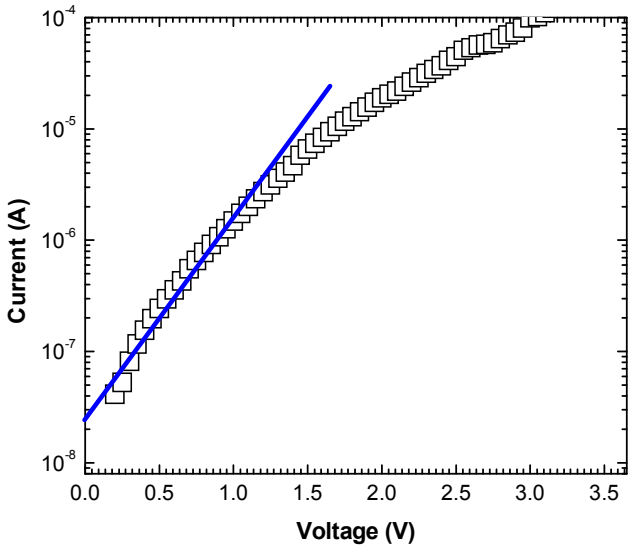

Figure 8.7: Semi-log *I-V* plot of p-CuCl/n-ZnO heterojunction diode

Figure 8.7 shows the semi-log *I-V* plot of the p-CuCl/n-ZnO heterojunction diode. From the slope and intercept of the linear fit in the lower bias voltage range, the values of n and ϕ_B have been extracted. The obtained values of n and ϕ_B are 4.6 and 0.72 eV, respectively.

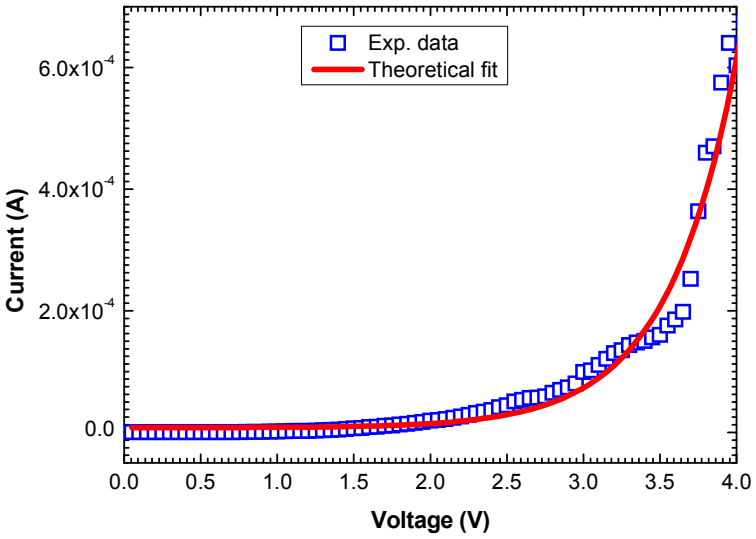

Figure 8.8: The plot of the Au/p-CuCl/n-ZnO/ITO structure forward bias current vs. applied voltage; the solid line is the theoretical fit.

To evaluate the barrier height of the Au/p-CuCl/n-ZnO/ITO structure the current-voltage experimental data was fitted by equation (8.1), and the comparison between experiment and theory is shown in **Figure 8.8**. Based on the fit of equation (8.2) and this experimental data the value of the barrier height and ideality factor was found to be 0.75±0.02 eV and 4.3, respectively. These values are very close to the estimated values obtained from equation (8.3) and (8.4). The value of the n is greater than unity, which indicates that the diode characteristic deviates significantly from ideal behaviour. This may be due to the high probability of electron and hole recombination in the depletion region between the p-CuCl and n-ZnO film, tunnelling currents or the presence of an interfacial layer [31]. The ideality factor value obtained for p-CuCl/n-ZnO heterojunction diode is a little higher than for comparable n-ZnO/p-AlGaN heterojunctions (n~3) and less than that for GaN p-n junction diodes (n~6) [29, 30].

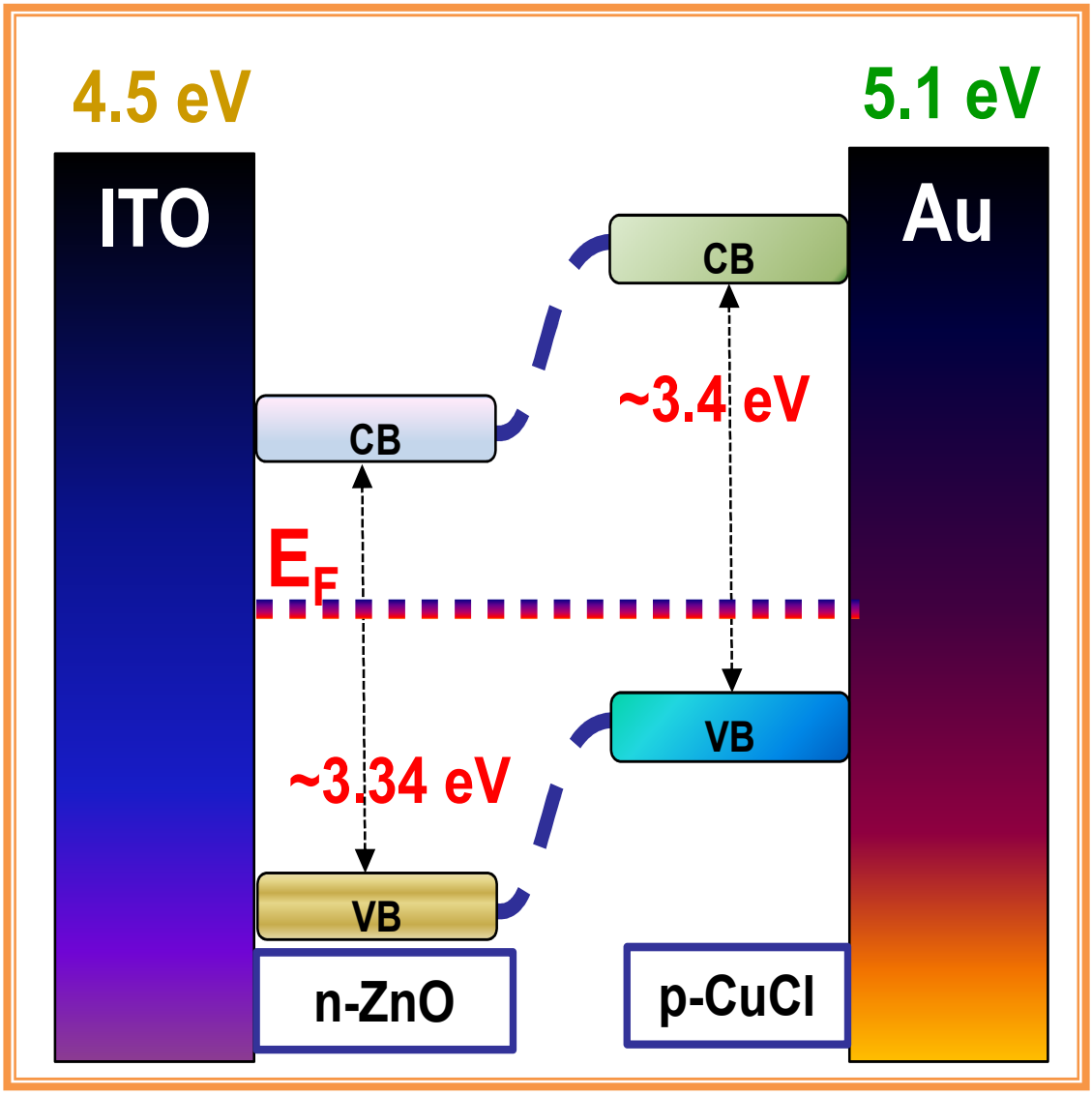

Figure 8.9: Proposed simplified energy band diagram of the Au/p-CuCl/n-ZnO/ITO heterojunction diode

We propose a simple energy band diagram for the Au/p-CuCl/n-ZnO/ITO heterojunction structure as shown in **Figure 8.9**. To construct the energy band diagram, the band gap energies (E_g) of n-ZnO and p-CuCl were assumed to be 3.37 eV and 3.4 eV, respectively [32, 33]. The electron affinity (ξ) of ZnO is 4.35 eV [32], but due to the lack of an electron affinity (ξ) value for CuCl, we could not estimate the energetic barrier for electrons and holes for this junction structure.

Summary

Proof-of-concept p-CuCl/n-ZnO heterojunction diodes were fabricated and their structural, optical and electrical properties were investigated. XRD measurements confirm that no intermediate compound form at the heterojunction and the obtained p-CuCl/n-ZnO heterojunction structure was structurally of high quality. The absorption characteristic for the heterojunction structure was almost same as for CuCl films, and this may be due to the higher absorbance of p-CuCl film in the same spectral region. Room temperature PL studies for the p-CuCl/n-ZnO heterojunction structure reveal that PL emission was similar to the ZnO film, which may be due a self-absorption phenomenon where photons emitted by the CuCl film were absorbed by the ZnO. Room temperature I-V characteristics show diode-like behaviour with typical barrier heights and ideality factors 0.72 eV and 4.6, respectively. Thus, while this structure may not be promising for UV emission, blue/UV photodetection and photovoltaics may be possible.

References

[1] M. Law, L. E. Greene, J. C. Johnson, R. Saykally, P. Yang; Nature Mater **4** (2005) 455

[2] L. J. A. Koster, W. J. van Strien, W. J. E. Beek, P. W. M. Blom; Adv. Funct. Mater **17** (2007) 1297

[3] W. J. E. Beek, M. M. Wienk, M. Kemerink, X. Yang, R. A. J. Janssen; J. Phys. Chem. **B** 109 (2005) 9505

[4] F. C. Krebs, Y. Thomann, R. Thomann, J. W. Andreasen; Nanotechnology **19** (2008) 424013

[5] Y. Liu, C. R. Gorla, S. Liang, N. Emanetoglu, Y. Lu, H. Shen, M. Wraback; J. Electron. Mater **29** (2000) 69

[6] S. Liang, H. Sheng, Y. Liu, Z. Huo, Y. Lu, H. Shen; J. Cryst. Growth **225** (2001) 110

[7] Z. K. Tang, G. K. L. Wong, P. Yu, M. Kawasaki, A. Ohtomo, H. Koinuma, Y. Segawa; Appl. Phys. Lett. **72** (1998) 3270

[8] A. Mitra and R. K. Thareja; J. Appl. Phys. **89** (2001) 2025

[9] X. Wang, J. Cole, A. M. Dabiran, H. O. Jacobs; NSTI-Nanotech **4** (2007) 526

[10] R. D. Vispute, V. Talyansky, S. Choopun, R. P. Sharma, T. Venkatesan, M. He, X. Tang, J. B. Halpern, M. G. Spencer, Y. X. Li, L. G. S. Riba, A. A. Iliadis, K. A. Jones; Applied Physics Letters **73** (1998) 348

[11] Y. I. Alivov, J. E. Van Nostrand, D. C. Look, M. V. Chukichev, and B. M. Ataev, Applied Physics Letters **83** (2003) 2943

[12] Y. I. Alivov, E. V. Kalinina, A. E. Cherenkov, D. C. Look, B. M. Ataev, A. K. Omaev, M. V. Chukichev, D. M. Bagnall, Appl. Phys. Let. **83** (2003) 4719

[13] A. Osinsky, J. W. Dong, M. Z. Kauser, B. Hertog, A. M. Dabiran, P. P. Chow, S. J. Pearton, L. Chernyak, Appl. Phys. Let. **85** (2004) 4272

[14] J. R. Duclère, R. O'. Haire, A. Meaney, K. Johnston, I. Reid, G. Tobin, J. P. Mosnier, M. G. Viry, E. McGlynn, M. O. Henry; J. Mater. Sci.**16** (2005) 421

[15] J. R. Duclèrea, M. Novotnyb, A. Meaneya, R. O'. Hairea, E. McGlynna, M. O. Henrya, J. P. Mosnier; Superlattices and Microstructures **38** (2005) 397

[16] F. O. Lucas, A Mitra, P. J. McNally, S. Daniels, A. L. Bradley, D. M. Taylor, Y. Y. Proskuryakov, K. Durose, D. C. Cameron; J. Phys. D **40** (2007) 3461

[17] Diffract plus-PDFMint-[JCP2.2CA:39-1058]

[18] L. O'Reilly, G. Natarajan, P. J. McNally, D. Cameron, O. F. Lucas, M. M. Rosas, L. Bradley, A. Reader; J. Mater. Sci: Mater. Electron **16** (2005) 415

[19] M. Nakayama, H. Ichida, H. Nishimura; J. Phys. **11** (1999) 45A

[20] A. Mitra, F. O. Lucas, L. O'Reilly, P. J. McNally, S. Daniels and G. Natarajan; J Mater Sci: Mater Electron **18** (2007) S21

[21] L. O'Reilly, O. F. Lucas, P. J. McNally, A. Reader, G. Natarajan, S. Daniels, D. C. Cameron, A. Mitra, M. M. Rosas, A. L. Bradley; J App. Phys. **98** (2005) 113512

[22] N. Shakti, P. S. Gupta; Applied Physics Research **2** (2010) 19

[23] C. Periasamy, P. Chakrabarti; J. Vac. Sci. Technol. B **27** (2009) 2124

[25] W. Z. Jun, W. Z. Jian, L. S. Chun, W. Z. Heng, L. Y. Ming, Y. J. Shan; Chinese Physics **13** (2004) 0750

[24] P. Zu, Z. K. Tang, G. K. L. Wong, M. Kawasaki, A. Ohtomo, H. Koinuma, and Y. Segawa; Solid State Communications **103** (1997) 459

[26] S. M. Sze; Physics of Semiconductor Devices 2nd edn (New York: Wiley) (1981)

[27] G. Horowitz; Adv. Mater **2** (1990) 287

[28] R. Kumar, N. Khare, V. Kumar, G. L. Bhalla, R. Srivastava, G. Chauhan, M. N. Kamalasanan; Semicond. Sci. Technol. **24** (2009) 045020

[29] Y. I. Alivov, E. V. Kalinina, A. E. Cherenkov, D. C. Look, B. M. Ataev, A. K. Omaev, M. V. Chukichev, D. M. Bagnall; Applied Physics Letters **83** (2003) 4719

[30] P. Deb, H. Kim, Y. Qin, R. Lahiji, M. Oliver, R. Reifenberger, T. Sands; Nano Lett. **6** (2006) 2894

[31] M. Campos, L. O. S. Bulhoes, C. A. Lindino; Sens. Actuators **87** (2000) 67

[32] T. P. Yang, H. C. Zhu, J. M. Bian, J. C. Sun, X. Dong, B. L. Zhang, H. W. Liang, X. P. Li, Y. G. Cui, G. T. Du; Materials Research Bulletin **43** (2008) 3614

[33] A. B. Kunz, R. S. Weidman, T. C. Collins; International Journal of Quantum Chemistry **16** (1979) 453

CHAPTER 9

CONCLUSIONS AND FUTURE WORK

9.1 Conclusions

CuCl is a direct bandgap material with potential for optoelectronic applications. In this research, the synthesis of CuCl nanocrystals embedded in a host matrix and deposited on flexible substrates via the spin coating technique was investigated. The optimization of its structural, optical and electrical properties was considered in order to fabricate an ELD.

γ-CuCl nanocrystals were synthesized based on the hydrothermal reaction of $CuCl_2.2H_2O$, alpha-D-glucose and de-ionized water. These were embedded into a glass-forming liquid as the host matrix, and successfully deposited on a variety of substrates by the spin coating method. The deposited films were heated at 120^o C for a range of time periods resulting in the formation of CuCl nanocrystals via a complexation-reduction-precipitation mechanism. XRD confirmed the preferential growth of CuCl nanocrystals whose average radius size was between ~14 and ~22 nm in the (111) orientation. Films annealed for 18 hours gave the optimum CuCl characteristics, and further annealing lead to a reduction of the CuCl (111) peak intensity. The average surface area of the CuCl hybrid films covered by the CuCl nanocrystals was roughly 40-60 % as revealed by the SEM measurements. EDX measurement confirmed that the composition of the incorporated crystals was Cu and Cl. The hybrid film surface roughness increased with annealing time. AFM measurements of the film's surface roughness gave an average value of between ~10 and ~14 nm.

FTIR spectroscopy measurements showed that the absorption peak intensities for CuCl hybrid films decreased with annealing time. XPS analysis revealed that the binding energy values obtained for Cu(2p) and Cl(2p) for typical 18 hour annealed hybrid film were consistent with the data in the literature for CuCl. Room temperature UV-Vis absorption increased with annealing time. All annealed films exhibited both the free exciton $Z_{1,2}$ absorption peak at ≈367.8 nm (≈3.371 eV) and the free exciton Z_3 peak at ≈37.1 nm (≈3.288 eV). At 15 K, the PL measurements confirmed the presence of free exciton (Z_3) at ≈3.213 eV, impurity bound exciton (I_1) at ≈3.191 eV, free biexciton (M) at ≈3.170 eV and impurity bound biexciton (N_1) at

≈3.141 eV emission peaks. XPS, UV-Vis and PL spectroscopy studies revealed that the 18 hour annealed gave the optimum optical properties for CuCl. As the temperature increased from 15 K to room temperature, the phonon induced interactions with exciton transitions had the following effects on the material properties: (a) decrease in PL intensity, (b) disappearance of transitions related to the impurity bound, free biexciton and impurity bound biexciton states due to the low binding energy of the impurity bound excitons, (c) PL emission line broadening due to an increase of the exciton-phonon interaction and, (d) a blue shift of the energy gap due to the interaction of lattice vibrations with excitons. CuCl hybrid films exhibit strong CL emissions in the UV region at room temperature. The optical properties of the organic-inorganic CuCl hybrid films were comparable with vacuum deposited and sputtered CuCl films. The structural and optical properties were somewhat influenced by the substrates.

The hole conductivity for the PSSQ-inorganic CuCl hybrid film was deduced to be $\approx 5.54\times10^{-9}$ Scm^{-1}. The activation energies of the CuCl hybrid films extracted from the Arrhenius plots for conductance were found to be 0.026 eV and 0.158 eV. At low fields, the current-voltage characteristics exhibited ohmic conduction, whereas high field conduction for $E > 1.5x10^{6}$ Vm^{-1} was shown to be an electrode limited Schottky emission conduction. The electronic parameters for Au/hybrid film/ITO diodes were evaluated and the values of barrier height, ideality factor and series resistance were found to be 0.84±0.05 eV, 1.12±0.8 and 50±2 MΩ, respectively, whereas the barrier height obtained from C-V measurement was 1.05±0.05 eV. The values of N_{SS} decreased with increasing E_{SS} -E_V values. The density distribution of the interface state changed from $\approx 6.2\ x10^{14}$ to $\approx 3.3x10^{14}$ $eV^{-1}cm^{-1}$. The hybrid film behaved as a single semiconducting material having a single electronic band structure. When the device was biased with a ≈100V (AC) supply, a strong room temperature electroluminescence emission at ≈384 nm (E≈3.229 eV) was observed for the Au/CuCl HF/ITO structure, which was attributed to Z_3 free exciton emission. The CuCl hybrid films structural, optical and electrical properties reveals promising results for optoelectronic applications.

Studies on the impact of ambient atmospheric ageing effects on CuCl hybrid films showed there was no significant change in measurements for samples aged for up to four months. Although CuCl is very hydroscopic, the hybrid film maintains its full material, electronic and optical properties for up to 4 months without any additional protective layer. Therefore, it was confirmed that the hybrid film is more stable than vacuum or sputter deposited CuCl thin films and its shelf life could be extended by blending with other polymer system such as PSSQ.

XRD measurements for p-CuCl/n-ZnO heterojunction diodes confirmed that no intermediate compound formed at the heterojunction. The absorption characteristic for the p-CuCl/n-ZnO heterojunction was dominated, whereas the PL feature was dominated by the n-ZnO thin film. Room temperature I-V characteristics for the p-CuCl/n-ZnO heterojunction structure show diode-like behaviour with the values of barrier height and ideality factor equal to 0.72 eV and 4.6, respectively. This diode structure may be useful for photodetection and photovoltaic cell fabrication, particularly for the blue/UV spectral regions.

9.2 Suggestions for Further Work

Film conductivity is an important parameter for electroluminescent device performance. We actually did attempt to embed the CuCl nanocrystals in a highly conductive polymer, poly(3,4-ethylenedioxythiophene) (PEDOT), but this quenched the CuCl $Z_{1,2}$ and Z_3 UV-Vis absorption as well as PL emission. CuCl nanocrystals were also embedded in a polyaniline (PANI) matrix; this improved the film conductivity ($\sigma \approx 2\times10^{-3}$ S cm^{-1}) but not enough. Another difficulty was related to the fact that the CuCl nanocrystals solutions were water based whereas most of the polymer solutions were not water based. Thus, when mixing the polymer matrix and CuCl solution the solutions were segregated. Some suggestions for further work that could lead to the fabrication of efficient electroluminescent devices, photovoltaic cells and photodetectors are highlighted below:

- **Improve film conductivity:** To increase the hybrid film conductivity, CuCl nanocrystals should be embedded into a highly conductive, transparent, miscible

low molecular weight polymer such as poly(dialkyldimethyl ammonium chloride), carboxymethyl cellulose (CMC), and methyl cellulose (MC). CuBr nanocrystals could be embedded into a highly conductive polymer, namely, PEDOT. Another possibility to improve the film conductivity could be the use of incorporated gold nanoparticles in the hybrid film.

- **p-n Junction based ELD:** In its natural state CuCl is a p-type semiconductor material; it is possible to produce n-type CuCl hybrid film by Zn doping [K. V. Rajani, F. O. Lucas, S. Daniels, D. Danieluk, A. L. Bradley, A. Cowley, M. M. Alam and P. J. McNally; *Thin Solid Films* **519** (2011) 6064], and one could envisage the eventual fabrication of a p-CuCl and n-CuCl:Zn hybrid film p-n homojunction light emitting diode. Another way to produce p-n nanojunctions may be by producing p and n type CuCl nanoparticles embedded into a polymer matrix.

- **As a reinforcing agent:** The inorganic CuCl nanoparticles may be embedded into organic polymers to increase the efficiency of organic light emitting diodes (OLED).

- **Photovoltaic Application:** Owing to the absorption effects observed for this prototype device structure (p-CuCl/n-ZnO), a potential avenue of research would be to investigate the changes in the I-V characteristics of the structure due to changes in the wavelength of light (e.g., red, blue, UV LED, etc.).

APPENDIX

Appendix A

Synthesis and Characterization of Copper (I) Chloride (CuCl) Nanocrystals in Conductive Polymer for UV light Emitters

A.1 Introduction

Intrinsic γ-Copper (I) Chloride is an ionic I-VII compound semiconductor material with relatively low conductivity. To fabricate an efficient electroluminescent device based on CuCl nanocrystals (NC) the conductivity of the CuCl NC film should be relatively high. In order to fabricate an efficient electroluminescent device, the electronic conductivity of the CuCl crystals must be improved. Thus, we present the preliminary results on CuCl nanocrystals embedded in Polyaniline. This composite structure opens up the possibility to develop efficient UV/white–light emitters based on CuCl technology. The room temperature UV-Vis absorption spectra for all CuCl films showed both $Z_{1,2}$ and Z_3 excitonic absorption features and the absorption intensity increased as the anneal time increased. Room temperature photoluminescence (PL) measurements of the hybrid films reveal very intense Z_3 excitonic emission. Room temperature X-ray diffraction (XRD) confirmed the preferential growth of CuCl nanocrystals whose average size is ≈ 40 nm in the <111> orientation. Resistivity measurements were carried out using a four-point probe system, which confirmed that the conductivity of the composite film was ~2×10^{-3} Scm^{-1}. This is an improvement when compared to the vacuum evaporated CuCl thin films (~ 2.3×10^{-7} Scm^{-1}).

A.2 Film deposition

CuCl nanocrystals were synthesized using $CuCl_2.2H_2O$ powder together with alpha-D-Glucose powder, with de-ionized water via a complexation-reduction-precipitation mechanism [1]. Subsequently the CuCl nanocrystals bearing aqueous solutions were mixed with 2.5 gm of the conductive polymer Polyaniline (PANI). The preparation of the conductive polymer polyaniline has been detailed previously [2, 3]. The solution was stirred for 5 minutes and finally filtered using a 0.2μm filter (Cellulose Acetate Filter Syringe). The films were deposited on glass substrate (~400 nm in

thickness) via spin coating by gradually increasing the speed from 0 to 2000 rpm over a period of one minute using a Laurell WS-400A-6PP/LITE spin coater in a class 100 clean room environment to avoid contamination. The coating was performed at room temperature. The films were subsequently heated at 140^{o}C for durations between 1 and 12 hours *in vacuo*. The structural properties of the hybrid films were measured by using XRD with measurements carried out in the locked coupled mode in the 2θ range of 5^{o} to 60^{o}. The optical absorption properties of the CuCl films were studied at room temperature using UV-Vis spectroscopy and PL spectroscopy employing a JY Horiba LabRam HR800 micro-PL system with a 325 nm He–Cd laser which was focused to a diameter of ~1 μm on the sample surface using a x40 UV objective lens. Current-Voltage (I-V) and resistivity measurements were carried out using a four point probe (Veeco) system.

A.3 Result and Discussion

Figure A.1 shows the room temperature θ-2θ X-ray diffraction spectrum of a typical nanocrystalline CuCl hybrid film, annealed for 4 hours at 140^{o} C, deposited on a glass substrate. This spectrum shows the two main diffraction peaks which correspond to (111) and (220) crystal plane orientations of cubic phase γ-CuCl, respectively.

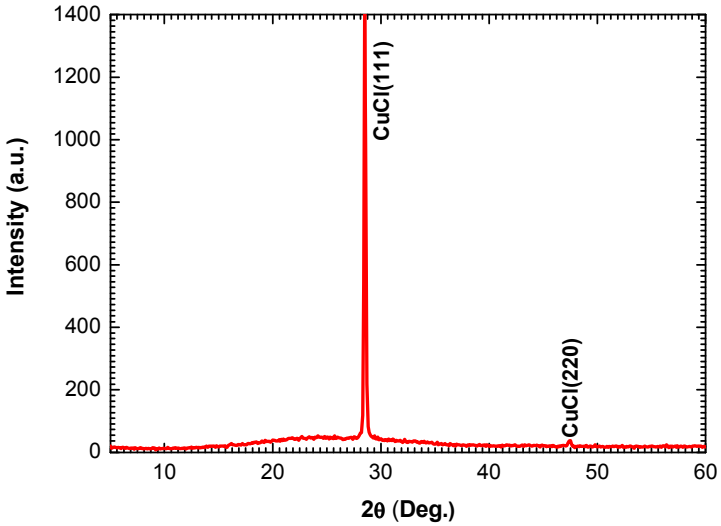

Figure A.1: X-ray θ-2θ diffraction spectrum of nanocrystalline CuCl hybrid film (CuCl/PANI) deposited on glass substrate and annealed at 140^{o} C for 4 hours.

This is in excellent agreement with data from our previous CuCl hybrid film [1]. The FWHM of the CuCl (111) peak was measured and an average crystallite size ≈40 nm was estimated using the Scherrer formula [4]. Figure A.2 show the room temperature UV-Vis absorption spectra of the nanocrystalline CuCl films deposited on glass substrates.

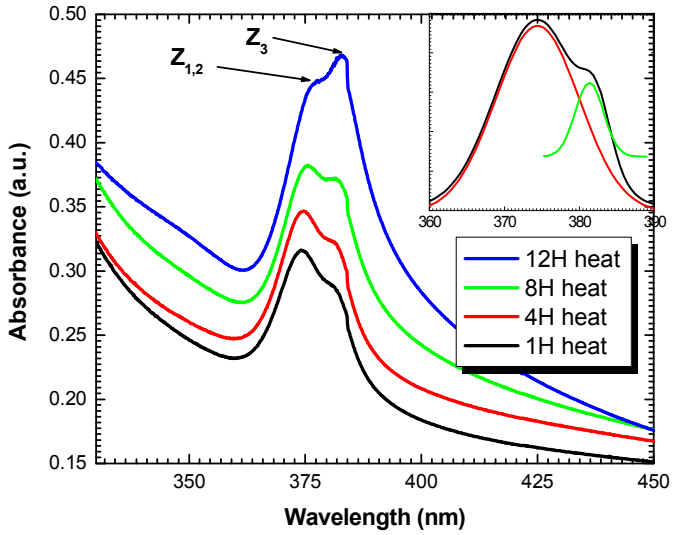

Figure A.2: Room temperature UV-Vis absorption spectra of nanocrystalline CuCl/PANI hybrid films deposited on glass substrates, and annealed at 140° C for varying periods of time as indicated (Inset: deconvolvted absorption peaks).

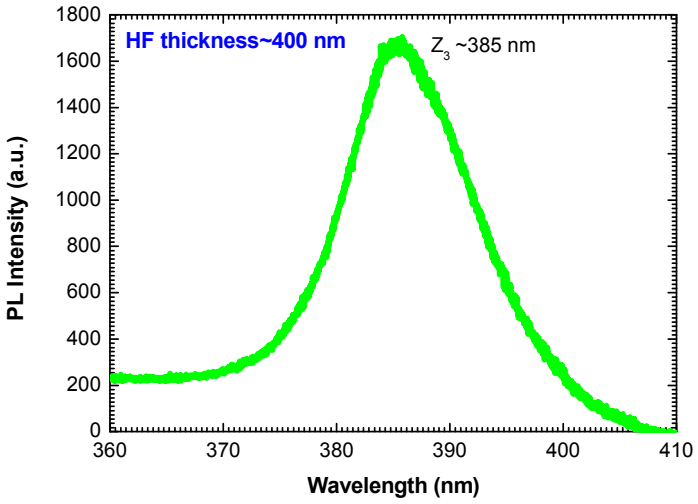

Figure A.3: Room temperature PL spectrum of nanocrystalline CuCl/PANI hybrid film deposited on glass substrate and annealed at 140° C for 4 hours.

In these spectra the films reveal both the usual $Z_{1,2}$ and Z_3 exciton absorption peaks. At room temperature, the hybrid films show the free exciton Z_3 absorption peak at ≈382 nm (~3.246 eV) and the free exciton $Z_{1,2}$ peak at ≈375 nm (~3.306 eV), which is in excellent agreement with previous hybrid, vacuum evaporated and sputtered films [1, 5, 6, 7]. The absorption intensity increases with increasing annealing times. Interestingly, the 12 hour annealed film exhibits a Z_3 free excitonic peak absorption intensity that is greater than the $Z_{1,2}$ excitonic peaks, which is opposite to the previously observed absorption characteristic of CuCl. The reason for this is currently unknown. Figure A.3 shows the room temperature PL spectrum of a typical spin coated CuCl/PANI hybrid film, annealed for 4 hours and deposited on a glass substrate. The hybrid film shows intense Z_3 free exciton-mediated PL emission at ≈385 nm (3.22 eV) again due to the large binding energy of the order 190 meV [8]. In general, the CuCl $Z_{1,2}$ peak is not observed in the PL emission spectra most likely due to self absorption [9].

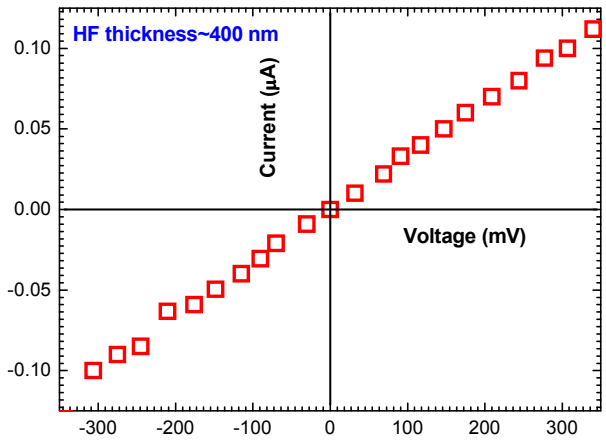

Figure A.4: Linear I-V characteristics of a typical nanocrystalline CuCl/PANI hybrid film deposited on glass substrate and annealed at 140^{o} C for 4 hours.

The resistivity of the hybrid film was also investigated using a standard four-point probe. The CuCl hybrid film current-voltage plot was found to be Ohmic in nature as shown in figure A.4. The conductivity of the hybrid film is ~2 × 10^{-3} Scm^{-1}, which is big improvement compared to PSSQ based CuCl hybrid films (~3.54 × 10^{-8} Scm^{-1}).

References

[1] M. M. Alam, F. Olabanji Lucas, D. Danieluk, A. L. Bradley, K.V. Rajani, S. Daniels, P. J. McNally, J. Phys. D: Appl. Phys. **42** (2009) 225307

[2] O. Ngamna, A. Morrin, A. J. Killard, S. E. Moulton, M. R. Smyth, G. G. Wallace, Langmuir. **23** (2007) 8569

[3] S. E. Moulton, P. C. Innis, L. A. P. KaneMaguire, O. Ngamna, G. G. Wallace, J. Appl. Phys. **4** (2004) 402

[4] B. D. Cullity and S. R. Stock, Elements of X-ray Diffraction, 3rd ed. Prentice Hall. (2001) 170

[5] L. O'Reilly, G. Natarajan, P.J. McNally, D. Cameron, O.F. Lucas, M. Martinez-Rosas, L. Bradley, A. Reader, J. Mater. Sci: Mater. Electron **16** (2005) 415

[6] A. Mitra, F. O. Lucas, L. O'Reilly, P. J. McNally , S. Daniels and Gomathi Natarajan, J Mater Sci: Mater Electron. **18** (2007) S21

[7] L. O'Reilly, O. F. Lucas, P. J. McNally, and A. Reader, Gomathi Natarajan, S. Daniels, and D. C. Cameron, A. Mitra, M. Martinez-Rosas, and A. L. Bradley, J App Phys. **98** (2005) 113512

[8] L. O'Reilly, A. Mitra , G. Natarajan O. F. Lucas, P. J. McNally, S. Daniels, D. C. Cameron , A. Reader, and A. L. Bradley, J Crystal Growth. **287** (2006) 139

[9] M. Ueta, H. Kanzaki, K. Kobayashi, Y. Toyozawa, E. Hanumara, Excitonic processes in Solids, Springer, Berlin, (1986) 122

Appendix B

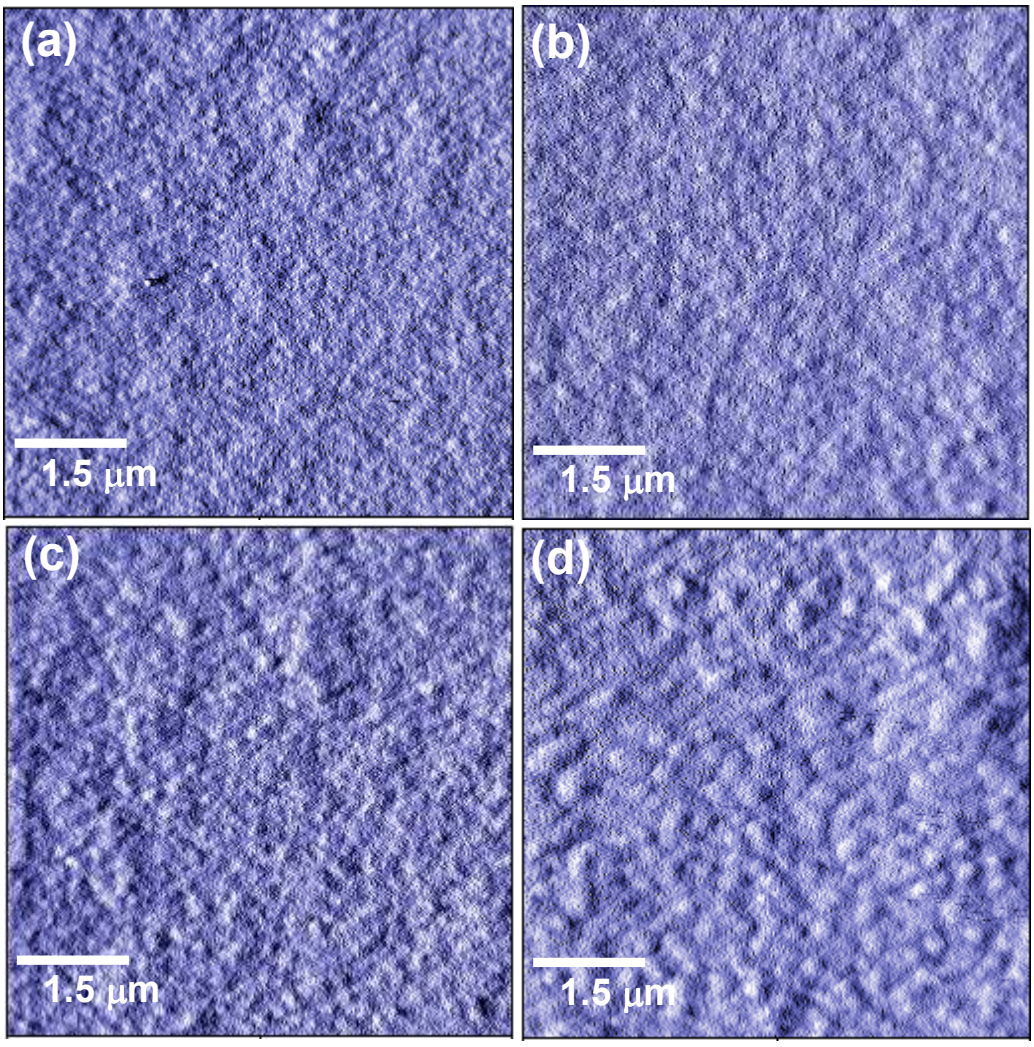

Figure B1: AFM images for the CuCl/PSSQ hybrid film deposited on glass substrate and annealed at 120^{o} C for different time durations:(a)1 H (b)12 H (c) 18 H and (d) 24 H. Thickness≈ 500 nm.

List of Tables

No.	Name of the Tables	Page No.
1.1	A selection properties of different semiconductor materials	07
1.2	Precursor materials, solvents and processing temperature for synthesis of GaN, ZnO and CuCl nanocrystals	09
2.1	Some Properties of Copper (II) Chloride	21
2.2	Some Properties of Copper (I) Chloride	23
2.3	Some physical properties of Dextrose	26
3.1	Luminescence types, applications and typical efficiencies	55
4.1	Expected ratios of different CuCl peaks from powder diffraction file	69
5.1	XPS experimental results for CuCl hybrid films	88

List of Figures

No.	Name of the Figure	Page No.
1.1	Global LED shipment forecast	04
1.2	Band structure and basic operation of a p-n junction ELD	06
1.3	Energy band diagram illustrating the six primary physical processes of importance for operation of an MIS based ELD	06
2.1	Crystal structure of copper (II) chloride	20
2.2	Crystal structure of copper (I) chloride	22
2.3	Schematic development of conduction and valence states due to s, p and d electrons at the Brillouin Zone Centre Γ in the cubic crystal field of the zincblende structure	24
2.4	Chemical structure of alpha-D-glucose	27
2.5	Chemical structure of Polysilsesquioxane in (a) cage form and (b) network form	28
2.6	Schematic diagram of the spin coating system used in this study	31
2.7	The film thickness depends on different process parameter	32
2.8	Flow diagram representing the optimum process parameters for synthesis of CuCl nanocrystalline hybrid films	34
3.1	The electromagnetic spectrum	40
3.2	Bragg's Diffraction Scheme	41
3.3	Basic Set–Up of D8 Advance X-Ray Diffractometer, Bragg-Brentano Geometry	42
3.4	Signals produced when an electron beam is incident on a sample	44
3.5	Schematic of (a) typical SEM and (b) Path of the electron beam in this system	45
3.6	Schematic representation of a typical modern AFM	47
3.7	The schematic diagram of a monochromatic XPS system	49
3.8	The schematic diagram of a UV-Vis spectrophotometer	51
3.9	Block diagram of FTIR spectrometer	53
3.10	Michelson interferometer	53
3.11	A typical interferogram	54

3.12	Schematic diagram of radiative transitions in a semiconductor material; (a) Conduction to valance band (b) excitonic recombination (c) donor and valance band (d) conduction band and (e) donor to acceptor	56
3.13	Typical set up for the measurement of PL	58
3.14	Schematic illustration of electroluminescence system	60
3.15	Schematic of the CuCl hybrid film electrical characterization system	61
4.1	X-ray θ-2θ diffraction spectra of CuCl hybrid films grown on glass substrates.	70
4.2	% Crystallinity of CuCl (a), FWHM and average crystallite size (b) vs. annealing time	71
4.3	X-ray θ-2θ diffraction spectra for 18 hours annealed CuCl hybrid films deposited on different substrates	73
4.4	SEM images of typical CuCl hybrid films grown on (a) glass (b) ITO and (c) silicon substrate.	75
4.5	EDX spectrum for 18 hours annealed CuCl hybrid films (a) area and (b) point scan	76
4.6	3D AFM micrographs of CuCl hybrid films deposited on silicon substrates for different anneal times.	79
4.7	Average film surface roughness as a function of annealing time. CuCl hybrid films on silicon substrates.	79
4.8	2D and 3D AFM micrographs of CuCl hybrid films deposited on (a) glass (b) ITO and (c) silicon substrates.	80
5.1	FTIR absorption spectra of CuCl hybrid films grown on silicon substrates	80
5.2	The survey scan XPS spectra of organic-inorganic CuCl hybrid films (a) as-deposited (b) annealed at 120^{o} C for 18 hours.	88
5.3	XPS spectra taken from the Cu2p and Cl2p regions of the CuCl hybrid film (a) ASD film (b) annealed film	90
5.4	UV-Vis absorption spectra of CuCl hybrid films grown on glass substrates.	91
5.5	UV-Vis absorption spectra for CuCl hybrid films annealed 18 hours	91
5.6	Low (15 K) temperature PL spectra of CuCl hybrid films	93

5.7	Room temperature PL spectra of a selection CuCl hybrid films	94
5.8	Room temperature Z_3 free excitonic emission peak position and FWHM for typical CuCl hybrid films as a function of annealing time.	94
5.9	Room temperature PL spectra CuCl hybrid films annealed for 18 hours	95
5.10	Photoluminescence spectra of CuCl hybrid film at different temperatures.	96
5.11	Fitted photoluminescence spectra of CuCl hybrid films with fit (solid curve) based on Lorentzian line shapes at 15 K	97
5.12	Photoluminescence spectra of CuCl hybrid films with fit (solid curve) based on Lorentzian line shapes at 300 K	97
5.13	Excitonic, biexcitonic and bound biexciton emission line intensity vs. excitation power analysis on double logarithmic scale.	98
5.14	Arrhenius plot of the integrated Z_3 excitonic PL intensity vs. inverse temperature. Fitting with a two-step thermal quenching process is shown with a solid line for CuCl hybrid film.	100
5.15	Temperature dependence of full width at half maximum (FWHM) of the CuCl hybrid film Z_3 free exciton peak; the solid line is the theoretical fit.	101
5.16	Z_3 free exciton emission peak position shift as a function of temperature; the solid line is the theoretical fit.	106
5.17	Room temperature CL spectrum of a typical CuCl hybrid film annealed for 18 hours on a silicon substrate	107
5.18	CL spectra of a typical CuCl hybrid film for different Accelerating Voltage	109
5.19	CL spectra of a typical CuCl hybrid film for different probe current, inset CL peak intensity as a function of probe current	109
6.1	Au/CuCl hybrid film/ITO diode structure	119
6.2	A typical current-voltage plot of organic-inorganic CuCl hybrid film	121
6.3	Arrhenius plot for conductance for CuCl hybrid film	122
6.4	The semi-logarithmic current-voltage characteristics of the Au/CuCl hybrid film/ITO Schottky diode.	123
6.5	I-V characteristics of the Au/CuCl hybrid film/ITO diode on double logarithmic scale.	124

6.6	Fowler-Nordheim plot of CuCl hybrid film.	126
6.7	Voltage dependence of current plot of log ($I/V^{1/2}$) vs. $V^{1/2}$	127
6.8	The plot of the Au/CuCl hybrid film/ITO structure forward bias current vs. applied voltage; the solid line is the theoretical fit.	129
6.9	The plot of *ln (I)* vs. *V* for the Au/CuCl hybrid film/ITO structure	130
6.10	The plot of *dV/dln(I)* vs. *I* for the Au/CuCl hybrid film/ITO structure.	131
6.11	The plot of *H(I)* vs. *I* for the Au/CuCl hybrid film/ITO structure.	132
6.12	The plots of *I* vs. *V* for obtained V_D and V_i values of Au/CuCl hybrid film/ITO structure.	132
6.13	Typical plots of C and $1/C^2$ versus V for the Au/hybrid film/ITO Schottky diode	134
6.14	Calculated interface state energy distribution of the Au/CuCl hybrid film/ITO Schottky diode	136
6.15	Schematic energy level diagram for the Au/CuCl hybrid film/ITO Schottky diode	137
6.16	Schematic diagram of the CuCl hybrid electroluminescent device	138
6.17	Average room temperature EL spectrum of 5 CuCl hybrid EL devices were biased with a 100 V AC (a) and a micrograph of the EL emission (b)	139
7.1	XRD patterns of CuCl hybrid films deposited on glass substrates.	148
7.2	FTIR absorption spectra of CuCl hybrid films deposited on silicon substrates.	149
7.3	UV-Vis absorption spectra of the ASD and 1-6 month aged CuCl hybrid films deposited on glass substrates.	150
7.4	Room temperature PL emission spectra of CuCl hybrid films deposited on silicon substrates, inset variation of FWHM with ageing time.	151
7.5	Room temperature EL spectrum of the ASD and 1-3 month aged CuCl hybrid ELD	152
8.1	Au/CuCl/ZnO/ITO diode structure	157
8.2	X-ray diffraction patterns of (a) n-ZnO/ITO, (b) p-CuCl/ITO, and (c) n-ZnO/p-CuCl heterojunction layers deposited on ITO coated glass substrate.	158

8.3 Room temperature UV-Vis absorption spectra of p-CuCl/n-ZnO heterojunction, and individual n-ZnO and p-CuCl films deposited on ITO coated glass substrate. 159

8.4 Plot of $(\alpha h\upsilon)^2$ vs. $h\upsilon$ (photon energy) for ZnO thin film deposited on ITO coated glass substrates for estimation of band gap energy. 160

8.5 Room temperature PL spectra of p-CuCl/n-ZnO heterojunction, and the individual n-ZnO and p-CuCl films deposited on ITO coated glass substrate. 161

8.6 A typical current-voltage plot of the p-CuCl/n-ZnO heterojunction diode 162

8.7 Semi-log I-V plot of p-CuCl/n-ZnO heterojunction diode 163

8.8 The plot of the Au/p-CuCl/n-ZnO/ITO structure forward bias current vs. applied voltage; the solid line is the theoretical fit. 164

8.9 Proposed simplified energy diagram of the Au/p-CuCl/n-ZnO/ITO heterojunction diode. 165

List of Publications

Journals

01. **M. M. Alam**, F. O. Lucas, D. Danieluk, A. L. Bradley, K.V. Rajani, S. Daniels and P. J. McNally; *"Hybrid Organic–Inorganic Spin-on-Glass CuCl Films for Optoelectronic Applications"* Journal of Physics D: Applied Physics, 42 (2009) 225307.

02. **M. M. Alam**, F Olabanji Lucas, A. Cowley, D. Danieluk, A L Bradley, S. Daniels and P. J. McNally, "*Temperature dependent photoluminescence of nanocrystalline γ-CuCl hybrid films"* Journal of Luminescence, LUMIN-D-11-00194 (2011)

03. **M. M. Alam**, A. Cowley, S. Daniels and P. J. McNally; *"Evaluation of conduction mechanism and electronic parameters for Au/Organic-Inorganic CuCl hybrid film/ITO structures"* Semiconductor Science and Technology, 26 (2011) 095021

04. A. Cowley, F. O. Lucas, E. Gudimenko, **M. M. Alam**, D. Danieluk, A L Bradley and P. J. McNally; *"Electroluminescence of γ-CuBr thin films via vacuum evaporation deposition"* Journal of Physics D: Applied Physics, 43 (2010) 165101.

05. K. V. Rajani, F. O. Lucas, S. Daniels, D. Danieluk, A. L. Bradley, A. Cowley, **M. M. Alam**, P. J. McNally; *"Growth of n-type γ-CuCl with improved carrier concentration by pulsed dc sputtering: structural, electronic and UV emission properties"* Thin Solid Films 519 (2011) 6064.

06. K. V. Rajani, S. Daniels, **M. M. Alam** and P. J. McNally; *"Ultra Thin Chromium Transparent Metal Contacts by Pulsed DC Magnetron Sputtering"* Phys. Status Solidi A 207 (2010) 1586.

07. **M. M. Alam**, F. Olabanji Lucas, A. Cowley, Karl Crowley, S.Daniels, K.V. Rajani, P. J. McNally; *"Synthesis and Characterization of Copper (I) Chloride (CuCl) Nanocrystals in Conductive Polymer for UV light Emitters"* MRS Conference Proceedings, Symp. C, DOI:1247-C04-21 (2010) (Accepted for publication)

08. K. V. Rajani, F. Olabanji Lucas, **M. M. Alam**, S. Daniels and P. J. McNally; *"Zn Doped Nanocrystalline CuCl Thin Films for Optoelectronic Applications"* MRS Conference Proceedings, Symp. T 1260 (2010) T10-07.

Conferences

01. **M. M. Alam**, F. Olabanji Lucas, S. Daniels and P. J. McNally; *"Synthesis, Structural and Optical properties of γ-CuCl hybrid films"* Oral presentation, *Photonics Ireland,* Kinsale, Co-Cork, Ireland 14-16, August, (2009).

02. **M. M. Alam,** F Olabanji Lucas, D. Danieluk, A L Bradley, K.V. Rajani, S. Daniels, P. J. McNally; *"Hybrid Organic–Inorganic Spin-on-Glass CuCl Films for Optoelectronic Applications"* Poster presentation, Symposium: K *European Materials Research Society, Spring Meeting,* Strasbourg**,** France, 8-12, June (2009).

03. K. V. Rajani, S. Daniels, P. J. McNally, F. O. Lucas, **M. M. Alam "**Ultra Thin Chromium Transparent Metal Contacts by Pulsed DC Magnetron Sputtering" *European Materials Research Society (EMRS), 2009, Strasbourg, France,* 8-12, June (2009).

04. K. V. Rajani, S. Daniels, F. O. Lucas, **M. M. Alam**, P. J. McNally "Transparent Electrodes for Optoelectronics Industry based on Ultrathin Chromium Films" *Photonics Ireland,* Kinsale, Co-Cork, Ireland 14-16, August, (2009).

05. **M. M. Alam,** S. Daniels and P. J. McNally; *"Fabrication of p-CuCl/n-ZnO heterojunction for UV-light emitting diode"* Faculty Research Day, Dublin City University, Dublin, Ireland, 12, May (2011).

06. **M. M. Alam,** S. Daniels and P. J. McNally; *"Synthesis and Characterization of Nanocrystalline CuCl Hybrid Films for Electroluminescence Device Fabrication"* Inspire Nanophotonics Videoconference Seminars, Dublin, Ireland, 16, February (2011).

List of Acronyms

AFM	Atomic Force Microscopy
LED	Light Emitting Diode
SSL	Solid-State Lighting
CFL	Compact Fluorescent Lamp
LED	Light Emitting Diode
OLED	Organic Light Emitting Diode
SSL	Solid-State Lighting
RGB	Red-Green-Blue
eV	electron Volt
MIS	Metal Insulator Semiconductor
ELD	Electroluminescent Device
EL	Electroluminescence
WLED	White Light Emitting Diode
UV	Ultra-Violet
Vis	Visible
SEM	Scanning Electron Microscopy
XRD	X-ray Diffraction
XPS	X-ray Photoelectron Spectroscopy
FTIR	Fourier Transform Infrared Spectroscopy
NC	Nano crystal
CuCl	Copper(I) Chloride
ZnO	Zinc Oxide
PSSQ	Polysilsesquioxane
EDX	Energy Dispersive X-ray analysis
CL	Cathodoluminescence
ITO	Indium Tin Oxide
ASD	As-deposited
HF	Hybrid Film
FWHM	Full Width at Half Maximum

PF	Pool-Frenkel
SE	Schottky Emission
FN	Fowler-Nordheim
HOMO	Highest Occupied Molecular Orbital
LUMO	Lowest Unoccupied Molecular Orbital
CB	Conduction Band
VB	Valence Band
PL	Photoluminescence